

UNIVERSITY OF TRIESTE

Physics Department



Master Degree in Physics

**Polarization of Gravitational Waves as a
Tool for Testing General Relativity**

**Polarizzazione di Onde Gravitazionali come Test per la
Teoria della Relatività Generale**

Candidate
Giuseppe Troian

Supervisor
Prof. Edoardo Milotti

Academic Year 2022/2023

*A Helen
e Fafa*

Contents

Introduzione	4
Introduction	7
1 Gravitational Waves	11
1.1 The Gravitational Wave Equation	11
1.2 The Transverse Traceless Gauge	14
1.3 Detection of Gravitational Waves	15
1.4 GW Generation and CBCs	22
2 GW Detectors	29
2.1 Noise in GW Detectors	29
2.2 GW Data Analysis	35
2.3 GW Facilities	37
2.3.1 Current Facilities	37
2.3.2 Third Generation Facilities	40
2.4 Antenna Patterns	43
2.4.1 Formal Derivation	43
2.4.2 Implementation in GWBENCH	45
2.4.3 The Mismatch with H. Asada	48
3 Non-GR Polarization Modes	55
3.1 Non-Tensor Polarization Modes	55
3.2 Null Streams	59
3.2.1 Approaching Real Data: GW170817	62
4 Localization of GW Sources	66
4.1 Triangulation with GW Detectors	66
4.1.1 Self-Triangulation	69
4.2 How Localization Behaves	74
4.2.1 Distance Dependence	74
4.2.2 Chirp Mass Dependence	76
4.2.3 Mass Ratio Dependence	77
5 Simulations for Measures of the Null Streams	81
5.1 The Code	81
5.1.1 The Stationary Phase Approximation	81
5.2 Results	88
5.2.1 Distance Dependence	89

5.2.2	Chirp Mass and η Dependence	94
5.3	Three Detector Maps	100
Conclusion		104
A Additional Tables		107
B Additional Plots		112

Introduzione

Le onde gravitazionali sono oggetto di interesse scientifico e di dibattito da prima che la teoria della relatività generale fosse teorizzata da Albert Einstein [1] nel 1915, trovando spazio in molte teorie della gravità successive a quella di Newton, spesso ispirate al formalismo della teoria elettromagnetica. Nel 1916 [2], lo stesso Einstein provò l'esistenza delle onde gravitazionali nell'ambito della relatività generale come conseguenza di un'emissione di quadrupolo di massa (riformulando la teoria nella sua versione corretta con un articolo del 1918 [3]), ottenendo anche un'espressione per l'energia trasportata da un'onda di questo tipo. Questo a verifica del fatto che le onde gravitazionali non siano dovute ad una semplice perturbazione del sistema di coordinate in uso (la questione è ridiscussa in termini più approfonditi nell'elaborato), ma ad un effettivo trasporto di energia.

La teorizzazione e realizzazione di una misura delle onde gravitazionali ha costituito un' ulteriore difficoltà per la comunità scientifica internazionale, i cui sforzi si sono capitalizzati grazie alla misura diretta avvenuta nel settembre del 2015 da parte dei rivelatori LIGO (*Laser interferometer Gravitational-Wave Observatory*) [4]. Questo ha permesso di focalizzare l'interesse scientifico su argomenti diversi fra loro: dal problema dell'osservazione delle onde gravitazionali si è passati alla fisica degli eventi astrofisici causa di questi segnali. Un altro campo in cui le onde gravitazionali si sono inserite come naturale strumento di misura è quello dei test di gravità. Un test di gravità consiste nella misura di eventuali deviazioni dal comportamento teorizzato dalla teoria comunemente accettata, che in questo momento è ancora la relatività generale. Attualmente, molti test sono già stati implementati (generalmente non coinvolgendo le onde gravitazionali), non fornendo tuttavia risultati significativi, confermando la relatività generale a livelli di accuratezza sempre migliori.

In questa tesi ci si pone l'obiettivo di delineare teoricamente un test di gravità basato sulle onde gravitazionali (lavoro compilativo) e di caratterizzare le capacità dei rivelatori attuali e di generazione futura nella realizzazione di un tale test (lavoro sperimentale).

Nella teoria della relatività generale le polarizzazioni possibili per le onde gravitazionali sono due, denominate "polarizzazioni tensoriali", e si ottengono esplicitamente considerando l'equazione delle onde gravitazionali nel sistema di riferimento *Transverse Traceless*, di cui si parlerà nei capitoli seguenti in termini rigorosi e matematicamente accurati. In una generica teoria di gravità si può invece arrivare a sei modi di polarizzazione complessivi: i due modi tensoriali della relatività generale, due modi vettoriali e due modi scalari [5]. Risulta quindi intuitivo pensare di poter provare la validità della relatività generale sulla base dei modi di polarizzazione delle onde gravitazionali.

In particolar modo ci si concentra sull'approccio matematico fornito dai *null stream*, combinazioni dei segnali misurati da almeno tre rivelatori contemporaneamente per un evento del tipo *Compact Binary Coalescence*, ovvero la coalescenza di due oggetti compatti (generalmente buchi neri o stelle di neutroni). Questi segnali permettono la misura dei null stream ad un ottimo livello di accuratezza [6].

I *null stream* sono quantità costruite *ad hoc* in modo da essere identicamente nulle nel caso il segnale misurato dai rivelatori contenga esclusivamente modi di polarizzazione tensoriali, restituendo valori non banali nel caso di modi aggiuntivi. Nell'approccio più semplice, i *null stream* non permettono il *disentangling* dei singoli modi di polarizzazione, ma restituiscono soltanto un'informazione circa il contenuto totale di polarizzazione non tensoriale in un segnale.

Ulteriormente, si possono costruire *null stream* avanzati, come viene ampiamente discusso nei capitoli che seguono, tramite i quali è possibile ottenere dei vincoli sui singoli modi di polarizzazione presenti nel segnale misurato.

Il lavoro presentato si concentra sulle capacità dei rivelatori di onde gravitazionali di generazione seconda e terza di misurare queste quantità.

L'attività di ricerca svolta si concentra dunque sulla simulazione di segnali gravitazionali e la rispettiva analisi con particolare attenzione alla localizzazione delle sorgenti (fondamentale per la definizione degli *antenna pattern*, elemento presente nell'espressione dei *null stream*). Per questi scopi si usa la libreria di simulazione e analisi GWBENCH [7]. Grazie all'implementazione del formalismo di Fisher, GWBENCH permette di simulare ed analizzare eventi di onde gravitazionali molto più velocemente rispetto agli algoritmi *Gauss-Markov Chain*, molto più usati in questo ambito.

Utilizzando un segnale con determinate caratteristiche (*signal-to-noise ratio* (SNR) e posizione della sorgente fra tutte) si può determinare la capacità di localizzazione di uno o più rivelatori. A partire da un errore sulla localizzazione di una sorgente, si può stimare un errore sugli *antenna pattern* che contribuisce alla fluttuazione dei *null stream*. Questa incertezza sui *null stream* fa sì che una *network* di rivelatori possa essere considerata valida o meno nel discriminare un segnale completamente tensoriale (quindi compatibile con la relatività generale) da un segnale con modi extra-tensoriali per un determinato SNR del segnale in questione.

I criteri di caratterizzazione dei rivelatori vengono ora qualitativamente riasunti. La procedura viene affrontata in termini più precisi nei capitoli successivi dell'elaborato.

Per un determinato segnale, in caso di segnale completamente tensoriale, si deve ottenere un *null stream* vicino a zero, non compatibile con il rumore degli strumenti in questione entro una determinata soglia di accettabilità. Questo significa che il *null stream* sarà in generale coperto dal rumore strumentale.

Inoltre, il segnale deve mostrare un *null stream* con un $\text{SNR} > t$, con t una determinata soglia, nel caso di *injection* di modi non tensoriali al segnale. Questo significa che il rumore strumentale non è troppo alto per coprire il *null stream*. A questo punto, la configurazione di rivelatori considerata può essere ritenuta buona per discriminare fra la relatività generale ed altre teorie per segnali di onde gravitazionali con un SNR come quello considerato.

L'elaborato viene strutturato in modo da dare una descrizione precisa del lavoro svolto, ma anche per contestualizzarlo in termini formali e scientifici. Per questo motivo, il capitolo 1 (*chapter 1*) introduce le onde gravitazionali

in maniera scolastica, aiutando anche a familiarizzare con il formalismo e la notazione utilizzati nella descrizione dell'attività svolta e più in generale nei capitoli successivi. Il capitolo 2 (*chapter 2*) riassume in termini generici le caratteristiche degli strumenti considerati, sia per i rivelatori attuali che per quelli di generazione futura. Il capitolo 3 (*chapter 3*) connette il campo delle onde gravitazionali con la teoria dei *null stream*, e gli sforzi fatti finora in questa direzione. Al capitolo 4 (*chapter 4*) si caratterizzano le capacità di localizzazione delle configurazioni di rivelatori considerate, osservandone il comportamento al variare di alcune caratteristiche dell'evento considerato: la distanza della sorgente, e due parametri relativi alla massa del sistema e dei singoli componenti. Questa parte può essere ritenuta preparatoria al lavoro di tesi. Il capitolo 5 (*chapter 5*) contiene l'effettivo lavoro di tesi, riassumendone la procedura ed i risultati. Si fa riferimento alle risposte delle configurazioni di rivelatori per segnali di onde gravitazionali con contributi scalari o vettoriali, e tali risposte vengono esaminate al variare degli stessi parametri per cui si è caratterizzata la localizzazione degli eventi al capitolo precedente. Alcuni dei risultati sono riportati in appendice (*Appendix A e B*) in modo da alleggerire il corpo della tesi.

L'elaborato viene redatto in lingua inglese per una maggiore compatibilità con i tecnicismi della materia trattata.

Introduction

Gravitational waves (GWs) have been a central subject for debating in the scientific community since earlier than 1915, namely when Albert Einstein provided the world with the theory of general relativity (GR) [1]. Many pre-GR theories deprecated the instantaneous action of gravitation as theorized in Newton's idea of gravitation, thus trying to relate to the nineteenth-early twentieth century's most developed and sophisticated physical theory: electrodynamics. As electromagnetic waves are easily predicted in a classic view of electrodynamics (quantum concepts are mentioned in the whole text), the concept of GWs was one of the first steps in the definition of such theories, being a very strong conceptual link to electrodynamics.

However, many of such pre-GR theories showed one several difference with respect to electrodynamics, given by the fact that no dipole radiation can exist for GWs, as long as nothing like negative mass is considered.

The theorization of GR quickly developed into a description of GWs with GR formalism [2]&[3], after years of shaping out the subject. Nevertheless, the topic was considered as a purely theoretical lucubration since even Einstein was skeptical about the effective detectability of such waves [8]. However, a conceptualization of the experiment being able to measure GWs was pursued with the 1957 Chapel Hill Conference [9], and found its realization (and final outcome) with the two GW interferometers LIGO (*Laser Interferometer Gravitational-Wave Observatory*) measuring a chirp signal from the coalescence of a binary black hole (BBH) [4]. A celebrated plot of the gravitational strain evolution with time is displayed at Fig. (1). This breakthrough, together with the following observations of GW events, marked the start of a new era, as the scientific goal changed from the detection of GWs to the availment of GWs for studying the astrophysical phenomena giving birth to such transients and the fundamental Physics made accessible by means of GWs.

Therefore, it is a natural consequence to implement this newer probe in the wide field of gravity tests. Gravity tests generally consist of experiments telling whether some phenomenon is compatible with GR (thus confirming it as the preferred theory for gravity at an accuracy level given by the limits of the experiment) or not. Many gravity tests have been attempted so far, but no one has ever showed any deviation with respect to the predictions of GR.

In this essay, the main goal is the illustration of a gravity test implementing GWs in a theoretical framework by compiling what has already been done by other scientists and characterizing the capabilities of current and future generation detectors in the realization of such a test (thus introducing newer results and predictions).

GR predicts the existence of two tensor polarization modes, which can be

obtained explicitly by working out the wave equation for GWs in the *Transverse Traceless* gauge, as the following chapters outline. However, in a general gravity theory, one can get up to six polarization modes, namely the two tensor modes of GR, two vector modes and two scalar modes [5]. At this point, it is quite intuitive to wonder about a discrimination between different gravity theories based upon GW polarization modes.

A very important figure of merit in this field is given by the null streams, as they are introduced in the following pages. Such quantities depend on the GW signals as measured by at least three detectors simultaneously and the antenna patterns (APs) of such detectors [6]. In fact, GW detectors have a sensitivity pattern depending on the direction of the GW source. Such pattern is described by the APs.

Furthermore, the observed signals need be emitted by a compact binary coalescence (CBC), namely, the coalescence of a binary neutron star (BNS), a binary black hole (BBH) or a neutron star (NS) and a black hole (BH). These are the only observable coherent signals at the current time. A simplified visual of a CBC is given at Fig. (2). Here one can see the signal signature of the inspiral phase, where the two objects just orbit around the same centre of mass, the violent merger phase, where the two objects collide, and the ringdown phase, where the final remnant reaches stability. Current knowledge of CBCs makes the inspiral phase the only one with a solid analytical representation (understandable also in a Newtonian fashion [10]).

Null streams are special quantities expressly built in order to be zero in case the GW signal contains only tensor modes, while, on the other hand, being non-zero for non-tensor signals.

In the most simple approach, null streams do not allow for a disentangling of the polarization modes, being limited to tell whether the GW signal contains any general non-tensor mode. Nevertheless, advanced versions of the null streams can be obtained in order to constrain the specific polarization modes contributing to the signal.

The research activity focuses on the generation of simulated GW signals and the consequent analysis of such signals by means of the GWBENCH software [7]. This tool provides with both simulation and analysis of CBC signals by means of a Fisher information formalism, making it faster with respect to Bayesian algorithms (generally preferred in this subject).

Therefore, a signal with a given signal-to-noise ratio (SNR) from a source at a given position can be used to test the localization accuracy of a network of detectors for that peculiar signal by means of GWBENCH. The uncertainty on the localization propagates generating an overall fluctuation of the null streams. If such fluctuation is smaller than some threshold, then the network can be considered valid in the discrimination between gravity theories for the specific kind of signal being considered.

More in detail, in the case of a purely GR signal (thus being just made of tensor modes), a null stream need be approximately zero, not compatible with zero within $n\sigma$, where σ is the standard deviation of the null stream and n is given by some acceptability threshold (to be defined), thus meaning that the null stream is dominated by the noise of the detectors.

Furthermore, the SNR of the null stream need be greater than some threshold t in the case non-tensor modes are injected into a GR signal, thus making it well distinguishable with respect to noise. A network meeting these requirements is

a good tool for the discrimination between GR and modified theories of gravity.

The whole essay is structured in order to give a precise outline of the research work and to put it in the right context in an accessible way. This means that both the formalism needed for the understanding of the subject and the precedent outcomes in this field need be introduced to the reader.

Therefore, chapter 1 introduces GWs in a standard fashion implementing the formalism and the notation being used in the research work. This knowledge is then applied in chapter 2, which is dedicated to the description of both the experimental facilities currently operating and those being planned for the next decades. In addition, chapter 3 gives a compilation of the theoretical treatment of null streams. A preliminary work is reported at chapter 4, where the localization capabilities of some networks of detectors are characterized as a function of the distance of the source and two mass parameters, relative to the mass of the whole binary and of the single components. The main topic is treated in chapter 5. Here the response of the networks to the null streams is studied while changing the same quantities considered for the previous chapter. A short introduction makes a summary of the implemented methods and then the most representative results are reported. Other results are reported at the Appendix A &B.

Most of the effort for this work has been dedicated to building a code for obtaining the desired results. However, the description of this code is condensed in a few pages of this essay. In fact, the detailed illustration of a very long code hasn't been considered interesting for the reader and has been discarded.

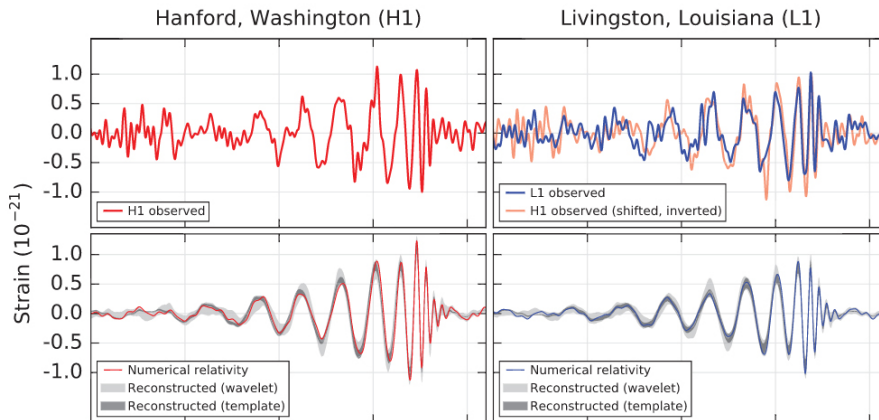


Figure 1: GW150914 strain as a function of time. The data are shown together with reconstructed events from a template library and with the wavelet approach [4].

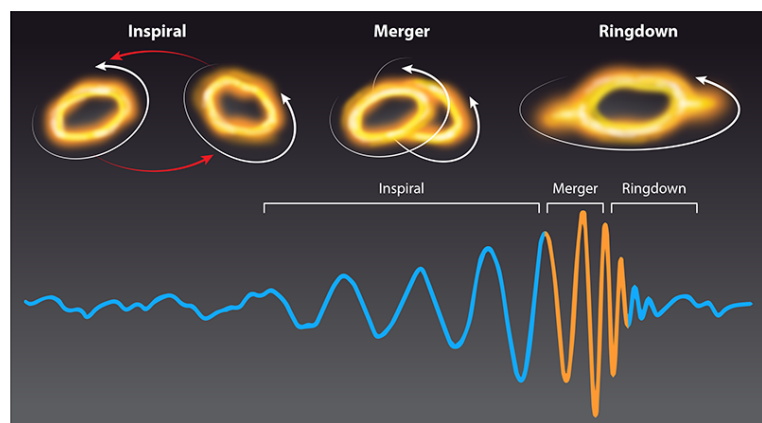


Figure 2: The evolution of a GW signal according to a CBC event. Picture taken from [11].

Chapter 1

Gravitational Waves

In this chapter, general remarks about GWs as they are taught in academic environments are presented. The approach being followed is that of a linearized theory of gravitation, a first-order perturbation theory applied to flat space within GR.

The treatment of GWs provided in these pages makes the assumption that readers be familiar with the basics of GR and differential Geometry as concepts like the geodesic equation, the Einstein equation, metric and so on are not explained. However, a good reference for being introduced to such stuff is given by [12], since it explains gravity in a very complete way, providing an intuitive view based on physical phenomenology together with an abstract treatment using differential Geometry.

The first section focuses on the GW equation in linearized gravity. Secondly, the TT gauge is introduced and considered as the natural reference frame for GWs. In conclusion, a theoretical (thus not involving any instrumental consideration) approach to the detection of GWs is pursued.

1.1 The Gravitational Wave Equation

The Minkowsky metric tensor used here has signature $(-1, 1, 1, 1)$ and is expressed with the symbol $\eta_{\mu\nu}$. Therefore, one can always consider in a frame where the general metric of space-time is:

$$g_{\mu\nu}(x^\alpha) = \eta_{\mu\nu} + h_{\mu\nu}(x^\alpha) \quad (1.1)$$

with x^α being a generic event on the space-time manifold and $|h_{\mu\nu}(x^\alpha)| \ll 1$. However, this expression is not covariant, meaning that if one finds a coordinate frame so that $g_{\mu\nu}$ meets (1.1) at a given x^α , it won't generally do so at $\tilde{x}^\alpha \neq x^\alpha$. This is due to the fact that a choice in the coordinate system does not constrain the metric function as a whole in x^α , but only its local value and first derivatives and thus can not generally allow to impose equation (1.1) but on a single event. However, one may be able to do differently, meaning that condition (1.1) might be naturally verified for a given macroscopic portion of the manifold in a fixed frame. This would be the case of a flat space-time being perturbed by $h_{\mu\nu}$.

This is the condition one wants to study when talking about GWs. If a perturbation happens to be local, it can be erased with a proper choice for coordinates, and can thus be addressed as a coordinate artifact. Otherwise, if it is not local, it is considered as a physical effect. This was a crucial point for the study of GWs in the first years, as it was not clear whether they are due to the gauge invariance of GR under arbitrary coordinate transformation or they have to be addressed as physical phenomena.

At this point, one can observe that $\eta_{\mu\nu}$ is not a covariant quantity, thus $h_{\mu\nu}$ is neither. However, it is easy to see that being $\Lambda_\alpha^\mu \Lambda_\beta^\nu \eta_{\mu\nu} = \eta_{\alpha\beta}$ with Λ_α^μ being a Lorentz transformation, one gets:

$$\Lambda_\alpha^\mu \Lambda_\beta^\nu g_{\mu\nu} = \tilde{g}_{\alpha\beta} = \eta_{\alpha\beta} + \tilde{h}_{\alpha\beta}$$

with $\tilde{h}_{\alpha\beta} = \Lambda_\alpha^\mu \Lambda_\beta^\nu h_{\mu\nu}$, therefore making $h_{\mu\nu}$ a tensor in special relativity (SR).

In this fashion, one can implement expression (1.1) in the Einstein equation:

$$R_{\mu\nu} - \frac{1}{2}g_{\mu\nu}R = \frac{8\pi G}{c^4}T_{\mu\nu} \quad (1.2)$$

where $R_{\mu\nu} = R_{\mu\alpha\nu}^\alpha$ is the Ricci tensor (contraction of the Riemann tensor) and $R = R_\alpha^\alpha$ is the Ricci scalar (contraction of the Ricci tensor); $T_{\mu\nu}$ is the stress-energy tensor.

The Riemann tensor is defined as follows:

$$R_{\alpha\beta\gamma}^\mu = \Gamma_{\alpha\gamma,\beta}^\mu - \Gamma_{\alpha\beta,\gamma}^\mu + \Gamma_{\alpha\gamma}^\rho \Gamma_{\rho\beta}^\mu - \Gamma_{\alpha\beta}^\rho \Gamma_{\rho\gamma}^\mu \quad (1.3)$$

with $\Gamma_{\mu\nu}^\alpha = \frac{1}{2}g^{\alpha\beta}(-g_{\mu\nu,\beta} + g_{\mu\beta,\nu} + g_{\nu\beta,\mu})$ the Christoffel symbols. This expression becomes, at first order in $h_{\mu\nu}$:

$$\Gamma_{\mu\nu}^\alpha \simeq \frac{1}{2}\eta^{\alpha\beta}(-h_{\mu\nu,\beta} + h_{\mu\beta,\nu} + h_{\nu\beta,\mu}) \quad (1.4)$$

Where the dependence upon x^α has been suppressed. One can plug this expression into (1.3) and obtain what follows:

$$R_{\alpha\beta\gamma}^\mu \simeq \frac{1}{2}\eta^{\mu\nu}(-h_{\alpha\gamma,\nu\beta} + h_{\gamma\nu,\beta\alpha} + h_{\alpha\beta,\nu\gamma} - h_{\beta\nu,\alpha\gamma}) \quad (1.5)$$

At this point, a perturbation of the coordinate is considered, so that: $\tilde{x}^\alpha = x^\alpha + \epsilon^\alpha$, while still keeping eq. (1.1) as valid. The transformation law for the metric tensor reads as:

$$\tilde{g}_{\mu\nu} = \frac{dx^\alpha}{d\tilde{x}^\mu} \frac{dx^\beta}{d\tilde{x}^\nu} g_{\alpha\beta}$$

thus giving:

$$\tilde{g}_{\mu\nu} = g_{\mu\nu} - \epsilon_{\mu,\nu} - \epsilon_{\nu,\mu} = \eta_{\mu\nu} + h_{\mu\nu} - \epsilon_{\mu,\nu} - \epsilon_{\nu,\mu} \quad (1.6)$$

Therefore, one gets: $\tilde{h}_{\mu\nu} \simeq h_{\mu\nu} - \epsilon_{\mu,\nu} - \epsilon_{\nu,\mu}$ for an infinitesimal change of coordinates.

By implementing such a coordinate tilt into (1.5), one gets that $\tilde{R}_{\alpha\beta\gamma}^\mu = R_{\alpha\beta\gamma}^\mu$.

Using Eq. (1.5) in (1.2) and truncating at first order in h , one gets:

$$\frac{1}{2} \left[-h_{\mu\nu, \alpha} + h_{\nu, \alpha\mu}^\alpha + h_{\mu\alpha, \nu}^\alpha - h_{\alpha, \mu\nu}^\alpha - \eta_{\mu\nu} h^{\alpha\beta}_{,\alpha\beta} + \eta_{\mu\nu} h^\alpha_{\alpha, \beta} \right] \simeq \frac{8\pi G}{c^4} T_{\mu\nu}$$

Setting:

$$\bar{h}_{\mu\nu} = h_{\mu\nu} - \frac{1}{2} \eta_{\mu\nu} h \quad (1.7)$$

with $h = h_\alpha^\alpha$ and observing that $\bar{h}_{\mu\nu} = h_{\mu\nu}$, the Einstein equation reduces to:

$$\bar{h}_{\mu\nu, \alpha} - \bar{h}_{\nu, \alpha\mu}^\alpha - \bar{h}_{\mu\alpha, \nu}^\alpha + \eta_{\mu\nu} \bar{h}^{\alpha\beta}_{,\alpha\beta} \simeq -\frac{16\pi G}{c^4} T_{\mu\nu} \quad (1.8)$$

It is possible to superimpose $\bar{h}_{\mu\nu, \mu} = 0$, namely what is referred to as the Lorentz gauge, by seeing that this means:

$$\begin{aligned} \bar{h}_{\mu\nu, \mu} &= \tilde{h}_{\mu\nu, \mu} - \frac{1}{2} \eta_{\mu\nu} \tilde{h}, \mu = \\ &= h_{\mu\nu, \mu} - \epsilon_{\mu, \nu}^\mu - \epsilon_{\nu, \mu}^\mu - \frac{1}{2} \eta_{\mu\nu} (h, \mu - 2\epsilon_{\alpha, \alpha}^\mu) = \\ &= \bar{h}_{\mu\nu, \mu} - \epsilon_{\nu, \mu}^\mu = 0 \end{aligned} \quad (1.9)$$

where \tilde{h} denotes a quantity expressed in the Lorentz gauge. This equation clearly has non-trivial solutions, therefore making the Lorentz gauge a mathematically justified choice.

It is straightforward to verify that the Lorentz gauge still leaves a gauge freedom expressed by: $\epsilon_{\nu, \mu}^\mu = 0$.

In the Lorentz gauge one gets the wave equation (all the following arguments are treated in the regime of linearized gravity and the \simeq symbol can become $=$ for sake of notation):

$$\bar{h}_{\mu\nu, \alpha} = -\frac{16\pi G}{c^4} T_{\mu\nu} \quad (1.10)$$

This equation is intensively used when treating the generation of GWs. However, for free space propagation, only the simple no-source term equation is needed, and the discussion being pursued now just makes use of the latter:

$$\bar{h}_{\mu\nu, \alpha} = 0 \quad (1.11)$$

having solution:

$$\bar{h}_{\mu\nu} = \Re \left[A_{\mu\nu} e^{ik_\alpha x^\alpha} \right] \quad (1.12)$$

Here, $k^\alpha = (c\omega, 0, 0, c\omega)$ is the wave 4-vector within the assumption of a wave propagating towards the z -direction of a Cartesian frame. The dispersion relation reads as $k^\alpha k_\alpha = 0$.

Moreover, the Lorentz gauge implies that $k^\mu A_{\mu\nu} = 0$, thus leading to $k^0 A_{0\nu} = -k^3 A_{3\nu}$, i.e.: $A_{0\nu} = -A_{3\nu}$.

Being the metric a symmetric tensor, one gets:

$$A_{\mu\nu} = \begin{pmatrix} A_{00} & A_{01} & A_{02} & -A_{00} \\ A_{01} & A_{11} & A_{12} & -A_{01} \\ A_{02} & A_{12} & A_{22} & -A_{02} \\ -A_{00} & -A_{01} & -A_{02} & A_{00} \end{pmatrix} \quad (1.13)$$

Furthermore, equation (1.10) together with the Lorentz gauge implies that $T_{\mu\nu}{}^\mu = 0$ which is the energy-momentum conservation law in SR (differently from $T_{\mu\nu;\mu} = 0$, holding in GR). This proves that linearized gravity is self-coherent and represents a physically justified approach.

1.2 The Transverse Traceless Gauge

The problem leading to the introduction of the transverse traceless (TT) gauge is that of simplifying equation (1.13). This can be achieved by using equations (1.9) and the fact that in the Lorentz gauge $\epsilon_{\nu,\mu}{}^\mu = 0$. A good solution is:

$$\epsilon_\mu = -\Re e \left[i \xi_\mu e^{ik_\alpha x^\alpha} \right] \quad (1.14)$$

With this expression, one can infer:

$$A_{\mu\nu}^{TT} = A_{\mu\nu} - \xi_\mu k_\nu - \xi_\nu k_\mu + \eta_{\mu\nu} \xi_\alpha k^\alpha \quad (1.15)$$

A set of equations for the six independent terms of $A_{\mu\nu}$ can be defined in the TT Gauge:

$$\begin{aligned} A_{00}^{TT} &= A_{00} + \omega c (\xi_0 - \xi_3) \\ A_{01}^{TT} &= A_{01} + \omega c \xi_1 \\ A_{02}^{TT} &= A_{02} + \omega c \xi_2 \\ A_{21}^{TT} &= A_{21} \\ A_{11}^{TT} &= A_{11} + \omega c (\xi_0 + \xi_3) \\ A_{22}^{TT} &= A_{22} + \omega c (\xi_0 + \xi_3) \end{aligned}$$

By setting the coefficients ξ_α so that:

$$\begin{aligned} \xi_0 &= -\frac{(A_{22} + A_{11} + 2A_{00})}{4\omega c} \\ \xi_1 &= -\frac{A_{10}}{\omega c} \\ \xi_2 &= -\frac{A_{20}}{\omega c} \\ \xi_3 &= -\frac{(A_{22} + A_{11} - 2A_{00})}{4\omega c} \end{aligned} \quad (1.16)$$

the amplitudes tensor $A_{\mu\nu}^{TT}$ is very simple:

$$A_{\mu\nu}^{TT} = \begin{pmatrix} 0 & 0 & 0 & 0 \\ 0 & A_{11} & A_{12} & 0 \\ 0 & A_{12} & -A_{11} & 0 \\ 0 & 0 & 0 & 0 \end{pmatrix} = \begin{pmatrix} 0 & 0 & 0 & 0 \\ 0 & A_+ & A_\times & 0 \\ 0 & A_\times & -A_+ & 0 \\ 0 & 0 & 0 & 0 \end{pmatrix} = \quad (1.17)$$

$$= \begin{pmatrix} 0 & 0 & 0 & 0 \\ 0 & A_+ & 0 & 0 \\ 0 & 0 & -A_+ & 0 \\ 0 & 0 & 0 & 0 \end{pmatrix} + \begin{pmatrix} 0 & 0 & 0 & 0 \\ 0 & 0 & A_\times & 0 \\ 0 & A_\times & 0 & 0 \\ 0 & 0 & 0 & 0 \end{pmatrix} = A_+ \epsilon_+ + A_\times \epsilon_\times$$

In this formalism the two tensor polarization modes of GR are explicit: the amplitude tensor for GW can be expressed as a function of just two coefficients, A_{11} and A_{21} . These coefficients represent the two different polarization modes for GR, usually referred to as tensor + and tensor \times . ϵ_+ and ϵ_\times are the polarization tensors for the two polarization modes.

1.3 Detection of Gravitational Waves

In this section the interaction of a GW with test masses is addressed. This subject hides few subtleties since a preferential frame, that is, the TT frame, has already been chosen for describing GWs. Finding a link between the TT frame and a potential detector frame is no piece of cake.

At this point, one can define an ideal detector made of freely falling test masses, that are described by a geodesic equation (namely, the motion equation for a freely falling mass [12]):

$$\frac{d^2x^\alpha}{d\lambda^2} + \Gamma^\alpha_{\mu\nu} \frac{dx^\mu}{d\lambda} \frac{dx^\nu}{d\lambda} = 0 \quad (1.18)$$

which can be worked out both from the parallel transport equation:

$$\frac{dx^\alpha}{d\lambda} V^\beta_{;\alpha} = 0$$

and from the variational principle as obtained by extremizing the action:

$$S = -m \int_{\tau_\beta}^{\tau_\alpha} d\tau \longrightarrow \frac{d^2x^\alpha}{d\tau^2} + \Gamma^\alpha_{\mu\nu} \frac{dx^\mu}{d\tau} \frac{dx^\nu}{d\tau} = 0$$

In fact $-md\tau$ can be proven to be proportional to the Lagrangian of a particle of mass m in free motion, where τ is the proper time along the path of the particle.

In particular, by superimposing the equality between the equation obtained from the parallel transport and that from the variational principle, one obtains that the natural quantity for the parametrization of a geodesic is the proper time τ and generally $\lambda = a\tau + b$, with a accounting for a redefinition of the time scale unit and b accounting for shifts.

Two nearby geodesics being separated by a 4-vector ξ^α can be considered. As already mentioned, one can always build up a dedicated coordinate frame such that at a given event (here called \bar{x}^α) on the manifold the metric is flat, and its first derivatives are 0 (what is called the *Riemann Normal Coordinates* frame). However, being the derivative a continuous function, the metric changes quite slowly next to \bar{x}^α , permitting to consider a nearly flat metric over a small neighbourhood of that event.

In particular, in a treatment like the one pursued here, it is important to state that flat metric means $\rightarrow g_{\mu\nu} = \eta_{\mu\nu} + h_{\mu\nu}$ in absence of GWs, with

$|\mathfrak{h}_{\mu\nu}| \ll |h_{\mu\nu}|$, namely the curvature of the space being much smaller than the metric perturbation caused by GWs. Therefore, ξ^α has to be small with respect to the coordinate scale of variation of the metric of a quantity of the same order of $h_{\mu\nu}$. This coordinate scale is called R_B , that is, the radius of curvature of the background so that $\mathfrak{h}_{\mu\nu}(x^i = R_B) \sim h_{\mu\nu}$. Furthermore, since the first derivatives of the metric are locally zero, the term $\mathfrak{h}_{\mu\nu}$ comes from the second-order term in the expansion of the metric around the point where it is defined to be exactly Minkowsky. Therefore, one can write, in a heuristic but qualitatively correct fashion, $\mathfrak{h}_{\mu\nu} = h_{\mu\nu} \left(\frac{r}{R_B} \right)^2$ where $r^2 = \eta_{ij} x^i x^j$.

Hence, one can constrain $|\xi^\alpha| \ll R_B$.

This lucubration has been done because ξ^α is always referred to as small, but usually it is extremely hard to find what it has to be small with respect to.

At this point, the geodesic deviation equation is introduced as a result of the subtraction of the two geodesics. One can prove that:

$$\frac{D^2 \xi^\alpha}{D\lambda^2} + R^\alpha_{\mu\nu} \xi^\beta \frac{dx^\mu}{d\lambda} \frac{dx^\nu}{d\lambda} = 0 \quad (1.19)$$

with:

$$\frac{D\xi^\alpha}{D\lambda} = \frac{dx^\sigma}{d\lambda} \xi^\alpha_{;\sigma}$$

One can now proceed using equations (1.18) & (1.19) and express them in the TT gauge in order to understand which reference frame it represents.

By using the geodesic equation (1.18) and assuming that the velocity of a test mass (the geodesic equation is referred to) is at rest at $\tau = 0$, one gets:

$$\frac{d^2 x^i}{d\tau^2} \Big|_{\tau=0} = - \left[\Gamma^i_{\mu\nu} \frac{dx^\mu}{d\tau} \frac{dx^\nu}{d\tau} \right]_{\tau=0} = \left[\Gamma^i_{00} \frac{dx^0}{d\tau} \right]_{\tau=0}$$

where latin indeces like i refer to spatial components, since $\Gamma^{\mu}_{00} = 0$ in the TT gauge. Therefore, a GW does not produce any coordinate acceleration.

However, since GWs have been constrained to be a physical effect, one can expect them to have an effect on the coordinate-independent quantity given by the proper distance between two events. In fact, ds^2 , that is an infinitesimal distance, can be obtained as a scalar product (which is coordinate-invariant):

$$ds^2 = g_{\mu\nu} \xi^\mu \xi^\nu \quad (1.20)$$

with ξ^μ being the four-vector of the coordinate distance between the two events.

If two test masses are freely falling, and thus described by two geodesics, and if they are initially at rest one with respect to the other, it has just been proven that they do not undergo any kind of coordinate acceleration due to the influence of GWs. However, one can see that the proper distance between them behaves like:

$$\begin{aligned} ds^2 &= (\eta_{ij} + h_{ij}) \xi^i \xi^j \simeq \left(\xi^i + \frac{h^i_j \xi^j}{2} \right) \left(\xi_i + \frac{h_{ij} \xi^j}{2} \right) = \\ &= \eta_{ik} \left(\xi^i + \frac{h^i_j \xi^j}{2} \right) \left(\xi^k + \frac{h^k_j \xi^j}{2} \right) = \sum_{i=1}^3 \left(\xi^i + \frac{h^i_j \xi^j}{2} \right)^2 \end{aligned} \quad (1.21)$$

namely, being dependent on the effect of GWs. This means that the TT gauge puts the observer in a sort of preferential frame proper of the GW, where the effect of the GW is not observable in terms of coordinate distances, since coordinates themselves stretch and shrink according to the GW.

This makes the TT frame very practical in terms of mathematical computations, while it is not appropriate for the measurement of GWs.

Before going onto tell more practical stuff, and reaching a good reference frame for the observation of GWs, another theoretical preamble is required.

A set of *Riemann Normal Coordinates* can be attached to each point of a geodesic, obtaining a special version of the geodesic equation (Christoffel symbols vanish since the metric derivatives are set to 0 in a *Riemann Normal Frame*):

$$\left. \frac{dx^\alpha}{d\tau} \right|_{\bar{x}_G^\mu} = 0$$

with \bar{x}_G^μ being an event on the geodesic. In fact, for such a frame, the first derivatives of the metric are identically zero.

This means that one can use $g_{\mu\nu}(x^\alpha) = \eta_{\mu\nu} + O(\frac{r^2}{R_B^2})$ for a generic x^α such that $x^i x_i = r^2$ [13], with $O(\frac{r^2}{R_B^2}) = h_{\mu\nu}$ as previously defined. The approximation can be kept at first order in $\frac{r}{R_B}$, and consider $g_{\mu\nu} = \eta_{\mu\nu}$ in the neighbourhood of the event the *Riemann Normal Coordinates* frame is defined on.

However, this frame is generally different for each event on the geodesic, since, even if the time coordinate is always the same along the geodesic, the spatial coordinates do not account for rotations of the axes. Nevertheless, a general way to overcome this problem consists in setting the three Cartesian axes following the directions as given by three imaginary gyroscopes connected to the freely falling mass. A formal description of this coordinate frame, usually referred to as *Fermi Normal Coordinates*, is given in [13]. In this discussion, not much effort is dedicated to this aspect, but the general result of a freely falling frame is used in the following lines.

In fact, the treatment provided here now switches from the familiar TT frame to the aforementioned *Fermi Normal Coordinates* (FNC).

In absence of a GW, the TT frame and the FNC frame show the same metric. Therefore, they can be accounted as the same reference frame, but for a translation, a definition of the units along the coordinate axes and a rotation of the axes.

If one considers two or more freely falling test masses initially at rest one respect to the other, the origin of the FNC and TT frames can be fixed on one of them, and the units on the axes can be defined in order to make them exactly the same reference frame (locally), except for a rotation.

Therefore, the coordinate separation between the origin-falling mass and another one is the same in the two frames = ξ^α .

Furthermore, one can set the time-coordinate on every test mass to be the same. Hence, the separation is given by the only space-components ξ^i .

If a GW passes by, the two frames are not the same anymore. The FNC frame displays a metric $g_{\mu\nu} = \eta_{\mu\nu}$ while the TT frame gives $g_{\mu\nu} = \eta_{\mu\nu} + h_{\mu\nu}$.

As previously obtained, the change in the coordinate distance as inferred in the TT frame is zero, therefore one can state that ξ_{TT}^α at every moment is equal to ξ_{FNC}^α before the wave, but in general it is not equal to $\xi_{FNC_{GW}}^\alpha$, namely the

coordinate distance in the FNC frame when the GW is passing by. The proper distance actually changes, without depending on the reference frame. One can infer the behaviour of the coordinate distance in the FNC frame:

$$\begin{aligned} ds^2 &= \sum_{i=1}^3 \left(\xi_{TT}^i + \frac{h^{iT^T}_j \xi_{TT}^j}{2} \right)^2 = \sum_{i=1}^3 \left(\xi_{FNC}^i + \frac{h^{iT^T}_j \xi_{FNC}^j}{2} \right)^2 = \\ &= \eta_{ij} \xi_{FNC_{GW}}^i \xi_{FNC_{GW}}^j = \sum_{i=1}^3 \xi_{FNC_{GW}}^i \end{aligned} \quad (1.22)$$

thus obtaining:

$$\xi_{FNC_{GW}}^i = \xi_{FNC}^i + \frac{h^{iT^T}_j}{2} \xi_{FNC}^j \quad (1.23)$$

and a Newton equation, which can be obtained also from the geodesic deviation:

$$\ddot{\xi}_{FNC_{GW}}^i = \frac{\ddot{h}^{iT^T}_j}{2} \xi_{FNC}^j \quad (1.24)$$

It has been demonstrated that the coordinate distance between freely falling test masses in a FNC frame change according to the GW as expressed in the TT frame and proportionally to the coordinate distances between these masses in absence of the GW.

For example, in the case of a + polarized wave, and for a FNC frame being exactly coaligned with the TT frame, one gets:

$$\begin{aligned} \xi_{FNC_{GW}}^1 &= \xi_{FNC}^1 + \frac{A_+}{2} \xi_{FNC}^1 \cos(\omega t) \\ \xi_{FNC_{GW}}^2 &= \xi_{FNC}^2 - \frac{A_+}{2} \xi_{FNC}^2 \cos(\omega t) \end{aligned}$$

The final step for this discussion consists in proving that the FNC frame is (or resembles) the frame for some real detector.

If one thinks about a detector made of test masses, initially at rest one respect to another, freely falling in space, then the FNC frame is the natural frame to apply for such facility.

However, currently operating detectors are not freely falling.

They implement test masses being suspended in the gravitational field of the Earth (at dominant order), comoving with the surface of the Earth.

One can show that, in the case of an Earth-bound detector, the metric can be written as $g_{\mu\nu} = \eta_{\mu\nu} + A(x^i) + B(\eta_{ij}x^i x^j) + O(\frac{r}{R'_B})$, oppositely to what happens in the case of FNC. In this case, R'_B is the curvature radius of the background metric in absence of a GW. Similarly to the previously analyzed case of *Riemann Normal Coordinates*, one can define this as the radius at which $O(\frac{r}{R'_B}) \sim h_{\mu\nu}$ and write it like $O(\frac{r}{R'_B}) = h_{\mu\nu}(\frac{r}{R'_B})$. Here $A(x^i)$ and $B(\eta_{ij}x^i x^j)$ are linear functions of their arguments which are not re-scaled by a factor R_B , meaning that, in general, their effect can also be greater than that of GWs.

These terms, together with the term linear in $\frac{r}{R_B}$ (and higher order terms too), are due to the acceleration with respect to the *Riemann Normal Coordinates* given by the surface of the Earth ($= -\vec{g}$) and the rotation of Earth (in

fact, the three imaginary gyroscopes defining the axes of a FNC frame need be comoving with the centre of the Earth, the freely falling object, not with the detector itself).

Therefore, Newtonian forces cause perturbations of the metric which may compete with the effect of GWs.

In particular, one obtains from the geodesic equation that a test mass m in such a frame would undergo an acceleration (in absence of GWs):

$$\frac{d^2x^i}{d\tau^2} = -g^i - 2(\vec{\Omega} \times \vec{v})^i + \frac{f^i}{m} + (\vec{\Omega} \times \vec{\Omega} \times \vec{r})^i + O(r) \quad (1.25)$$

being g^i the gravity acceleration on the surface of the Earth and $\vec{\Omega}$ the angular velocity of the detector as the Earth rotates about its axis. In general, the amplitude of GW effects on the Newton equation of a test mass are weaker than those displayed in equation (1.25).

However, current detectors show a good sensitivity on a bandwidth going from ~ 10 to $\sim 10^4$ Hz, while the noise level becomes very loud at way lower frequencies. The time scales for the Newtonian effects of equation (1.25) are much larger than the inverse of the minimum frequency of such bandwidth.

Therefore, Newtonian effects, together with instrumental noise, dominate at lower frequencies, thus making GWs impossible to detect below few Hz with Earth-bound facilities. On the other hand, it is possible to achieve good sensitivity and small contribution from Newtonian effects at higher frequencies.

Therefore, one has that at high frequencies it is possible to suppress the terms like $A(x^i)$, $B(\eta_{ij}x^i x^j)$, and $O(\frac{r}{R'_B})$. One ends up with the same expression used for freely falling detectors, that is, the one implementing FNC.

Finally, the argument of small contribution at high frequencies allows for the neglecting of the deviations of the frame of an Earth-bound detector with respect to a FNC frame.

Furthermore, the FNC frame displays deviations from the flat space on a scale much larger than that of the coordinate distance between the test masses used to pursue the observations of GW, thus permitting to obtain the behaviour of the distance between the two test masses (equation (1.23)) within a representation at first order in $h_{\mu\nu}$.

Nevertheless, it has been shown that the coordinate distance between two test masses is indeed what one wants to measure; but how to measure it, this is another major issue. The solution to this problem is a central subject in the following discussion.

The first approach to the detection of GWs was carried on from equation (1.19), since it clearly resembles a dissipation-less harmonic oscillator. The most intuitive way to measure such a phenomenon was to introduce a dissipation term able to gather some of the energy of the GWs passing by.

This led Joseph Weber to the invention of resonating bars [14], namely cylinders of aluminium with piezoelectric generators on them. Such a bar works in the frame where its dimension is considered as the separation vector ξ^i . A GW allows the bar to shrink and expand, thus generating an evolving voltage in the piezoelectric plates. This electric signal can be used to see GWs. The bar, however, works as a very efficient bandpass filter too, like every damped oscillator, its bandwidth being ~ 20 Hz at a sensitivity of $\sim 10^{-20}$ Hz $^{-1/2}$ [15]. Many

GW-like transients had been observed when these detectors were widely used, but no significant claim has ever been done.

This weakness allowed the modern interferometric detectors to overtake such resonating bars, since they display a much wider bandwidth and better sensitivity.

The next chapter unveils some of the details of GW interferometers. The main focus is now on the understanding of how they work.

In particular, GW interferometers are Michelson interferometers, with some significant modification partly addressed in the following pages. The main principle of such interferometers is that of light impinging onto test masses with high reflectivity, and the observation consists in measuring the optical path of the light reflected by these test masses. This can be done by performing a measure of the light interference from two arms of the detector.

By assuming an extremely simplified version of a Michelson interferometer detector (like the one at Fig. (1.1)) one can write the equation for the electric field at the viewing screen. Here, the beam splitter has reflectivity $r = 1/2 = t$ with t the transmittivity. The end mirrors have reflectivity -1. The distance between the beam splitter and M_1 (as in the figure) is l_x , the distance between the beam splitter and M_2 is l_y . A monochromatic light beam is considered, and the vector nature of light has not been involved yet.

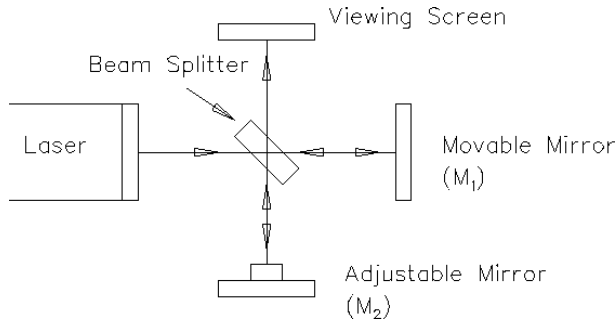


Figure 1.1: Scheme of a Michelson interferometer.

$$E_{out}(t) = \frac{1}{2} E_{in} \exp(-i\omega t) \left[\exp\left(i\left(\frac{\omega 2l_x}{c}\right)\right) - \exp\left(i\left(\frac{\omega 2l_y}{c}\right)\right) \right] \quad (1.26)$$

which, in the case of a + polarized GW passing by, becomes:

$$E_{out}(t) = \frac{1}{2} E_{in} \exp(-i\omega t) \left[\exp\left(i\left(\frac{\omega 2l_x}{c}(1+h/2)\right)\right) - \exp\left(i\left(\frac{\omega 2l_y}{c}(1-h/2)\right)\right) \right]$$

After some calculus, this gives:

$$E_{out}(t) = i E_{in} \exp\left[i\left(\omega t + \frac{\omega(l_x + l_y)}{c} + \frac{\omega(l_x - l_y)h}{2c}\right)\right] \sin\left(\frac{\omega(l_x - l_y)}{c} + \frac{\omega(l_x + l_y)h}{2c}\right)$$

The power output is given by:

$$P_{out}(t) = P_{in} \sin^2\left(\frac{\omega(l_x - l_y)}{c} + \frac{\omega(l_x + l_y)h}{2c}\right) \quad (1.27)$$

so that one can conceptually understand how this output can be used for measuring GWs.

Without going deeper into this kind of calculations, eventually involving more technical stuff, the problem of GW detection is now addressed. In (1.26) and following, no peculiar attention has been given to the frequency of the light ω . However, one can think that such frequency is affected by the GWs too. An example of a similar behaviour is that of light from very distant galaxies being affected by the non-steadiness of the Universe's metric. A little digression is now presented to show that the two cases are different.

In an expanding Universe with a non-Minkowsky metric (that is, the Friedmann-Robertson-Walker (FRW) metric [16]), light from very distant galaxies is red-shifted and its wavelength dilates accordingly to the expansion of the Universe.

The FRW metric can be considered writing the proper distance element (a flat Universe is considered, the arguments of Cosmology are not addressed here):

$$ds^2 = -c^2 dt^2 + a^2(t) [dr^2 + r^2 d\Omega] \quad (1.28)$$

For a photon $ds = 0$. Furthermore, the Universe can be considered as very slowly evolving. Therefore, an emission interval Δt_{em} can be defined so that the Universe may be considered steady during this short span of time. Therefore:

$$\begin{aligned} \int_{t_{em}}^{t_{obs}} \frac{c dt}{a(t)} &\simeq \int_{t_{em}+\Delta t_{em}}^{t_{obs}+\Delta t_{obs}} \frac{c dt}{a(t)} \\ \hookrightarrow \frac{c \Delta t_{em}}{a(t_{em})} &\simeq \frac{c \Delta t_{obs}}{a(t_{obs})} \\ \hookrightarrow \lambda_{obs} &\simeq \frac{\lambda_{em}}{a(t_{em})} \end{aligned}$$

With $a(t_{obs}) = 1$ and $a(t_{em}) < 1$. Hence, one gets the dilation of wavelengths for cosmological applications.

However, it has been proven that GW detectors work within a FNC frame, *i.e.* a frame for which $g_{\mu\nu} = \eta_{\mu\nu}$, not in the TT frame for which $g_{\mu\nu}^{TT} = \eta_{\mu\nu} + h_{\mu\nu}^{TT}$.

Therefore, in the FNC frame one cannot write:

$$ds^2 = -c^2 dt^2 + \eta_{ij} dx^i dx^j = -c^2 dt^2 + a^2 [dr^2 + r^2 d\Omega]$$

with $a \neq 1$. For the equation to hold, a need be equal to 1.

At this point, $\lambda_{obs} = \lambda_{em}$ even in presence of GWs.

It has been shown that the choice of a FNC frame for the detector, together with the fact that the proper distance covered by a photon is always zero, permits to state that light does not change any property along its travel to the mirrors and back. Therefore, the approach implemented in equations (1.23) and subsequent is trustworthy, since the frequency of light, ω is unaffected by the GW.

The objection, raised by many people in the previous years, of the detectors not being able to measure GWs because of the light contracting and expanding accordingly to the test masses can thus be discarded.

At this point, more in-depth considerations about the theoretical computations of GWs can be made; the following section illustrates the GW emission and the evolution of the signal with time.

This part is crucial for the definition of the computing methods being implemented in the research work.

1.4 GW Generation and CBCs

Equation (1.10) strongly resembles what one sees when studying electrodynamics, so that a solution can be worked out:

$$\bar{h}_{\mu\nu}(t, \vec{x}) = -\frac{4G}{c^4} \int_V \frac{T_{\mu\nu}(ct - |\vec{x} - \vec{x}'|, \vec{x}')}{|\vec{x} - \vec{x}'|} d\vec{x}' \quad (1.29)$$

representing the GW strain at the position \vec{x} , far away from the source delimited by the V volume and spanned by the position vector \vec{x}' . This solution accounts for the retardation given by the distance $|\vec{x} - \vec{x}'|$.

Keeping in mind the example of a rotating dumbbell representing the Newtonian approximation of a CBC, one understands that the frequency of GWs originating from such a system is $\omega \sim \frac{v}{d}$, with d being the dimension of the source (the separation between compact objects) and v the typical internal velocity of the source. This means that $\lambda \sim \frac{c}{v}d$. In a source with $v \ll c$, one has that $\lambda \gg d$. This consideration is made in order to understand why it is convenient (with some approximation) to consider only the lowest multipole modes in a GW source, being the emission governed by macroscopic motions in the source.

This happens expressing:

$$T_{\mu\nu}(ct - |\vec{x} - \vec{x}'|, \vec{x}') \simeq T_{\mu\nu}(ct - r, |\vec{x}'|) + \frac{x'^i n^i}{c} \partial_t T_{\mu\nu} \Big|_{(ct - r, |\vec{x}'|)} + \dots \quad (1.30)$$

and selecting just the zero-order term $T_{\mu\nu}(ct - r, |\vec{x}'|)$, with $r = |\vec{x}'|$ and $\vec{n} = \vec{x}'/r$.

At this point, while keeping latin indeces for labelling spatial components of tensors and 0 for the time components, one can see that:

$$\int_V T^{ij} d\vec{x} = \int_V \partial_0 T^{i0} x^j d\vec{x} \simeq \frac{1}{c} \frac{d}{dt} \int_V T^{i0} x^j d\vec{x}$$

where the last equality once again comes from the assumption $v \ll c$.

Furthermore, one has that:

$$\begin{aligned} \int_V T^{i0} x^j d\vec{x} &= \frac{1}{2} \int_V \partial_0 T^{00} x^i x^j d\vec{x} \\ &\rightarrow \int_V T^{ij} d\vec{x} \simeq \frac{1}{2c^2} \frac{d^2}{dt^2} \int_V T^{00} x^i x^j d\vec{x} \end{aligned}$$

which is of course something very useful when computing $h_{\mu\nu}^{TT}$, since in the TT gauge the strain h only has spatial components.

All these computations have been done using the Stokes theorem and the fact that $T^{\mu\nu} = 0$ on the surface of the source.

Keeping in mind the $v \ll c$ approximation, one can write $T^{00} \simeq \rho c^2$, thus obtaining:

$$\bar{h}^{ij}(t, \vec{x}) \simeq -\frac{2G}{c^4 r} \frac{d^2}{dt^2} \int_V \rho x'^i x'^j d\vec{x}' = -\frac{2G}{c^4 r} \frac{d^2}{dt^2} Q^{ij} \quad (1.31)$$

with the quadrupole tensor $Q^{ij} = \int_V \rho x'^i x'^j d\vec{x}'$. This expression explicitly shows that the leading term in GW generation is given by quadrupole emission. Monopole and dipole emission are discarded for the general reason that mass (given by $\frac{1}{c^2} \int_V T^{00} d\vec{x}$) and momentum (given by $\frac{1}{c} \int_V T^{0i} d\vec{x}$) are conserved quantities.

This is a consequence of purely Newtonian arguments. In particular, there is no net force acting on the whole system. This means that the whole momentum of the source is conserved and equal to $\frac{1}{c} \int_V T^{0i} d\vec{x}$. Moreover, mass can only have positive values, thus accounting only for an attractive gravitational force. In the case there were some negative mass accounting for a repulsive force, it would be possible to work out a dipole oscillation radiation like that of electrodynamics, where a positive and a negative charge oscillate around a centre of charge. However, even in electrodynamics, the monopole term is zero, because of the overall charge conservation.

A method for inferring the behaviour of a CBC signal is illustrated, working out its evolution with time. One generally finds that, given some orbital parameters, a CBC signal is always coherent and deterministic. This fact has great importance in the research work, because it accounts for an improved localization accuracy for GW detectors.

In order to get this time evolution, one has to compute the power content of a GW event, thus computing the energy carried by a GW: this is a task of great conceptual importance, since it is momentarily breaking the linearized theory used so far.

The fact that a GW carry energy should not be in doubt at this point, since it has been proven that GWs set in motion the test masses of an interferometer. Thinking about a connection between masses with some friction (namely, what Weber thought about), one understands that some energy gets stored in the connecting medium. The origin of such energy is the GW itself.

However, if GWs carry some energy with them, the Einstein equation tells that they cause curvature of space-time. This means that views require to be broadened. In particular, GWs are defined as perturbations on a perfectly flat metric, satisfying a wave equation within a suitable gauge choice. Nevertheless, if a GW curves space-time with its energy, one has to consider a non-flat background metric. The curvature caused by the energy carried by GWs generally has nothing to do with a wave equation, thus it must not be treated as GWs. By constraining the background metric to be flat, one would unavoidably rule out every effect of energy carried by GWs, thus ending up with zero GW energy. Conversely, allowing it to be non-flat, one obtains:

$$g_{\mu\nu}(x^\alpha) = \tilde{g}_{\mu\nu}(x^\alpha) + h_{\mu\nu}(x^\alpha) \quad (1.32)$$

with $\tilde{g}_{\mu\nu}$ being the *non-exactly flat* background metric (one may write: $\tilde{g}_{\mu\nu}(x^\alpha) = \eta_{\mu\nu}(x^\alpha) + \mathfrak{C}_{\mu\nu}(x^\alpha)$, with $\mathfrak{C}_{\mu\nu}$ accounting for the GW energy-induced curvature). Nevertheless, this equation is much more complicated than that

of linearized theory, since one can not know how to disentangle GWs from the curvature induced by the GW energy.

Namely, measuring just the metric with a GW detector, one can not discriminate between the two sources of perturbation with respect to the flat metric. However, a natural separation happens if the two sources have very different scales of frequency. If λ is the wavelength of a GW, and L_{BKG} is the spatial scale of background curvature, a very convenient situation is that in which: $\lambda \ll L_{BKG}$, thus permitting to recover a situation where the background metric, even if not flat, is still smooth with respect to the ripples given by GWs. This assumption is considered henceforth.

The Einstein equations (1.2) can be cast in the form:

$$R_{\mu\nu} = \frac{8\pi G}{c^4} \left(T_{\mu\nu} - \frac{1}{2} g_{\mu\nu} T \right) \quad (1.33)$$

with $T = T^\mu_\mu$. The stress energy tensor contains only terms from matter. Expanding it to order $\sim h^2$:

$$R_{\mu\nu} = \tilde{R}_{\mu\nu} + R_{\mu\nu}^{(1)} + R_{\mu\nu}^{(2)} + \dots \quad (1.34)$$

In linearized theory $\tilde{R}_{\mu\nu}$, being given just by the background contribution, is zero, since the background is exactly flat. Furthermore, the expansion is order one, therefore $R_{\mu\nu}^{(1)}$ is the term giving the GW equation within this approach.

A further assumption one needs to relax is that of monochromaticity of the waves, thus ending up with:

$$h_{ij}(\vec{x}) = \int \frac{d\vec{k}}{(2\pi)^3} \left(\mathfrak{A}_{ij}(\vec{k}) e^{i\vec{k}\cdot\vec{x}} + \mathfrak{A}_{ij}^*(\vec{k}) e^{-i\vec{k}\cdot\vec{x}} \right) \quad (1.35)$$

with, in general, \mathfrak{A}_{ij} describing a narrow peak function of $k = |\vec{k}|$, to be centered on $\frac{2\pi}{\lambda} = k_{GW}$, so that $k_{GW} \pm \Delta k \gg k_{BKG} = \frac{2\pi}{L_{BKG}}$, and Δk being the spread in of \mathfrak{A}_{ij} in k -space. From (1.35), one understands that a term quadratic in h , like $R_{\mu\nu}^{(2)}$, is proportional to high frequency terms $\sim 2k$ and to low frequency terms $\sim \Delta k$. However, Δk can be comparable with low frequencies along the lines of $\tilde{R}_{\mu\nu}$, *i.e.* the background term (which, by definition, is characterized by low spatial frequency/high spatial scale).

Conversely, the high frequency terms have frequencies \sim the same order of magnitude of $R_{\mu\nu}^{(1)}$, since the latter is only proportional to h , and therefore it is characterized by high frequency terms only.

Separating these different frequency terms, one ends up with two different equations, where the superscripts *Low* and *High* denote low frequencies and high frequencies respectively:

$$\begin{aligned} \tilde{R}_{\mu\nu} &= - \left[R_{\mu\nu}^{(2)} \right]^{Low} + \frac{8\pi G}{c^4} \left(T_{\mu\nu} - \frac{1}{2} g_{\mu\nu} T \right)^{Low} \\ R_{\mu\nu}^{(1)} &= - \left[R_{\mu\nu}^{(2)} \right]^{High} + \frac{8\pi G}{c^4} \left(T_{\mu\nu} - \frac{1}{2} g_{\mu\nu} T \right)^{High} \end{aligned} \quad (1.36)$$

Intuitively, the low frequency equation is the one giving the energy of GWs, since it accounts for macroscopic curvature effects.

In order to obtain $\left[R_{\mu\nu}^{(2)} \right]^{Low}$ from $R_{\mu\nu}^{(2)}$, and same for $T_{\mu\nu}$, one can average over a length scale much larger than λ , but much smaller than L_{BKG} . This procedure rules out high frequency terms, while keeping the low frequency ones. Therefore, the low frequency equation becomes:

$$\tilde{R}_{\mu\nu} = - < R_{\mu\nu}^{(2)} > + \frac{8\pi G}{c^4} \left\langle T_{\mu\nu} - \frac{1}{2} g_{\mu\nu} T \right\rangle \quad (1.37)$$

where $<>$ denotes the spatial average. The background curvature now depends upon matter and a new term, represented by $- < R_{\mu\nu}^{(2)} >$.

One can thus define the stress-energy tensor of GWs as:

$$t_{\mu\nu} = - \frac{c^4}{8\pi G} \left\langle R_{\mu\nu}^{(2)} - \frac{1}{2} \tilde{g}_{\mu\nu} R^{(2)} \right\rangle \quad (1.38)$$

(high frequency terms of $g_{\mu\nu}$ have been averaged out).

The procedure for computing $t_{\mu\nu}$ is matter of (a lot of) calculus, the final result being:

$$t_{\mu\nu} = \frac{c^4}{32\pi G} \left\langle \partial_\mu h_{\alpha\beta} \partial_\nu h^{\alpha\beta} \right\rangle \quad (1.39)$$

However, given some h measure, one only has $h_{\mu\nu}^{TT}$, so that the energy flux can be inferred using:

$$t_{00} = \frac{c^2}{32\pi G} \left\langle \dot{h}_{ij}^{TT} \dot{h}_{TT}^{ij} \right\rangle \quad (1.40)$$

so that one need expressing h_{ij}^{TT} as a function of $\frac{d^2 Q^{TT}}{dt^2}$.

In order to make a 2-index tensor transverse and traceless, an apposite operator can be built:

$$\begin{aligned} \Lambda_{mn}^{ij} &= P_m^i P_n^j - \frac{1}{2} P^{ij} P_{mn} \\ \text{with } P_m^i &= \delta_m^i - n^i n_m \end{aligned} \quad (1.41)$$

with \vec{n} being the propagation unit vector.

After some non-trivial computations, expressing $Q_{ij}^{TT} = \Lambda_{ij}^{mn} Q_{mn}$, one gets:

$$P_{GW} = ct_{00} = \frac{G}{5c^5} \left\langle \ddot{\tilde{Q}}_{ij} \ddot{\tilde{Q}}^{ij} \right\rangle \quad (1.42)$$

with $\tilde{Q}_{ij} = \int_V \rho(x^i x^j - \frac{1}{3} \eta^{ij} r^2) d\vec{x}$, i.e. the reduced quadrupole moment.

If one considers a rotating dumbbell as the situation represented by two compact objects orbiting each other (with masses M_1 and M_2 , here considered as point masses), the power emitted in GWs is given by:

$$\begin{aligned} P_{GW} &= \frac{32G}{5c^5} \frac{M_1^2 M_2^2}{(M_1 + M_2)^2} (r_1 + r_2)^4 \omega^6 = \\ &= \frac{32G^{\frac{7}{3}}}{5c^5} \frac{(M_1 M_2)^2}{(M_1 + M_2)^{\frac{2}{3}}} \omega^{\frac{10}{3}} \end{aligned} \quad (1.43)$$

with r_1 and r_2 being the distance of the two point masses from the center of mass, and ω the angular frequency of their motion. The third Kepler law has been used in order to obtain the second expression.

In a Newtonian description, the total energy of such a system is given by:

$$\begin{aligned} E_{tot} &= \frac{1}{2} M_1 r_1^2 \omega_1^2 + \frac{1}{2} M_2 r_2^2 \omega_2^2 - G \frac{M_1 M_2}{r_1 + r_2} = \\ &= -\frac{1}{2} \frac{GM_1 M_2}{r_1 + r_2} = \\ &= -\frac{1}{2} G^{\frac{2}{3}} \frac{M_1 M_2}{(M_1 + M_2)^{\frac{1}{3}}} \omega^{\frac{2}{3}} \end{aligned} \quad (1.44)$$

where the third Kepler has been used in the computations.

An evolution law for frequency can thus be obtained noting that $P_{GW} = -\frac{dE_{tot}}{dt}$:

$$\omega^{-\frac{11}{3}} \frac{d\omega}{dt} = \frac{96}{5} \frac{G^{\frac{5}{3}}}{c^5} \frac{M_1 M_2}{(M_1 + M_2)^{\frac{1}{3}}} \quad (1.45)$$

The frequency of the emitted GWs is $f = \frac{\omega}{\pi}$. Inserting this into the previous equation, and integrating from t to a given t_{max} , with $t_{max} > t$, one obtains:

$$f^{-\frac{8}{3}}(t) = \frac{256}{5} \pi^{\frac{8}{3}} \mathcal{M}^{\frac{5}{3}} \frac{G^{\frac{5}{3}}}{c^5} (t_{max} - t) + f_{max}^{-\frac{8}{3}} \quad (1.46)$$

with:

$$\mathcal{M} = \frac{(M_1 M_2)^{\frac{2}{3}}}{(M_1 + M_2)^{\frac{1}{5}}} \quad (1.47)$$

being the chirp mass of the system.

In the subject, f_{max} is the maximum frequency one can achieve while still being able to consider Newtonian mechanics as dominant, and GR effects as lower order terms.

This frequency is achieved at the innermost stable circular orbit (ISCO), that is, at the innermost distance between the compact objects where they define a stable circular orbit. In GR, one has that a point mass orbiting a much more massive object reaches its ISCO at a distance from the center of mass given by $d = 3R_S = \frac{6GM}{c^2}$, with M the mass of the heavier object and R_S the Schwarzschild radius of the massive object.

However, for a CBC, the two Schwarzschild radii are comparable in size. The ISCO at this point is not given by some easy argument like that of superimposing $R_1 = 3R_{S_1}$ and $R_2 = 3R_{S_2}$: one may need searching for more internal orbits [17].

Moreover, there is another issue. The ISCO is an orbit where GR effects are not negligible, so that multipole terms beyond the quadrupole start raising their level and, in addition, the dynamics can not be described with a fully Newtonian approach.

These mathematical preambles need not be more complicated, since the Newtonian-describable early inspiral phase is enough for the work being presented. This is why the last parts of the inspiral phase are being cut out, thus

discarding the situations when GR effects become important. In this discussion, one can use $f_{max} = f(t_{max})$ as the frequency when the distance between the two compact objects becomes $d = R_1 + R_2 = 3R_{S_1} + 3R_{S_2}$. This is the maximum frequency for every kind of CBC ever considered in the presented work, and it can be expressed as:

$$f_{max} = \frac{1}{\pi 6^{\frac{3}{2}}} \frac{c^3}{G(M_1 + M_2)} \quad (1.48)$$

It has been illustrated that equation (1.46) gives a precise evolution law for the frequency of GWs. By measuring $f(t_1)$ and $f(t_2)$ of a given GW signal, one can find the chirp mass and thus infer the frequency evolution at future times, before t_{max} . This means that the signal as seen by a detector *at a fixed position* at future times (way before the merger) can be predicted with some advance.

This find can be very useful for enhancing the localization capabilities of GW detectors, as shown in chapter 4.

Furthermore, this can help to work out a maximum frequency generally required for the computations with GWBENCH. In particular, the software makes use of a post Newtonian expansion for generating GW waveforms (different numerical models can be used); however, as already mentioned, only the early inspiral phase is considered. The evolution of an early inspiral signal can be treated within a fully Newtonian approach.

This chapter has illustrated a theoretical description of GWs, trying to avoid instrument-related arguments, when possible. In particular, the GW equation has been obtained in a Lorentz gauge, and then specified to a TT gauge for sake of mathematical simplicity. This formalism allows one to work out the well known GR tensor polarization modes, + and \times . Consequently, it has been shown that the reference frame of freely falling as well as grounded detectors can be addressed (with some approximation) as an always-Minkowskian frame, namely what has been called the FNC frame.

The effect of a GW in this frame is given by actual motion of test masses, which can be parametrized very easily using the quantities computed in the TT gauge (even if FNC frames do not always match with TT frames).

At this point, one is able to perform a very short analysis of the detection of GWs with a laser interferometer, a subject which comes at hand in the next chapter, where it is also widened and deepened. Without trying to be accurate in this subject, enough information has been gathered to understand that GWs can be detected using laser interferometers, and that the objection that the wavelength of light changes according to the GWs (therefore spoiling the experiment) is false.

The concluding section of this chapter has focused on the emission of GWs and the energy carried by such waves. The emission of GWs has been addressed with the assumption of non-relativistic motions in the source. It has been proved that, for considerations about the energy transported by GWs, linearized theory has to be broadened and improved, allowing for the energy carried by GWs to curve space-time on large scales. Consequently, an expression for the power emitted by GWs in the reference frame of the source has been worked out.

Comparing this power with the time derivative of the total energy of a CBC (dumbbell-like system), as computed in a fully Newtonian approach, has led to the representation of the time evolution of the waves' frequency, thus providing with a powerful tool for the work being presented in the following chapters.

After showing in this chapter that GWs can be detected by means of laser interferometry, the next chapter focuses on detectors, starting from equation (1.23), and working out a crucial preamble for this essay. This part includes the definition of the sensitivity curve for a GW detector, after working out the noise sources for such an instrument. These (qualitative) results end up in a short summary of data analysis in common GW experiments, and the methods used by `GWBENCH`. Furthermore, a quick presentation of the existing and up to come facilities is done, with special care on ground-based third generation detectors. In conclusion, the sensitivity patterns of detectors is worked out as a function of the source direction in the local reference frame of the detector, thus defining the antenna patterns of the detectors.

Chapter 2

GW Detectors

In this chapter, a more detailed representation of GW detectors is presented. In particular, the discussion starts with a natural prosecution of the end of the previous chapter, that is, the interferometric detection of GWs: this aspect is addressed more in detail, even though many optics-related stuff are cut out. To be specific, the discussion is addressed in a fashion where the structure of the interferometer gets abruptly simplified.

Namely, the main focus of the first section is the understanding of the main contributors to the sensitivity curve of a ground-based interferometer. The noise contributions too are treated in a very simplistic view, and the illustration provided here settles for a qualitatively, rather than quantitatively, correct formulation. This subject permits to better understand the meaning of some argumentations being carried on in the following chapters of the essay.

The treatment of noise provides the preamble for a short introduction about the approaches for data analysis. This is a good starting point for the understanding of the main features of the software being used for simulation and data analysis in the presented work, `GWBENCH`.

After that, a short break from calculations: a review of current and future generation ground-based facilities is presented. This is pursued in a very simplistic way too, trying to point out the main differences between the different detectors. This part is addressed in the third section.

Furthermore, a mathematical approach brings another result, permitting to work out the antenna patterns (APs) in a fashion where GWs only show time dependence. This approximation is proved to be correct for current ground-based detectors, while a parenthesis is still left open for future generation ones. This is the approximation implemented in `GWBENCH`.

2.1 Noise in GW Detectors

Some introductory discussion about the importance of different noise contributions can be achieved implementing a few complications to the arguments which have led us to equation (1.27).

In fact, by using equation (1.27), one can try to work out some operating points for a GW interferometer, and see which one is the most appropriate.

By constraining $\omega(l_x - l_y)/c \simeq n\pi/2$, where n is an odd integer, one gets:

$$P_{out}(t) = P_{in} \sin^2 \left(n \frac{\pi}{2} + \frac{\omega(l_x + l_y) h}{2c} \right) \simeq P_{in} \left(1 + \frac{\omega^2(l_x + l_y)^2 h^2}{2c^2} \right)$$

which is second order in h and highly disturbed by an offset $= P_{in}$. A second try can be obtained by setting $\omega(l_x - l_y)/c \simeq n\pi/4$, where n is an odd integer:

$$P_{out}(t) = P_{in} \sin^2 \left(n \frac{\pi}{4} + \frac{\omega(l_x + l_y) h}{2c} \right) \simeq P_{in} \frac{1}{2} \left(1 + \frac{\omega(l_x + l_y) h}{c} \right)$$

being linear in h , but still being disturbed by an offset term. The noise caused by this offset could overtake the effect of a GW.

The final try is given by $\omega(l_x - l_y)/c \simeq n\pi$:

$$P_{out}(t) = P_{in} \sin^2 \left(n\pi + \frac{\omega(l_x + l_y) h}{2c} \right) \simeq P_{in} \frac{\omega^2(l_x + l_y)^2 h^2}{4c^2}$$

being second order in h .

The dark fringe is more interesting in order to reduce the effect of offset-induced noise. However, a special strategy is needed in order to obtain a result linear in h .

This strategy consists in mixing the (ideally) monochromatic light with a modulating signal in order to obtain an input electric field entering the interferometer like: $E_0 \exp(i[\omega t + \beta \sin(\Omega t)])$, with β a given amplitude parameter and Ω a modulating frequency.

This expression can be rewritten in terms of the Bessel base [18] as:

$$E_{in} = E_0 \sum_{n=0}^{\infty} J_n(\beta) e^{i[n\Omega t + \omega t]} + J_{-n}(\beta) e^{i[-n\Omega t + \omega t]} \quad (2.1)$$

A widely spread approximation consists in considering only order 0 and order 1 Bessel functions, so that:

$$E_{in} = E_0 \left[J_0 e^{i\omega t} + J_1(\beta) e^{i[\Omega t + \omega t]} - J_1(\beta) e^{i[-\Omega t + \omega t]} \right] \quad (2.2)$$

This expression can be implemented in the computations, noting that, one has to account for the frequency modulation.

In particular, the electric field at the output depending on the frequency of the beam is given by:

$$E_{out}(\tilde{\omega}, t) = i \bar{E}_0(\tilde{\omega}) \Psi(\tilde{\omega}, t) \sin \left(\frac{\tilde{\omega}(l_x - l_y)}{c} + \left(\frac{\tilde{\omega}(l_x + l_y) h}{2c} \right) \right) \quad (2.3)$$

where $\tilde{\omega} = \omega \pm \Omega$ with $\bar{E}_0(\tilde{\omega})$ being equal to $\pm E_0 J_1(\beta)$ and

$$\Psi(\tilde{\omega}t) = e^{[i(\tilde{\omega}t + \tilde{\omega}(l_x + l_y)/c + \tilde{\omega}(l_x + l_y) h/2c)]}$$

By constraining $\omega(l_x - l_y)/c = n\pi$, one can see that $\sin \left[\frac{\omega \pm \Omega}{c} [(l_x - l_y) + (l_x + l_y)/2] \right] \simeq \pm \sin \left[\frac{\Omega}{c} (l_x - l_y) \right]$ (since $\frac{\Omega(l_x - l_y)}{c}$ has no notable value, unlike $\frac{\omega(l_x - l_y)}{c}$) and therefore:

$$\begin{aligned}
E_{out}(t) = iE_0 \Psi(\omega, t) & \left(2 J_1(\beta) \sin \left[\frac{\Omega}{c} ((l_x - l_y) + h \frac{(l_x + l_y)}{2}) \right] \cos \left[\Omega(t + \frac{(l_x + l_y)}{c}) \right] + \right. \\
& \left. + J_0(\beta) \sin \left[\frac{\omega(l_x - l_y)}{c} + \frac{\omega h(l_x + l_y)}{2c} \right] \right)
\end{aligned} \tag{2.4}$$

meaning that the output power contains a term linear in h , here called $P(\sim h)$. This power produces a voltage output at a photodiode where a mixer averages the term $\cos \left[\Omega(t + \frac{(l_x + l_y)}{c}) \right]$ to a constant factor. Therefore, one gets:

$$V_{out} = V_0 \sin \left[\frac{\omega(l_x - l_y)}{c} + \frac{\omega h(l_x + l_y)}{2c} \right] \sin \left(\frac{\Omega(l_x - l_y)}{c} \right) \tag{2.5}$$

which is linear in h noting that $\sin \left[\frac{\omega(l_x - l_y)}{c} + \frac{\omega h(l_x + l_y)}{2c} \right] \simeq \frac{\omega h(l_x + l_y)}{2c}$ and can be maximized with $\sin \left(\frac{\Omega(l_x - l_y)}{c} \right) = 1$, thus giving some very precise constraints on $(l_x - l_y)$, generally referred to as the Schnupp asymmetry. A reference for these concepts can be found at [19].

Equation (2.5) can be differentiated in order to have an initial idea of the main noise contribution affecting a GW measure. Before doing that, one has to rewrite it in order to understand what are the aleatory variables of the expression. These variables are (essentially) given by an uncertainty on the amplitude of light, thus giving a fluctuation on the term V_0 , and by a phase uncertainty one can understand by adding to the previous expression an aleatory term $\tilde{\Phi}$, to be centered in zero but with non-zero variance:

$$V_{out} = V_0 \sin \left[\frac{\omega(l_x - l_y)}{c} + \frac{\omega h(l_x + l_y)}{2c} + \tilde{\Phi} \right] \tag{2.6}$$

One can go onto differentiate the expression considering the usual law for the propagation of uncertainties:

$$\begin{aligned}
\Delta^2 V_{out} = \Delta^2 V_0 & \left| \sin \left[\frac{\omega(l_x - l_y)}{c} \right] \right|^2 + \Delta^2 \tilde{\Phi} V_0^2 \left| \cos \left[\frac{\omega(l_x - l_y)}{c} \right] \right|^2 \\
& + \left(\frac{\omega h(l_x + l_y)}{2c} \right)^2 V_0^2 \left| \cos \left[\frac{\omega(l_x - l_y)}{c} \right] \right|^2
\end{aligned} \tag{2.7}$$

Therefore, the fluctuation on the amplitude gets suppressed by the term $\sin \left[\frac{\omega(l_x - l_y)}{c} \right]$, while the phase uncertainty is the factor that mostly threatens the GW measure.

This kind of argument shows why it is common usage to implement the *squeezing of light*. This practice allows to reduce the contribution of noise by making use of the Heisenberg uncertainty principle for states of light $\Delta n \Delta \phi \geq h$, where n is the number of photons being carried by a quantum state, ϕ is the phase of the light and h is the Planck constant. By thinking about using a

minimum uncertainty state, that is, a state for which the Heisenberg equality holds, one can think about reducing $\Delta\phi$ while raising Δn .

This practice allows to reduce the overall noise contribution, since Δn is proportional to the amplitude noise as expressed in (2.7), which is not the first contributor, while $\Delta\phi$ is proportional to the phase noise, which, on the other hand, is a louder noise source.

A simple and celebrated approach to the *squeezing of light*, both in its theoretical and practical aspects, is given at [20].

Equation (2.7) does not involve any information about the frequency dependence of the different kinds of noise.

In order to obtain that, a different approach is due. In particular, one needs to account for a time domain treatment of the GW signal. In fact, the oscillation of the GW strain with time has been completely neglected so far. This computation is mathematically harder, so that one may go back to the first approximation of *no*-frequency modulation, thus getting rid of the modulating frequency Ω .

A simple Michelson interferometer with no further complications is considered henceforth.

In this case, one has that the infinitesimal time interval taken by a photon to travel along a space interval being affected by a GW is given by:

$$cdt = \left(1 + \frac{1}{2}h(t)\right) dx \quad (2.8)$$

Meaning that the original (*i.e.* in absence of GWs) length of an arm of the interferometer is given by:

$$L_x \simeq c \int_{t_0}^{t_1} \left(1 - \frac{h}{2} \cos(\omega_h t)\right) dt \quad (2.9)$$

where t_0 is the time when photons interact for the first time with the beam splitter, t_1 is the time when photons impinge on the end mirror, and t_2 is the time when light gets back to the beam splitter, so that twice the length of the interferometer's arm is given by:

$$2L_x = c(t_2 - t_0) \frac{c}{2} \int_{t_0}^{t_2} h \cos(\omega_h t) dt \quad (2.10)$$

by approximating the integral extremity $t_2 \simeq t_0 + \frac{2L_x}{c}$ what one gets is:

$$\begin{aligned} t_2 - t_0 &\simeq \frac{2L_x}{c} + \frac{h}{\omega_h} \sin\left(\frac{L_x \omega_h}{c}\right) \cos\left(\omega_h(t_0 + \frac{L_x}{c})\right) = \\ &= \frac{2L_x}{c} + \frac{L_x}{c} \operatorname{sinc}\left(L_x \frac{\omega_h}{c}\right) h\left(t_0 + \frac{L_x}{c}\right) \end{aligned} \quad (2.11)$$

Doing the same computation for the y direction one can obtain that the electric field of light from the two arms is out of phase by a factor:

$$\begin{aligned} \frac{\omega(L_x - L_y)}{c} + \Delta\Phi &\simeq \frac{\omega(L_x - L_y)}{c} + \\ &+ h \frac{\omega(L_x + L_y)}{2c} \cos\left[\omega_h\left(t - \frac{(L_x + L_y)}{2c}\right)\right] \operatorname{sinc}\left[\frac{\omega_h(L_x + L_y)}{2c}\right] \end{aligned}$$

Special care need be paid to the fact that ω is the frequency of light and ω_h is the frequency of GWs.

This means that the output power in absence of GWs is given by:

$$P_{out} = P_{in} \sin^2 \left[\frac{\omega(l_x - l_y)}{c} \right] \quad (2.12)$$

At this point, one can introduce the shot-noise within a quantum depiction of light, therefore expressing:

$$P_{in} = \frac{n\hbar\omega}{t} \quad (2.13)$$

where n is the number of photons impinging on the photodetector during the sampling time t . Implementing a Poisson approach for the arrival of photons:

$$\Delta P_{SN} = \frac{\sqrt{n}\hbar\omega}{t} = \sqrt{\frac{\hbar\omega P_{in}}{t}} \quad (2.14)$$

On the other hand, defining $\Delta\tilde{\Phi}$ (the noise induced by phase fluctuations) is not as easy as for the shot noise. One can infer the force as given by the radiation pressure of photons hitting a mirror (in this case, only end mirrors are considered) like:

$$F = \frac{2n\hbar\omega}{ct} \quad (2.15)$$

and obtain a fluctuation on it as dictated by the shot noise:

$$\Delta F = 2 \left(\frac{\hbar\omega P_{in}}{c^2 t} \right)^{\frac{1}{2}} \quad (2.16)$$

the single-sided spectrum of this fluctuation is given by:

$$S_F(\omega) = 2 \int_{-\frac{t}{2}}^{\frac{t}{2}} \Delta^2 F e^{-i\omega t} \frac{d\omega}{2\pi} = 2t\Delta^2 F \quad (2.17)$$

This is the spectrum of the fluctuation of the force acting on an element of an end mirror due to the radiation pressure of photons. In order to infer the spectrum of the spatial oscillations induced by such force fluctuations, one can use the Langevin formalism as explained and used in [21], thus obtaining:

$$S_x(\omega_h) = \frac{S_F(\omega_h)}{m^2 \omega_h^4} = \frac{8\hbar\omega P_{in}}{c^2 m^2 \omega_h^4} \quad (2.18)$$

and one can define:

$$\begin{aligned} \Delta P_{GW} &= P_{in} 2 \sin \left(2 \frac{\omega(l_x - l_y)}{c} \right) \frac{\hbar\omega(l_x + l_y)}{2c} \operatorname{sinc} \left[\frac{\omega_h(L_x + L_y)}{2c} \right] \\ \Delta P_{SN} &= \left(\frac{\hbar\omega}{t} P_{in} \right)^{\frac{1}{2}} \left| \sin \left(\omega \frac{(l_x - l_y)}{c} \right) \right| \\ \Delta P_{\tilde{\Phi}} &= P_{in} \sin \left(2 \frac{\omega(l_x - l_y)}{c} \right) \Delta\tilde{\Phi} = P_{in} 2 \sin \left(2 \frac{\omega(l_x - l_y)}{c} \right) \frac{\omega}{c} S_x(\omega_h)^{\frac{1}{2}} \end{aligned} \quad (2.19)$$

At this point, the final shot noise and radiation pressure related noise amplitude spectral densities (ASDs) are defined like:

$$\begin{aligned} ASD_{SN}(\omega_h) &= \frac{\Delta P_{SN}}{\Delta P_{GW}} \cdot h t^{\frac{1}{2}} \propto \frac{\omega_h}{\sin(\omega_h \frac{(l_x+l_y)}{2c})} \\ ASD_{RP}(\omega_h) &= \frac{\Delta P_{\Phi}}{\Delta P_{GW}} \cdot h t^{\frac{1}{2}} \propto \frac{1}{\omega_h \sin(\omega_h \frac{(l_x+l_y)}{2c})} \end{aligned} \quad (2.20)$$

These are the main dependencies being observed in the sensitivity plots commonly used to address the capabilities of GW detectors. However, there are many other contributors for the vibration of mirrors together with radiation pressure from the laser beam. There are thermal excitations leading to coating and substrate Brownian noise, there is seismic noise propagating to the mirrors by means of the optimal, but not perfect, vibration attenuators, and so on. A plot taken from the website of Cosmic Explorer containing the curves for the current LIGO detectors and a few future generation facilities is displayed at figure (2.1).

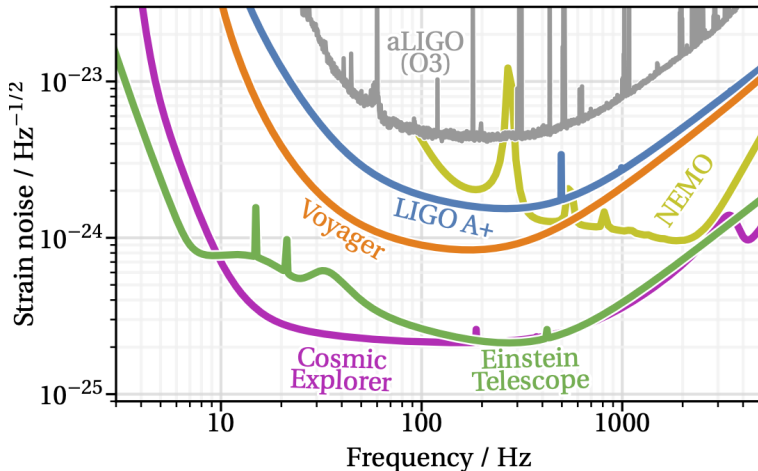


Figure 2.1: Sensitivity curves in term of noise ASDs for LIGO and future generation detectors.

A plot which may come very useful for the understanding of the noise contributions is displayed at figure (2.2), putting in evidence each noise contribution, as inferred in [22]. Shot noise and radiation pressure noise are here addressed as quantum fluctuations, the vibration making it through the attenuating system is addressed as seismic vibration, while the gravity gradients caused by seismic events, or general perturbations of the local stress-energy tensor, are addressed as Newtonian gravity.

The dominant thermal noise contribution comes from coating Brownian noise of the mirrors, while Brownian effects from the substrates are less invadent. Thermo-optic noise refers to the variations in optical properties of mirrors due to heating (one over all is the phenomenon of birefringence).

The residual gas term is given by the fact that the interferometers do not work in a perfect vacuum: it accounts for the presence of residual air molecules.

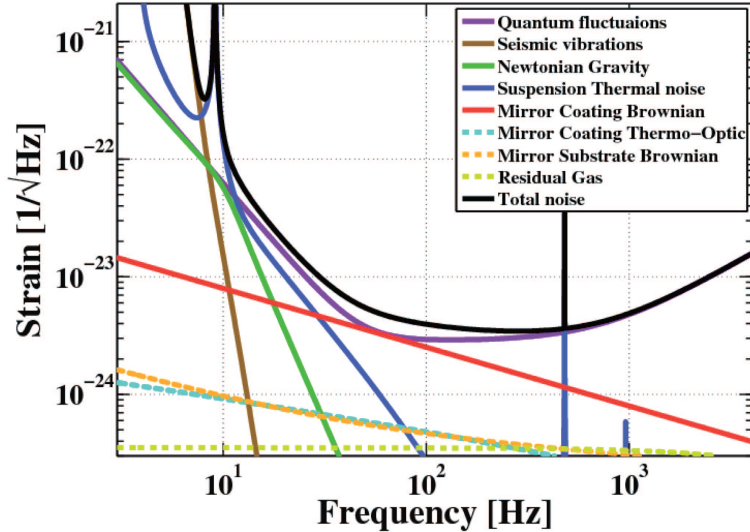


Figure 2.2: ASD of every noise source. Picture taken from [22].

2.2 GW Data Analysis

This section is dedicated to the understanding of how the knowledge of noise comes into play in the data analysis performed for GW experiments, and to the implementations of these concepts in GWBENCH.

This comes very useful in the understanding of the deal represented by this software, which provides a good (but not optimal) inference of parameters, while being much faster with respect to Bayesian inference.

However, one can see that GWBENCH implements some results inferred from the Bayesian theorem itself, but it treats them from a frequentist point of view.

The Bayes theorem is defined as follows:

$$P(H|D) = \frac{P(D|H)P(H)}{P(D)} \quad (2.21)$$

where D represents the data, and H is a hypothesis. The $P(H)$ is generally called *prior* term, $P(D|H)$ is the definition of the *likelihood*, namely the probability that the data matched with the hypothesis. $P(D)$ is a normalization factor, usually expressed like $\sum_i P(D|H_i)P(H_i)$, and called *evidence*.

One of the great assumptions of simplified GW data analysis is considering white Gaussian noise, displaying no correlation in time: GWBENCH works with this assumption. This kind of noise can be treated as an aleatory variable $n(t)$ describing a noise process centered on zero and defining an autocorrelation function $\langle n(t)n(t') \rangle = \sigma^2\delta(t-t')$. Therefore, one finds that the noise spectrum is given by the Fourier transform of this autocorrelation function, that, given a sampling time Δt , is given by: $S_n(\omega) = 2\sigma^2\Delta t$

This means that a Gaussian probability can be considered for the noise in absence of h strain in the detected signal (that is, what can be called the *null hypothesis*). The multivariate distribution accounting for all the time steps of the observation is given by:

$$P(D|H_0) \sim e^{-\frac{\sum_i s^2(t_i)}{2\sigma^2}} = e^{-\frac{\sum_i s^2(t_i) \Delta t}{2\sigma^2 \Delta t}} \simeq e^{-\frac{\int |s|^2(t) dt}{S_n(\omega)}} = e^{-\frac{\int |\tilde{s}|^2(\omega) d\omega}{S_n(\omega)}} \quad (2.22)$$

where the last equality is given by the Parseval theorem.

With this result, one can define a scalar product in the following way:

$$(x, y) = 2 \int_{-\infty}^{\infty} \frac{\tilde{x}(\omega) \tilde{y}^*(\omega)}{S_n(\omega)} d\omega \quad (2.23)$$

so that:

$$P(D|H_0) \sim e^{-\frac{(s, s)}{2}} \quad (2.24)$$

Considering an alternative hypothesis H_1 where the signal contains a GW signal h :

$$P(D|H_1) \sim e^{-\frac{(s-h, s-h)}{2}} = e^{-\frac{(s, s) - 2(s, h) + (h, h)}{2}} \quad (2.25)$$

where the equality comes from the assumption of signal and strain both real in the frequency domain.

A ratio of the two likelihood functions (what is called the *Bayes factor*) is used in frequentist statistics since it does not involve any information about the prior distribution of the hypothesis.

What one obtains for this ratio is:

$$\frac{P(D|H_1)}{P(D|H_0)} = e^{+(s, h) - \frac{(h, h)}{2}} \quad (2.26)$$

where (s, h) contains the observed signal s and the GW strain h . This is addressed as the main figure of merit, that has to be maximized in a procedure called *matched filtering*. In fact, one can implement template waveforms sampling the parameter space and find the h_{max} related to the hypothesis $H_{1_{max}}$ by maximizing the *Bayes factor*, thus inferring the physical parameters for the event being observed.

Of course, this is a maximization process which only focuses on H_1 ; hence, maximizing the *Bayes factor* is the same as maximizing the likelihood function for H_1 .

This method as it is described here does not consider any incorporation of the prior information for the single hypotheses being considered.

However, the process as described here could take very long. An optimized way to find the physical parameters can be worked out directly from the likelihood function of H_1 as given in equation (2.25). Its value increases when $(s-h, s-h)$ shrinks, reaching an optimal value when it approaches a minimum, *i.e.* a stationary point.

If one sets $E(\vec{\Theta}) = (s-h, s-h)$ with $\vec{\Theta}$ the array of parameters, the following expansion in the neighbourhood of a minimum (represented by $\vec{\Theta}^*$) can be pursued:

$$E(\vec{\Theta}) \simeq E(\vec{\Theta}^*) + \frac{1}{2} \left. \frac{\partial^2 E}{\partial \Theta_i \partial \Theta_j} \right|_{\vec{\Theta}^*} \Delta \Theta_i \Delta \Theta_j \quad (2.27)$$

where:

$$\frac{\partial^2 E}{\partial \Theta_i \partial \Theta_j} \Bigg|_{\vec{\Theta}^*} = (\partial_{\Theta_i} h, \partial_{\Theta_j} h) - 2(\partial_{\Theta_i \Theta_j}^2 h, s - h) \quad (2.28)$$

which reduces to:

$$\frac{\partial^2 E}{\partial \Theta_i \partial \Theta_j} \Bigg|_{\vec{\Theta}^*} = (\partial_{\Theta_i} h, \partial_{\Theta_j} h) \quad (2.29)$$

since the noise has zero mean.

One can define: $(\partial_{\Theta_i} h, \partial_{\Theta_j} h) = \Gamma_{ij}$, namely the ij -th component of the Fisher information matrix (FIM), so that:

$$P(D|H_1) \sim e^{-\frac{1}{2} \Gamma_{ij} \Delta \Theta_i \Delta \Theta_j} \quad (2.30)$$

Therefore, the assumption of Gaussian noise leads to the equation:

$$\Sigma = \Gamma^{-1} \quad (2.31)$$

being Σ the covariance matrix. At this point, one just needs to invert the FIM in order to obtain all the information about variances and covariance terms. This approach is followed in GWBENCH, both for inferring the parameters by maximizing the likelihood function and for finding the covariance matrix by means of the FIM [23]. This strategy, however, is not new in the subject of GWs, and it has already been assessed for the analysis of CBC events [24], even if Bayesian inference methods based on Gauss-Markov chains are now the standard way for GW data analysis.

With respect to such chains, the FIM formalism does not involve any prior distribution for hypothesis, and does not allow to obtain the marginalized posterior distribution for all the single parameters.

2.3 GW Facilities

Figure (2.1) points out the multitude of existing GW detectors and projects for future facilities. However, this plot is just a way to address the usual shape and orders of magnitude of the sensitivity curves for GW detectors, but it does not pretend to show *all and only* the GW facilities considered for the work presented in this essay.

An introductory illustration of the GW interferometers is needed in order to keep in mind the strengths and weaknesses of the considered instruments while describing methods and results in the next chapters. This is the topic of the next section.

2.3.1 Current Facilities

The characteristics of current facilities are illustrated in this paragraph. These detectors are ground-based, and have collected all the GW data known to date.

LIGO Detectors

LIGO detectors are 2 L-shaped Michelson interferometers placed in Hanford (Washington) and Livingston (Louisiana), US, with 4 km long arms. Such detectors are almost coaligned, meaning that their APs (as calculated in the next section) for a given polarization mode are quite similar. This is a major help for raising the SNR of a GW event and for ruling out a vast majority of noise induced triggers. However, this peculiarity comes as a disadvantage when considering just the LIGO detectors to disentangle the two GR polarization modes. This aspect is treated more in depth in the next chapter.

LIGO detectors have been evolving very fast, and the present configurations, usually referred to as Advanced LIGO, are way different from the initial ones.

However, this essay does not focus on the description of the optical structure or technology of the interferometers. What need be reported is an assessment of the overall LIGO sensitivity as currently considered. This is displayed by an ASD plot at figure (2.3).

GWENCH addresses future detectors, namely involving only noise ASDs for future configurations. This implies that the current sensitivity (namely, that of O4) is not even considered, and one eventually has to artificially include it into the software. For the present work, only the O5 sensitivity (already implemented in the software) has been used. Moreover, GWENCH does not actually implement these curves with all their spectral features (*i.e.* it does not take account of all the resonances). It just keeps track of the continuum and the greatest peaks.

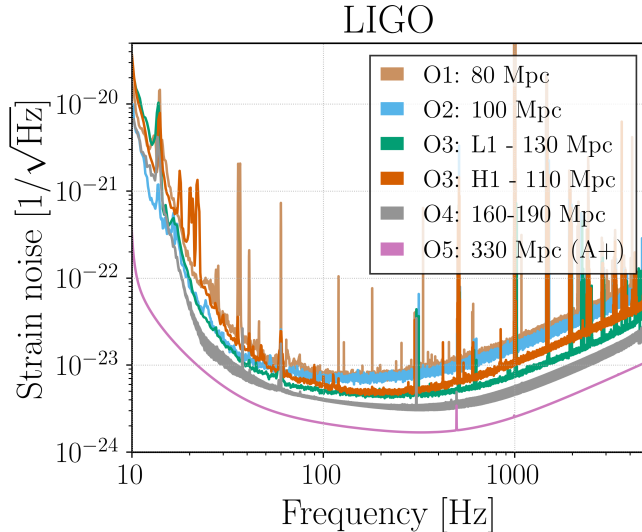


Figure 2.3: Sensitivity curves for LIGO for different observing runs. Plot taken from [25].

Virgo Detector

The European counterpart to the LIGO detectors is represented by the celebrated Virgo detector, located near Pisa, Italy.

While globally resembling the LIGO detectors, this interferometer presents some differences when studied at a deeper level. First of all, its arms are only 3 km long; one can remember from chapter 1 that $\Delta l = l h/2$, thus representing a disadvantage. Its greater strength with respect to LIGO is the super-attenuator technology implemented for the vibration insulation and absorption system. It consists of cascading passive filters cutting noise off above a threshold frequency and an active filter working at lower frequencies [26]. This makes an outstanding job in the reduction of the seismic noise contribution at very low frequencies.

However, the thermal insulation and the overall optical elements are weaker than in LIGO. This makes Virgo a modern instrument with some very good capabilities at lower frequencies, but with weaker performances than LIGO on medium and high frequencies.

The overall noise sensitivity curve for Virgo is plotted at figure (2.4).

Once again, GWBENCH only implements the sensitivity for O5, in particular, considering the lower bound of the purple shaded area in figure (2.4), thus being quite optimistic about the improvement capabilities of Virgo.

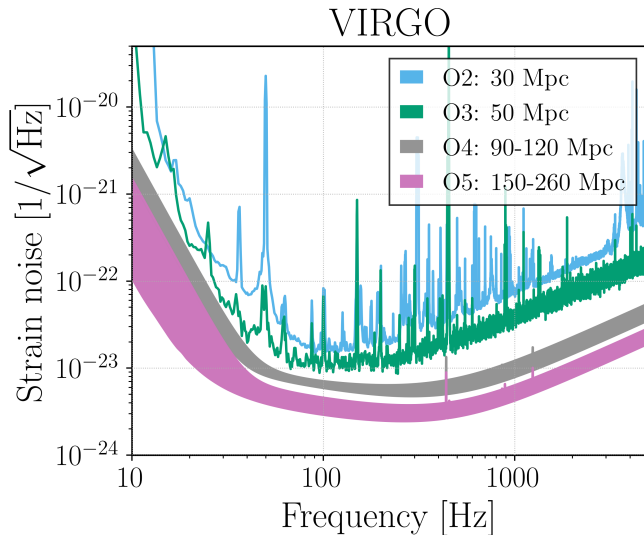


Figure 2.4: Sensitivity curves for Virgo for different observing runs. Plot taken from [25].

KAGRA Detector

The Japanese GW detector KAGRA will be involved in GW observations starting with the currently ongoing observation run, even if its performances are still lame with respect to the level set by the other facilities. This is due to the fact that KAGRA is built underground in order to minimize the effect of seismic noise, and it implements a cryogenic technology for keeping the optics

at very low temperature, thus reducing the overall thermal noise effects. This technology still needs to be refined. Regarding other aspects, it resembles the already mentioned facilities, being L-shaped with 3 km long arms.

KAGRA implements sapphire optics, differently from other current detectors implementing fused silica. In fact, fused silica would display large mechanical dissipation at low temperatures.

Moreover, sapphire shows better performances in terms of birefringence effects (the variation of the refractive index due to temperature gradients); the magnitude of such variations is order $\sim 10^{-6}$ smaller with respect to fused silica at room temperature.

Finally, it has an advantage in terms of radiation pressure noise, since it is harder than fused silica, meaning that the excitation of oscillations in the material is rarer.

A rough sensitivity estimate for KAGRA during O4 is given at figure (2.5).

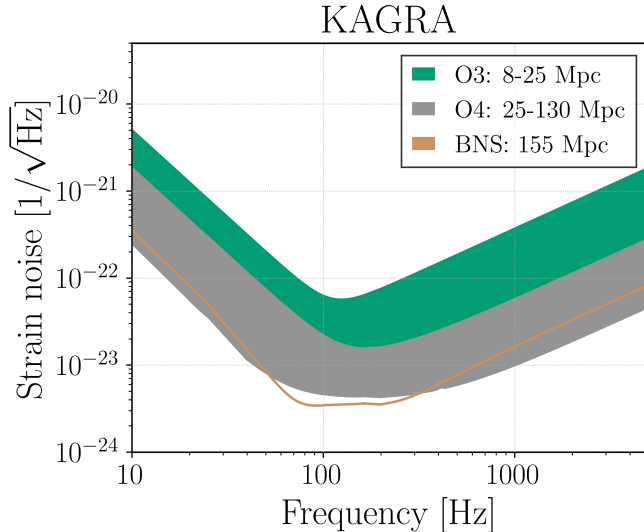


Figure 2.5: Sensitivity curves for KAGRA for different observing runs. Plot taken from [25].

2.3.2 Third Generation Facilities

As Advanced LIGO, Virgo, and KAGRA are second generation (2G) detectors, other facilities being currently projected and still in a preparatory phase are addressed as third generation (3G) detectors.

One of the most followed of such projects is LISA (*Laser Interferometer Space Antenna*), a space based GW interferometer orbiting around a Lagrangian point. This detector will be freely falling, and will not be disturbed by all those low frequency perturbations listed in chapter 1. This makes LISA a very suitable observatory for low frequency GW events, thus leading to more in-depth studies of supermassive BHs. At higher frequencies, the sensitivity of LISA is worsened by the extremely long interferometer arms ($\sim 10^6$ km). This

effect gives a highest detectable frequency \sim Hz [27]. However, the research work being presented does not refer to this kind of events; only high frequency signals are treated in this analysis, like those from BNS and stellar mass BBH. Hence, no further discussion regarding LISA is pursued.

On the other hand, ground-based 3G detectors are addressed now. They are commonly referred to as the prosecutors of current facilities, both in term of science goals and implemented technology.

The two main candidates for this projects are Cosmic Explorer (CE) for the US and Einstein Telescope (ET) for Europe.

An extra word is dedicated to the recently approved project of LIGO-India, which should not be assessed as a real 3G detector, even though it still has to undergo a refined scientific projecting phase. Therefore, it is momentarily assessed as a future generation facility.

Cosmic Explorer

Generally, ground-based 3G detectors are being designed and planned with a motivation which is far beyond that of LIGO. Namely, LIGO had been designed in order to maximize the SNR of a given signal, meaning that the two detectors are almost coaligned, so that their antenna patterns overlap quite perfectly, thus being able to detect the same GW sources and average noise out. However, antenna patterns display blind spots where GW sources can not be detected by the interferometers. If the antenna patterns of the two facilities overlap, then there will be spots from where only one GW polarization will be detectable.

CE is an American project accounting for two detectors which, on the other hand, are going to be placed in order not to have common blind spots for a given GR polarization. This approach limits the improvement achievable on the SNR, which is nevertheless expected to be way better than that of LIGO because of the improved technology implemented in the detectors.

Moreover, CE detectors will have 20 and 40 km long arms, greatly overtaking the dimensions of current facilities. Such detectors will need to be separated by a great distance in order to achieve the goal of homogeneously probe the sky for different polarization modes.

The setting for these instruments is now a great issue, since their huge dimensions do not allow them to be placed anyway on the continental United States. Therefore, in-sea solutions are being weighted right now.

A forecast for the sensitivity curve of CE is displayed at figure (2.1).

The peak sensitivity $\sim 10^{-25}$ Hz $^{-1/2}$ shall guarantee that mergers from the first stars ever born will be observable.

In particular, it is planned to be built in a *vanilla* version resembling a scaled up version of current generation detectors. Future upgrades will add currently undeveloped technologies like 2 μ m lasers and cryogenic silicon mirrors.

Mirrors are planned to be twice the diameter of currently implemented mirrors, and their substrates will be made of silicon. Silicon meets the performance requirements at very low temperatures (\sim 10 K) that fused silica fails. On the other hand, the material of coatings is still being debated. Silicon, as well as GaAs and AlGaAs, have been proposed for their performances in terms of thermoelastic noise.

Furthermore, current technologies implemented for the squeezing of light need be revised for CE, since its observing goals require it to set 10 dB of

frequency dependent noise reduction (current top performance is 6 dB).

The power to be injected in the interferometer will need be ~ 150 W, thus resulting in ~ 10 MW arm power (when accounting for power recycling cavity and Fabry Pérot cavities, that are planned to have finesse $\mathfrak{F} \sim 1000$).

[28] proves a 20+40 km configuration of L-shaped detectors implementing this technology to meet the scientific requirements for a 3G facility in terms of astrophysics and fundamental physics. However, it also shows that CE alone would be lame with respect to a network of detectors with both CE and ET.

Furthermore, the results of the work put up here stress the fact that CE alone can not pursue a measure of non-tensor GW polarizations, thus making the gravity test being presented accessible only with a network involving both CE and ET.

Einstein Telescope

ET will not just be a European counterpart of CE. Nevertheless, it is also designed in order not to maximize the SNR of a detectable GW source, but to be sensitive to the different polarizations at every position on the sky.

This goal is achieved by means of the construction of two or more non-coaligned detectors, just as CE. However, the most celebrated concept for ET (implemented also in the present work) is that of three detectors with arms forming an angle of 60 degrees, arranged to form a triangle.

This geometrically innovative solution (being considered also for LISA), permits to have two non-coaligned detectors plus a third one being coaligned to a linear superimposition of the other two. This is not the same as having three non-coaligned detectors, and this fact plays an important role in the following chapters.

ET traditionally proposes the idea of a "xylophone" detector, in the sense that each interferometer in the configuration accounts for a room temperature high frequency detector and a cryogenic low frequency one, with the foresight of implementing sapphire or silicon for the latter.

Differently from CE, ET will probably have 10 km long arms.

This configuration is generally good for more isotropic antenna patterns and it is extremely advantageous when the construction of very large L-shaped interferometers is not feasible. In particular, the configuration is already optimized and there is not the problem of perfecting the position and orientation of the detectors one respect to the other.

However, the issue of identifying a feasible place for the detector is still there, even though some credible hypotheses have already been proposed, as a consequence of seismic investigations in several locations in Europe and the US. For such sites, the super-attenuator as it is currently implemented in Virgo is considered as an adequate seismic insulation system.

ET will implement 1 μm and 1.5 μm lasers for the high and low frequency detectors respectively, the former at 3 MW and the latter at 18 kW (arm power). However, the shape of the high frequency detector laser will not be that of the currently implemented Gaussian beam: it will implement higher order modes, that are being studied since they allow for a better distribution of power on the optical elements, therefore reducing the thermal noise gradients. However, they carry few issues related to the purity of the laser beam. More stuff about this subject can be found at [29].

A combination of these measures allows ET to challenge the boundary pushed by the technology of CE, and also improve it at the very low frequencies (< 10 Hz) [30].

LIGO India

LIGO India is a project approved by the Indian government in order to strengthen the roster of current generation detectors. The concept of this detector resembles current facilities, as it is planned to have 4 kilometers long arms and operate with $\sim 10^2$ kW arm power, thus way lower than the CE and ET standards. These values naively match those of Advanced LIGO and Virgo [31].

In spite of the technology and conceptual design which resemble that of current generation facilities, LIGO India has been conceived with the same purpose of 3G detectors: allowing for an improved sky coverage considering a combination with LIGO and Virgo and for an enhanced localization of GW sources using the triangulation method (~ 1 order of magnitude)[32]. In fact, for achieving good localization capabilities, a third detector has to be placed at great distances from the others.

Furthermore, the following chapters pin point that a third non-coaligned detector is of great importance for the study of the polarization content of GWs.

However, practical details about the realization of this detector are still quite vague: an accurate project has not been presented at the current date, while the Indian government has already funded the initiative, foreseeing its completion in early 2030s. However, its location and orientation are already defined, and therefore implementable in computations like those pursued in the next sections: in fact, LIGO India is already available in GWBENCH.

After this short review of GW detectors, the next section focuses on the definition and mathematical derivation of the APs, which provide a fundamental tool for this essay.

2.4 Antenna Patterns

2.4.1 Formal Derivation

APs are analytical expressions defining the sensitivity pattern of a given detector as a function of angular coordinates expressed in the reference frame of the detector itself. This section focuses on the computation of the AP for +-polarized GWs as detected by a L-shaped detector.

In particular, for a photon propagating towards the x -direction: $cdt \simeq (1 + \frac{h_+}{2})dx$.

Applying the same notation as in section 2.1, one can write down the time of the light impinging on the beam splitter after travelling along an interferometer arm as:

$$t_2 \simeq t_0 + \frac{2l_x}{c} + \frac{\cos^2(\theta)}{2c} \int_0^{l_x} h_+ \left[t_0 + \frac{x}{c}(1 - \sin(\theta)) \right] dx + \frac{\cos^2(\theta)}{2c} \int_0^{l_x} h_+ \left[t_0 + \frac{l_x}{c}(1 - \sin(\theta)) + \frac{x}{c}(1 + \sin(\theta)) \right] dx \quad (2.32)$$

where t_0 is the time of first transmission/reflection at the beam splitter. Here θ is the projection on the zx -plane of the angle between the z (zenith) direction at the interferometer location and the direction of propagation of the GW.

One can see that this approach makes use of the same approximation used in section 2.1, thus ignoring the effect of Fabry-Pérot cavities along the arms of the interferometer.

Moreover, equation (2.32) manifestly neglects the spatial dependence of a GW: this is given by the assumption that the addressed GWs display a wavelength which is way larger than the length of the interferometer arms, so that even at $\theta = \pi/2$ one can consider the beam splitter and the end mirror on a given arm to coincide in phase at a given time.

The next step is obtained deriving equation (2.32) with respect to t_0 and expanding h_+ around t_0 . This leads to the following equation:

$$\frac{dt_2}{dt_0} \simeq 1 + \frac{1}{2} \left[(1 + \sin(\theta)) \left(h_+(t_0) + \dot{h}_+(t_0) \frac{2l_x}{c} \right) + \right. \\ \left. - (1 - \sin(\theta)) h_+(t_0) + 2 \sin(\theta) \left(h_+(t_0) + (1 + \sin(\theta)) \frac{l_x}{c} \dot{h}_+(t_0) \right) \right] \quad (2.33)$$

which can be proven to be equal to:

$$\left. \frac{dt_2}{dt_0} \right|_{x-arm} = 1 + \frac{l_x}{c} \cos^2(\theta) \dot{h}_+(t_0) = \\ = 1 + \frac{l_x}{c} \dot{h}_{+ij} \hat{e}_x^i \hat{e}_x^j \quad (2.34)$$

where h_{+ij} is the ij -th component of the spatial 3×3 tensor of the GW and \hat{e}_x^i is the i -th component of the unit vector directed as the x -arm of the interferometer.

Similarly, one can perform the same computation referring to the y -arm and obtain:

$$\left. \frac{dt_2}{dt_0} \right|_{y-arm} = 1 + \frac{l_y}{c} \dot{h}_{+ij} \hat{e}_y^i \hat{e}_y^j$$

The output of the detector is given by the time shift between the arrival times of light travelling along the x and y -arms, respectively.

Therefore, in a situation where originally $l_x = l_y = L$, one obtains:

$$\left. \frac{dt_2}{dt_0} \right|_{x-arm} - \left. \frac{dt_2}{dt_0} \right|_{y-arm} = \frac{d\delta t_2}{dt_0} = \frac{L}{c} \dot{h}_{+ij} (\hat{e}_x^i \hat{e}_x^j - \hat{e}_y^i \hat{e}_y^j) \\ \hookrightarrow \delta t_2 = \frac{L}{c} h_{+ij} (\hat{e}_x^i \hat{e}_x^j - \hat{e}_y^i \hat{e}_y^j) = \frac{L}{c} h_{+ij} d^{ij} \quad (2.35)$$

with d^{ij} being the detector tensor $d^{ij} = \hat{e}_x^i \hat{e}_x^j - \hat{e}_y^i \hat{e}_y^j$.

At this point, the mismatch in the length of the two arms, as induced by a GW, is given by:

$$\frac{\delta L}{L} = \frac{1}{2} h_{+ij} d^{ij} \quad (2.36)$$

and can be written as $\frac{\delta L}{L} = h_+ F_+$, *i.e.* the combination of the GW strain in the TT gauge and a quantity which is called the antenna pattern for the +-polarization mode, with:

$$\begin{aligned} F_+ &= \frac{1}{2} \epsilon_+^{ij} d_{ij} \\ \hookrightarrow F_{POL} &= \frac{1}{2} \epsilon_{POL}^{ij} d_{ij} \end{aligned} \quad (2.37)$$

where the expression for the + AP is generalized to that for a general polarization mode.

The polar angle θ has already been defined, however the source direction can depend on an additional angle ϕ given by the projection on the xy plane of the angle between the local zenith direction of the interferometer and the source direction. Moreover, one can define the polarization angle ψ as the rotation between the x and y coordinates on the plane of the interferometer reference frame (where, once again, z defines the zenith direction) and the coordinates of the TT gauge of the GW on the plane orthogonal to the propagation direction.

For instance, if $\psi = \frac{\pi}{4}$, the +-polarization of the GW looks like a \times -polarization as detected if $\psi = 0$.

More precisely, by rotating the detector's frame to the TT frame proper of the GW accounting for θ and ϕ , one finds a frame rotated by an extra degree of freedom so that the + and \times -polarization modes in this frame are related to the TT ones by the relations:

$$\begin{aligned} E_+ &= \epsilon_+ \cos(2\psi) + \epsilon_\times \sin(2\psi) \\ E_\times &= -\epsilon_+ \sin(2\psi) + \epsilon_\times \cos(2\psi) \end{aligned} \quad (2.38)$$

where E_+ and E_\times are the + and \times -polarization tensors in the rotated frame, and ϵ_+ and ϵ_\times are the TT frame polarization tensors as they have been defined in equation (1.17) and following.

Finally, one can compute the APs related to the two GR polarization modes as functions of θ , ϕ and ψ , obtaining:

$$\begin{aligned} F_+ &= \frac{1}{2} \left(1 + \cos^2(\theta) \right) \cos(2\phi) \cos(2\psi) - \cos(\theta) \sin(2\phi) \sin(2\psi) \\ F_\times &= \frac{1}{2} \left(1 + \cos^2(\theta) \right) \cos(2\phi) \sin(2\psi) - \cos(\theta) \sin(2\phi) \cos(2\psi) \end{aligned} \quad (2.39)$$

2.4.2 Implementation in GWBENCH

The APs as they are computed in GWBENCH, however, are not expressed like in (2.39).

In fact, the definition of the three angular coordinates θ , ϕ and ψ changes depending on the detector being considered. This means that, in order to implement equations (2.39), the angular coordinates for each detector are required. Nevertheless, inferring the angular coordinates for a given detector knowing their values for another detector at another latitude and longitude with respect to the first one is not an easy task.

Computationally, it is way more convenient to use the tensor expression at equation (2.37).

However, it need be pointed out that both ϵ_{POL}^{ij} and d^{ij} must be computed in the same reference frame.

The computation takes place in the reference frame of an ideal detector placed at the centre of the Earth (that is called "standard frame"), with its x -arm pointing towards the direction of the Greenwich Prime Meridian, the z -direction pointing towards the North Pole, and co-rotating with the Earth.

This means that the detector tensor d_{ij} need be expressed in this standard frame.

In particular, the orientation in space of a real detector is obtained with a first trasformation allowing for a rotation of the x and y -arms on the plane orthogonal to the z -direction (accounting for the longitude of the interferometer); secondly, a rotation about the (freshly re-defined) y -axis rotates the z -direction of an angle accounting for the latitude, thus obtaining the zenith direction; finally, another rotation about the zenith direction is pursued accounting for a rotation of the detector with respect to local axes, as defined by the previous transformation.

At this point, the inverse rotation matrices have to be defined:

$$\begin{aligned} R_i^{-1}(x) &= \begin{pmatrix} 1 & 0 & 0 \\ 0 & \cos x & -\sin x \\ 0 & \sin x & \cos x \end{pmatrix} \\ R_j^{-1}(x) &= \begin{pmatrix} \cos x & 0 & \sin x \\ 0 & 1 & 0 \\ -\sin x & 0 & \cos x \end{pmatrix} \\ R_k^{-1}(x) &= \begin{pmatrix} \cos x & -\sin x & 0 \\ \sin x & \cos x & 0 \\ 0 & 0 & 1 \end{pmatrix} \end{aligned} \quad (2.40)$$

The unit vectors \hat{e}_x and \hat{e}_y represent the x and y directions in the reference frame of the real detector. For an L-shaped detector, such unit vectors are directed like the arms of the interferometer, defining the detector tensor in equation (2.35) and following.

For triangle-shaped detectors, the unit vectors along the arms are defined like:

$$\begin{aligned} \hat{e}_1^\Delta &= \hat{e}_x \\ \hat{e}_2^\Delta &= (\hat{e}_x + \sqrt{3}\hat{e}_y)/2 \\ \hat{e}_3^\Delta &= (-\hat{e}_x + \sqrt{3}\hat{e}_y)/2 \end{aligned} \quad (2.41)$$

In order to express the arm vectors in the standard frame, one needs to inversely rotate such vectors by an angle accounting for the orientation of the

detector with respect to local axes (γ angle, that is, the angle from the "due East" direction to the y -arm), an angle accounting for the latitude of the detector (β angle, equal to $\frac{\pi}{2}$ – latitude) and an angle accounting for its longitude (α angle, equal to the longitude).

As a result (where the std superscript labels quantities expressed in the standard frame):

$$\hat{e}_i^{std} = R_{\hat{k}}^{-1}(\alpha) R_{\hat{j}}^{-1}(\beta) R_{\hat{k}}^{-1}(\gamma) \hat{e}_i \quad (2.42)$$

Hence, the detector tensor is intuitively computed as follows:

$$d_{std}^{ij} = \hat{e}_x^{stdi} \hat{e}_x^{stdj} - \hat{e}_y^{stdi} \hat{e}_y^{stdj} \quad (2.43)$$

The product being defined between two vector quantities with a tensor output is of course a Kronecker tensor product.

Also the GW metric perturbation tensor has to be expressed in the same standard frame for equation (2.37). However, the rotation under consideration here has nothing to do with the previously defined α , β and γ .

Conversely, the direction of the GW source is identified by means of a polar and an azimuth coordinate here addressed as θ and ϕ . Furthermore, as previously mentioned, one has to account for a polarization angle ψ . With a detector ideally built coherently with the standard frame being considered, the expression for the APs of this detector would be the same as in equations (2.39).

Also ϵ_{POL}^{ij} can be expressed as a Kronecker product. The unit vectors defining the axes of the TT frame of the GW are expressed as \hat{w}_x , \hat{w}_y and \hat{w}_z , with the latest being the propagation direction.

Therefore, for the GR polarization modes:

$$\begin{aligned} \epsilon_+^{ij} &= \hat{w}_x^i \hat{w}_x^j - \hat{w}_y^i \hat{w}_y^j \\ \epsilon_\times^{ij} &= \hat{w}_x^i \hat{w}_y^j + \hat{w}_y^i \hat{w}_x^j \end{aligned} \quad (2.44)$$

In the standard frame:

$$\begin{aligned} \hat{w}_i^{std} &= R_{\hat{k}}^{-1}(\phi) R_{\hat{j}}^{-1}(\theta) R_{\hat{k}}^{-1}(\psi) \hat{w}_i \\ \hookrightarrow \epsilon_+^{stdij} &= \hat{w}_x^{stdi} \hat{w}_x^{stdj} - \hat{w}_y^{stdi} \hat{w}_y^{stdj} \\ \epsilon_\times^{stdij} &= \hat{w}_x^{stdi} \hat{w}_y^{stdj} + \hat{w}_y^{stdi} \hat{w}_x^{stdj} \end{aligned} \quad (2.45)$$

Finally, one can sum everything up using the most complete (and heavy) imaginable notation: as a result, GWBENCH computes the AP of a given polarization mode as follows:

$$F_{POL}^{det} = \frac{1}{2} \epsilon_{POL_{std}}^{ij} d_{ijstd}^{det} \quad (2.46)$$

As a concluding remark, a plot displaying APs is given at figure (2.6). In these plots, the APs of a given detector are plotted in spherical coordinates in the reference frame of that specific detector using equations (2.39), with θ and ϕ being the polar and azimuth angles of spherical coordinates, and with the radial coordinate $r = |F_{POL}|$. The polarization angle ψ is assumed to be zero. Since

GWBNCH uses the standard frame of the ideal detector at the centre of the Earth, this plot can be obtained using $\alpha = \beta = \gamma = 0$, therefore computing the AP of the ideal detector as seen in the reference frame of the ideal detector itself. This is the same as using the frame of a real detector as the standard frame and computing its own APs in this peculiar frame. However, it is important to mention that this is not equal to the AP of a real detector computed in the frame of the ideal detector. These remarks can sound redundant, but they become very important in the next section.

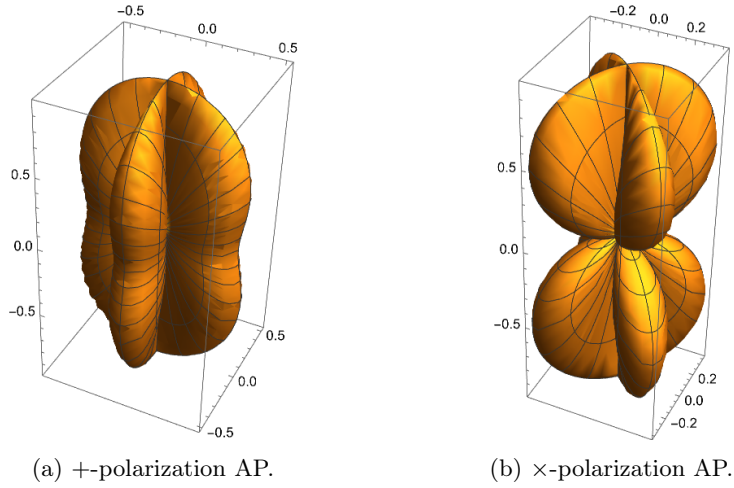


Figure 2.6: APs for GR polarization modes.

2.4.3 The Mismatch with H. Asada

This chapter requires mentioning one of the most problematic parts of the whole work: namely, recovering the results provided by H. Asada et al. in their papers ([33] & [34]). Since such papers constitute a great part of the theoretical basics for the work being presented, one of the obvious preliminary tasks consists in reproducing what is obtained in those works. However, the results can not be recovered using GWBNCH. The next chapters show that this work requires the definition of many direction-dependent quantities, that are never found to be consistent with the results of Asada and collaborators. This outcome can be addressed to the fact that the definition of the APs in Asada's works is different from that of GWBNCH.

The mismatch has been observed when testing GWBNCH before starting the effective research work. Therefore, after being provided with the original code from Asada and collaborators, the computations for the APs have been analyzed, and are now summarized in order to understand the reasons of this mismatch.

The first step of this approach is that of considering a preferential standard reference frame. In order to be coherent with GWBNCH, this can be chosen to match the ideal detector at the centre of the Earth. At this point, two rotation matrices must be defined (already considered in the GWBNCH computations): $R_{\hat{k}}^{-1}(\phi) R_{\hat{j}}^{-1}(\theta) R_{\hat{k}}^{-1}(\psi) = R_{GW}^{-1}(\theta, \phi, \psi)$ and $R_{\hat{k}}^{-1}(\alpha) R_{\hat{j}}^{-1}(\beta) R_{\hat{k}}^{-1}(\gamma) = R_{GR}^{-1}(\alpha, \beta, \gamma)$.

$R_{det}^{-1}(\alpha, \beta, \gamma)$. The first matrix is used in order to find the direction of the source in the reference frame of the ideal detector: $\hat{w}_z^{std} = R_{GW}^{-1}(\theta, \phi, \psi) \hat{w}_z$, where the same notation of the previous paragraph is used (and w_i is the i -th unit vector in the TT reference frame). Using the second matrix, one finds \hat{e}_i^{std} as it has been obtained with the method of GWBENCH (previous section).

So far, the definitions seem leading to the same conclusions as GWBENCH, but now the approach suddenly changes: Asada and collaborators do not consider the detector tensor d^{ij} as was done in the previous paragraph. Conversely, they obtain the polar and azimuth coordinates of the source in the reference frame of the real detector with:

$$\begin{aligned}\cos(\theta^{det}) &= -\hat{w}_z^{std} \cdot \hat{e}_z^{std} \\ \sin(\theta^{det}) &= |\hat{w}_z^{std} \times \hat{e}_z^{std}| \\ \cos(\phi^{det}) &= \frac{-\hat{w}_z^{std} \cdot \hat{e}_x^{std}}{\sin(\theta^{det})} \\ \sin(\phi^{det}) &= \hat{e}_z^{std} \cdot \left[(\hat{w}_z^{std} - \hat{e}_z^{std} \frac{\cos(\theta^{det})}{\sin(\theta^{det})}) \times \hat{e}_x^{std} \right]\end{aligned}\quad (2.47)$$

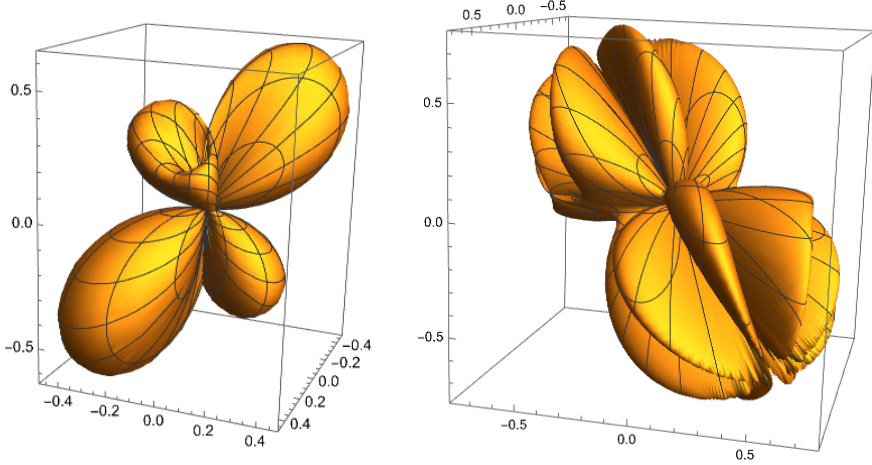
These expressions have been proven to be correct by means of analytical calculus, and can be implemented in the expressions at (2.39). However, the polarization angle ψ^{det} at the frame of the detector has to be inferred in order to get the APs in this fashion. Hence, one has to compute the \hat{w}_i^{det} , that is, the unit vectors along the axes of the TT frame as seen by the real detector and *expressed in the reference frame of the ideal detector*. This part sounds quite awkward; however, since rotations do not commute: $\hat{w}_i^{det} = R_{det}^{-1}(\alpha, \beta, \gamma) R_{GW}^{-1}(\theta^{det}, \phi^{det}, \psi^{det}) \neq \hat{w}_i^{std}$, namely the i -th axis of the TT gauge rotated to the frame of the real detector and then rotated to the frame of the ideal detector is not equal to the i -th axis of the TT gauge rotated to the frame of the ideal detector directly.

Asada and collaborators address the angle between \hat{w}_x^{std} and \hat{w}_x^{det} as ψ^{det} :

$$\begin{aligned}\cos(\psi^{det}) &= \hat{w}_x^{std} \cdot \hat{w}_x^{det} \\ \sin(\psi^{det}) &= -\hat{w}_z^{std} \cdot (\hat{w}_x^{std} \times \hat{w}_x^{det})\end{aligned}\quad (2.48)$$

This is the crucial point where the two approaches to the representation of APs differ. In particular, assuming the real detector to be placed at the same position of the ideal detector, one can see that $\psi^{det} = 0$ and obtain the same results as illustrated at figure (2.6). In other words, one obtains that the code correctly reproduces the shape of the APs of a detector in the reference frame of that given detector. However, in the presented work a coherent description of several detectors at different positions is required: therefore, the APs have to be represented in reference frames different from that of the detector they refer to. In a very predictable way, henceforth, the standard reference frame is that of the ideal detector at the centre of the Earth. If one tries to visualize the $|F_+|$ of a real detector located at some α, β and $\gamma \neq 0$ and expressed in the frame of the ideal detector, figure (2.7) can be obtained:

The mismatch is evident and one can see that the two methods do not agree for any of the detectors that have been enumerated so far.



(a) +-AP with GWBENCH (KAGRA). (b) +-AP with Asada's code (KAGRA).

Figure 2.7: Comparison between the computations of F_+ for KAGRA.

At this point, it is not easy to understand which of the two methods is giving a wrong result. A solution would be that of working out an expression of the AP from the two codes as a function of the only $\alpha, \beta, \gamma, \theta$ and ϕ and try to see where they differ. However, working the solution out in an analytical way for a real detector is not an option since not even Wolfram Mathematica [35] (applying all the simplifications, when possible) is able to pursue the whole computation. In practice, this method brings to hundreds of lines of sines and cosines.

A reference plot regarding the APs of a real detector is that of $F_+^2 + F_\times^2 = A^2$, namely the square of the tensor APs amplitude. This plot has the same shape for every detector, but for a shift accounting for the fact that the detectors are located at different coordinates and can be found at [36].

The examined quantity is A_{KAGRA} : both the codes reproduce the same result, as it is shown at figure (2.8). Here the plot is done in the frame of (RA, DEC). However, RA and DEC are time independent coordinates, while the position of the detectors, together with their APs, moves with the Earth. Therefore one expects the sensitivity pattern to be time dependent, not related to fixed coordinates like RA and DEC, unless one makes the assumption of detecting the signal with the Earth oriented always in the same way. This assumption is used now, and henceforth: the merger time of the signal matches the exact time when the Greenwich Mean Sidereal Time (GMST) equals zero. With such a correspondence one can make a unique correspondence between Earth-comoving coordinates and fixed space coordinates like RA and DEC.

The fact that this quantity is preserved for both methods means that the APs are only rotated one respect to the other. However, this rotation is direction-dependent, and is quite awkward to work out.

Nevertheless, another quantity from the original article could be used to better understand the situation. Before fully understanding its importance, few arguments are needed. In particular, following the same track as the original article, one can express:

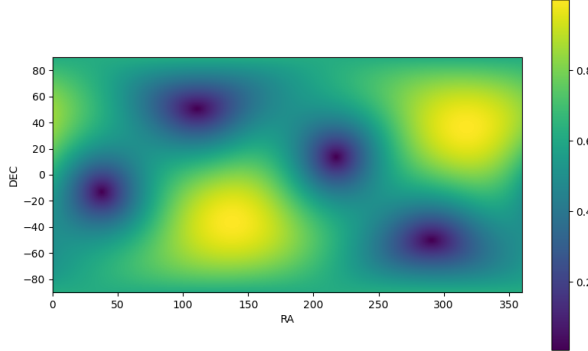


Figure 2.8: Tensor AP Amplitude for KAGRA (both methods).

$$\begin{aligned} F_+ &= \cos(\epsilon) \sin(2\psi) + \sin(\epsilon) \cos(2\psi) = \sin(2\psi + \epsilon) \\ F_\times &= \cos(\epsilon) \cos(2\psi) - \sin(\epsilon) \sin(2\psi) = \cos(2\psi + \epsilon) \end{aligned} \quad (2.49)$$

defining ϵ as orientation-dependent $\epsilon = \epsilon(\alpha, \beta, \gamma, \theta, \phi)$. As said, the explicit computations in presence of non-zero α , β and γ are quite tedious: one can find the whole argument and results at [37]. It can be shown that from (2.46) one can recover this expression, which is valid for the GWBENCH computations. In the case of Asada's mathematics, this expression becomes trivial since ψ is defined to be zero in the ideal detector frame.

Thus, one has that:

$$\epsilon = \tan^{-1}\left(\frac{F_+}{F_\times}\right) - 2\psi \quad (2.50)$$

At this point:

$$\delta^{ij} = F_+^i F_\times^j - F_+^j F_\times^i = A_i A_j \sin(\epsilon^i - \epsilon^j) \quad (2.51)$$

Therefore, the quantity \mathcal{F}^{ij} can be defined as:

$$\mathcal{F}^{ij} = \frac{\left| \sin(\epsilon^i - \epsilon^j) \right|}{\sqrt{\frac{A_j^2}{A_i^2} + \cos^2(\epsilon^i - \epsilon^j)}} \quad (2.52)$$

and it can be another test for the computation method of the APs since it is reported in the original paper with $i = \text{LIGO Hanford}$ and $j = \text{LIGO Livingston}$.

Therefore, by definition:

$$|\delta^{ij}| = \mathcal{F}^{ij} A_i A_j \sqrt{\frac{A_j^2}{A_i^2} + \cos^2(\epsilon^i - \epsilon^j)} \quad (2.53)$$

The plot for this quantity as obtained with GWBENCH is reported at figure (2.9). The plot obtained with Asada's mathematics is given at figure (2.10) .

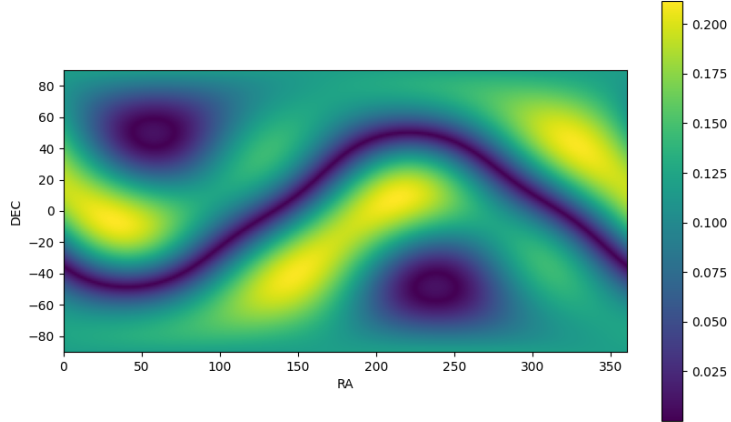


Figure 2.9: $|F_+^i F_\times^j - F_+^j F_\times^i| = \mathcal{F}^{ij} A_i A_j \sqrt{\frac{A_j^2}{A_i^2} + \cos^2(\epsilon^i - \epsilon^j)}$ with GWBENCH.

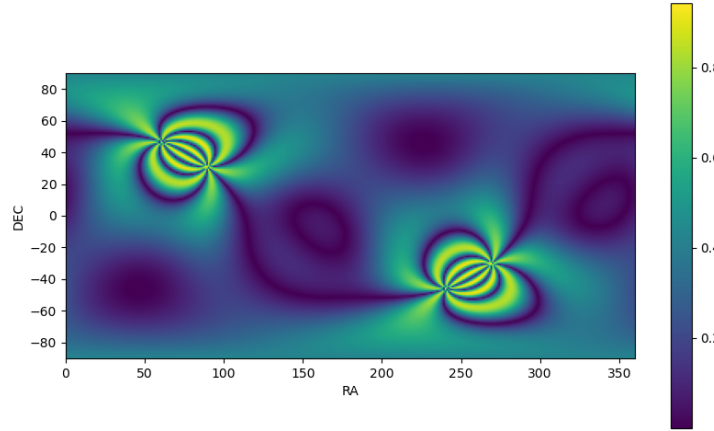


Figure 2.10: $|F_+^i F_\times^j - F_+^j F_\times^i| = \mathcal{F}^{ij} A_i A_j \sqrt{\frac{A_j^2}{A_i^2} + \cos^2(\epsilon^i - \epsilon^j)}$ with Asada's code.

The aforementioned paper shows plots of \mathcal{F}_{ij} for Hanford and Livingston and GWBENCH reproduces the same plot, while Asada's method produces a completely different shape. At figures (2.11)&(2.12) the plots obtained with the two methods are shown. One can refer to figure 2 of [36] and confirm that it matches with (2.11).

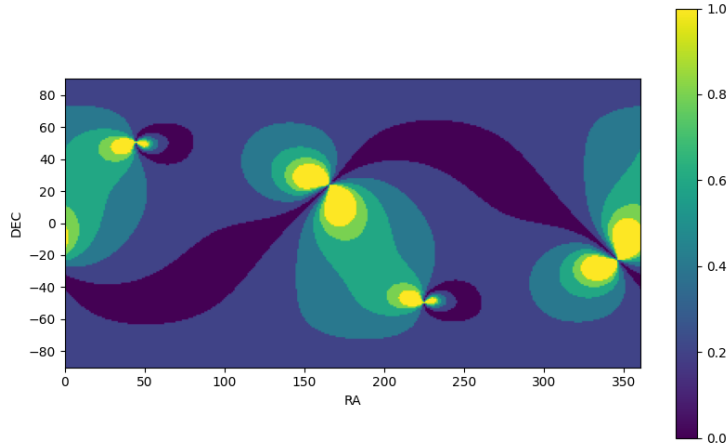


Figure 2.11: \mathcal{F}_{ij} with GWBENCH method.

As shown at figure (2.12), the quantity \mathcal{F}^{ij} as computed with Asada's mathematics differs from that of obtained with GWBENCH and plotted at figure (2.11). The latter is consistent with the arguments made by Wen & Schutz in [36] and by Jaranowski et al. in [37], while the former is not. At this point, since it has been chosen not to perform the full computation following an analytical approach, one can not claim the correctness of GWBENCH at 100 %, but indeed it is supported by an important contributor of the literature in the subject. Therefore, the computation of the APs as provided by GWBENCH is used henceforth.

In this chapter, all the notions regarding the experimental detection of GWs that are necessary to the next chapters have been defined.

Nevertheless, this has been achieved with large use of approximations. However, the presented approach is generally effective for a qualitative understanding of the subject.

The theoretical basics provided in chapter 1 have been used in order to achieve basic knowledge about laser interferometer detection. In this chapter, the interferometer response has been worked out considering a phase modulation allowing for an output power linear in the GW strain. However, this realistic add-on has been neglected in the treatment of noise effects, for sake of simplification. Furthermore, no contribution from Fabry-Pérot cavities has been considered in the computations.

The theoretical knowledge of noise has been implemented in a qualitative description of GW data analysis, which allows for the illustration of the parameter inference method used by GWBENCH.

The noise treatment pursued at the beginning of the chapter has come at hand when a short compendium of current and future laser interferometer GW facilities has been made: more in detail, this has allowed for a better description of the GW facilities, also displaying the noise curves relative to such facilities as they are implemented in GWBENCH.

The final sections of this chapter have been dedicated to the general derivation of APs, considering the long-wavelength approximation, thus neglecting

the spatial evolution of GWs being detected with respect to the arms of the interferometers. Once again, this is a more limiting factor the longer such arms become with future facilities: in a precise derivation, this complication has to be accounted for.

The explicit derivation has been pursued for the +-polarization mode, highlighting how antenna patterns differ for different polarization modes. However, the analytical expression has been discarded, since `GWENCH` implements a more compact tensor expression, thus speeding up computations, which have been summarized in the conclusive section. The `GWENCH` formalism for APs has been then compared to that used by professor Hideki Asada and collaborators in a series of articles regarding the subject that give different results. In particular, this alternative approach hasn't been proven to be correct or wrong as compared to `GWENCH`. However, the two different results have been compared to a standard landmark in the subject, that is, an article by Bernard Schutz and Linqing Wen, which has turned out to be consistent with the outcomes of `GWENCH`. On the basis of this comparison, the `GWENCH` approach has been chosen for the prosecution of this discussion.

The following chapter focuses on modified theories of gravity from a simplified point of view, thus momentarily forgetting the experimental stuff studied in the present chapter.

However, only few references are provided and much of the formal derivations has been skipped.

Conversely, much of the effort for the next chapter goes into the definition and understanding of the null streams, *i.e.* the expressions characterizing this whole analysis.

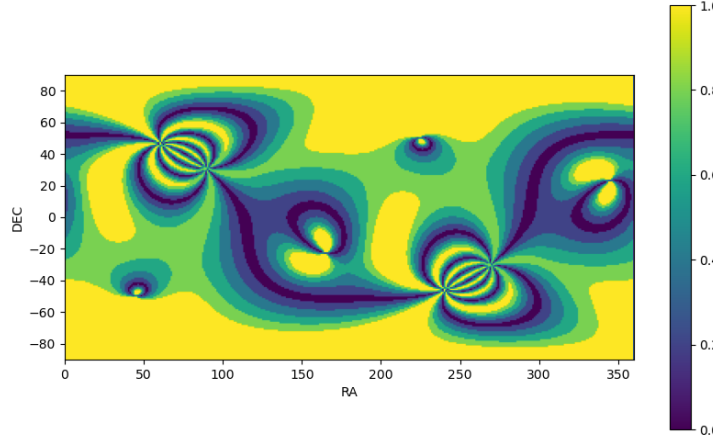


Figure 2.12: \mathcal{F}_{ij} with Asada's method.

Chapter 3

Non-GR Polarization Modes

The theoretical description of GR polarization modes, together with a qualitative treatment about their detection with current and future facilities, have been the subject of this essay so far.

These topics match with the current knowledge and assumptions for gravity: it is consistent with GR, and can be probed by means of GWs, which come in two polarizations, + and \times .

Such modes are detected differently by laser interferometers, whose geometry inevitably leads to preferential directions for the two modes. This concept has been described by means of APs.

Nevertheless, modified theories of gravity carry different approaches to the subject, thus leading to differences in the way GWs are derived in terms of analytical calculus. Such changes account for differences at the core of physics, not to be confused with some sort of gauge invariance. In fact, modified theories of gravity predict, among the other things, the existence of further polarization modes besides those GR accounts for. Such further modes are not to be considered as modified versions or different gauge versions of the GR ones, but as brand new polarization modes.

In this chapter, a short review of the main differences one finds in modified theories of gravity when speaking about polarization of GWs is given, and the polarization modes in a general theory of gravity is illustrated.

In addition, the research work is introduced in its theoretical aspects with the definition of the null streams as functions for characterizing the polarization content of GWs, and, more in general, for discriminating among gravity theories.

3.1 Non-Tensor Polarization Modes

Modified theories of gravity are generally defined complicating the minimal assumptions one makes when working out GR from a differential geometry approach. In particular, one can modify the minimal coupling in the Einstein-Hilbert action by adding some scalar and covariant terms in the Lagrangian density, while still keeping a universal coupling between curvature and matter.

This is one of the most intuitive approaches, even if it can not account for the whole modified theories of gravity one can think of. However, it is enough to infer the presence of non-tensor polarization modes for GWs. In this section,

it is not shown how to get the non-tensor polarization modes, since it is matter of harder computations than those pursued so far. Conversely, the interested reader is redirected to a the most general and simple theories of gravity, that modify the Einstein-Hilbert action and predict all the six polarization modes for GWs: for instance, a mathematically simple theory can be found at [38].

However, one can find out that a content of up to six polarization modes in a general theory of gravity is obtainable by means of an abstract approach. In what is called the *Newman Penrose formalism* one can find that, for the Riemann tensor, only six components are algebraically independent in the plane-wave approximation (when the propagation direction is always along the Cartesian z -direction). The proof of this is not being reported here, for the sake of simplicity, but can be found at [39].

An instructive application of this formalism, even if applied to a theory accounting only for four polarization modes, is given at [40], namely in the case of a Lagrangian density with higher order terms in the Ricci scalar.

These six independent modes are considered for describing, in a given frame, the six polarization modes one can infer from a general theory of gravity. These modes are generally classified by how they behave under Lorentz transformations [41]. However, from a field-theory point of view, it is much easier to classify as tensor, vector and scalar modes the 2, 1 and 0 helicity states of a massless spin-2 particle (the graviton).

All the computations are skipped, from those regarding the *Newman Penrose formalism* to the computation of the six independent modes, to the wave equations in modified theories, and the *translation* of the effect of a given GW mode to a set of test masses at a detector's frame. However, these results are summarized at figure (3.1), representing the effect of all the polarization modes on a set of masses disposed in a circle, and at (3.1), showing the analytical expression of the polarization tensors.

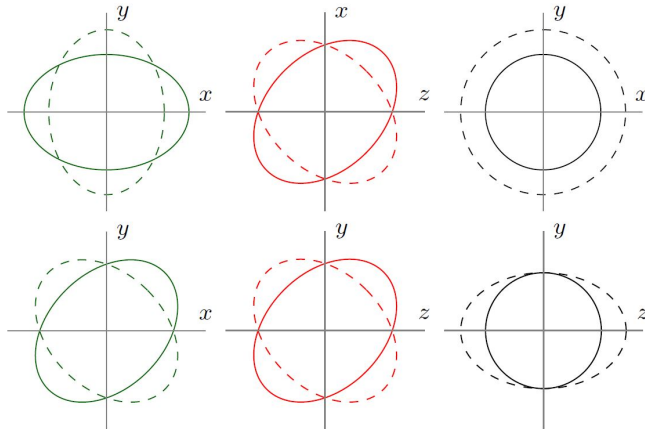


Figure 3.1: Representation of the effect of the different polarization modes on masses in a circle. Picture taken from [5].

$$\begin{aligned}\epsilon_V &= \begin{pmatrix} 0 & 0 & 1 \\ 0 & 0 & 0 \\ 1 & 0 & 0 \end{pmatrix} & \epsilon_W &= \begin{pmatrix} 0 & 0 & 0 \\ 0 & 0 & 1 \\ 0 & 1 & 0 \end{pmatrix} \\ \epsilon_B &= \begin{pmatrix} 1 & 0 & 0 \\ 0 & 1 & 0 \\ 0 & 0 & 0 \end{pmatrix} & \epsilon_L &= \begin{pmatrix} 0 & 0 & 0 \\ 0 & 0 & 0 \\ 0 & 0 & 1 \end{pmatrix}\end{aligned}\tag{3.1}$$

In equation (3.1) V and W represent the two vector (helicity ± 1) modes, while B and L represent the scalar modes with 0 helicity.

These tensors can be inserted in expression (2.46) in order to obtain the APs for the different modes: this makes it very easy to compute these APs by means of GWBENCH. However, also the analytical expression (similar to equations (2.39)) can be obtained in the reference frame of the detector:

$$\begin{aligned}F_V &= -\sin(\theta) \sin(2\phi) \cos(\psi) + \sin(\theta) \cos(\theta) \cos(2\phi) \sin(\psi) \\ F_W &= \sin(\theta) \sin(2\phi) \cos(\psi) + \sin(\theta) \cos(\theta) \cos(2\phi) \cos(\psi) \\ F_B &= -\frac{1}{2} \sin^2(\theta) \cos(2\phi) \\ F_L &= +\frac{1}{2} \sin^2(\theta) \cos(2\phi)\end{aligned}\tag{3.2}$$

where the degeneracy between the two scalar modes is evident by the fact that they differ just because of an overall minus sign.

This makes the scalar modes degenerate in the detection, because one can always write the signal S_{DET} , as detected by a detector DET , like:

$$S_{DET} = F^+ h_+ + F^\times h_\times + F^V h_V + F^W h_W + F^B (h_B - h_L)\tag{3.3}$$

This fact has consequences on all the future arguments and computations. In particular, there is no way to measure the two scalar modes independently, and this means that one must always consider up to five independent polarization modes.

At this point, as it has been done in figure (2.6), the APs in spherical coordinates at the detector's frame can be plotted. These plots are given at figure (3.2).

Once again, the degeneracy between the two scalar modes B and L is evident.

Generally, when not explicitly referred to as B and L , the scalar modes are addressed with the subscript S .

Therefore, it is clear that for five detectors, one gets five equations like (3.3), where the signal S_{DET} is measured, the APs are already known, and thus one ends up with five unknowns: the strains for the two tensor modes, the two vector modes, and the strain difference $h_B - h_L$.

This means that, in a network with five detectors operating simultaneously, one ends up with 5 equations and 5 unknowns, thus being able to disentangle the overall tensor, vector and scalar contributions to the GW signals.

However, one really has to pay attention to the fact that such five detectors need be non-coaligned. In fact, coaligned detectors show the same APs for each polarization mode. This means that, besides a noise term (now neglected) and

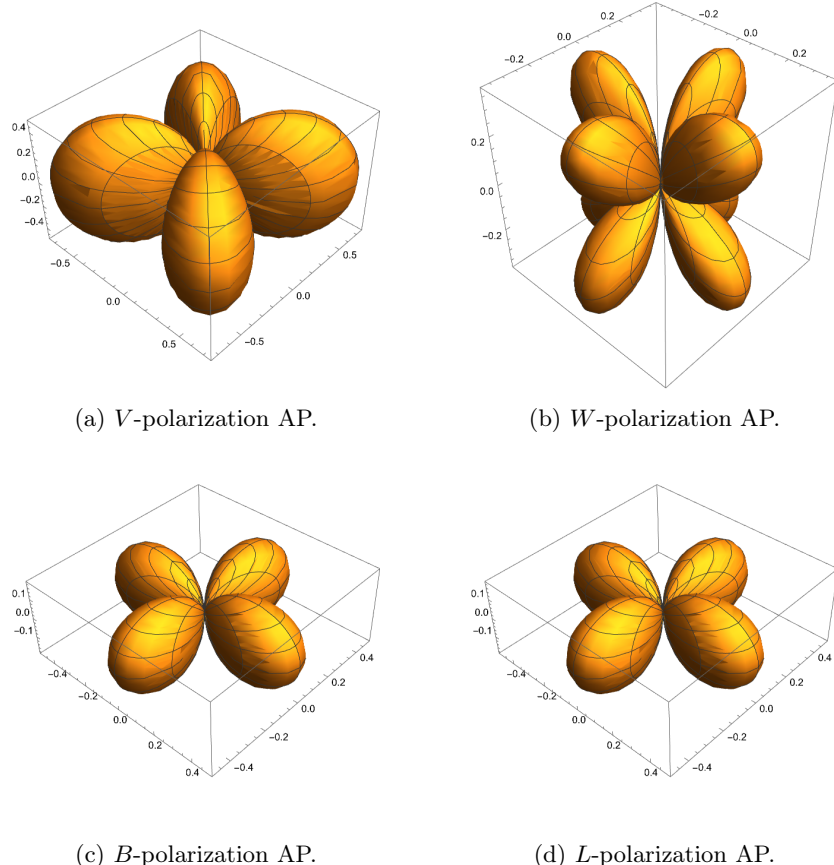


Figure 3.2: APs for non-GR polarization modes.

a phase term due to the distance between the detectors, the two signals and the coefficient for the strains at the different modes would be identical. This ends up reducing the effective number of equations in the set of five, while still keeping five unknowns. Hence, the set of equations becomes unsolvable.

Figures (3.2), together with figures (2.6), do not point out only the different geometrical shape of the APs: for instance, the sensitivity of an L-shaped interferometer on the preferential direction for tensor modes is greater than for scalar modes.

An additional set of images is provided: namely, the APs for all the six polarization modes for a triangular shaped detector, like ET (figures (3.3)).

In the research work, lots of GR and non-GR signals are simulated by means of GWBENCH. Hence, for testing a method for discriminating between different theories, the injection of non-GR polarizations is needed. This is not a trivial matter, since from the information provided so far, it is not clear how to express the amplitude and frequency evolution of such modes. Their geometry and the way they interact with detectors have been described shortly, but the behaviour of signals is matter of lots of computations.

In particular, one needs to infer all the results regarding the stress energy tensor carried by GWs in such theories, find the emission (which may not even be

quadrupole dominated) and then constrain the power emitted to be equal to the energy loss rate in a given model (as a reminder, the Newtonian approximation has been used in chapter 1 for tensor modes).

All this work is summarized in [42], and only the most important results are being reported here. In particular, referring to equation (3.3), it is possible to express all the non-tensor polarization modes as follows:

$$\begin{aligned} h_V &= A_V \sqrt{\frac{525}{56}} \sin(2\iota) \frac{h_+}{\frac{5}{2}(1 + \cos^2(\iota))} \\ h_W &= A_W \sqrt{\frac{15}{2}} \sin(\iota) \frac{h_+}{\frac{5}{2}(1 + \cos^2(\iota))} \\ h_B &= A_B \sqrt{\frac{225}{8}} \sin^2(\iota) \frac{h_+}{\frac{5}{2}(1 + \cos^2(\iota))} \\ h_L &= -A_S \sqrt{\frac{45}{2}} \sin(\iota) \frac{h_+}{\frac{5}{2}(1 + \cos^2(\iota))} \end{aligned} \quad (3.4)$$

where ι is a geometrical parameter of the CBC, that is the inclination angle of the orbiting plane with respect to the observer. The A_i terms are normalization factors that are expected to be zero in GR, and non-zero in a more general theory. These expressions are used to artificially inject non-tensor modes into GR signals, and test the response of the network to such modified signals.

3.2 Null Streams

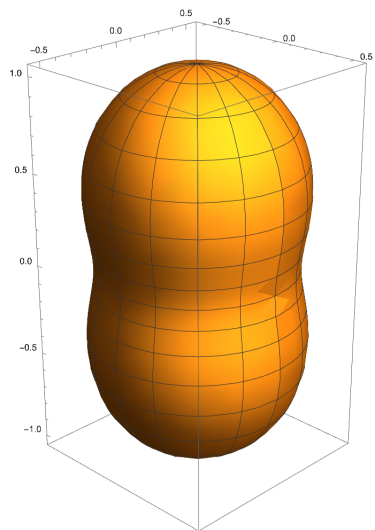
What has been obtained in the first two chapters, together with the knowledge gathered about non-GR polarization modes, provides the requisites to introduce the tools of the computational work being reported in the next chapters. These tools are given by the null streams, that are given by combinations of the APs and of the strain measured by a given numbers of detectors. In fact, the number of detectors defines different kinds of null streams.

Hence, assuming it is possible to obtain the strain from three GW detectors with uncorrelated noise, each one non-coaligned with any of the others, one can assume to detect a CBC GW signal, and to localize it with outstanding accuracy. Therefore, little to no fluctuation affects the APs at the position of the source, since they only depend on the coordinates on the sky in a given reference frame. This allows to shift the signal in time at the different detectors: in fact, a GW signal hits different detectors at different times, due to its limited speed, equal to the speed of light c .

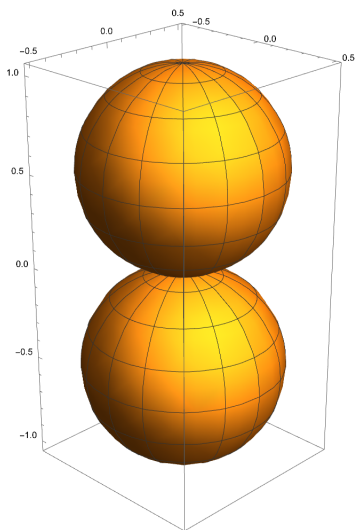
At this point, a detector being labelled with a (with a running over indices 1, 2 and 3, respectively referred to the three different detectors) measures a signal S_a so that:

$$S_a = F_a^+ h_+ + F_a^\times h_\times + F_a^V h_V + F_a^W h_W + F_a^B (h_B - h_L) + n_a \quad (3.5)$$

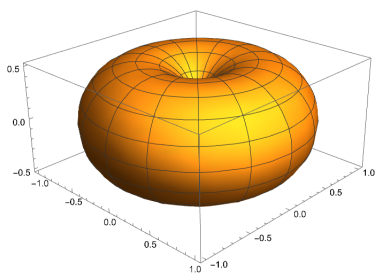
with n_a representing a noise component on the signal, which is also the only difference between this equation and equation (3.3), that is going to be the reference for this theoretical discussion.



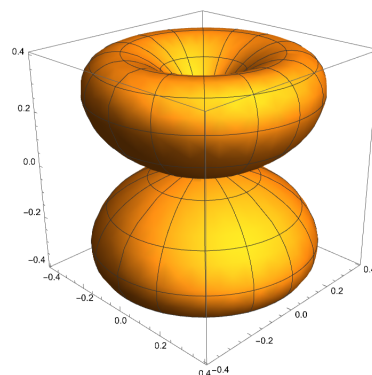
(a) $+$ -polarization AP.



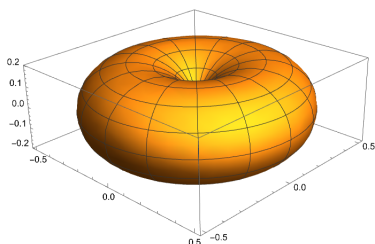
(b) \times -polarization AP.



(c) V -polarization AP.



(d) W -polarization AP.



(e) B -polarization AP.

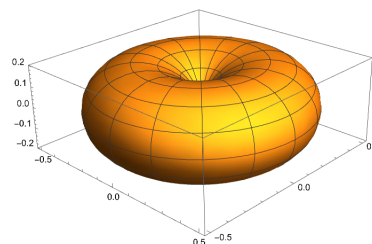


Figure 3.3: APs for all polarization modes as seen by a triangular detector.

One can define:

$$\delta_{ab} = F_a^+ F_b^\times - F_b^+ F_a^\times \quad (3.6)$$

Furthermore, *i.e.* $P^a = (\delta_{23}, \delta_{31}, \delta_{12})$ can be defined to be a sort of *vector*. This *vector* can be multiplied by means of a *scalar product* with the *covector* $S_a = (S_1, S_2, S_3)$.

In the case of a general GW signal, one gets:

$$\begin{aligned} P^a S^a &= \delta_{23} S_1 + \delta_{31} S_2 + \delta_{12} S_3 = \\ &= P^b F_b^V h_V + P^c F_c^W h_W + P^d F_d^B (h_B - h_L) \end{aligned} \quad (3.7)$$

that is, a three detector null stream, *i.e.* a null stream involving the APs and signals from three facilities. It is immediate to see that such quantity is identically zero when the signal is purely tensor-polarized [43].

A null stream can work as a trigger quantity, reaching non-zero values in the case of non-tensor GWs, while it is ideally zero when signals are tensor. This quantity can work as a very effective and intuitive tester for gravity, while still not being able to disentangle the different polarization modes, but only to tell whether any non-tensor content is present. However, the effect of detector noise on such measures can not be neglected. The magnitude of the null stream may not make it to reach above the sensitivity of the detectors: this would make a non-GR signal look like a purely GR one. Furthermore, in a real application, the localization accuracy is not infinite, propagating and allowing for a fluctuation of the null stream. Even in the case of a purely tensor-signal, the values of a null stream may rise to (and above) the noise of the detector, thus making a GR signal look like a non-GR one.

A work of characterizing the effects of localization accuracy and detector noise need be done in order to understand how useful a null stream approach can be in real applications.

The research work of this thesis proposes to answer this question. In particular, this is done for more combinations of three (or four, as it is now explained) detectors.

As already stated, direct disentangling of the five independent polarization modes is possible when data from five non-coaligned detectors is available. Thus, one need not consider a null stream approach in the case of five detectors, being it superfluous.

This means that the null stream approach may come useful also when using four detectors. In particular, the previous notation can be easily expanded with index a running on $(1, 2, 3, 4)$. At this point, one has that P_a can be generalized to a four-*vector*: $P_a = (\delta_{23}, \delta_{31}, \delta_{12}, 0)$, and the signals *covector* accounts also for the response of the fourth detector.

The *scalar product* $P^a S_a$ still leads to equation (3.7). However, in this situation, one can define multiple null streams. This is done by defining three four-*vectors*:

$$\begin{aligned} Q^a &= (0, \delta_{34}, \delta_{42}, \delta_{23}) \\ R^a &= (\delta_{34}, 0, \delta_{41}, \delta_{13}) \\ S^a &= (\delta_{24}, \delta_{41}, 0, \delta_{12}) \end{aligned} \quad (3.8)$$

Therefore, one ends up with four null streams, obtainable in the same way as the first one. However, it can be observed that for each detector added to an observing network, one gets rid of one degree of freedom: in fact, two detectors can disentangle the two tensor modes in the case of purely GR signals. With three detectors, even if not able to disentangle the polarization modes, it is possible to infer the overall non-tensor content of a GW signal. It is unlikely that adding a fourth detector would help in getting rid of other three degrees of freedom. Thus, of the four aforementioned null streams, only two can be addressed as independent: this means that a third and a fourth detector just lead to 2 constraints (as expected). One can always prove that it is possible to use two of the four null streams to infer the other two.

In the numerical applications following this introduction, the two independent null streams are:

$$\begin{aligned} P^a S^a &= \delta_{23} S_1 + \delta_{31} S_2 + \delta_{12} S_3 = \\ &= P^b F_b^V h_V + P^c F_c^W h_W + P^d F_d^B (h_B - h_L) \\ Q^f S^f &= \delta_{34} S_2 + \delta_{42} S_3 + \delta_{23} S_4 = \\ &= Q^g F_g^V h_V + Q^i F_i^W h_W + Q^j F_j^B (h_B - h_L) \end{aligned} \quad (3.9)$$

Each of the two expressions involves only the APs and signals from three of the four detectors. The derivation for this expression has been taken from [33]&[44].

It is straightforward to show that any three detector null stream can be expressed in a compact way by means of the Levi-Civita tensors [34]:

$$\epsilon_{ijk} F_+^i F_\times^j S^k \quad (3.10)$$

with indices i , j and k running over three detectors.

At this point, one can obtain the expression for four detector null streams, *i.e.* null streams involving the APs and measured signals from four detectors. This is obtained with:

$$\epsilon_{ijkl} F_+^i F_\times^j F_X^k S^l \quad (3.11)$$

which allows to get rid of the two tensor modes (similarly to the three detector case) plus one extra non-tensor mode, represented by X . These quantities are addressed as four detector null streams.

It has to be observed that also the null stream approach being pursued here is valid only when considering non-coaligned detectors: for two coaligned detectors called 1 and 2, the quantity $\delta_{12} = 0$ identically. This makes both the 3 and the 4 detectors case inapplicable.

3.2.1 Approaching Real Data: GW170817

The tools that have been defined so far can be applied to real data when an accurate localization is available. Hence, it is worth reporting the results obtained in [33]. Such results are not worth mentioning because of the outcomes, but as a first null stream approach to take a cue from.

Such results come from the application of the three detector null stream to GW170817, a GW event from a BNS also responsible for the emission of a short

Gamma Ray Burst, and the most celebrated one since it formally gave birth to experimental multimessenger astrophysics [45]. The EM transient as seen by high energy facilities allowed for an outstanding localization, much better than that of other GW events: $\sim 28 \text{ deg}^2$. Therefore, the prerequisite of a good localization for a precise computation of the APs seems fulfilled, making this event a good candidate for testing the freshly introduced tools. The GW event was observed by the LIGO facilities and Virgo only, since KAGRA was still under construction. That's why one can not even consider more than three detectors in the computations for this event.

In this case, the three detector null stream shows no chirp signal at all above the strain sensitivity of the operating detectors, which during the observations in 2017 was $\sim 10^{-23} \text{ Hz}^{-1/2}$. It is thus credible that eventual deviations from GR fall below this value: namely, the dimensionless coefficients A_i are fainter than a certain threshold value defined for the network involved in the data collection.

A second glance at this event makes it clear that the results from future generation facilities, and improved current detectors as well, will lead to way more accurate results. Firstly, as just mentioned, only three interferometers detected this event, thus enabling only few considerations. Secondly, two of these detectors, namely the two LIGO ones, are almost coaligned. As stated, this means that their APs almost match. The tiny difference in such APs would be enough if the localization were so precise to make $[F_{POL}^L - \sigma_{AP}^L, F_{POL}^L + \sigma_{AP}^L]$ not compatible with $[F_{POL}^H - \sigma_{AP}^H, F_{POL}^H + \sigma_{AP}^H]$, with σ_{AP} the AP deviation because of the localization fluctuation, but this is not the case.

In fact, the localization accuracy is still below the standards for this kind of measure. This means that the null stream, as computed here, is very noisy, and not a good tool for providing accurate results. Nevertheless, the obtained results in [33] only account for a computation of the null stream in the mean value of the localization interval, and the noise on the final quantity is only given by a superposition of the instrumental noise of the detectors. That is why, even if these results provide a didactic example for the application of the new methods, they should be considered with a grain of salt. A graphical summary of such results is displayed at figure (3.4).

This chapter has focused on what is the main scope of the research, namely non-tensor polarization modes. Such modes arise from general treatments of gravity in a bunch of different ways, of which only a general introductory view has been given. In fact, the general purpose of this work is not that of inferring the presence of non-GR modes in a given theory, but rather that of defining a way to detect them with interferometric measures.

Therefore, special care has been dedicated to the the null streams, that are very important quantities in the subject of this essay. These tools can improve in precision and effectiveness by raising the number of the detectors operating at the same time. Thus, one can get a three detector null stream, being able to tell whether a GW signal contains any generic non-tensor mode. This is done building an expression which is identically zero in presence of tensor modes only. Four detector null streams can be obtained too, and provide a tool to get rid of the two tensor modes and an extra non-tensor mode. As an example, such a null stream could get rid of the tensor modes and the scalar contribution (which can

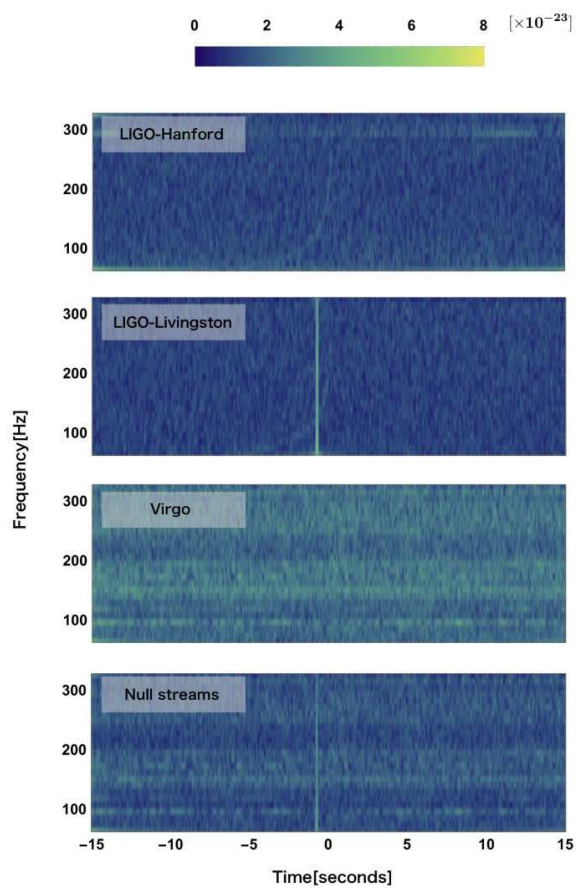


Figure 3.4: Frequency *vs.* time plots for the data of GW170817 as detected by the three operating detectors, and the three detector null stream at the *bottom*.

be considered as a single independent mode), thus telling whether the observed signal is vector or not. Of course, this is a more powerful object with respect to three detector null stream, even if it requires more non-coaligned detectors to be operative at once.

As a conclusion, a summary of the results for GW170817 has been presented, since it is an event with a great localization accuracy, as reported in a previous article ([33]). However, no significant outcome has been obtained in this case, while it still provides a didactic example for the usage of null streams.

Chapter 4

Localization of GW Sources

The importance of the localization capabilities has already been outlined several times in this essay. This comes from the definition of the APs, which are used to define the null streams, being dependent on the direction of the GW source and allowing the uncertainty on the localization to propagate to the null streams themselves. The resulting fluctuation allows one to tell whether the network being implemented in such a measure is reliable for a polarization test.

Nevertheless, the accuracy of up to come facilities in this field will be way better than that of current ones. This is a consequence of the improved sensitivity of the detectors and their arrangement on the Earth's surface. In fact, just like other probes for transient astrophysical phenomena, also GW detectors can implement the technique of the triangulation (used, for instance, by the InterPlanetary Network for High Energy EM transients [46]). In this chapter, the mechanisms of this approach are explained, and what are the peculiarities of this strategy applied to GW facilities.

Secondly, the main results of the localization tests are summarized and their importance is consequently outlined. In particular, the behaviour of the localization accuracy as a function of mass parameters, luminosity distance and position is highlighted. Such characteristics are extremely important in the definition of how well would a null stream perform under some constraints.

It is appropriate to remind the reader that all the inference as performed by `GWBENCH`, localization included, is performed by means of the Fisher information formalism.

4.1 Triangulation with GW Detectors

The most efficient way to localize the source of a given signal within a given precision solid angle when no imaging is available is given by the triangulation. This method can be explained in a few lines as it is conceptually very simple. One can make use of figure (4.1), taken from [47], which, however, refers to the localization of Gamma Ray Bursts (GRBs) by means of a network of at least three detectors (which, for the GRB case, are satellites, but it works the same as for ground-based detectors and GW sources).

The picture shows as the time difference in the arrival of a given signal at the three different locations constitutes the base of the triangulation system.

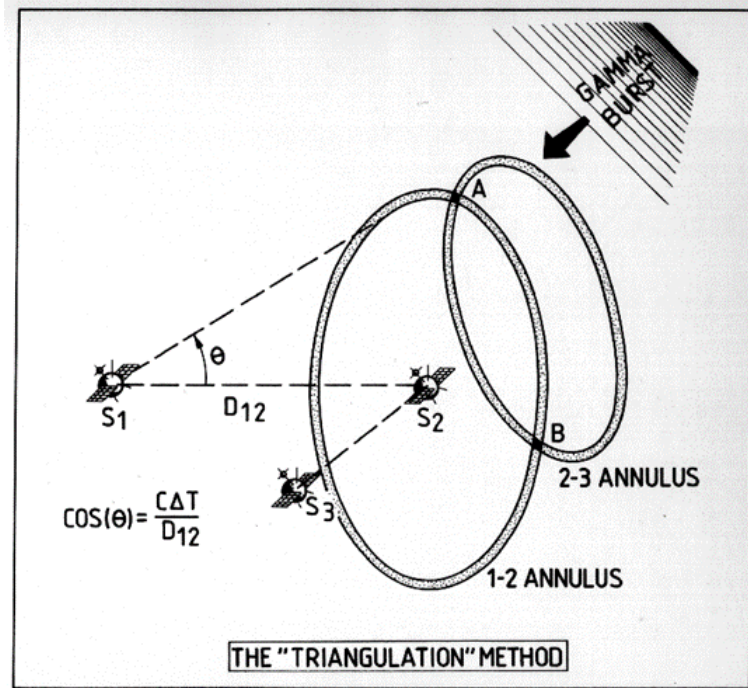


Figure 4.1: Didactical sketch of the triangulation method (taken from [47]).

In particular, the time difference between the arrival of a signal at two different facilities, 1 and 2, is connected to the cosine of the angle between the direction of the source as seen by the first detector (which is labeled as 2 in the picture) and the direction of the line connecting the two detectors. One has that $\Delta t_{12} = D_{12} \frac{\cos \theta_{12}}{c}$, with D_{12} the distance between the two facilities. This angle defines a circle centered on detector 2 (the first one detecting the signal). The source, as seen by the second detector (number 1 in the picture), lies somewhere on this circle, making the localization incomplete. However, a third detector can do the same work (detector 3) and define a circle centered on detector 2. The two circles can intersect in two points, thus almost constraining the direction of the source. Now, of course, a fourth detectors would do the job of removing this degeneracy.

However, one can observe that EM facilities as well as GW detectors have a limited timing precision, thus knowing the time delay between the arrival of a signal at two detectors only to a precision given by their clocks. This makes the circle more like an annulus, that gets shrunk when the sampling frequency is raised.

This is the main point where the discussion about GW facilities goes far beyond that for GRBs. In fact, the latter can only refer to the arrival time of the signal, or eventual (but not deterministic) features in the light-curve of the event. However, if a light curve does not show peculiar signatures, the time shift of a GRB detected by multiple detectors may not even be limited by the sampling frequency, or more in general, by the instrumental limits. GWs, conversely, show a coherent signature, which has been analytically derived and expressed

in chapter 1 in a Newtonian approach. This means that the comparison between the data from two different detectors can be done time-step by time-step, with a procedure that is not generalizable to EM transients. However, there is the noise of the two different detectors spoiling the great precision of such measure, therefore the final localization accuracy needs to account also for the detector noise and not only the quantization noise from the time sampling. One can think that high SNR GW events are able to suppress this kind of noise, thus being time-precision dominated. Anyhow, this is the main strength of the application of the triangulation method to GW events with respect to the GRB case, since one can not think about coherence in the GRB signals.

A visual representation of this concept is given by the plots at (4.3). It is evident that GW events are easier to superimpose with good accuracy, and thus to find the shift in time among different detectors, with respect to GRBs, which show different light-curve shapes at different detectors.

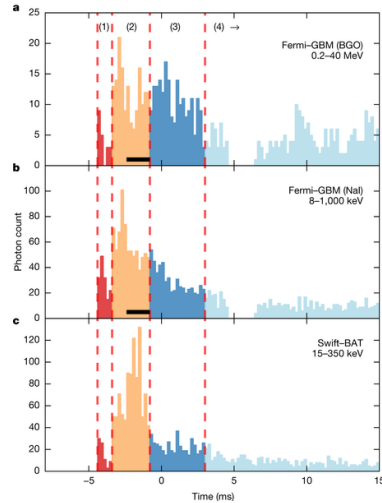


Figure 4.2: GRB200415A light-curves for different detectors (taken from [48]).

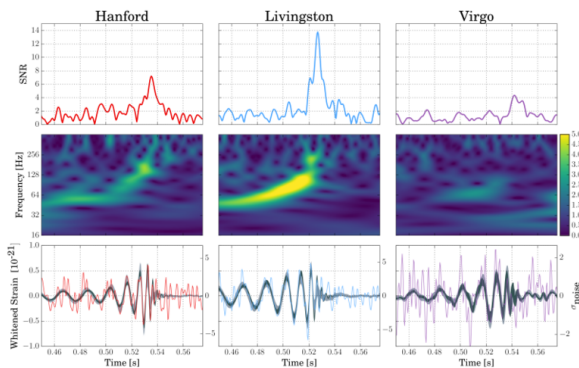


Figure 4.3: GW170814 (taken from [49]).

4.1.1 Self-Triangulation

The improved time resolution down to clock precision is not the only advantage of having a coherent signal while studying the localization of GW events. In fact, slow-evolving GW sources produce long-lasting signals, such as those from BNS. Such signals can be seen for a long span of time by a detector with some appropriate sensitivity and a large bandwidth (requisites which can be assumed *a priori* for the present discussion). For 3G detectors, this time span is order some hours. The Earth rotates during this time, thus allowing a single facility to detect a signal at different spots along its path (this happens also for way shorter signals of course, but, in practice, the strategy depicted here is only applicable in the case of very long signals).

But, equation (1.46) only applies to static detectors (limit of Earth rotating very slowly with respect to the evolution of the signal, thus short signals). This means that, at a given time t_1 , a detector at a given position \vec{x}_1 measures a signal and one can propagate this signal at future times with expression (1.46) as seen by a detector at the same exact location, thus obtaining a simulated signal. However, the true detector will have moved away to \vec{x}_2 at time $t_2 > t_1$ since it rotates with the Earth, and will thus measure something slightly different from the simulated signal. In fact, for a steady detector at position \vec{x}_2 , the incoming signal will generally be time-shifted with respect to that at the previous location. Also at \vec{x}_2 one can think of extrapolating a signal as seen by a steady detector in that position.

This argument can be done also with all the successive time steps, thus understanding that one can virtually work out up to a very high number of simulated signals corresponding to different locations, each one shifted in time with respect to the others. This procedure allows to perform a very precise triangulation method, which can be henceforth called time-delay self-triangulation. All the required computations are already implemented in GWBENCH.

The time sampling of the instruments does not happen at infinite frequency. Conversely, there is a limit frequency that can be thought to be around 5000 Hz both for current and future facilities. Pictures in chapter 2 show that the sensitivities are not cut-off below this frequency limit, so that it can be considered a good proxy for half of the sampling frequency (because of the Nyquist theorem). GWBENCH implements a limit frequency of 7000 Hz for all the facilities being considered, the only exception being ET ($\sim 10^4$ Hz). However, only a rough order of magnitude estimate is needed at the present time.

In fact, one can compute the minimum duration of a signal for the time-delay self-triangulation to be used efficiently.

This happens when:

$$\frac{v_{rot} t_{sig}}{c} \gtrsim t_{sample} = \frac{1}{f_{sample}} \quad (4.1)$$

with v_{rot} the velocity for the rotation of the Earth, t_{sig} the duration of the signal and t_{sample} the duration of each sampling interval.

This expression can be rewritten as:

$$t_{sig} \gtrsim \frac{c}{v_{rot} f_{sample}} = t_{min} \sim 60s \quad (4.2)$$

where v_{rot} is the rotation velocity at a latitude of 45 and f_{sample} is 10^4 Hz.

The t_{signal} is computed for a given detector from equation (1.46) considering $f_{max} \rightarrow \infty$ (one may also consider, more accurately, $f_{max} \rightarrow f_{ISCO}$, even though the results change of few percents; GWBENCH uses the limit at infinity) and f_{low} given by a lower limit on the frequency as obtainable by looking at the sensitivity curve of the detector. With a 3G detector, one obtains that 60 seconds is the duration of the GW signal from a CBC with $\mathcal{M} = 45.5 M_\odot$ and equal masses for the two components. With these methods, namely the standard and the time-delay self-triangulation, the localization of a source depends on the other parameters only by means of the SNR of the signal: the lower the SNR, the worse is the extrapolation of the signal, the more errors one can do when comparing this signal with that of another detector at the same time step. Therefore, it is possible to infer the localization by performing time-delay interferometry, obtain the values of the APs at the inferred location, and then implement the Fisher formalism to get all the physical parameters of the source.

It is now reported a result concerning the localization accuracy of some remarkable networks of interferometers when detecting high-chirp mass signal. This is related to the localization accuracy of the network when performing the standard triangulation, without taking advantage of the rotation of the Earth. At figures (4.4), (4.5) & (4.6) one can see the localization confidence area at 90 % expressed in deg^2 as a function of the position in terms of *right ascension* (RA) and *declination* (DEC). The networks being considered are: LIGO Hanford + LIGO Livingston + Virgo + KAGRA (HLVK), LIGO Hanford + LIGO Livingston + Virgo + KAGRA + LIGO India (HLVKI), ET + CE (North and South) (ETCE). The chirp mass of the event is high ($35 M_\odot$), but still realistic, thus leading to a credible SNR and localization capabilities for all the considered networks. This value for the chirp mass has been used in order to speed up the computations: it leads to numerical values which are way lower than those obtained with BNS-like chirp masses, but the overall shape of the plot is the same for high and low masses. Furthermore, one can perform an estimate of the maximum radiated power of the source (at $f = f_{max}$) by considering equations (1.43) & (1.48):

$$P_{max} = \frac{32G^{\frac{7}{3}}}{5c^5} \frac{(M_1 M_2)^2}{(M_1 + M_2)^{\frac{2}{3}}} \left(\frac{c^6}{8G^2} \frac{1}{(M_1 + M_2)^2} \right) = \\ = \frac{c^5}{5G} \frac{q^2}{(1+q)^4} = \frac{c^5 \eta^2}{5G} \quad (4.3)$$

with $q = \frac{M_2}{M_1}$ and $\eta = \frac{q}{(1+q)^2}$. It is obvious that higher *eta* leads to more powerful events (and higher SNR). The maximum value for η is 0.25 (with $q = 1$). However, $\eta = 0.249$ obtained with $q = 0.9$, has been used. In fact [50] shows that this is the highest probability value for q . It need be mentioned that GWBENCH only allows values < 0.25 . The luminosity distance being considered is 1 Gpc. It is worth mentioning that another input for GWBENCH is given by the lowest frequency value. The value for ETCE is $f_{low} = 3$ Hz, while for 2G networks it is $f_{low} = 20$ Hz. These values have been obtained heuristically from figure (2.1) as the values where the ASD of the sensitivity reaches 10^{-23} for each network. These assumptions regarding the lowest frequency value are kept during the whole essay.

Furthermore, it has to be kept in mind that (RA,DEC) are defined since the GMST is assumed to be zero at the merger time. This assumption gives a unique relation between the coordinates in the frame of GWBENCH (the standard frame) and (RA,DEC). At $\text{GMST} \neq 0$, these figures would look shifted in the two directions, while preserving their geometrical shape.

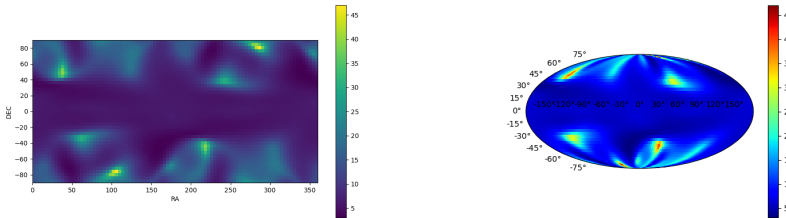


Figure 4.4: Map of the localization accuracy in terms of deg^2 for HLVK.

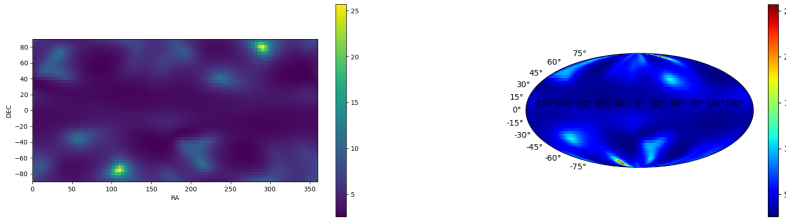


Figure 4.5: Map of the localization accuracy in terms of deg^2 for HLVKI.

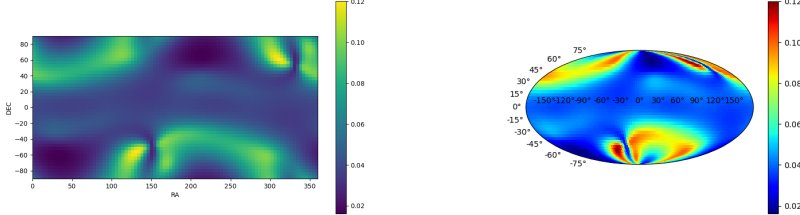


Figure 4.6: Map of the localization accuracy in terms of deg^2 for ETCE.

At first glance it is easy to see how the 3G network clearly enhances the localization capabilities of GW sources just by giving a look at the color bar of these plots.

Figures (4.4), (4.5) & (4.6) have been obtained performing a simulation of the detection of a GW event by means of the given networks with the source located at each (RA,DEC) position on the map. This kind of simulation is the main instrument used in the thesis work. Such a simulation is performed considering a great number of parameters:

- the ψ angle (here assumed to be 0);
- the inclination of the CBC-orbiting plane with respect to the line of sight (here assumed to be $\iota = \pi/4$);
- the spin magnitude of the two compact objects (2 separated parameters, both assumed to be 0);
- the polar and azimuth angle for the spin vectors of each of the two objects with respect to the plane formed by the line of sight and the total angular momentum (4 parameters, all assumed to be 0);
- an arbitrary reference time for the merger t_c (here assumed to be 0);
- the phase of the binary at time t_c , ϕ_c (here assumed to be 0);
- the already mentioned chirp mass \mathcal{M} ;
- the already mentioned η ;
- the already mentioned (RA,DEC) parameters (2 separated parameters);
- the already mentioned luminosity distance d_L ;

resulting in fifteen parameters [51]. Another input value for the code is the frequency range, which is given by the sensitivity curve for each detector. For a given network, only the detector with the most narrow bandwidth is considered for defining the frequency range. Furthermore, the frequency resolution interval df (generally equal to $1/T$ with T the duration of the signal) has been kept constant and equal to 0.0625 Hz (standard value used by GWBENCH for making the computations faster when no high spectral resolution is needed, as in this situation).

In this essay, the chirp mass of a binary is given in the rest frame of the binary. However, GWBENCH only uses the mass in the reference frame of the observer. The latter is given by $\mathcal{M}_{obs} = (1+z)\mathcal{M}_{rest}$. Here, z is the cosmological redshift, which can be obtained from the luminosity distance with the assumption of some cosmological parameters. In fact, the following relation has been inverted numerically for inferring z from d_L :

$$d_L = (1+z) \int_0^z \frac{cdz'}{H(z')} \quad (4.4)$$

with $H(z')$ the Hubble parameter at z' : this quantity depends upon the cosmological parameters. The reference values at [52] have been used. However, the chirp masses mentioned in this essay are always expressed in the rest frame of the binary.

With such parameters, one can build a NETWORK object detecting a waveform simulated by means of the simulation model *TaylorF2* [53]. Other simulation models are available, but this one is the most efficient one in terms of computation time. At this point, it is possible to compute the covariance matrix on all the parameters. Therefore, a confidence ellipse for (RA,DEC) can be obtained from the (RA, DEC) covariance sub-matrix. *gwbench* makes it at a confidence level of 90 %. The value reported in the color scales of figures (4.4), (4.5) & (4.6) is therefore the area of such ellipses in deg^2 as a function of the injection values of (RA, DEC).

Both the standard and self-triangulation have been addressed as time-delay techniques so far. However, this is not the whole story; not for the self-triangulation. In particular, also the APs rotate with the Earth. This means that, at each time step, one expects to see a different modulation of the signal given by the fact that at a given position on the sky, the value of the AP of a detector for each polarization mode has changed. Assuming that a signal contains only tensor modes, one can infer the position of a source just by looking at the AP modulation in the data. This is not a straightforward duty along the lines of finding the time shift between two detectors. In fact, in order to achieve the AP modulation, one has to know the polarization + and \times contents respectively in the case of a tensor signal (which depend on the chirp mass, η , ι and the other parameters). In turn, these quantities are affected by the knowledge of the APs (the localization), or the other physical parameters of the CBC. In this case, one can not infer the localization separated from the other physical parameters. Conversely, it has to be obtained from the Fisher formalism as well. That's why in the covariance matrix given as an output by GWBENCH one finds the localization variables RA and DEC too. The correlation factors between these variables and other parameters are generally non-zero. This makes the self-triangulation method more powerful since it implements both time-delay and AP modulation: the latter only requires that the duration of the whole GW event be greater than the sampling time interval (one needs masses $\gg 100 M_\odot$ for this not to be valid, and such mass ranges are never considered in the presented work). This means that when the expression (4.2) is not satisfied the self-triangulation contribution is dominated by the AP modulation, while one can not make any assumptions for when it is satisfied.

The Earth rotation is always used for improving the localization capabilities of every network, in presence of high and low mass events. However, one has to observe that networks with three or more detectors have their accuracy limited by the accuracy of the standard triangulation method. For such networks, the self-triangulation does not allow for a substantial improvement of the performance, but for a few percents.

At this point, the effect of self-triangulation is treated. In this case one can perform a simulation like the previous ones, but keeping the location of the source fixed (no maps are needed now). Such a simulation can be pursued for a high mass event (which can be predicted to be not susceptible to the self-triangulation), and a low mass one, which, conversely, should show an enhancement of the localization accuracy when implementing the self-triangulation. Such simulations are performed for different networks: two detector networks, where the self-triangulation is expected to bring an outstanding improvement to the accuracy, and three or more detector networks, where one expects to see the consequences of the self-triangulation as small effects. GWBENCH does not allow to test the localization accuracy of a single detector, not even including the self-triangulation.

Table (4.1) shows the results obtained for a CBC with $\mathcal{M} = 35$ and $1.2 M_\odot$. The latter is a standard value for the chirp mass of BNS, and provides a good testbed for the self-triangulation since the inspiral phase for such binaries takes very long.

In this table all the values are expressed in deg^2 and only a qualitative

Network	$35 M_{\odot}$ off	$35 M_{\odot}$ on	$1.2 M_{\odot}$ off	$1.2 M_{\odot}$ on
HL	∞	$3.4 \cdot 10^2$	$1.4 \cdot 10^2$	3.2
HLV	$1.5 \cdot 10^{-3}$	$1.5 \cdot 10^{-3}$	$5 \cdot 10^{-2}$	$5 \cdot 10^{-2}$
HLVK	$1.2 \cdot 10^{-3}$	$1.2 \cdot 10^{-3}$	$6.7 \cdot 10^{-3}$	$6.7 \cdot 10^{-3}$
HLVKI	$8.6 \cdot 10^{-4}$	$8.6 \cdot 10^{-4}$	$3.2 \cdot 10^{-3}$	$3.2 \cdot 10^{-3}$
ET	∞	$5.4 \cdot 10^2$	∞	$7.6 \cdot 10^{-1}$
CE (1 & 2)	$2.5 \cdot 10^{-1}$	$7.8 \cdot 10^{-2}$	$1.6 \cdot 10^{-1}$	$6.2 \cdot 10^{-3}$
ETCE	$1.6 \cdot 10^{-6}$	$1.6 \cdot 10^{-6}$	$1 \cdot 10^{-4}$	$1 \cdot 10^{-4}$

Table 4.1

treatment has been considered, in order to give a hint of how things work.

The table shows that the expectations are generally fulfilled, since the self-triangulation improves the localization performance, or it leaves it unchanged in the case of three or more detectors.

Moreover, the improvement due to self-triangulation at high masses (mostly attributable to the AP modulation alone, even if the time-delay method still plays a role) is not just a perturbation effect in the case of two detector networks.

In this simulations, in order to raise the SNR, the luminosity distance of the source has been changed to 10 Mpc.

The networks used in the following description are HLVK, HLVKI and ETCE, for which the localization method always implements the self-triangulation.

4.2 How Localization Behaves

In the following paragraphs, some arguments are reported in order to explain how the localization accuracy depends on other physical parameters. As already mentioned, when working with GWs, one deals with up to fifteen parameters. However, the localization behaviour is now depicted only as a function of the luminosity distance, chirp mass and mass ratio.

4.2.1 Distance Dependence

The localization behaviour as a function of the injected source location has been carried on together with an in-depth characterization of the self-triangulation method, which is widely used in the next parts. However, the localization accuracy depends on other injection parameters. In general, the luminosity distance is inversely proportional to the SNR, meaning that one expects it to simply re-scale the results obtained for the localization accuracy in terms of a power law: if A is the area of the ellipse at 90 % confidence for the localization, one expects that $A \propto d_L^\alpha$ with $\alpha > 0$. Another way to see this is giving a look to the expression of the power SNR of a GW event, which comes from equation (2.22) as it is twice the absolute value of the exponent in this formula.

In particular, one has the power SNR ρ^2 (in the first similarity the usual assumption of white noise is considered in order to have simple computations):

$$\begin{aligned}\rho^2 &= 2 \int_{-\infty}^{+\infty} \frac{|\tilde{h}(\omega)|^2}{S_n(\omega)} d\omega = \sim 2 \int_{-\infty}^{+\infty} \frac{h(t)^2}{S_n} dt = \\ &\sim 2 \sum_{i=1}^N \frac{h^2(t_i)}{2 \Delta t \sigma^2} \Delta t = \sum_{i=1}^N \frac{h^2(t_i)}{\sigma^2} = \sum_{i=1}^N \rho_i^2\end{aligned}\quad (4.5)$$

where ρ_i^2 is the power-SNR of the i -th time step in the data. In this equation, h is the signal at the detector location. Furthermore, using equations (1.40) & (1.42), the power over solid angle at the detector location P_D is:

$$P_D = \frac{P_{GW}}{4 \pi d_l^2} \propto h^2 \quad (4.6)$$

so that one has that $h \propto d_L^{-1}$

Therefore:

$$\rho^2 = \sum_{i=1}^N \frac{h^2(t_i)}{\sigma^2} = \frac{1}{d_L^2} \sum_{i=1}^N \frac{h_S^2(t_i)}{\sigma^2} \quad (4.7)$$

where h_S is the strain GW signal at the source.

However, the behaviour when changing the mass parameters, \mathcal{M} and η is not limited to a scale factor, since also the length of the signal comes into play. Thus, the dependence on the mass parameters is more complicated.

In this essay, it is reasonable to assume that the dependence on d_L can be separated from the other dependencies. This means that one can perform a new set of simulations sampling different distances in order to characterize the behaviour of the localization errors (once again, by means of the area of the ellipse at 90 % confidence). In this case, the distances are considered in an interval from 10 to 10^4 Mpc, while the chirp mass is $35 M_\odot$ in order to speed up the computations and $\eta = 0.249$.

The results match with the expectations as the *log-log* plot at figure (4.7a) clearly shows a linear behaviour, which is the consequence of a scaling power law like that mentioned few lines above.

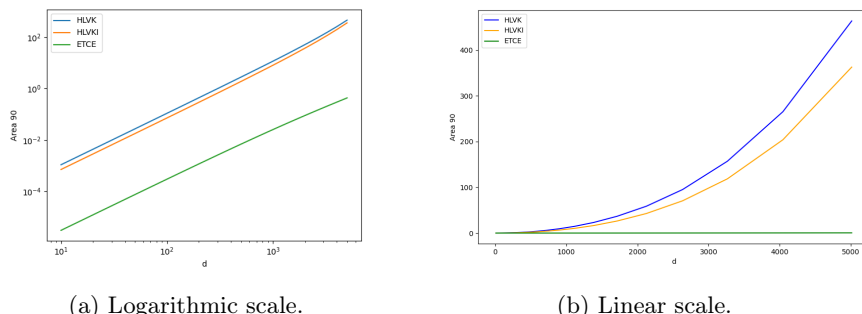


Figure 4.7: Localization accuracy as a function of d_L ($\mathcal{M} = 35 M_\odot$ and $\eta = 0.249$).

In particular, an easy linear regression obtained for the logarithmic data gives a linear coefficient $\alpha = 2$ with any of the networks. An error on α is not

displayed since GWBENCH does not return an uncertainty on the errors. This means that a fit is obtained without considering real fluctuations on A neither on d_L : therefore, there is no sense in reporting fluctuations on the estimations of the parameters, nor test-statistics of any kind.

One can note that the plot in logarithmic scale displays a non-linearity at very high distances: this is given by the fact that great distances affect the chirp mass at the frame of the observer by means of the redshift, thus increasing it (while not increasing the amplitude of the wave). A greater apparent chirp mass translates into a shorter signal, therefore leading to magnified errors.

4.2.2 Chirp Mass Dependence

As anticipated, the dependence of the localization accuracy on the mass parameters is a completely different subject. In a soft approach to the problem, the assumption of variables separability is considered also for \mathcal{M} and η . This is to be considered an oversimplification, which may lead to advantages in terms of the time taken by computations. One can see the dependence on the chirp mass at figure (4.8) where the sky area at 90 % confidence is plotted.

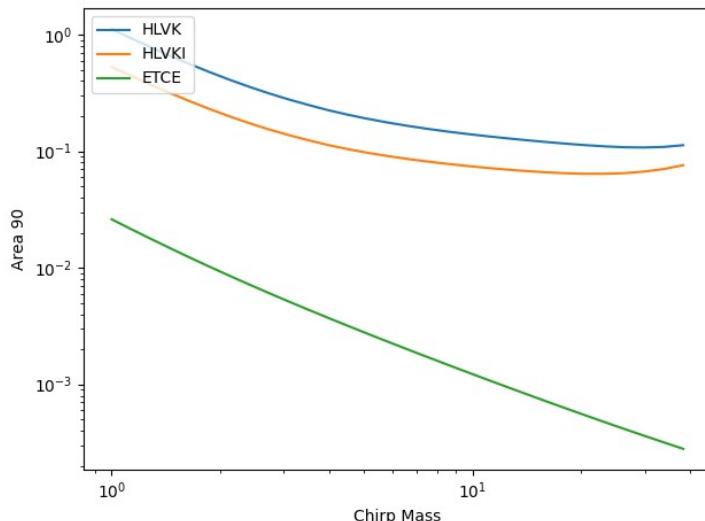


Figure 4.8: Localization accuracy as a function of the chirp mass ($\eta = 0.249$).

Especially from the behaviour of the accuracy for the 2G networks in the logarithmic plot one can see that it is not true that $A \propto \mathcal{M}^\beta$, since there is no linear behaviour. However, complicated function forms are avoided for the interpretation of this dependence, and it is fitted to the easiest form one can find. In a qualitative way, the expectations are fulfilled since one sees that the sky area shrinks when the chirp mass is raised.

In this case the fit has been more difficult to perform; once again, the Mathematica software [35] has been used in order to pursue a parameter estimation. Special care need be payed to the fact that only a suitable mathematical description is sought for the behaviour of the sky area as a function of the mass, not what this behaviour is due to. Therefore, it is enough to reconstruct a

qualitatively working function without paying attention to the physics within it.

Within a quick and simplified approach to the fit, a common function form has been obtained for all the networks:

$$f(\mathcal{M}) = A + B \cdot \exp \left[-C \cdot x^D \right] \cdot x^E + F \cdot x^G \text{ deg}^2 \quad (4.8)$$

with $x = \frac{\mathcal{M}}{M_{\odot}}$ and where (A , B , C , D , E , F , G) depend on the chosen network. In particular, one finds the numerical values for the parameters as they are reported at table (4.2):

Network	A (deg^2)	B (deg^2)	C	D	E	F (deg^2)	G
HLVK	$1.04 \cdot 10^{-1}$	$9.17 \cdot 10^{-1}$	$9.55 \cdot 10^{-2}$	1	-1.72	$-7.07 \cdot 10^{-4}$	1.21
HLVKI	$5.87 \cdot 10^{-2}$	$4.24 \cdot 10^{-1}$	$1.05 \cdot 10^{-1}$	1	-1.75	$-8.29 \cdot 10^{-4}$	$9.02 \cdot 10^{-1}$
ETCE	$1.16 \cdot 10^{-2}$	$2.29 \cdot 10^{-2}$	$7.06 \cdot 10^{-2}$	1	-1.69	$1.01 \cdot 10^{-2}$	$4.54 \cdot 10^{-2}$

Table 4.2

As stated, the scatter on these parameters can not be obtained, since GW-BENCH returns no uncertainty on the data. However, one can get convinced of the effectiveness of the fit by visualizing the data and the reproducing function, plotted at figure (4.9).

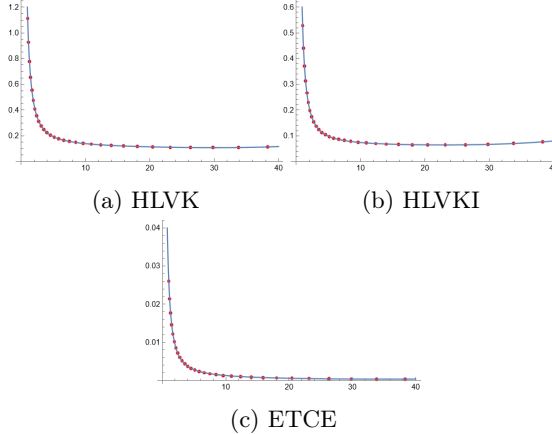


Figure 4.9: Localization accuracy as a function of \mathcal{M} . The x -axis represents \mathcal{M} expressed in solar masses, while the y -axis is the sky area in deg^2 .

4.2.3 Mass Ratio Dependence

As in the previous paragraph the results for chirp mass dependence have been summarized, now the dependence on η is addressed in the case of constant chirp mass $\mathcal{M} = 38M_{\odot}$, where η is a direct function of the mass ratio in the range $]0, 0.25[$.

The approach used here is the same already used in the previous subsection, and in general, only approximate fits as provided by Mathematica are used, without reporting fit statistics at all.

Nevertheless, in this case the situation is a bit more complicated, since the mathematical expression for the fitting function changes slightly for the three different networks.

For the 3G network:

$$f(\eta) = 2.44 \cdot 10^{-6} \cdot \frac{\exp[1.89 \cdot (1.72 + \eta)]}{\eta^{0.74}} \text{ deg}^2 \quad (4.9)$$

while for HLVK and HLVKI one has, respectively:

$$\begin{aligned} f(\eta) &= 10^{-1} + \frac{6.29 \cdot 10^{-9} \cdot \exp[1.89[1.72 + \eta]]}{\eta^{6.28}} \text{ deg}^2 \\ f(\eta) &= 10^{-1} + \frac{4.34 \cdot 10^{-9} \cdot \exp[1.89[1.72 + \eta]]}{\eta^{6.28}} \text{ deg}^2 \end{aligned} \quad (4.10)$$

The plots showing the appropriateness of the fitting functions are reported at figure (4.10).

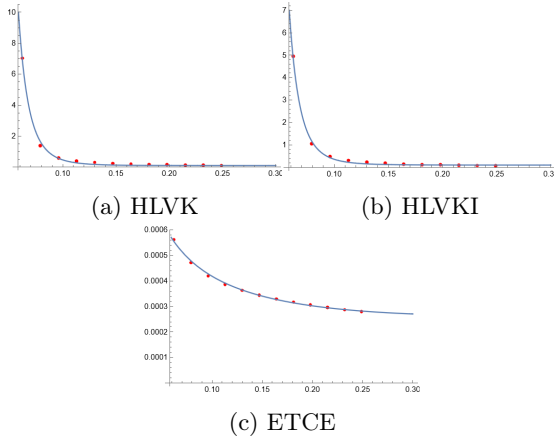


Figure 4.10: Localization accuracy as a function of η . The x -axis represents η , while the y -axis is the sky area in deg^2 .

The next step would be that of deriving a general behaviour as a function of the two variables, \mathcal{M} and η , simultaneously. However, this is not a trivial step in the present case, since the global behaviour can not be effectively obtained by the composition of the expressions for the simple dependence on the chirp mass and η .

Because of the difficulty in finding such a fitting function, this section ends reporting only the graphical behaviour of localization accuracy as a function of \mathcal{M} and η : figure (4.11).

One finds that the main differences (besides normalization) of these plots are given by the behaviour at high mass and low η , for which an analytical

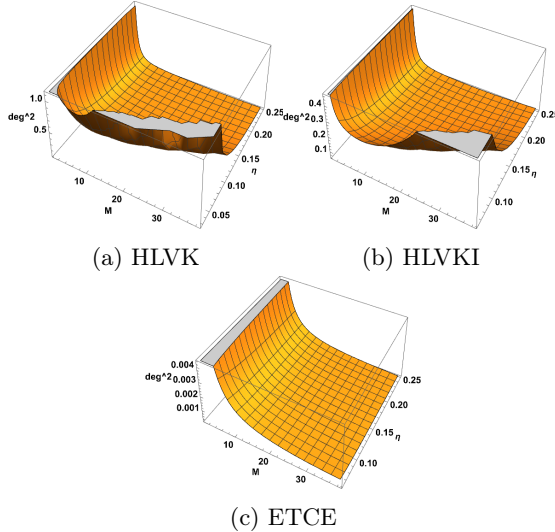


Figure 4.11: Behaviour of the sky area for the localization as a function of both \mathcal{M} and η .

fit has been obtained while keeping the mass fixed. In fact, one can see a net aggravation of the localization capabilities for HLVK and HLVKI in this region. This happens because massive binaries reach a quite low f_{max} . Furthermore, if the two masses are exasperately asymmetric, this upper limit shrinks even more, thus allowing a detector to measure a signal for a shorter time, therefore reducing its overall SNR (and negatively affecting the errors in the inference of parameters). The f_{max} eventually falls below the low frequency limit imposed by the facilities, and this is represented by the gray (no data) spots in the HLVK and HLVKI plots at figure (4.11). For 3G detectors, the low frequency limit is much smaller than that of 2G detectors, thus allowing only for a small worsening of the performances, without allowing f_{max} to fall below it.

The main concepts regarding source localization by means of GW facilities have been outlined in this chapter, with peculiar attention to the methods and strategies adopted by GWBENCH, which is the main tool used in this work. The idea of triangulation for standard astrophysical objects has been provided, together with a special argument regarding GW sources, which gain great precision from this method since their modulation is deterministic in time (as shown in chapter 1) and in the direction of the source (because of the APs). The idea of triangulation performed using data from a single facility by means of these methods has been called "self-triangulation".

Since the presented subject concerns a comparison between current and future detectors, the second part of the chapter has reported the behaviour of the localization capabilities as a function of the direction of the source, of its luminosity distance and its mass parameters. Specifically, the luminosity distance causes a simple re-scaling of the localization accuracy which can be factorized as $\propto d_L^{-2}$. However, this argument is not suitable for the dependence on mass

parameters, that is, the chirp mass \mathcal{M} and the mass asymmetry term η . The behaviour of the localization accuracy has been obtained as a function of \mathcal{M} only for when $\eta = 0.249$ and as a function of η only for when $\mathcal{M} = 38\text{M}_\odot$.

However, by plotting the localization sky area as a function of both the mass parameters, one understands that the analytical function describing it is far more complicated than just the composition (or product) of the single dependencies.

This preliminary work can help in understanding some of the results presented at the end of the following chapter, when the precision of a null stream as measured by a detector is characterized, reminding that such quantities are position dependent and consequently affected by fluctuations on the observed position.

Chapter 5

Simulations for Measures of the Null Streams

So far, the main background topics regarding the science concerned here have been presented. More specifically, all the previous chapters have got the reader acquainted with the necessary prerequisites for understanding the computations and outcomes presented in this chapter.

This chapter begins with a global view of the code implemented for the computation of the output from GW facilities. More specifically, the main problems and critical issues of the computer aspects are pointed out. In the first section there is space for a brief introduction about High Performance Computing (HPC) facilities as they have been used for obtaining the presented results in shorter times. Afterwards, the main outcomes are reported, focusing on the behaviour of the null streams as a function of the luminosity distance and mass parameters.

Few final arguments are made as combinations of null streams can provide newer quantities which may add further information at given locations on the sky.

5.1 The Code

The main idea behind the code used for inferring the null streams and their fluctuation, at a given point in the parameter space, consists in deriving such fluctuation as a propagation of the localization uncertainty.

Assuming all the parameters for the already mentioned *TaylorF2* model, one can construct a simulation for a given GW event as described in chapter 4. This event is used to generate a purely tensor GW signal. Each detector in a given network modulates this signal by means of its APs, and sees it with a given shift in time with respect to the ideal frame at the centre of the Earth, because of the limited speed of GWs.

5.1.1 The Stationary Phase Approximation

It is now outlined a detail that has been neglected in the previous chapters. Generally, `GWBENCH` performs all the computations in the frequency domain

since model *TaylorF2* does the same. However, this means that the APs need be computed in the frequency domain too, or the GW signal need be transformed to the time domain. In general, one can remember the definition of the APs as modulating terms multiplying the GW strain to be in time-domain. However, one notes that, in general:

$$\mathfrak{F}\left(\sum_i^N F_i(t) h^i(t)\right) \neq \sum_i^N \mathfrak{F}(F_i)(f) \cdot \mathfrak{F}(h^i)(f) \quad (5.1)$$

because of the convolution property of the Fourier transform (here denoted by \mathfrak{F}). What one can see in GWBENCH is that the signal, as measured by a given detector in the frequency domain, is given by:

$$S = \sum_i^N F_i(f) h^i(f) \quad (5.2)$$

which seems to be in contrast with equation (5.1). However, the different notation implemented in the two expressions is not by chance. In fact, GWBENCH correctly considers the AP definition given in chapter 2, namely the time-domain AP. By considering a GW strain $h(t)$ one naturally has $S = \sum_i^N F_i(t) h^i(t)$.

Indeed, one can always express t as a function of f in the case of a CBC with given masses: this concept has been already seen in the Newtonian approximation, in chapter 1, namely expression (1.46). Therefore, it is matter of straightforward computations to express $F_i(t)$ as $F_i(t(f)) = F_i(f)$.

By knowing this, one can implement the stationary phase approximation (SPA) [54] and compute the Fourier transform of $S_i = F_i(t) h^i(t)$. In this fashion, one has that $S_i(t) = \mathcal{S}_i(t) \cos(\Phi(t))$, with $\mathcal{S}_i(t) = F_i(t) \cdot A_i(t)$ being a slowly changing amplitude term containing the time dependence of the AP and the increasing amplitude term of the GW strain, while $\Phi(t) = \int_{-\infty}^t 2\pi f(t') dt'$ is the rapidly changing phase.

The SPA allows one to write down:

$$\begin{aligned} \mathfrak{F}_{SPA}(S_i)(f) &= \frac{1}{2} \mathcal{S}_i(t) \left(\frac{df}{dt} \right)^{\frac{1}{2}} \exp \left[i(2\pi ft - \Phi(t) - \pi/4) \right] = \\ &= \frac{1}{2} F_i(t) A_i(t) \left(\frac{df}{dt} \right)^{\frac{1}{2}} \exp \left[i(2\pi ft - \Phi(t) - \pi/4) \right] = \\ &= \frac{1}{2} F_i(t(f)) A_i(t(f)) \left(\frac{df}{dt} \right)^{\frac{1}{2}} \exp \left[i(2\pi ft(f) - \Phi(t) - \pi/4) \right] = \\ &= F_i(f) \mathfrak{F}_{SPA}(h^i)(f) = F_i(f) h^i(f) \end{aligned} \quad (5.3)$$

where $h^i(f)$ is the stationary phase-approximated Fourier transform of the GW strain and $F_i(f)$ is the time domain AP after a change of variable, and not the Fourier transform of the time domain AP. One can see the difference between the two things by plotting the time domain AP $F_+(t)$ (where no change of variables is considered) for an event at a fixed position in the (RA,DEC) space

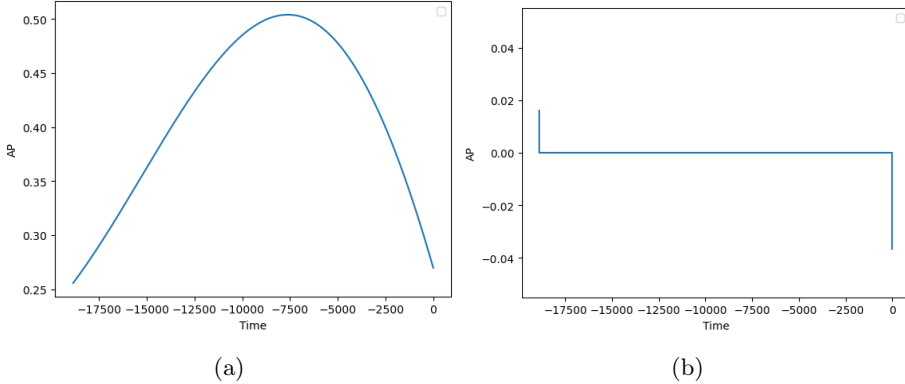


Figure 5.1: Time-domain F_+ for LIGO Hanford at $(45^\circ, 45^\circ)$ when expressing t as a function of f (left) and with the inverse Fourier transform of $F_+(f)$ (right).

and the inverse Fourier transform of $F_+(f)$: they are obviously not the same thing, and the second one is clearly wrong.

More detailed considerations about the use of SPA in this case are given in [24], yet the computations at (5.3) are sufficient for addressing the formalism provided in equation (5.2) in the SPA fashion.

By means of these simplified mathematics, the response of each detector in the network is computed for a simulated event with given input parameters. In general, one may simulate the response of the detector to a tensor signal (which is the standard waveform computed by GWBENCH) or sum it to a non-tensor contribution by means of expressions (3.4). In particular, the work being presented implements both the possibilities. A high spectral resolution ($df \sim 1/T$) response signal is obtained for all the frequency domain quantities. This is where the Fisher Information formalism comes at hand, since it is needed for inferring the parameters of the CBC event and their uncertainties.

The computations in this part of the code are not being reported since the main concepts have already been explained in chapter 2. However, it must be outlined that the covariance matrix is computed by taking into account all the parameters, thus the errors on the localization quantities (RA,DEC) are affected also by the uncertainty on every other parameter: this is accounted for in order to imitate a real situation of data analysis without introducing further simplifications. However, it is observed that, within the implemented Fisher approach, the localization errors improve of factors $\approx 3\%$ if all the other parameters are fixed.

A critical point about this step is given by the fact that the Fisher formalism implemented in GWBENCH only makes use of tensor signals for inference. This is not always realistic in the current fashion, since also non-tensor signals are being injected. Therefore, the only way to pursue this part by means of this code is that of considering the non-tensor contribution as a perturbation to the whole network response during this step ($h^{nT}/h^T \ll 1$). Table (4.1) shows that low mass events are better localized when implementing self-triangulation,

which in the case of GWBENCH is given by tensor APs modulation and time-delay interferometry. The modulation for tensor modes of course differs from that of non-tensor ones, meaning that using it for a general signal clearly leads to systematics, unless the strain of the non-tensor component has an amplitude way lower than that of the tensor ones. Henceforth, the localization is always achieved treating the signal as purely tensor.

The null streams are measured by multiplying the response of each detector with a combination of the APs of the other detectors in the network. The response of a detector is obviously fixed, thus the only quantity being affected by measure uncertainties are the APs, which carry just the propagation of the localization uncertainties, since they depend on position only.

Therefore, only the covariance matrix relative to the localization parameters is considered henceforth. More specifically, it is used to generate 32 draws of a 2-Gaussian distribution in the two variables (the number 32 is explained soon).

Such draws are then used to compute the APs of each polarization mode at their positions. Such APs are then used to compute the null stream for each draw, in order to see the effect of the obtained distribution on the null stream and on the effectiveness of the gravity test, therefore corresponding to the realistic situation where known response data need be combined with uncertain APs. Making it a bit clearer: the response signal in the null streams is that obtained from the detectors' response to the GW event simulation, while the APs are drawn from the distribution dictated by the localization error from the aforementioned simulation.

For each draw, the null streams are computed in the frequency domain, and their power spectral density (PSD) is computed as well. It is worth mentioning that if the location used for the computation of the APs does not exactly match the input value of the GW event then the null stream is affected by a systematic error, meaning that it is not expected to be exactly zero for tensor signals anymore. However, it should be very small, hopefully much smaller than the detectors instrumental noise. Therefore, the value of each null stream is averaged over the 32 draws and its standard deviation is obtained as well. More specifically, the null streams computed for each network are:

$$\begin{aligned} \text{NS1} &= \epsilon_{ijk} F_+^i F_\times^j S^k \\ \text{NS2} &= \epsilon_{ijkl} F_+^i F_\times^j F_B^l S^k \\ \text{NS3} &= \epsilon_{ijkl} F_+^i F_\times^j F_W^l S^k \\ \text{NS4} &= \epsilon_{ijkl} F_+^i F_\times^j F_V^l S^k \end{aligned} \tag{5.4}$$

with indices running on (1, 2, 3, 4), namely the labels for the four detectors measuring the null stream. For the three networks:

- ETCE (3G network): ET1, ET2, CE North, CE South;
- HLVKI (2G network with LIGO India): LIGO Livingston, Virgo, KAGRA, LIGO India;
- HLVK (2G network without LIGO India): LIGO Hanford, LIGO Livingston, Virgo, KAGRA.

The HLVKI network, being made of 5 detectors, would be able to completely disentangle all the independent polarization modes. However, since the Hanford and Livingston facilities are almost aligned one another, it is credible that such disentangling would not be so straightforward for every event. It is reasonable to use the full network only to improve the localization capabilities and then treat it as if it were made of just four facilities for calculating the null streams; in particular, the completely unaligned detectors have been used, and LIGO Hanford has been discarded.

The three detector null stream NS1 as computed by 3G network for a $35M_{\odot}$ and $\eta = 0.249$ CBC, with APs computed at the exact position of the event, can be transformed to time domain and is plotted at figure (5.2a) ; conversely, at figure (5.2b), one finds the same quantity with the APs computed in a position drawn from the (RA,DEC) distribution dictated by the localization uncertainty.

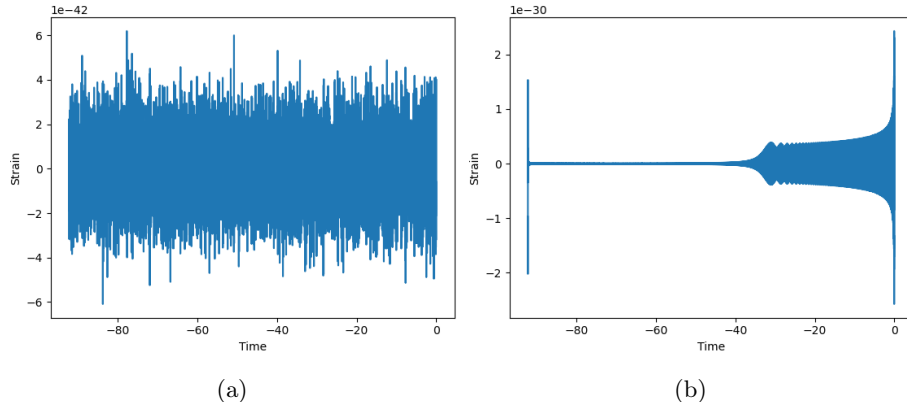


Figure 5.2: Time-domain null stream in the case of APs computed at the same exact location of the GW event (45 , 45) at (5.2a), and at a nearby location within the localization uncertainty (45.001 , 45.002) at (5.2b) (ETCE).

Figure (5.2a) is clearly the effect of a perfect null stream, which is not identically zero only because of floating point precision noise (truncation noise) in the computations. Oppositely, figure (5.2b) shows a deterministic behaviour, resembling a scaled-down (amplitudes are much smaller) version of the GW strain for a CBC. It is obvious that the tilt in the position ideally breaks the null stream, while still keeping it very small.

A tensor signal has been simulated at 200 Mpc, with $\eta = 0.249$ and $\mathcal{M} = 35.0M_{\odot}$ for each of the three networks, and the average PSD of NS1 is plotted at figure (5.3) and compared to the noise PSD for one of the detectors of the network.

It can be observed that the SNR of $\text{PSD} + 3\sigma$ with respect to the noise PSD is generally smaller for ETCE ($\lesssim 10^{-2}$, while for the other configurations the SNR is $\lesssim 10^{-1}$), thus making it harder for the null stream to overtake the detector noise in absence of non-tensor modes for the 3G network. This means that there is a smaller probability for ETCE to erroneously claim the presence of non-tensor modes.

Moreover, the HLVKI network performs better than the HLVK, since the SNR for both the mean value of the null stream and for the mean value $+ 3\sigma$,

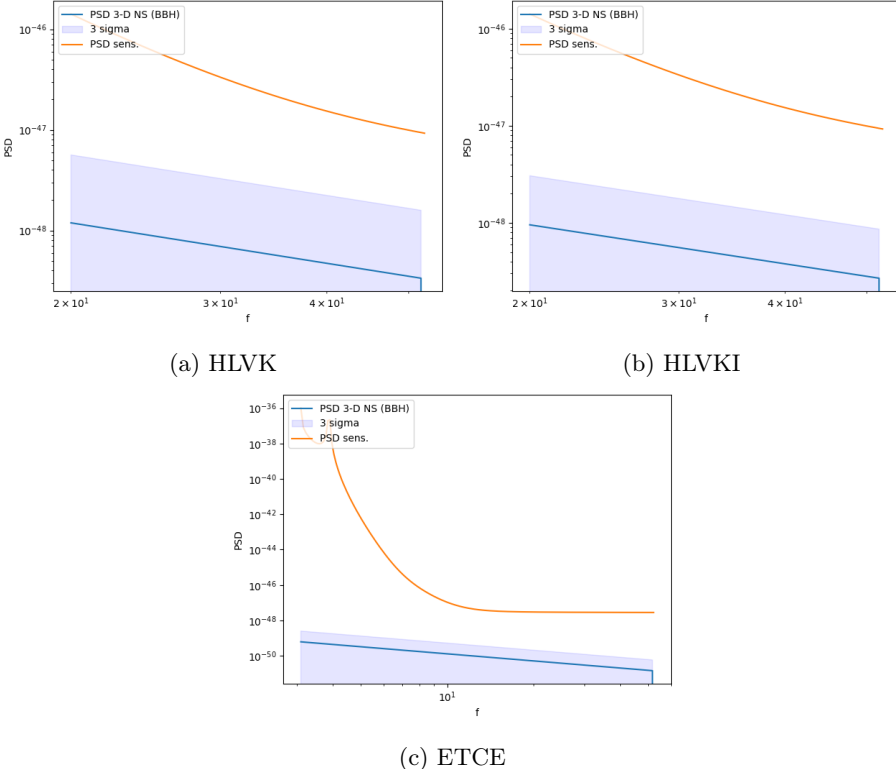


Figure 5.3: PSD for NS1 in absence of non-tensor modes.

with an SNR which is 0.25 times that of the HLVK network.

When a vector W mode (defined in chapter 3) is injected, the PSDs for the same event are plotted at figure (5.4).

It is clear from this images that each of the networks is able to measure a null stream with $\text{SNR} \gtrsim 10$, with a peak performance of ~ 100 for the 3G network. This means that the ETCE network has a lower probability to deny the presence of non-tensor modes when observing a GW event with vector W mode content.

The HLVKI network performs better than the HLVK one, since in this case it returns a higher SNR, ~ 10 times larger than the HLVK network.

The qualitative arguments reported here concerning the performance differences among networks are generally valid also for different values of distance, \mathcal{M} and η and for the injection of different polarization modes, even if the absolute numerical values generally change.

High Performance Computing

The code summarized in the previous paragraph can take a lot of memory, especially for low mass events (BNS), that cause very long data arrays: in fact, the duration of the signal for low distance events with $\mathcal{M} = 1\text{M}_\odot$ is around 22000 seconds considering a low frequency limit of 3 Hz (for 3G networks). The signal is then sampled at 4096 Hz, meaning that one data array has up to $\sim 10^8$ entries.

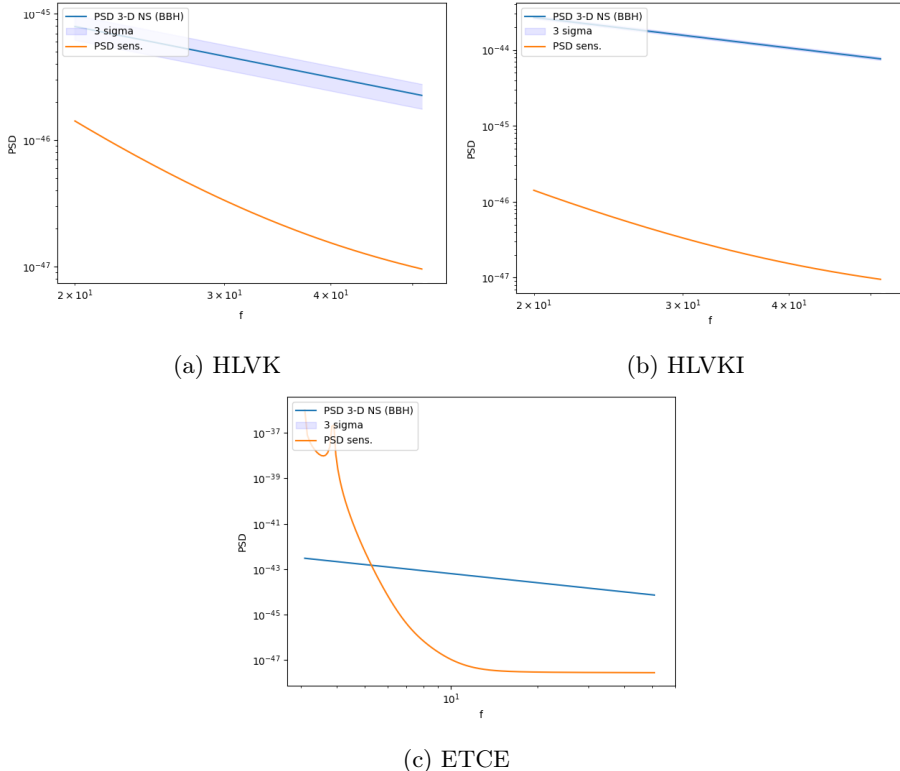


Figure 5.4: PSD for NS1 in presence of a scalar mode added to the tensor signal.

Such entries need to be of kind FLOATING POINT - 64, thus making $8 \text{ bytes} \times 10^8 \sim 1 \text{ GB}$. Of course, one has to keep track of the APs behaviour during the whole duration of the signal, thus having at least 20 additional arrays (one for each AP for every detector in the network), and four null streams. Furthermore, the APs need to be computed for a number N of draws which, in order to be statistically relevant, has to be $N \geq 10$, thus making the code occupy $\sim 250 \text{ GB}$ for one network, at one value of d_L and η . This load of memory is still addressable by a simple laptop, but if one wants to study the behaviour of the null streams while changing some of the aforementioned parameters, it is not possible to run more than few (order unity) codes at the same time. Therefore, running more codes in parallel is not possible above a very low limit. Running such codes "in series" (starting a new one as soon as another one ends) is possible, but one of these codes takes ~ 3 hours (when the N draws are parallelized on the different cores of the laptop) for a single run. Running more than four codes one after another means harming a laptop (all the cores are running for more than 12 hours bringing it to very high temperatures) with low effective advantages. Making the code run on less cores reduces the harm to the laptop, while however increasing the computation time, which may reach above 30 hours. It is also possible to reduce the amount of memory load for each code by *un-vectorizing* the code and performing step-by-step computations on arrays (or at least along some direction). However, this procedure also raises the computation time to

huge values.

These are the premises which led to the usage of the advanced computation facilities provided by CINECA, especially the *Leonardo* machine [55]. On such a cluster, it is possible to use up to 256 nodes at a time, thus running up to 256 codes together. Furthermore, each node has 32 cores, meaning that different parts of the code can work in parallel on different cores: this brought to the decision of working with 32 draws of the (RA,DEC) distribution, which is statistically more relevant than working with just ten.

This short paragraph is due since the main results presented later have been obtained mainly thanks to such computing facilities.

The final goal for this kind of research would be that of seeing how the networks measure the four quantities as in equations (5.4) while varying the three aforementioned parameters for the dependence of the localization accuracy: the luminosity distance d_L , the chirp mass \mathcal{M} , the mass asymmetry parameter η . As stated in the previous chapter, one could verify the dependence on up to 15 parameters. Of these, many happen to be disjoint from the examined subject, meaning that changing some of them would lead to small-to-no change in the performance of a network. This is the case of (see chapter 4) ϕ_c , t_c , the individual spin magnitude and direction.

However, that does not apply to other parameters the polarization content of a signal depends on, such as the polarization angle ψ , the orbit inclination angle ι , RA and DEC, which determine the way each detector sees the different polarization modes. The dependence on these parameters has been (unfairly) neglected giving preference to the distance and mass parameters. Nevertheless, it is evident that including the dependence on these extra quantities would have led to a huge increase of the coding and computation time. It can be left as a challenge for future progression in this subject to include this additional study.

5.2 Results

In this section, the obtained results are summarized by means of graphs, and the most important outcomes of the total work are outlined.

In particular, the computations have been performed for what follows.

- Each of the null streams of (5.4) has been computed in each code for a given network and for a given signal, with fixed binary parameters, and its power SNR has been obtained integrating the ratio $\text{PSD}_{\text{NS}}(f)/\text{PSD}_{\text{noise}}(f)$ on frequency.
- The codes *always* compute the null stream response in 4 situations: with a full tensor signal, a tensor+scalar longitudinal mode signal, a tensor+ V signal and a tensor+ W signal; where non-tensor contributions are present, they have been considered with a dimensionless amplitude $A_i = 1$ (see equation (3.4)).
- This job has been pursued while keeping $\mathcal{M} = 35\text{M}_\odot$ and $\eta = 0.249$ and changing the luminosity distance by logarithmically spacing the range 10

$\text{Mpc} \rightarrow 10^{3.7} = 5012 \text{ Mpc}$ in order to see the behaviour of the responses as a function of d_L .

- This procedure has been pursued also while keeping $d_L = 100 \text{ Mpc}$ and moving on a 2-D array defined by a chirp mass axis and an η axis; the former has been logarithmically sampled on a range $1 \rightarrow 38 \text{ M}_\odot$ while the latter has been linearly sampled in the range $0.028 \rightarrow 0.249$.
- Finally, each of these arrays of jobs has been done for each of the three aforementioned networks: HLVK, HLVKI, ETCE.

5.2.1 Distance Dependence

The dependence of the power SNR on the luminosity distance is expected to resemble what has been observed for the localization accuracy. In particular, in chapter 3 it has been observed that the sky area for the localization grows like d_L^2 . In this case, the SNR of a null stream depends on the distance only by means of the GW strain h_+ as worked out at (3.4). In particular, the SNR is expected to behave like $\sim h_+^2 \sim d_L^{-2}$. The only exception to this behaviour should be that of the completely tensor signal: in this case, the SNR has to be very small and dominated by fluctuations induced by the localization error, thus hiding the dependency.

The obtained power SNRs for the null stream NS1 (the one obtainable with three detectors) for non-GR signals are plotted on a logarithmic scale at figure (5.5) as a function of $\log(d_L)$, together with an intuitive linear fit.

There are some features which is worth mentioning before moving ahead. In particular, the HLVKI and the HLVK configurations do not superimpose on the plots, even though they both compute NS1 with the same combination of detectors, LVK. This behaviour is given by the different localization accuracy of the two networks, which accounts for a greater deviation of the APs from their original values. Furthermore, 2G facilities show a quite good behaviour, even if worse than that of 3G: for $A_i^2 > 8/\text{SNR}$ HLVK is able to observe non-tensor modes with power $\text{SNR} > 8$ (which, as previously stated, is the standard threshold for claims in this subject). For instance, at $d_L \sim 10^{1.5} \simeq 32 \text{ Mpc}$, a scalar mode with $A_S \gtrsim 0.1$ would give a power $\text{SNR} \sim 8$.

In these plots, the power SNR for a three detector null stream is reported in the case of four or more detector networks. This means that, after a re-labelling of the facilities, one could find other versions of NS1 for each network, as illustrated at (3.9).

It is important to observe that the linear coefficient for all the linear fits is now $\simeq -1.8$, thus sensibly different from 2.0. As a final outcome of this section, it need be mentioned that linear fitting functions like those plotted at figure (5.5) do not perfectly match with the simulated behaviour.

In fact, increasing the luminosity distance means increasing the redshift z of a source. In particular, this means that raising d_L corresponds to making it detectable for a shorter span of time, thus reducing the performance of the network. However, one would expect the behaviour of the simulated data to fall below the linear fit, but the figure shows this is not always true.

A fitting function with better performances has been obtained, and it is given by:

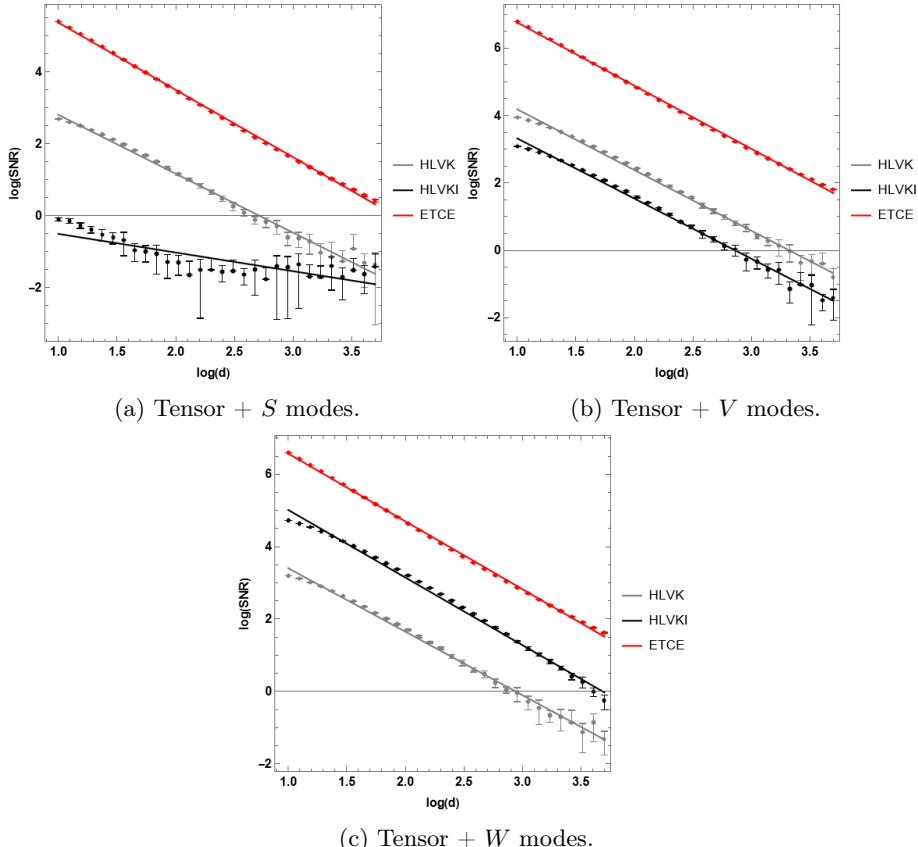


Figure 5.5: Power SNR for NS1.

$$f(d_L) = A + B \cdot d_L \cdot \cos[C \cdot d_L + D] \quad (5.5)$$

The same data of figure (5.5) are shown with this improved fitting function at (5.6).

The estimated parameters are reported at tables (A.2), (A.4) and (A.6), for the HLVK, HLVKI and ETCE networks respectively. The fits have been obtained with and without the localization uncertainty errors. A weighted average from the two methods is reported, together with the corresponding uncertainty. The same thing has been done for the linear fit, and the results have been reported at tables (A.1), (A.3) and (A.5), implementing the notation: $y = A \log d_L + B$.

In order to be a good working quantity for a measure of zero, the null stream has to be consistent with zero when tensor modes only are present. This is the case of figure (5.9). In this case, the fit can not result in anything meaningful.

Things become even more interesting when considering the four-detector null streams, namely NS2, NS3 and NS4, which are expected to be zero when the signal is purely tensor or contains only, respectively, scalar, V or W contribution.

Only the results for NS2 are reported in the text, since NS3 and NS4 behave similarly with different mode contributions. NS2 gets rid of scalar modes, thus

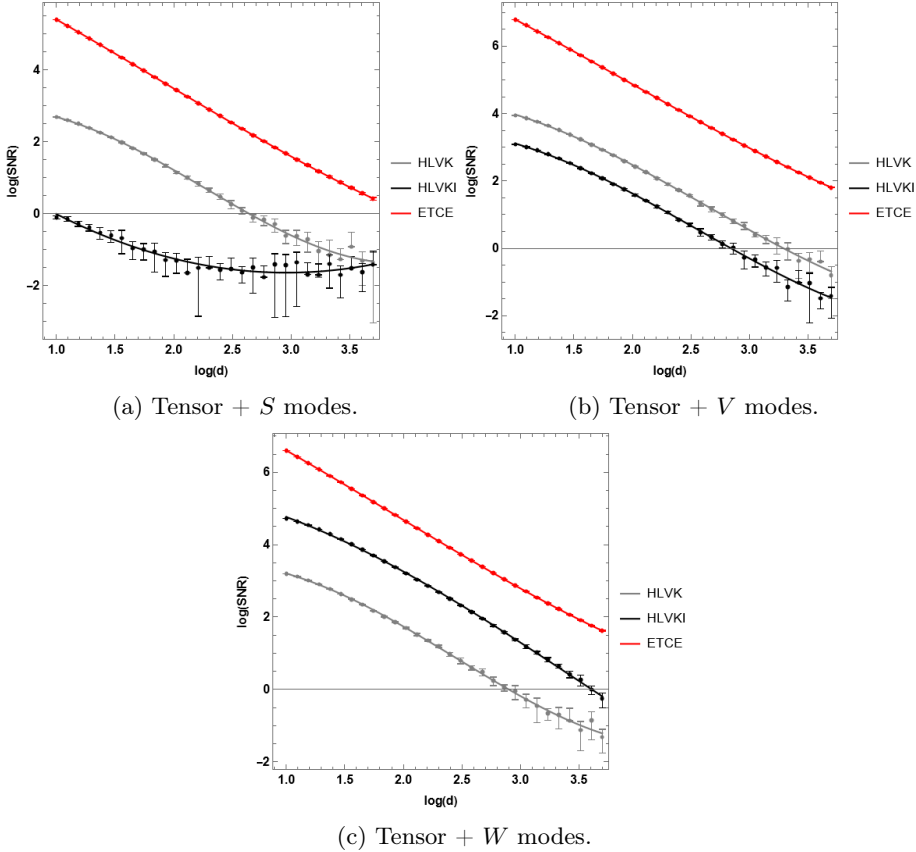


Figure 5.6: Power SNR for NS1.

showing whether vector modes contribute to the signal. In the case of only tensor modes and tensor+scalar modes the results are displayed at figure (5.8).

It is evident that in the case of a scalar mode contribution, the HLVK network raises its SNR to notable levels, thus making NS2 possibly ambiguous if one wants to discriminate between vector and scalar modes: there is a higher possibility that the power SNR of NS2 may overtake the threshold value = 8, thus leading to a wrong claim for the presence of vector modes.

However, when the main interest is proving whether there are non-tensor modes, NS2 generally performs better than NS1 for each network. In particular, for the given event being simulated, HLVK seems more reliable than ETCE, returning lower values than the latter.

It is important to keep in mind that the three networks perform differently at different locations, polarization and inclination angles. This is a consequence of the different geometries of the configurations: generally, one should expect ETCE to outperform HLVK. The unexpected behaviour of figure (5.8) for HLVK need be tested as a function of these further quantities. Similarly, the weak performance of HLVKI when dealing with NS1 in presence of scalar modes should be investigated when changing these parameters. Currently, only the 3G network always shows an optimal behaviour.

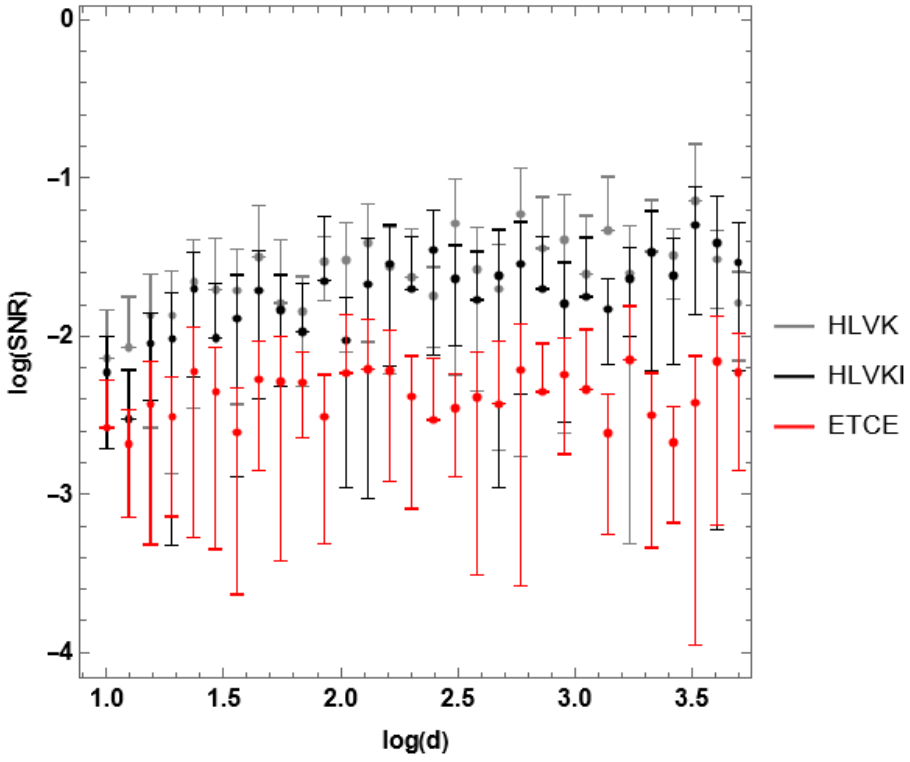


Figure 5.7: Power SNR of NS1 with tensor modes only.

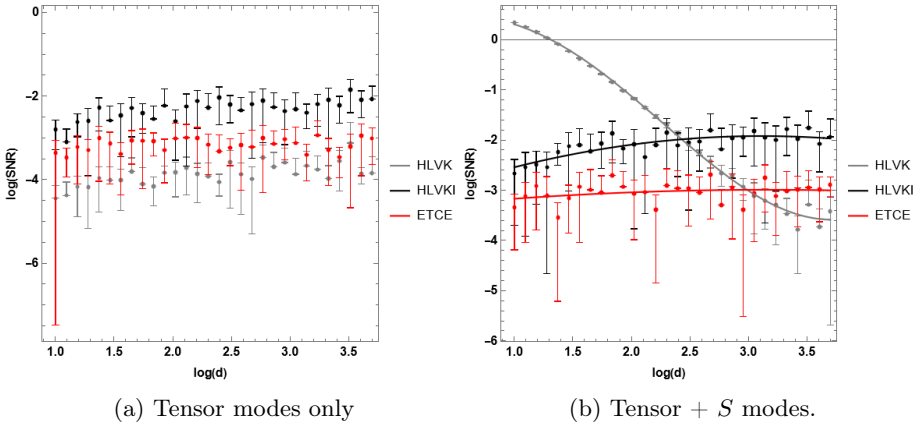


Figure 5.8: Power SNR for NS2.

Figure (5.9) displays the results for the injection of the vector W mode with $A_W = 1$.

The plot shows how the power SNR of NS2 raises to very high values, especially for the 3G network and the HLVKI configuration.

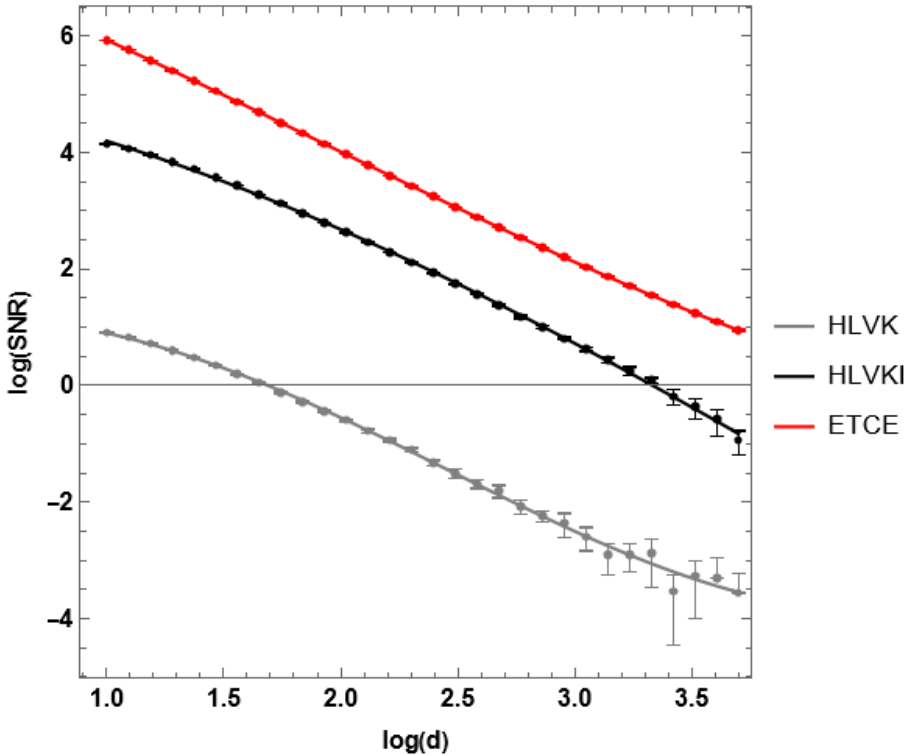


Figure 5.9: Power SNR of NS2 with tensor + W modes.

Many similar plots are displayed at section B.1. One would expect NS3 and NS4 to be dominated by noise effects when the GW strain is given by tensor modes only, or by tensor and V or W respectively. It is worth mentioning that, when the null streams are not dominated by noise, they are always well reproduced by a fitting function like that in (5.5). However, it has to be kept in mind that, like in chapter 4, the fitting function is adopted only as a way to reproduce the data, and it has no theoretical background: more precisely, there is nothing like a formal derivation justifying the analytical form of the function. At least, it has not been found within the endeavour for this thesis.

By observing the plots at Figure 5.4 and following, one can see again the awkward behaviour of HLVK: the four detector null streams discarding a given non-tensor mode display a loud SNR when the signal accounts for that peculiar mode and the tensor ones. Indeed, a general variability of the SNR is expected: the mean angular displacement due to localization uncertainty causes it to distance from the results for more accurate networks. However, in some cases, the SNR reaches very high levels, thus raising questions about the cause of this behaviour. Moreover, table (A.2) shows that the errors on the parameters of the fitting function are order $\lesssim 10\%$ in these cases. This result contrasts with the other networks, for which the errors on the parameters grow of ~ 5 orders of magnitude.

For addressing this problem, one should verify that it can be generalized

to all the directions, polarization angles and orbital inclinations. As aforesaid, this work does not include this kind of analysis, but it should be considered for future developments.

5.2.2 Chirp Mass and η Dependence

This subparagraph reports the most representative results and graphs for the dependence of the null streams on mass parameters.

The procedure follows the previous part, keeping a parameter fixed (d_L here) and changing the two mass quantities. This has been done for a logarithmically spaced interval of values for the chirp mass and a linearly spaced interval for η .

The results as obtained for the ETCE configuration only are reported for first, as they are the most *succeeded* ones. Later, the results for the other configurations are too, with a summary of the main differences between the networks.

As a starting point, the NS1 as seen by ETCE is analyzed for different cases of GW strain. In the case of a tensor-only GW signal, the plot of the data is given at figure (5.10).

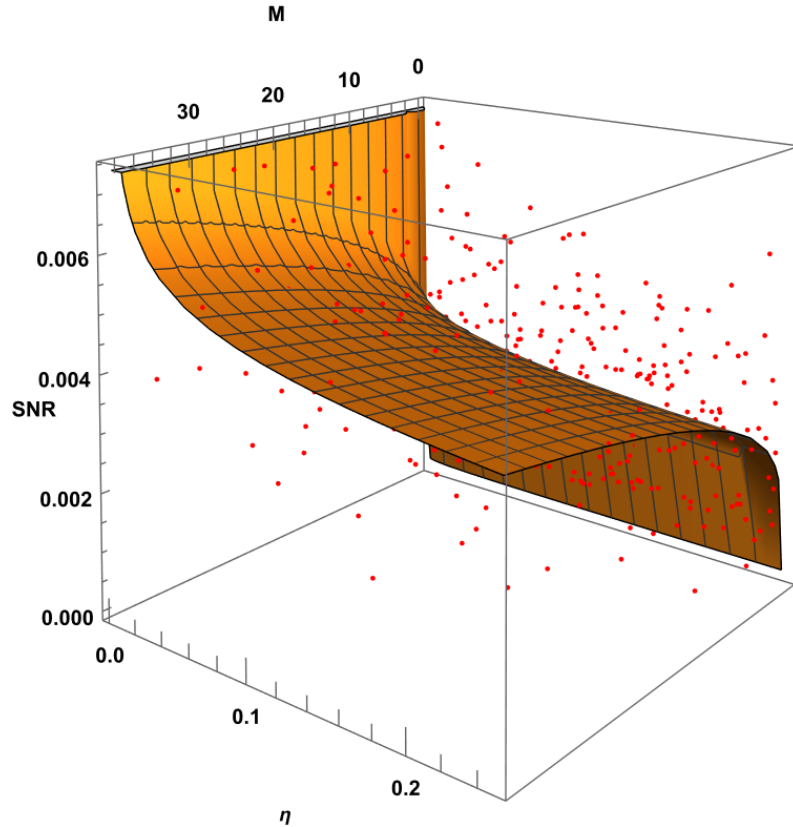


Figure 5.10: Power SNR of NS1 with tensor modes only (ETCE).

Without going into further detail, the scatter caused by the localization uncertainty dominates the simulated data (the red points) in this plot. The

orange sheet is given by a fitting function trying to interpolate the data. In this case it has scarce importance, but it is worth mentioning it now, since it becomes more interesting by adding non-tensor modes to the signal:

$$A \cdot \sin \left[B \cdot (x \cdot \eta^C)^D \right] \cdot \eta^E \cdot x^F \quad (5.6)$$

with $x = M/M_\odot$.

The importance of this fitting function can be understood while adding a scalar mode ($A_S = 1$) to the tensor signal. One sees that, besides the expected increase of the power SNR, the fitting function works almost perfectly. This can be seen at figure (5.12).

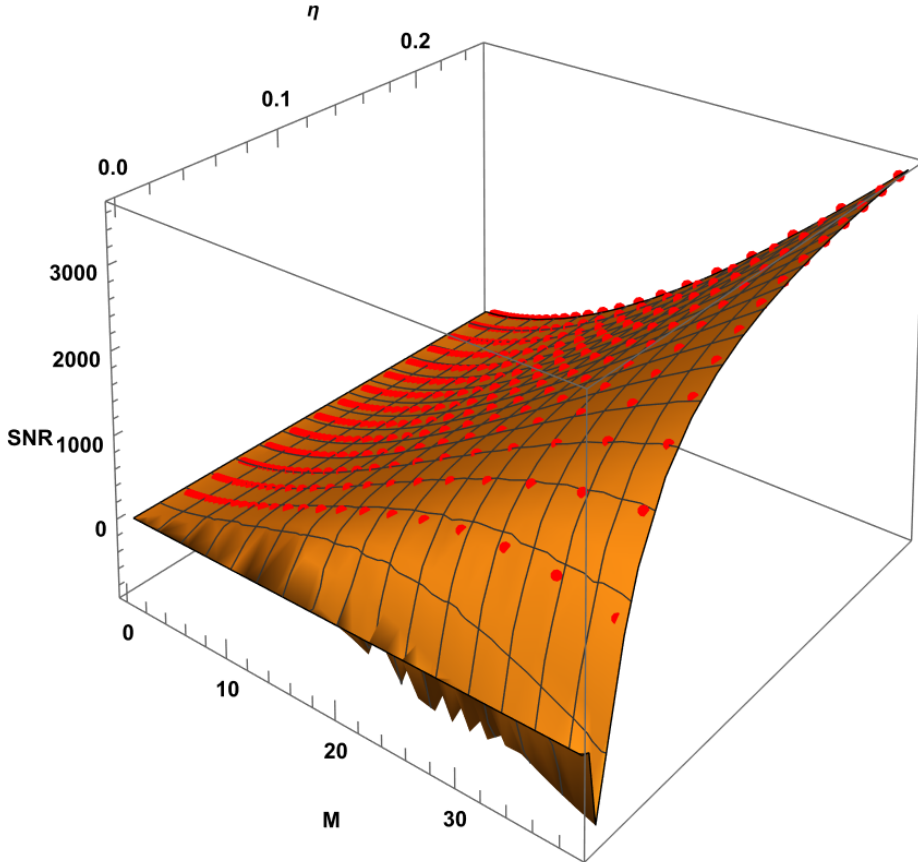


Figure 5.11: Power SNR of NS1 with tensor + S modes (ETCE).

However, for a true understanding of how the fit and the data behave, the results at figure (5.12) can be plotted in a more understandable way, as shown at figure (5.12).

This plot needs no additional comment, since it is clear that the fitting function works very well for the simulated data (represented by dots). the error bars caused by the propagation of the localization uncertainty are smaller than

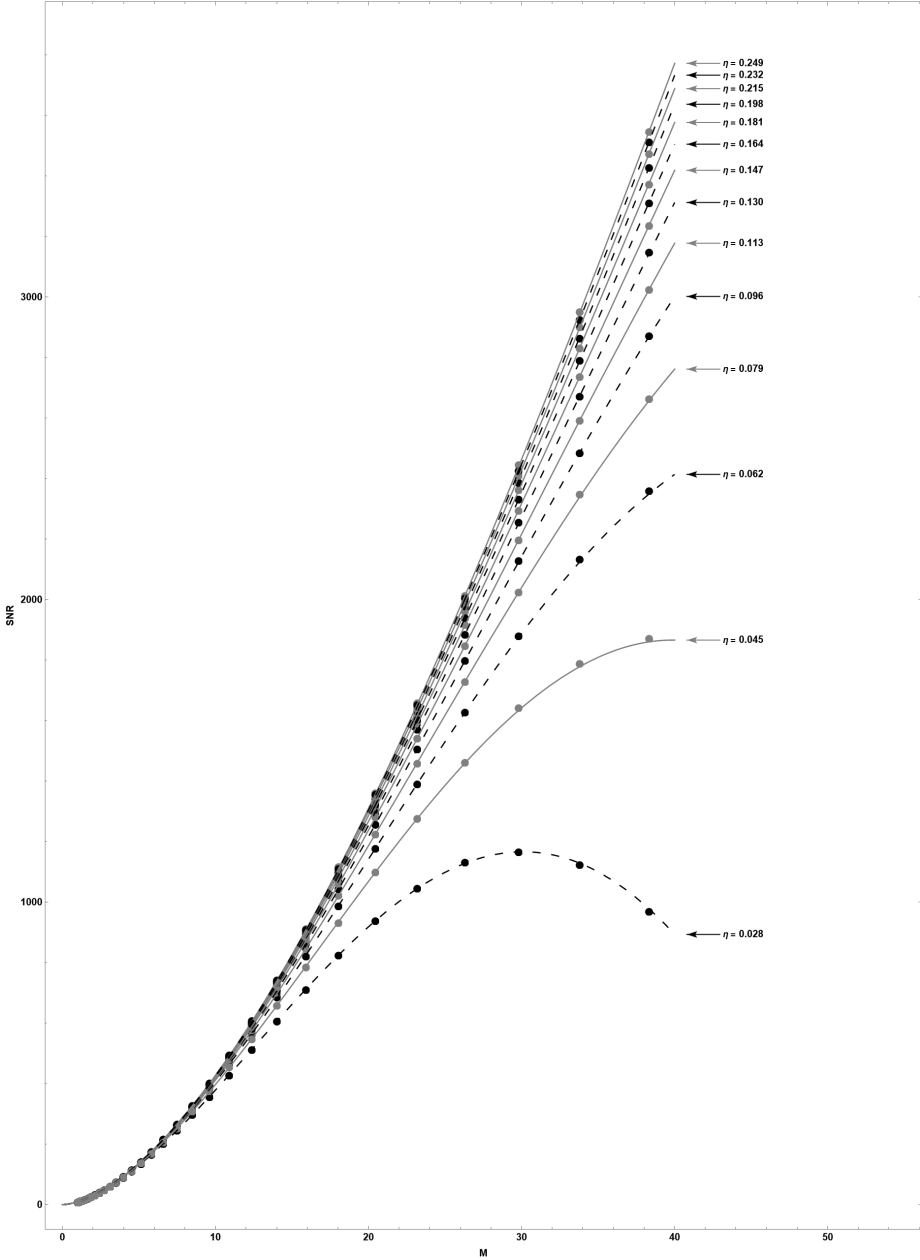


Figure 5.12: Power SNR of NS1 with tensor + S modes (ETCE).

the dimension of the dots. The numerical values of the parameters for equation (5.6) are reported at section A.2 for several cases.

One example of four detector null stream is due, since they are conceptually different from the three detector ones. At figure (5.13) the full dimensional plots for NS2 in the case of tensor, tensor + S and tensor + W signal as seen by ETCE are displayed.

In this case, the fit for the injection of the W mode looks very good too, and

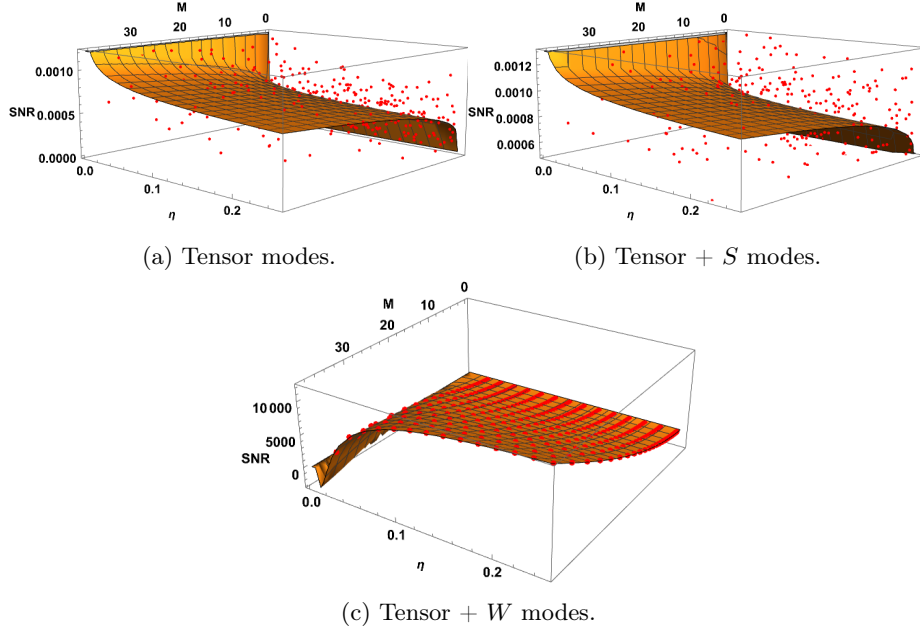


Figure 5.13: Power SNR for NS2 (ETCE).

one can recover a plot equal to figure (5.12), but re-scaled to higher values for the power SNR: it is not displayed here for space sake, but one can get convinced of the goodness of the fit just looking at figure (5.13c). All the other figures are reported at (B.2).

While working with 2G networks, the results do not change by a qualitative point of view, in the sense that NS1 is dominated by the localization uncertainty when tensor modes only are present, same for NS4 with tensor or scalar modes. Nevertheless, the numerical values of the SNRs change, generally resulting in quite lower performances. Furthermore, the fit obtained with the expression at (5.6) becomes way more sloppy in reproducing the behaviour of the simulated data. In the case of HLVKI, figure (5.14) displays a comparison of the response of NS1 with a tensor signal and a tensor + scalar signal respectively.

(5.8).

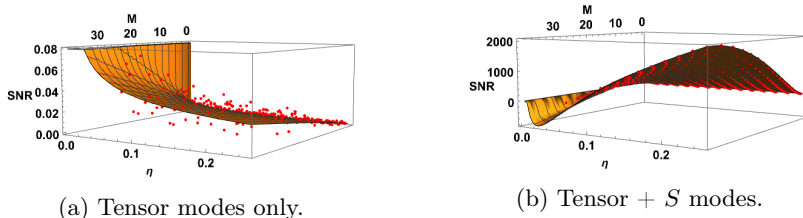


Figure 5.14: Power SNR for NS1 (HLVKI).

Figure (5.14b) clearly shows that the qualitative behaviour is the same as with ETCE, with a difference given by the numerical values of the power SNR, and with a systematic asymmetry of the residuals of the data with respect to the fitting function. The latter aspect can be visualized in a more effective plot (resembling figure (5.12)): this graph is displayed at figure (5.15).

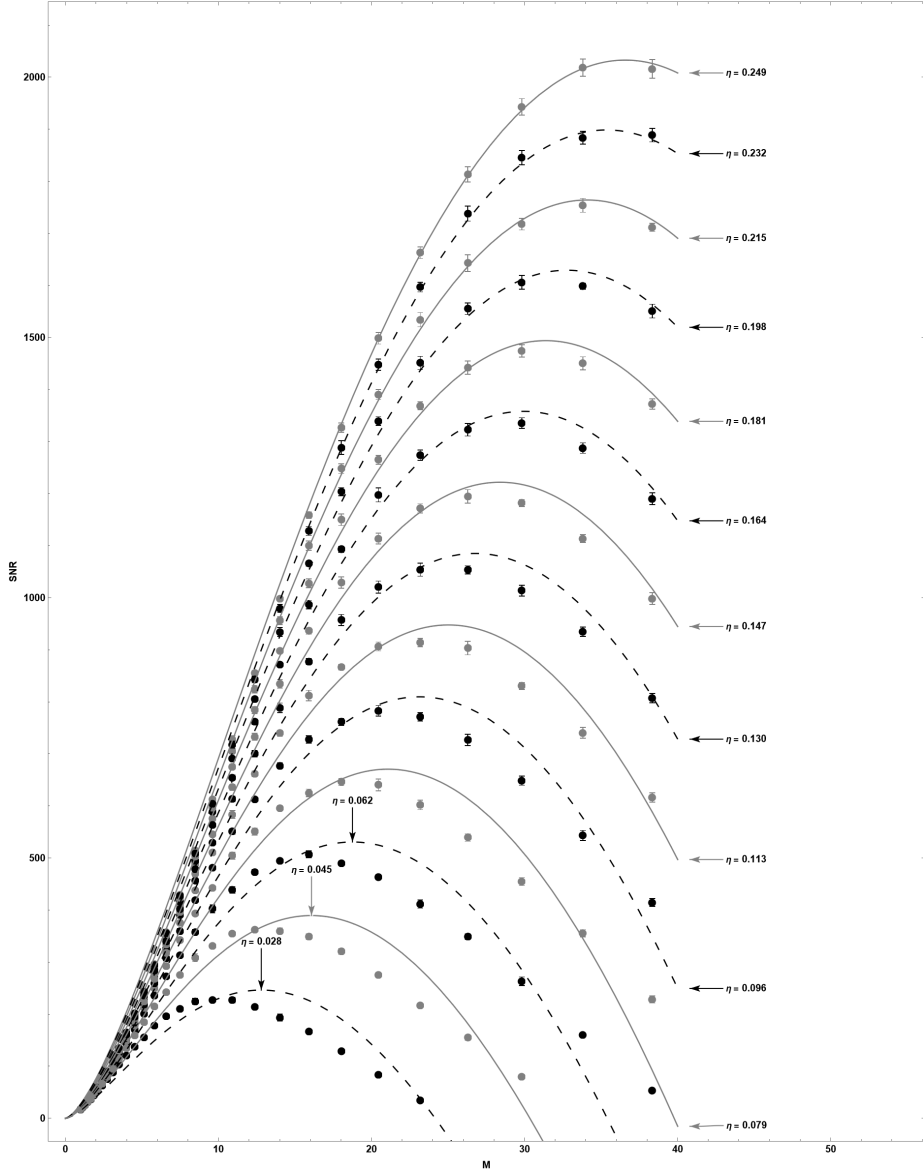


Figure 5.15: Power SNR of NS1 with tensor + S modes (HLVKI).

Of course, the parameters for the expression at (5.6) are expected to change. However, in this case it is the whole function which is no more appropriate for the correct representation of the simulated data. As the plot suggests, the systematic errors shrink as η approaches its maximum value = 0.249. Nevertheless,

the fitting expression can be considered a good proxy for an order of magnitude estimate of the expected behaviour, represented by the data. In this plot, the error bars are very small, but visible.

The behaviour of NS2 is represented at (5.16) , and it needs no other comment than stating the fact that it confirms the qualitative expectations. Also in this case the high SNR case can be reproduced by the chosen fitting function with less accuracy than for ETCE.

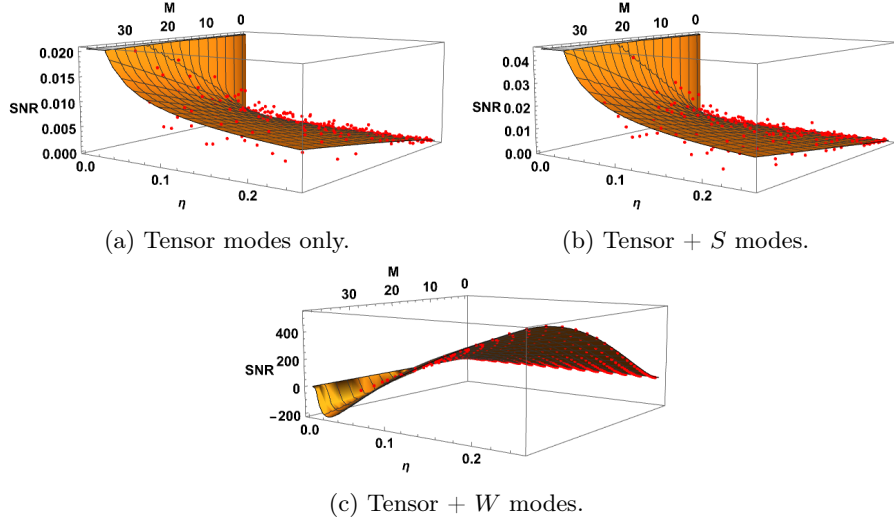


Figure 5.16: Power SNR for NS2 (HLVKI).

As for the ETCE network, the results of NS3 and NS4 mostly follow the expectations as NS1 and NS2 do, being dominated by fluctuations when tensor modes only or tensor and V or W modes respectively are present.

The results for the HLVK network mostly resemble those of HLVKI, including the inaccuracy in the fit of the simulated data, the only differences being a general shrinking of the power SNR numerical values with respect to HLVKI and the systematics already pointed out in the previous paragraph. All the plots regarding this discussion can be found at section B.2.

However, from the plots and tables one can see that there are also few deviations from the behaviour of ETCE. In particular, these deviations correspond to the unexpected behaviours obtained in the previous section. In fact, the scalar mode is awkwardly suppressed by NS1 with HLVKI. Furthermore, the four detector null streams seem not working properly for HLVK.

In general, one should expect the behaviour of the null streams to be followed by the fitting function only when the null stream is expected to be non-zero: this expectation is verified with ETCE. However, as a consequence of the mentioned systematics, the 2G networks do not always fulfill it. Only the succeeded fits are reported at section A.2 and section B.2.

To sum up, the 2G networks seem to work well, despite few awkward features. They have to be characterized by a deeper study accounting for different positions, ψ and inclinations in order to be implemented safely. These outcomes are quite promising since a test of gravity could be performed without having to wait for 3G facilities.

Nevertheless, ETCE works outstandingly better for the given case, but it has to be better characterized too. It is definitely more efficient than the 2G counterparts, providing a more significant test for GR on a wider range of luminosity distance, chirp mass and η . Furthermore, it seems more reliable since it has not shown any awkwardness so far.

At the beginning of this chapter, the localization procedure has been simplified by considering only the tensor contribution of the signal for the parameter estimation. The non-tensor component has been relegated to a mere perturbation. This assumption is coherent with the expectations, since current facilities haven't been able to infer any meaningful result so far. For instance, going back to chapter 3 where GW170817 has been tested for non-tensor content, the search outlined that even for a well localized event, the amplitude of non-tensor modes can not trigger a null stream to significant level. But so, how have the presented results been characterized by dimensionless amplitudes $A_i = 1$? In fact, $A_i = 1$ means $h_{NT}/h_T \sim 1$, thus resembling a contradiction with the previous assumption of very small non-tensor modes. However, this is not a contradiction. In fact, the aim of the obtained numerical results is that of giving a reference power SNR normalized to $A_i = 1$. This quantity can be called SNR_{norm_i} . The results one should expect for a realistic case are bound to the case $A_i \ll 1$, and in general they behave like: $\text{SNR}_i = A_i^2 \cdot \text{SNR}_{norm_i}$. More concisely, the numerical values in this essay provide a standard reference that has to be scaled with the dimensionless amplitude of realistic non-tensor mode contributions.

This section has to be addressed as the most important and most meaningful of the whole work. The results for the power SNR of the null streams as functions of different physical parameters of the CBC have been reported. The main focus is on the luminosity distance while keeping the mass parameters fixed, and then on the mass parameters while keeping $d_L = 100$ Mpc. However, only the most representative and meaningful examples have been displayed in the text. In fact, working with four quantities in the case of four kinds of signal (tensor, tensor+scalar, tensor+ V and tensor+ V), and three networks, one would come up having lots of graphs, which are reported in the appendix. A naive description of the simulated data has been given: for both the dependencies, a fitting function has been found. Unfortunately, these expressions still lack a physical interpretation and understanding. Furthermore, the expression for the power SNR of null streams as a function of \mathcal{M} and η reproduces the simulated data for the 2G networks in a very sloppy way: there is evidence of systematic errors, which slack off as η increases.

Besides the summarized results, also the possibility for an additional work has been presented, as the dependence of the network performances on many CBC parameters hasn't been uncovered yet.

5.3 Three Detector Maps

As the most meaningful results have been reported in the previous section, a secondary subject can be addressed. It is important to observe that, so far, the null streams have been considered only in their position-independent fashion.

In general, a three detector null stream is zero when the GW signal is tensor, while it is not when the signal has some non-tensor contribution. This qualitative argument is position independent, because it is valid independently from the direction of the incoming wave. However, one need observe that, say, the scalar content of a signal may be suppressed due to the scalar mode AP being almost zero at the source location for all the detectors in the network: quite an unfortunate case. More in general, the SNR of a null stream in presence of non-tensor modes is not identically zero, but can reach arbitrarily low values depending on the position of the source, its orbital inclination angle ι and so on. This point has been outlined at the beginning of the previous section and, as aforesaid, the behaviour of the null streams for different positions on the sky is not described here. Another position dependent behaviour is described now, which may lead to additional information when observing GW signals with four facilities simultaneously.

Recovering the expressions at (3.9) (that can be rewritten here in order to ease the understanding of the subsequent calculus):

$$\begin{aligned} P^a S^a &= \delta_{23} S_1 + \delta_{31} S_2 + \delta_{12} S_3 = \\ &= P^b F_b^V h_V + P^c F_c^W h_W + P^d F_d^B (h_B - h_L) \\ Q^f S^f &= \delta_{34} S_2 + \delta_{42} S_3 + \delta_{23} S_4 = \\ &= Q^g F_g^V h_V + Q^i F_i^W h_W + Q^j F_j^B (h_B - h_L) \end{aligned} \quad (5.7)$$

As stated, these quantities are measured with a precision which, in the case of an observable non-tensor component, is dominated by the localization capabilities of the network. Therefore, the left hand terms of both these equations are addressed as known quantities. This couple of equations represents a system of two equations and 3 unknowns, namely h_V , h_W and $(h_B - h_L)$. Is there a way to have a system of two equations and two unknowns? The answer would be yes, if there were some spots on the sky where both $P^j F_j^B$ and $Q^j F_j^B$ vanished simultaneously (these quantities can be shown to be position dependent): thus, signals coming from these spots would have unknown scalar component, but their vector modes would be easy to disentangle. Alternatively, one may want to get rid of the vector V mode: if there were spots in the sky where $P^j F_j^V$ and $Q^j F_j^V$ vanished simultaneously, in such spots one could disentangle the W mode and the scalar contribution. Same if one wanted to get rid of the W mode. The only limitation is given by the fact that the two scalar modes can not be measured independently one another.

Assuming one wants to get rid of the scalar contribution, it has to be $P^j F_j^B = C1 = 0$ and $Q^j F_j^B = C2 = 0$ (where $C1$ and $C2$ are arbitrary names given in order to make notation easier).

Now, one can make the usual simplifying assumption of being at GMST = 0 and the (RA,DEC) space can be sampled with a precision $\sim 1 \text{ deg}^2$. At this point, MAX_{12}^* is defined as the maximum value between $|C1^*|$ and $|C2^*|$, where the * indicates that a quantity is computed at the position (RA*, DEC*). The maximum value that MAX_{12} reaches on the whole (RA,DEC) space is labelled by M . At this point, one can define:

$$\rho^* = \frac{M - \text{MAX}_{12}^*}{M} \quad (5.8)$$

and get convinced that if $\rho^* = 1$, then at $(\text{RA}^*, \text{DEC}^*)$ the two quantities $C1^*$ and $C2^*$ are identically zero. The same procedure can be done if one wants to get rid of one of the two vector modes redefining $C1$ and $C2$.

The behaviour of $1 - \rho$ is displayed at figure (5.17) as a function of (RA, DEC) for the HLVK network.

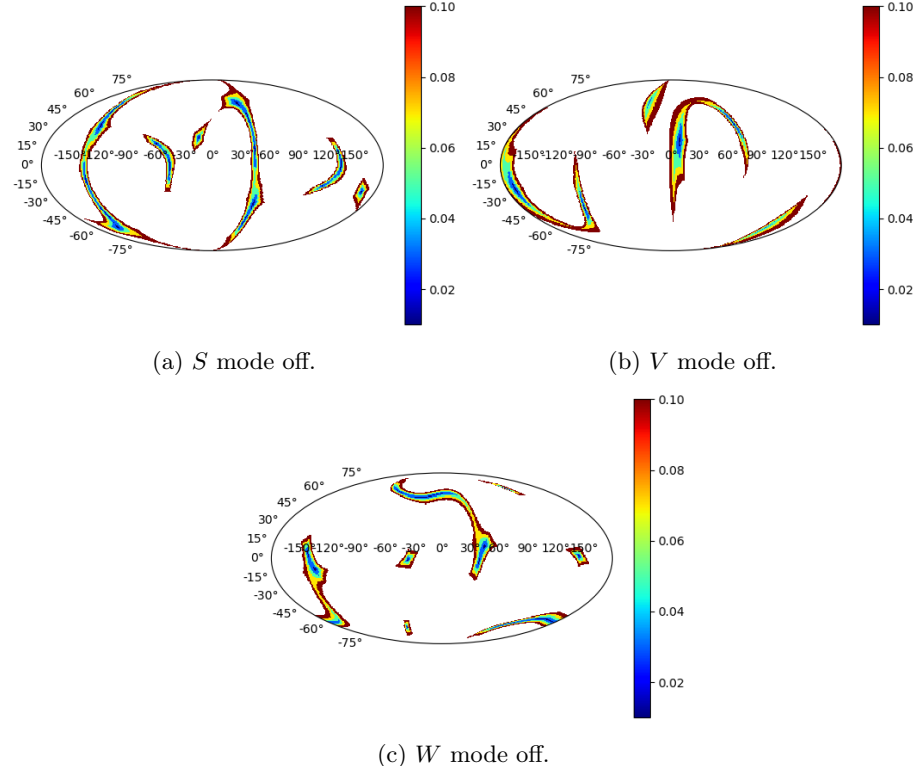


Figure 5.17: Maps for HLVK.

When using LIGO India in a LVKI network, the results are those shown at (B.46). The maps for HVKI, HLKI and HLVI are displayed at (B.47), (B.48) and (B.49) respectively.

For an ETCE network considering two out of the three ET facilities, the obtained results are shown at figures (B.50).

It need be mentioned that the plots for the ETCE newtork do not change when a different combination of ET facilities is considered; namely, only two of the three interferometers in ET have been used, but the results do not change choosing a different couple of ET facilities.

When using all the available ET facilities and only one CE, one gets the results reported at (B.51) and (B.52), for CE North and South respectively. As already stated, one can use up to two ET facilities in one null stream, since they are coaligned.

One can work out a huge number of networks made of four detectors, but only some examples are shown at the appendix.

One last additional argument is that of getting rid of the two vector modes simultaneously. This would make equation (3.9) a redundant system of two

equations and just one unknown. The procedure for obtaining this map is similar to that outlined in the previous lines. In practice, at every location (RA^*, DEC^*) the maximum between C1 and C2 for getting rid of the V mode is given by $M_{12_V}^*$, and similarly $M_{12_W}^*$ for eliminating the W mode. Differently from the previous case, an additional definition is needed: $M_{12_{VW}}^*$, namely the maximum between $M_{12_V}^*$ and $M_{12_W}^*$. At this point, one can proceed defining the overall maximum M_{VW} , and a quantity $\rho_{VW}^* = \frac{M_{VW} - M_{12_{VW}}^*}{M_{VW}}$ so that $\rho_{VW}^* = 1$ means that at (RA^*, DEC^*) one can measure just the scalar contribution. The plots for the spots where V and W vanish simultaneously are displayed at (B.3) together with the other plots of the respective network.

As expected, this stronger requisite makes the maps scarcer, since there are only few and very small regions where it is fulfilled. Of course, one can work out similar plots also for different configurations, like HVKI, HLKI, HLVI and so on. More in general, one may mix 3G and 2G detectors in a sort of hybrid network. This situation has not been treated in the previous section, and it is not addressed now. Nevertheless, it can stand out as one of the natural prosecutions in the field.

This short section comes as an addition to the presented work, showing how one can get rid of two tensor modes and one extra non-tensor mode at given positions by means of three detector null streams. As already stated, this approach is different from that given by the four detector null streams because it is position dependent, while the four detector case gives a measure of zero which works at every position, even if with different numerical outcomes. Furthermore, since in a network of four detectors one can build up to two independent three detector null streams, this position dependent approach allows for a disentanglement of the two remaining modes: this is not possible when using four detector null streams. In this sense, reminding the results from the previous section, the four detector quantities allow for a bigger difference in term of power SNR when comparing GR and non-GR signals. Therefore, they can be addressed as the most powerful tool for claiming the presence of non-tensor polarization modes. However, the three detector approach seems more appropriate for trying to infer some information about the single polarization modes, even though it is clear that its position dependence makes it applicable in very few cases (namely, a GW signal has to come from some preferred positions). Furthermore, the information provided by the three detector method is never enough for directly disentangling all the polarization modes: this would be given by a five detector network. However, in this section it has been neglected the fact that with future facilities, an event may have a great duration. For instance, an observer at the centre of the Earth may see a GW source moving in and out of a spot that allows one to get rid of, say, scalar modes. When the source stays in the spot, it one can infer the vector modes and disentangle them. When the source exits the spot, one can measure the scalar contribution, and disentangle it, since the other modes are already known.

Studying the capabilities of a detector to localize a source in and out of a given spot would be another natural prosecution to this additional section.

Conclusion

The conclusion of this work is proposed in order to give a global view of the presented work, together with a summary of the preliminary notions outlined in the first three chapters.

The script has verged on a tool which could be used for testing the presence of non-tensor modes in GW signals. Such quantities, called null streams, have been defined as functions of the GW signals measured by different detectors in a network of three or four facilities and the APs relative to such facilities.

In order to explain the meaning of the purpose, the methods and the results of the presented work, a few chapters have been dedicated to a formal introduction to the topics. In chapter 1, the main concepts about GWs have been introduced: the gravitational wave equation has been obtained from linearized GR, followed by the illustration of preferential reference frames, the reference frame proper of GW (the TT frame) and the detector frame. After this description of GWs, few pages and computations have been dedicated to the generation of GWs: the quadrupole radiation has been discussed, together with the behaviour of frequency of GWs from a CBC as a function of time. These computations have introduced some very important parameters for CBCs, like the chirp mass and the mass asymmetry term η . Furthermore, also the concept of f_{max} , namely the maximum frequency reached during the inspiral phase, has been introduced at the end of the first chapter. All these concepts are very useful for understanding how GW events are simulated, and which parameters can be changed in order to see a different behaviour in the results.

Secondly, chapter 2 has introduced the real nature of GW detectors: a short treatment about their working principle has been done, together with an informal derivation of their noise curve, by taking into account the most important noise sources affecting the experiments. Such noise curves come up in the work as they are used to define the power SNR of the null streams in the frequency domain. In particular, the main characteristics and problems of current facilities and future ones have been outlined. Furthermore, the APs have been introduced in a formal way as the geometrical consequence of the peculiar shape of the detectors. A comparison between two methods for calculating the APs is reported, namely, that of GWBENCH, the software implemented for performing much of the computations, and that used by professor H. Asada and collaborators. While still being unable to analytically discard one of the two methods, one can find that a peculiar result obtained by B. Schutz can be reproduced by means of GWBENCH only. A definitive proof for which code to choose would be required, but it has not been possible to find it within the pursued work. This can be a first cue for future additional efforts in this subject. Since GWBENCH has been used for parameter estimation in the subsequent chapters, also a quick

introduction to the Fisher formalism, implemented in the code, has been given in order to understand how this software makes it to perform computations where other ones implement Bayesian inference methods.

So far, all the topics have been concerned with GR. However, in chapter 3, the main references to modified theories of gravity can be found. This work does not aim at depicting modified theories of gravity and how non-tensor polarization modes can be found within those theories. Therefore, the main focus of this chapter has been put on the depiction of the APs for five non-tensor modes and the definition of three and four detector null streams. It is easy to argue that, in the realistic situation where the response of each detector is measured and known, the uncertainty on these quantities comes from the propagation of the fluctuation of the APs, which are functions of the source location and the polarization angle ψ . The contribution from the localization errors on this fluctuation has been considered as the main source of uncertainty. In addition, a theoretical definition of the non-tensor strains as a function of the tensor + strain has been given: such definition has not been obtained by means of direct computations; conversely, it has been taken from a paper illustrating the problems of non-tensor signal injection.

As a concluding remark, there is a mention of the main results obtained by Asada and collaborators, finding that the GW event with localization enhanced by its EM counterpart, GW170817, shows no evidence of non-tensor contributions.

As the localization uncertainty has been identified as the responsible of the uncertainty on the null streams, chapter 4 gives a summary of the localization capabilities of different networks. In particular, its focus is on two 2G networks (HLVK and HLVKI) and a 3G network (ETCE). In this chapter, the localization capabilities are treated by means of the sky area (in deg^2) within that one has 90 % of probability of finding the real direction of the GW source. This quantity has been studied as a function of the luminosity distance of the event and its mass parameters, that is, the chirp mass and η .

The main effort for this thesis has been reported in chapter 5. Here, the behaviour of three and four detector null streams in presence of different species of signals has been obtained as a function of the luminosity distance and of the mass parameters. This has been done by simulating GW signals at different distances and with different chirp mass and η . More precisely, a fitting function has been obtained for the power SNR of the null streams in each case. The one with d_L as a variable correctly reproduces the simulated data for all the kinds of signals (tensor, tensor+scalar, tensor+vector of any kind), for all the null streams and all the networks. The fitting function for the mass parameters dependence is appropriate for describing the data of the 3G network, while it is quite sloppy in reproducing those of 2G networks. In general, one finds that the four detector null streams are more effective in discriminating between tensor and non-tensor signals, with the higher reliability obtained with the 3G network ETCE. While marking a step ahead in the characterization of the null streams, the presented approach still misses parts, which can be achieved with further effort in this field. Namely, the dependence of the performances on the sky position, the polarization angle, or the orbit inclination angle ι has not been depicted, even though it has been shown that these parameters generally affect the numerical outcomes of the simulations.

An additional part concerns the fact that the null streams work as discrimi-

nating quantities independently from the position of the GW source. Nevertheless, one can find extra constraints when working with four detectors by means of the three detector null stream approach. Such constraints are position dependent, and allow to get rid of one non-tensor mode on specific spots on the sky. This outcome provides a method for the disentangling of two non-tensor modes, even though it is a method based on the fact that sources have to be localized in special sky regions in order to make it possible, and generally such regions are very small when compared to the whole sky area.

Another cue for a prosecution is given at the end of this section, since this part has been addressed within the assumption of instantaneous GW transients. A time dependent approach to this subject would be mark a step ahead in the understanding of how these quantities behave.

As mentioned many times, the results reported in this thesis come from a code that has been written using GWBENCH: writing this code, and making it work out with different inputs, represented a huge effort. In general, the description of a long code is not the main interest of who the reader, though. Therefore, only a short summary of the main logic behind the code has been given at the beginning of chapter 5. It has been preferred to dedicate part of this essay to the explanation of the conceptual requisites, and the rest in displaying the most representative results.

The wait for third generation facilities is still long and quite hazy; at the same time, the road for advancing current facilities seems nebulous, as some of them are facing huge problems in the fulfilling of more and more stringent requisites. However, there is a lot of preparatory work that must be done in order to understand the full potential of this future instruments. The hope is that this essay may be useful in this perspective by adding new physical arguments and possible outcomes for these detectors, together with spurring further effort in this direction.

Appendix A

Additional Tables

A.1 Fit for Distance Dependence

A.1.1 HLVK

NS	Inj.	A	B
NS1	S	-1.64 \pm 0.03	4.44 \pm 0.07
	V	-1.80 \pm 0.02	5.98 \pm 0.05
	W	-1.75 \pm 0.02	5.15 \pm 0.06
NS2	S	-1.64 \pm 0.04	2.1 \pm 0.1
	V	-1.80 \pm 0.03	3.68 \pm 0.07
	W	-1.77 \pm 0.03	2.89 \pm 0.06
NS3	S	-1.83 \pm 0.02	4.89 \pm 0.06
	V	-1.39 \pm 0.05	2.8 \pm 0.1
	W	-1.72 \pm 0.03	4.42 \pm 0.07
NS4	S	-1.70 \pm 0.02	4.16 \pm 0.06
	V	-1.82 \pm 0.02	5.44 \pm 0.05
	W	-1.75 \pm 0.02	4.52 \pm 0.06

Table A.1: Parameters for equation the linear fit.

NS	Inj.	A	B	C	D
NS1	S	2.9 ± 0.2	1.2 ± 0.07	0.61 ± 0.06	1.1 ± 0.2
	V	4.5 ± 0.2	1.4 ± 0.06	0.4 ± 0.05	1.6 ± 0.1
	W	3.5 ± 0.2	1.3 ± 0.06	0.53 ± 0.05	1.3 ± 0.2
NS2	S	0.2 ± 0.2	1.1 ± 0.06	0.7 ± 0.07	0.8 ± 0.2
	V	1.9 ± 0.2	1.3 ± 0.07	0.5 ± 0.06	1.3 ± 0.2
	W	1.1 ± 0.3	1.3 ± 0.08	0.55 ± 0.07	1.2 ± 0.2
NS3	S	3.3 ± 0.1	1.4 ± 0.05	0.4 ± 0.04	1.5 ± 0.1
	V	1.5 ± 0.2	1.0 ± 0.06	0.76 ± 0.06	0.8 ± 0.2
	W	2.6 ± 0.25	1.2 ± 0.07	0.6 ± 0.07	1.0 ± 0.2
NS4	S	2.6 ± 0.2	1.2 ± 0.06	0.56 ± 0.05	1.2 ± 0.2
	V	4.0 ± 0.2	1.5 ± 0.05	0.37 ± 0.04	1.6 ± 0.1
	W	2.9 ± 0.2	1.3 ± 0.07	0.5 ± 0.06	1.3 ± 0.2

Table A.2: Parameters for equation (5.5).

A.1.2 HLVKI

NS	Inj.	A	B
NS1	S	-0.52 ± 0.06	0 ± 0.2
	V	-1.78 ± 0.02	5.10 ± 0.06
	W	-187 ± 0.03	6.88 ± 0.06
NS2	S	0.2 ± 0.04	-2.6 ± 0.1
	V	-1.80 ± 0.02	4.61 ± 0.05
	W	-1.88 ± 0.03	6.32 ± 0.07
NS3	S	-1.86 ± 0.02	6.57 ± 0.06
	V	-1.87 ± 0.02	7.49 ± 0.06
	W	0.21 ± 0.04	-2.2 ± 0.1
NS4	S	-1.65 ± 0.04	4.22 ± 0.09
	V	0.14 ± 0.04	-1.6 ± 0.1
	W	-1.87 ± 0.03	7.08 ± 0.06

Table A.3: Parameters for the linear fit.

NS	Inj.	A	B	C	D
NS1	<i>S</i>	2.1 ± 0.8	15 ± 10^3	0.03 ± 2	5 ± 11
	<i>V</i>	3.6 ± 0.3	1.36 ± 0.08	0.45 ± 0.07	1.5 ± 0.2
	<i>W</i>	5.6 ± 0.1	1.67 ± 0.06	-0.26 ± 0.03	1.3 ± 0.2
NS2	<i>S</i>	\sim	\sim	\sim	\sim
	<i>V</i>	3.0 ± 0.1	1.36 ± 0.03	0.46 ± 0.03	1.4 ± 0.1
	<i>W</i>	5.1 ± 0.1	1.9 ± 0.2	-0.18 ± 0.06	4.36 ± 0.07
NS3	<i>S</i>	5.27 ± 0.09	1.65 ± 0.05	-0.26 ± 0.03	4.46 ± 0.06
	<i>V</i>	6.2 ± 0.07	1.72 ± 0.05	-0.24 ± 0.02	4.44 ± 0.05
	<i>W</i>	\sim	\sim	\sim	\sim
NS4	<i>S</i>	2.4 ± 0.2	1.10 ± 0.07	0.72 ± 0.07	0.8 ± 0.2
	<i>V</i>	\sim	\sim	\sim	\sim
	<i>W</i>	5.75 ± 0.07	1.66 ± 0.04	-0.26 ± 0.02	4.48 ± 0.05

Table A.4: Parameters for equation (5.5).

A.1.3 ETCE

NS	Inj.	A	B
NS1	<i>S</i>	-1.873 ± 0.009	7.25 ± 0.02
	<i>V</i>	-1.873 ± 0.009	8.63 ± 0.02
	<i>W</i>	-1.873 ± 0.009	8.45 ± 0.02
NS2	<i>S</i>	0.06 ± 0.04	-3.2 ± 0.1
	<i>V</i>	-1.873 ± 0.009	7.57 ± 0.02
	<i>W</i>	-1.873 ± 0.03	7.77 ± 0.02
NS3	<i>S</i>	-1.873 ± 0.009	8.55 ± 0.02
	<i>V</i>	-1.873 ± 0.009	8.55 ± 0.02
	<i>W</i>	0.08 ± 0.04	-3.3 ± 0.1
NS4	<i>S</i>	-1.873 ± 0.009	7.44 ± 0.02
	<i>V</i>	0.03 ± 0.05	-2.8 ± 0.1
	<i>W</i>	-1.873 ± 0.009	8.16 ± 0.02

Table A.5: Parameters for the linear fit.

NS	Inj.	A	B	C	D
NS1	S	7.11 ± 0.02	1.842 ± 0.006	-0.210 ± 0.004	3.73 ± 0.02
	V	8.482 ± 0.005	1.836 ± 0.002	-0.216 ± 0.001	3.755 ± 0.006
	W	8.29 ± 0.005	1.835 ± 0.002	-0.217 ± 0.001	3.758 ± 0.005
NS2	S	\sim	\sim	\sim	\sim
	V	7.418 ± 0.005	1.8352 ± 0.001	-0.217 ± 0.001	3.757 ± 0.005
	W	7.621 ± 0.005	1.834 ± 0.002	$0.0-0.217 \pm 0.001$	3.759 ± 0.005
NS3	S	7.903 ± 0.006	1.837 ± 0.002	-0.214 ± 0.002	3.749 ± 0.007
	V	8.402 ± 0.005	1.836 ± 0.002	-0.216 ± 0.001	3.755 ± 0.005
	W	\sim	\sim	\sim	\sim
NS4	S	7.288 ± 0.005	1.834 ± 0.002	-0.218 ± 0.001	3.762 ± 0.005
	V	-2.77 ± 0.04	0.03 ± 0.02	2.3 ± 0.9	-0.6 ± 3
	W	8.008 ± 0.005	1.837 ± 0.002	-0.215 ± 0.001	3.751 ± 0.006

Table A.6: Parameters for equation (5.5).

A.2 Fit for Chirp Mass and η Dependence

A.2.1 HLVK

NS	Inj.	A	$B \cdot 10$	$C \cdot 10$	$D \cdot 10$	$E \cdot 10$	F
NS1	S	1.4 ± 0.8	3 ± 1	-4.79 ± 0.08	5 ± 1	4.9 ± 0.8	1.0 ± 0.2
	V	20 ± 10	3 ± 1	-0.484 ± 0.07	4.9 ± 0.9	4.8 ± 0.7	1.0 ± 0.2
	W	4 ± 2	3 ± 2	-0.484 ± 0.07	4.9 ± 0.9	4.9 ± 0.8	1.0 ± 0.2
NS2	S	$3 \cdot 10^{-4} \pm 2 \cdot 10^{-4}$	3 ± 1	-4.84 ± 0.8	5.0 ± 0.9	4.8 ± 0.8	1.0 ± 0.2
	V	0.1 ± 1	3 ± 1	-4.84 ± 0.07	4.9 ± 0.9	4.7 ± 0.8	1.0 ± 0.2
	W	0.005 ± 0.003	0.9 ± 0.3	-4.78 ± 0.09	7.4 ± 0.7	6.7 ± 0.5	0.6 ± 0.1
NS3	S	1.7 ± 0.9	3 ± 1	-4.82 ± 0.07	4.9 ± 0.9	4.8 ± 0.8	1.0 ± 0.2
	V	0.07 ± 0.07	3 ± 3	-4.6 ± 0.1	5 ± 2	4 ± 1	1.00 ± 0.3
	W	0.9 ± 0.5	3 ± 1	-0.484 ± 0.07	5 ± 1	4.8 ± 0.8	1.00 ± 0.2
NS4	S	0.5 ± 0.3	0.3 ± 0.1	-4.80 ± 0.08	5 ± 1	4.9 ± 0.8	1.0 ± 0.2
	V	6 ± 3	3 ± 1	-4.84 ± 0.07	4.9 ± 0.9	4.8 ± 0.7	1.0 ± 0.2
	W	1 ± 0.6	3 ± 1	-4.84 ± 0.08	5 ± 1	4.9 ± 0.8	1.0 ± 0.2

Table A.7: Parameters for equation (5.6).

A.2.2 HLVKI

NS	Inj.	A	B · 10	C · 10	D · 10	E · 10	F
NS1	<i>S</i>	~	~	~	~	~	~
	<i>V</i>	3.2 ± 2	3 ± 1	-4.83 ± 0.07	5 ± 1	4.8 ± 0.8	1.0 ± 0.2
	<i>W</i>	140 ± 80	3 ± 1	-4.83 ± 0.07	4.9 ± 0.9	4.8 ± 0.7	1.0 ± 0.2
NS2	<i>S</i>	~	~	~	~	~	~
	<i>V</i>	1.0 ± 0.5	3 ± 1	-4.84 ± 0.07	4.9 ± 0.9	4.8 ± 0.7	1.0 ± 0.2
	<i>W</i>	40 ± 20	3 ± 1	-4.82 ± 0.07	4.9 ± 0.9	4.8 ± 0.7	1.0 ± 0.2
NS3	<i>S</i>	70 ± 40	3 ± 1	-4.83 ± 0.07	4.9 ± 0.9	4.8 ± 0.7	1.0 ± 0.2
	<i>V</i>	500 ± 300	3 ± 1	-5.00 ± 0.08	5 ± 1	4.6 ± 0.9	1.0 ± 0.2
	<i>W</i>	~	~	~	~	~	~
NS4	<i>S</i>	0.7 ± 0.4	3 ± 2	-5.99 ± 0.01	8.60 ± 0.02	5.32 ± 0.01	0.776 ± 0.003
	<i>V</i>	~	~	~	~	~	~
	<i>W</i>	200 ± 100	3 ± 1	-4.83 ± 0.07	4.9 ± 0.9	4.8 ± 0.7	1.0 ± 0.2

Table A.8: Parameters for equation (5.6).

A.2.3 ETCE

NS	Inj.	A/100	B · 100	C · 10	D · 10	E · 10	F
NS1	<i>S</i>	4.60 ± 0.2	2.1 ± 0.1	-5.97 ± 0.02	8.26 ± 0.06	5.02 ± 0.04	0.831 ± 0.007
	<i>V</i>	46.00 ± 3	4.7 ± 0.2	-6.30 ± 0.03	6.79 ± 0.09	4.04 ± 0.07	1.01 ± 0.01
	<i>W</i>	32.00 ± 2	4.3 ± 0.2	-6.26 ± 0.03	6.93 ± 0.08	4.13 ± 0.06	0.99 ± 0.01
NS2	<i>S</i>	~	~	~	~	~	~
	<i>V</i>	9.2 ± 0.2	2.27 ± 0.05	-6.10 ± 0.01	8.05 ± 0.04	4.97 ± 0.02	0.842 ± 0.004
	<i>W</i>	18.0 ± 0.4	1.88 ± 0.03	-5.98 ± 0.01	8.43 ± 0.03	5.17 ± 0.02	0.803 ± 0.004
NS3	<i>S</i>	17.7 ± 0.7	3.28 ± 0.1	-6.16 ± 0.02	7.41 ± 0.06	4.48 ± 0.05	0.929 ± 0.007
	<i>V</i>	39 ± 2	4.5 ± 0.2	-6.29 ± 0.03	6.82 ± 0.09	4.05 ± 0.07	1.00 ± 0.01
	<i>W</i>	~	~	~	~	~	~
NS4	<i>S</i>	9.7 ± 0.2	1.7 ± 0.2	-5.99 ± 0.01	8.60 ± 0.02	5.32 ± 0.01	0.776 ± 0.003
	<i>V</i>	~	~	~	~	~	~
	<i>W</i>	19 ± 1	3.8 ± 0.2	-6.23 ± 0.02	7.14 ± 0.07	4.30 ± 0.05	0.96 ± 0.01

Table A.9: Parameters for equation (5.6).

Appendix B

Additional Plots

B.1 Distance Evolution Plots

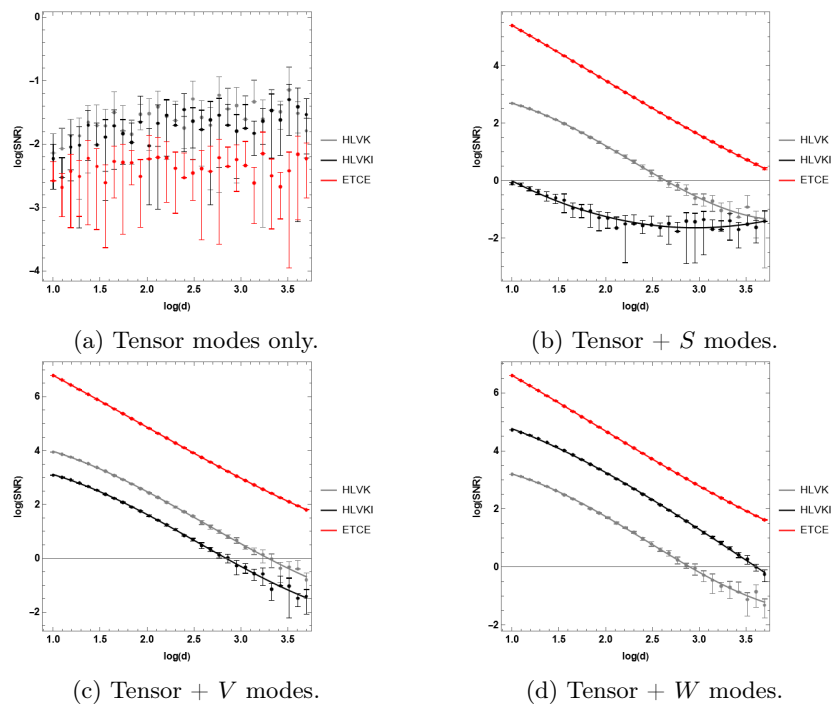


Figure B.1: Distance dependence plots for NS1.

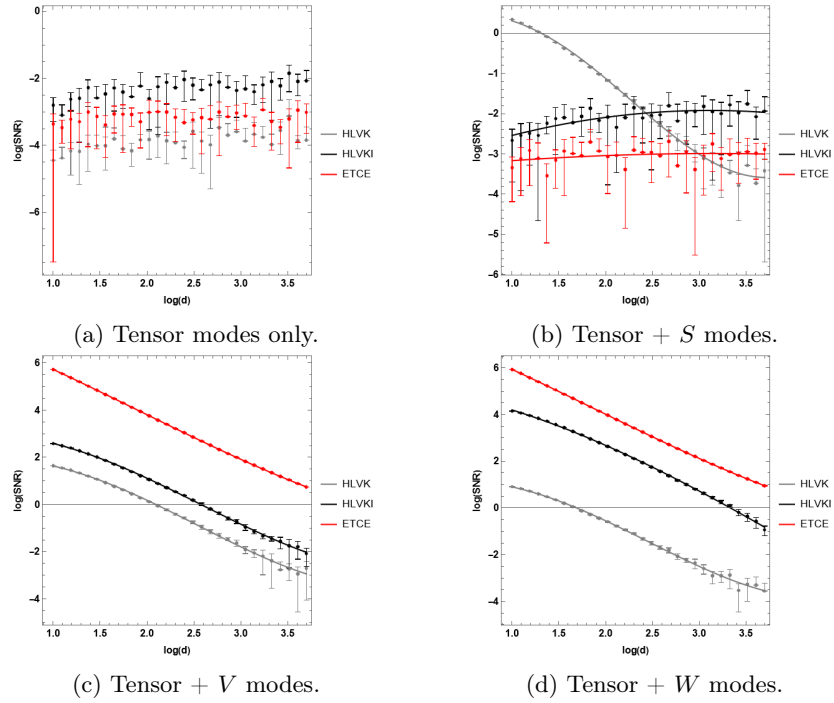


Figure B.2: Distance dependence plots for NS2.

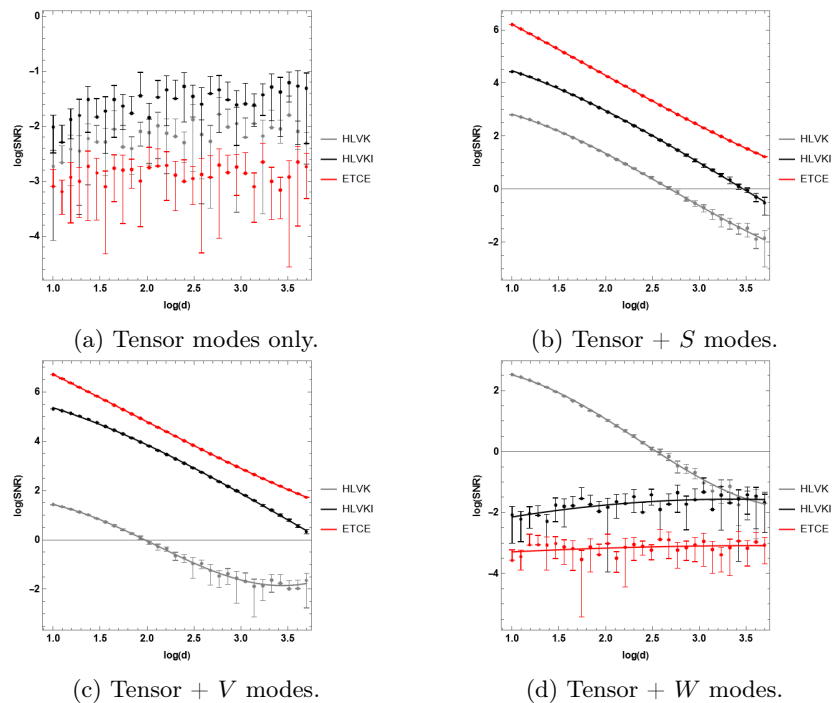


Figure B.3: Distance dependence plots for NS3.

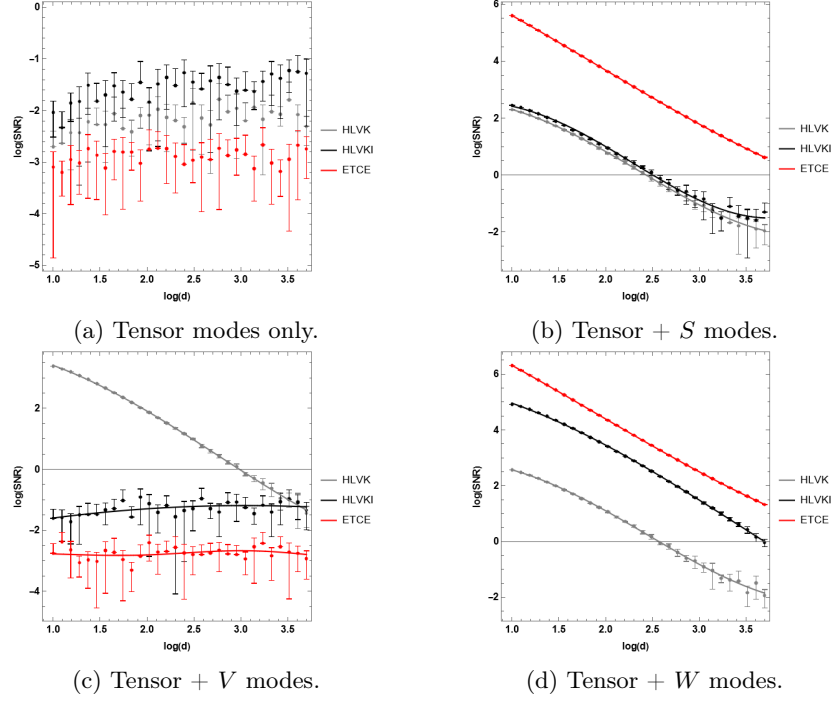


Figure B.4: Distance dependence plots for NS4.

B.2 Chirp Mass and η Evolution Plots

B.2.1 3D Plots

HLVK

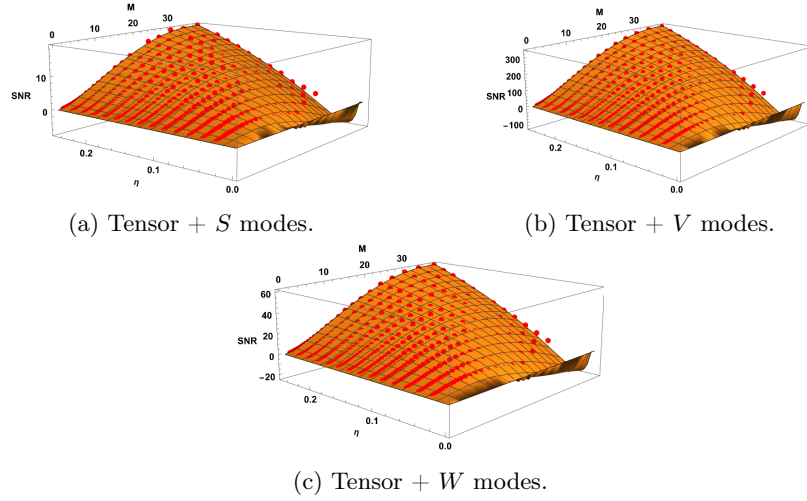


Figure B.5: Power SNR for NS1.

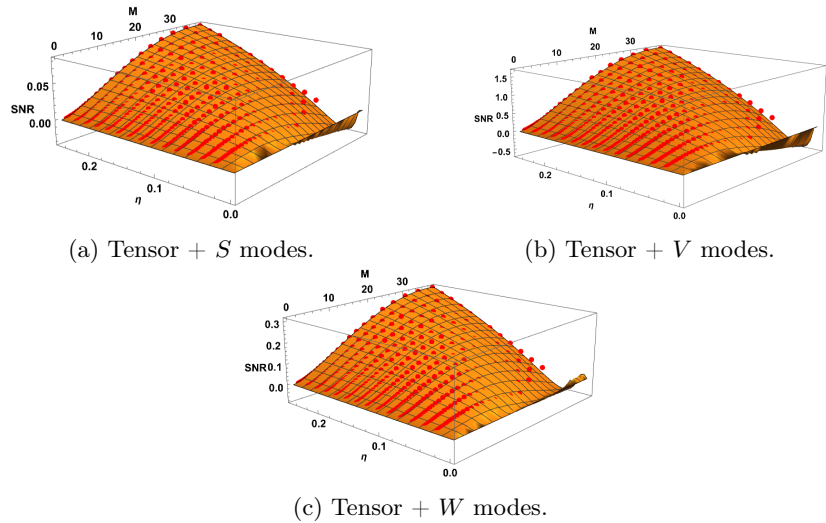


Figure B.6: Power SNR for NS2.

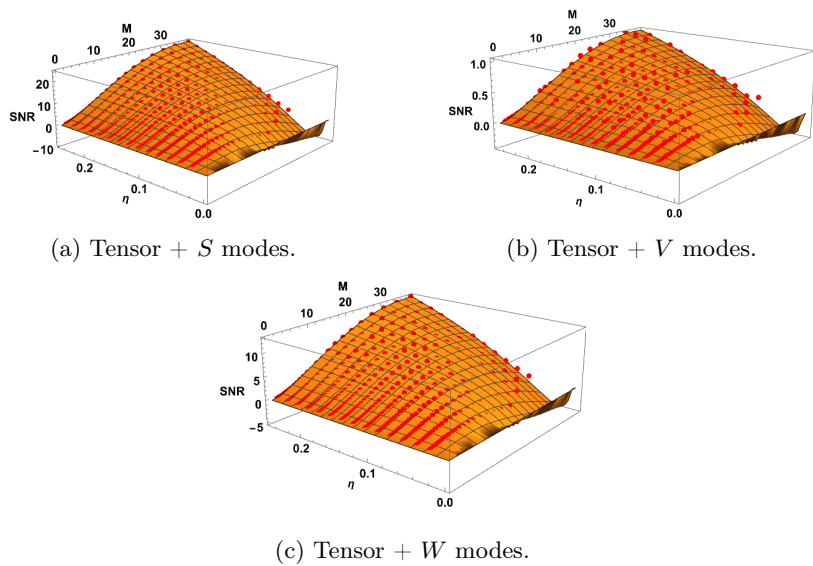


Figure B.7: Power SNR for NS3.

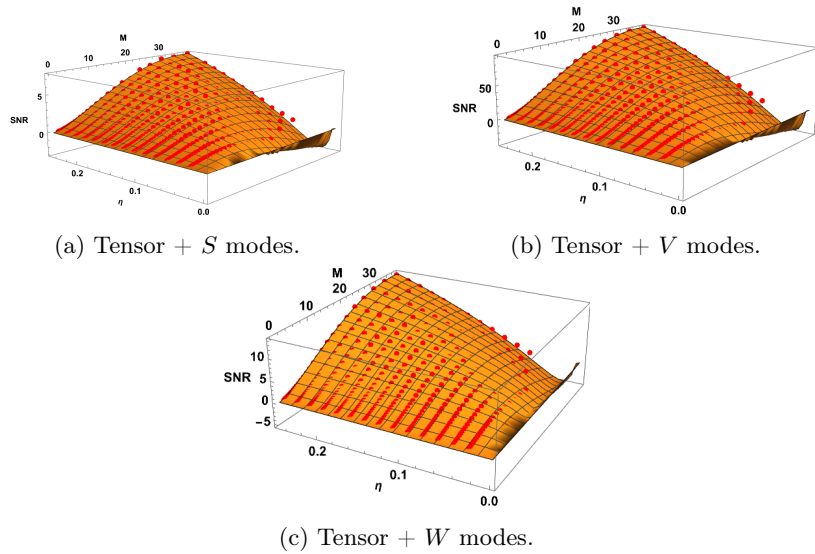


Figure B.8: Power SNR for NS4.

HLVKI

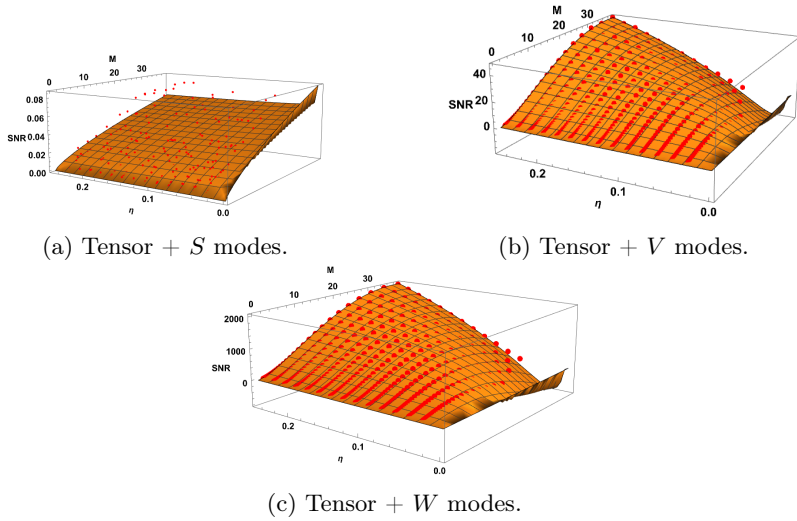


Figure B.9: Power SNR for NS1.

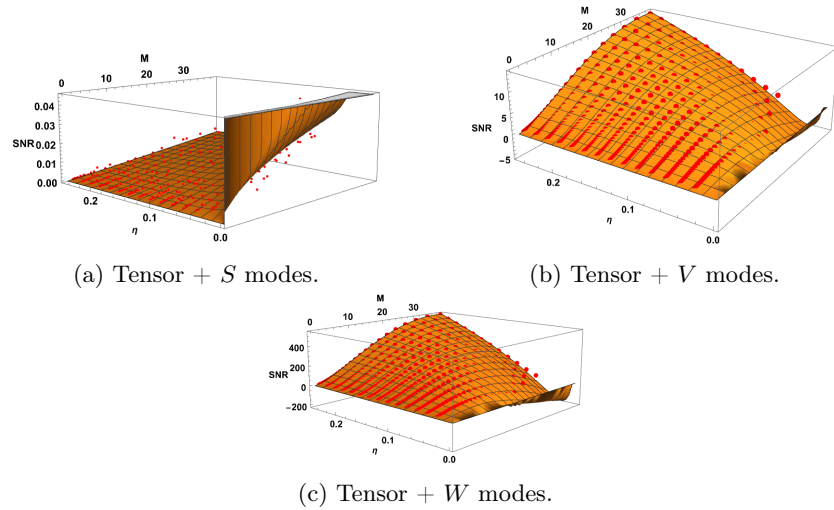


Figure B.10: Power SNR for NS2.

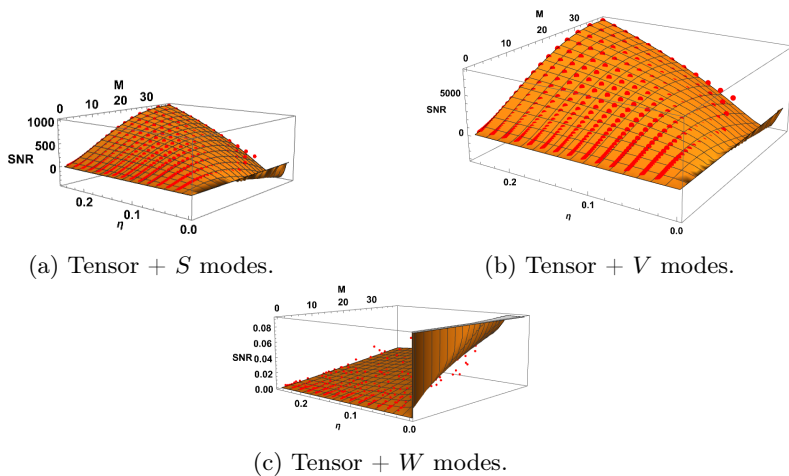


Figure B.11: Power SNR for NS3.

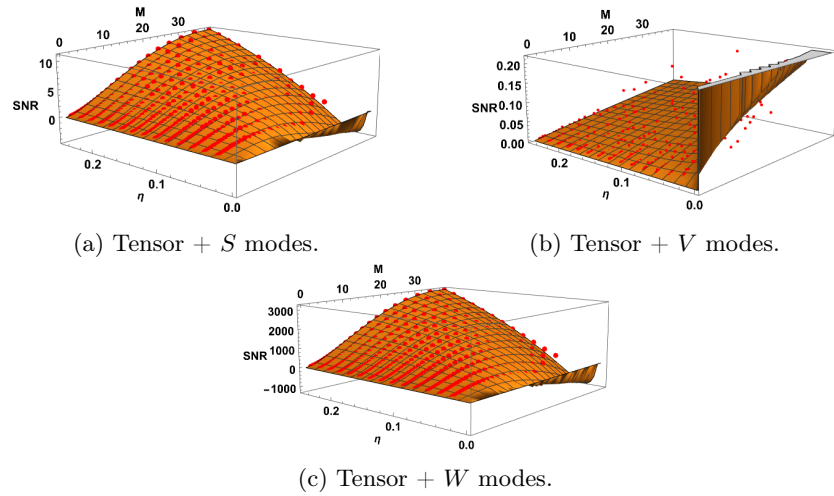


Figure B.12: Power SNR for NS4.

ETCE

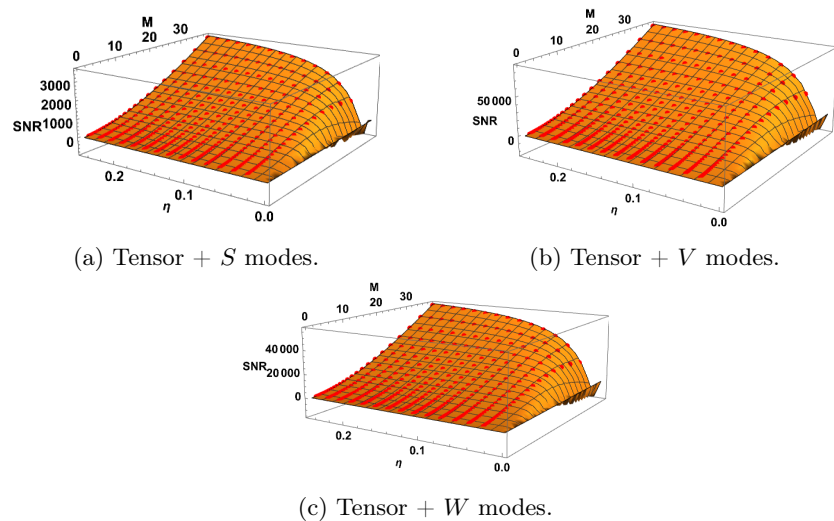


Figure B.13: Power SNR for NS1.

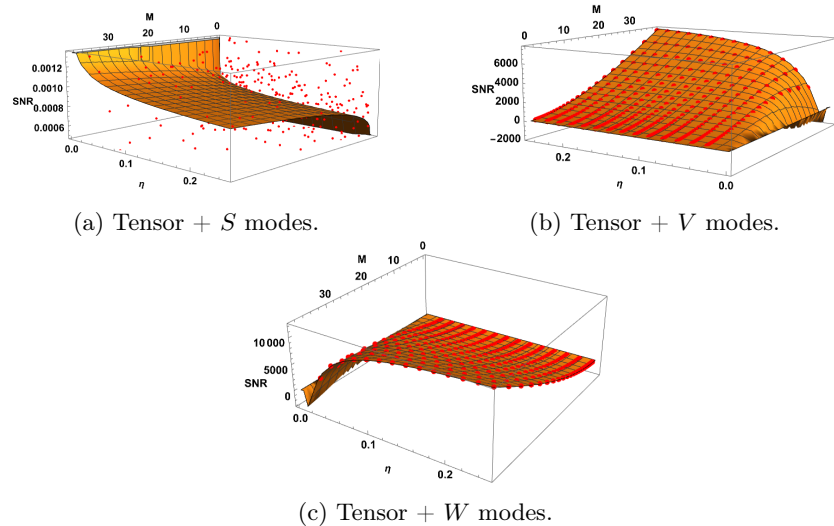


Figure B.14: Power SNR for NS2.

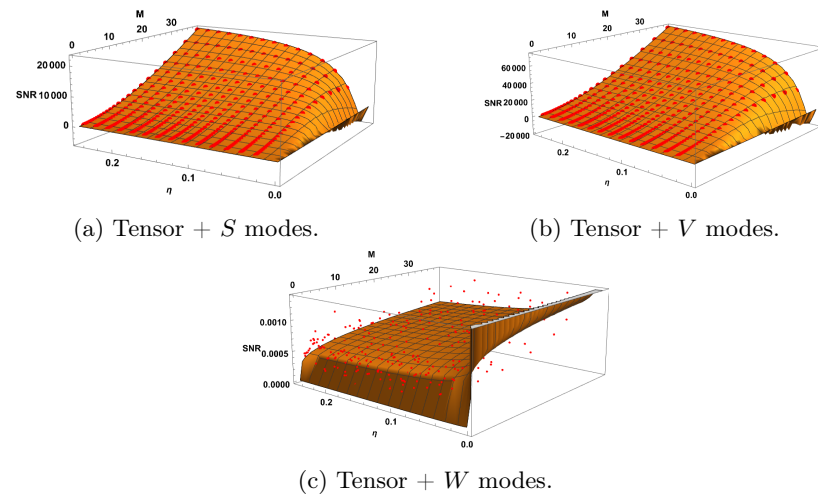


Figure B.15: Power SNR for NS3.

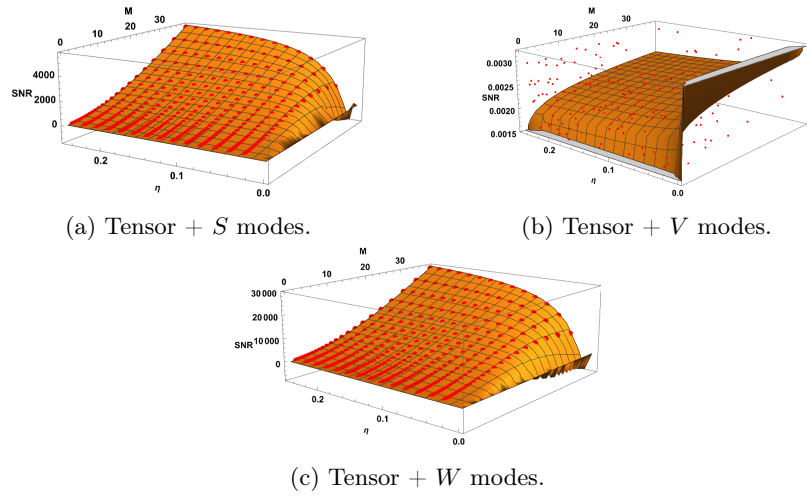


Figure B.16: Power SNR for NS4.

B.2.2 2D Plots

HLVK

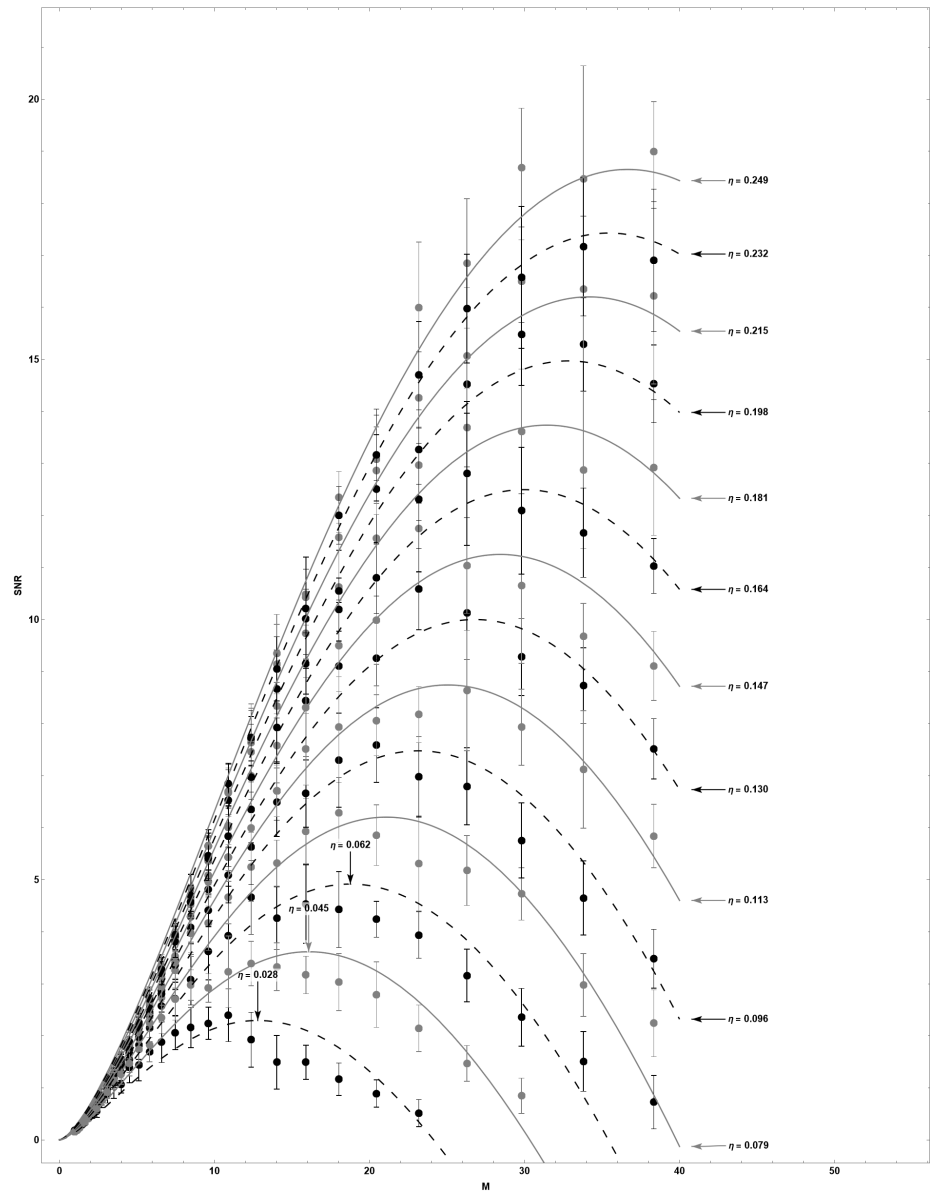


Figure B.17: Power SNR of NS1 with tensor + S modes.

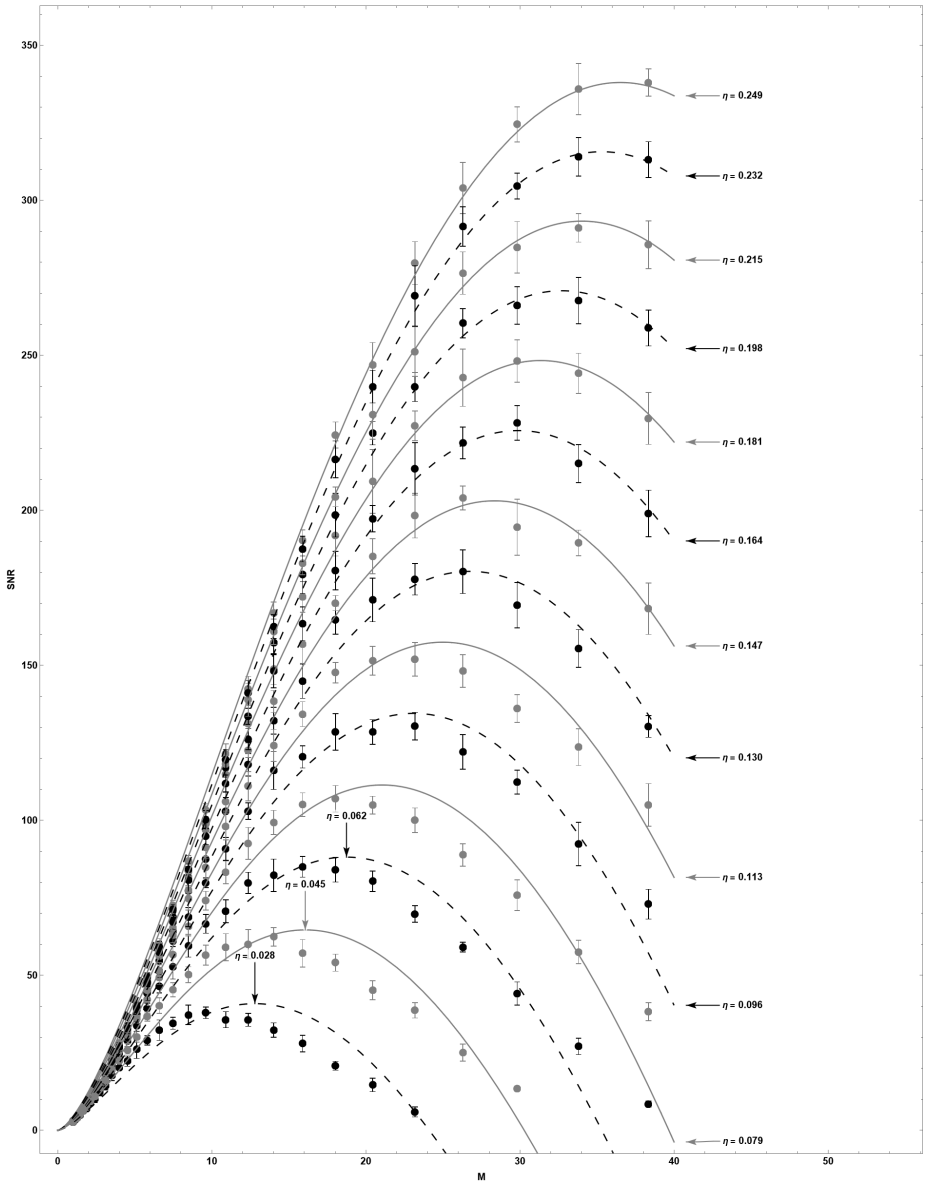


Figure B.18: Power SNR of NS1 with tensor + V modes.

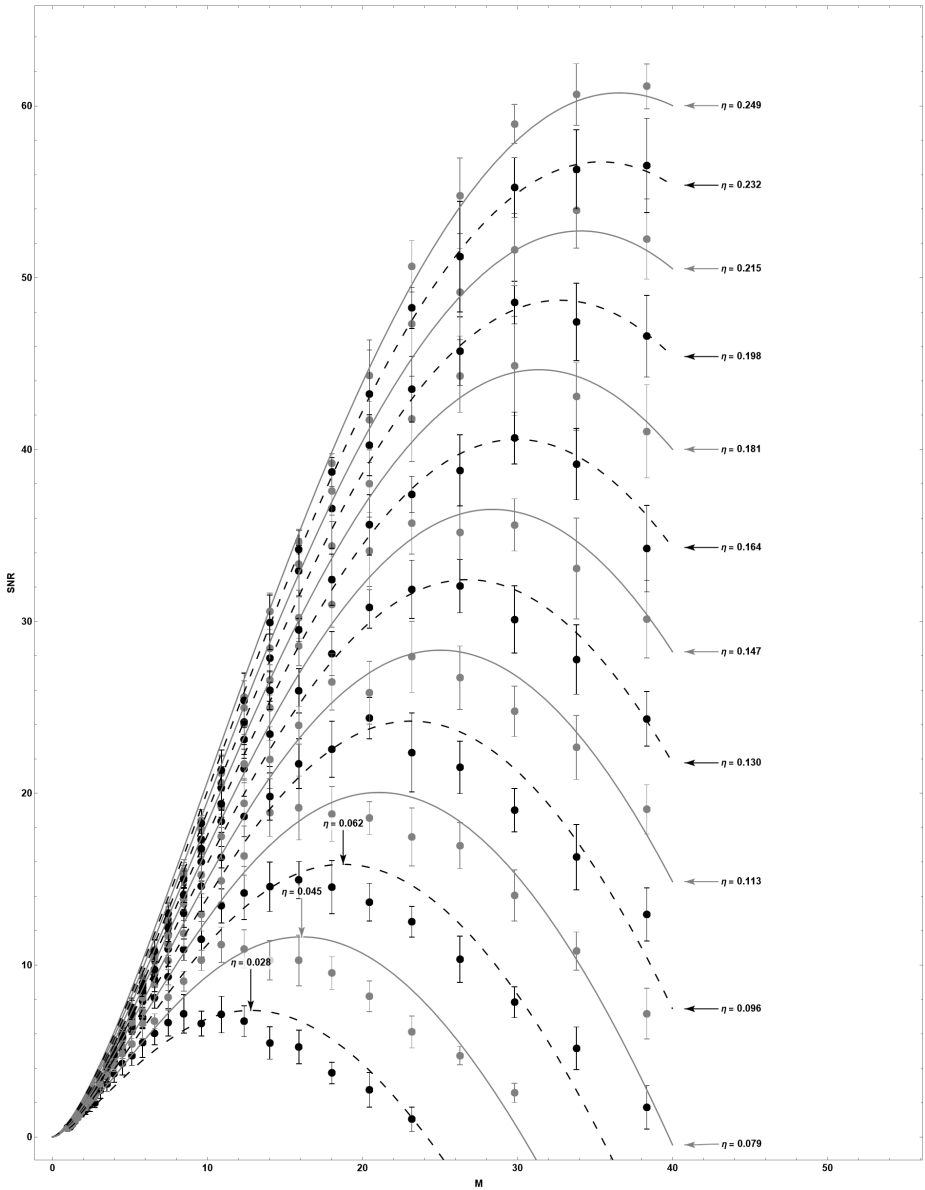


Figure B.19: Power SNR of NS1 with tensor + W modes.

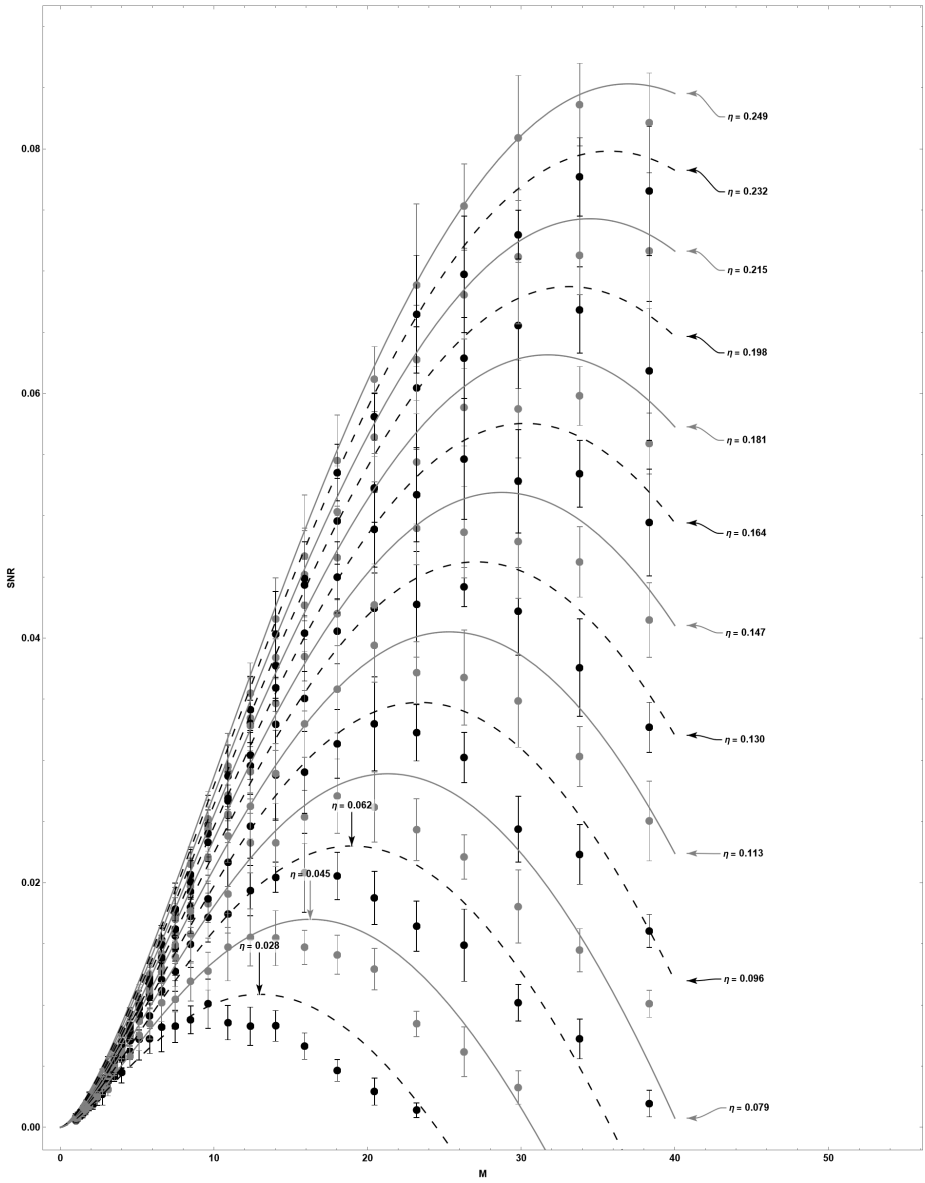


Figure B.20: Power SNR of NS2 with tensor + S modes.

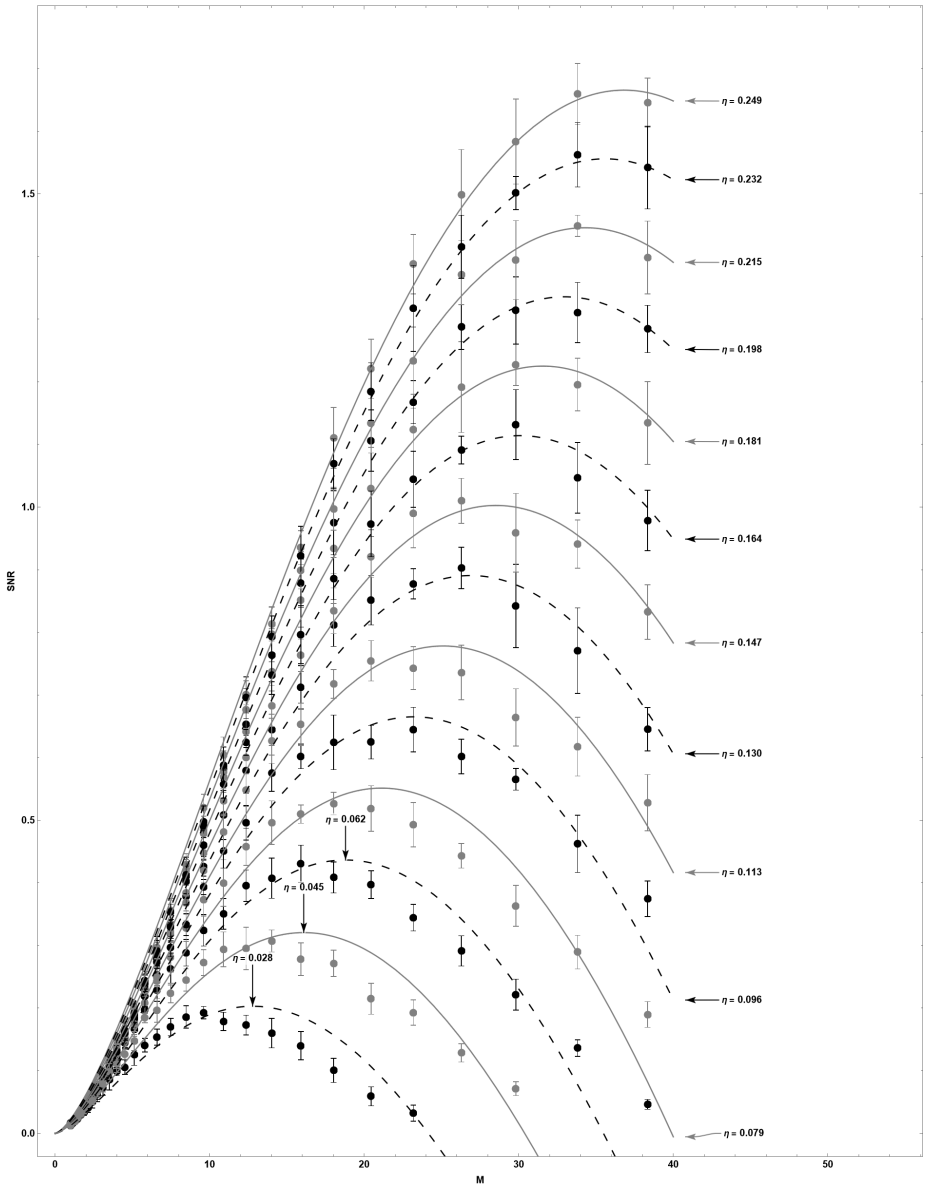


Figure B.21: Power SNR of NS2 with tensor + V modes.

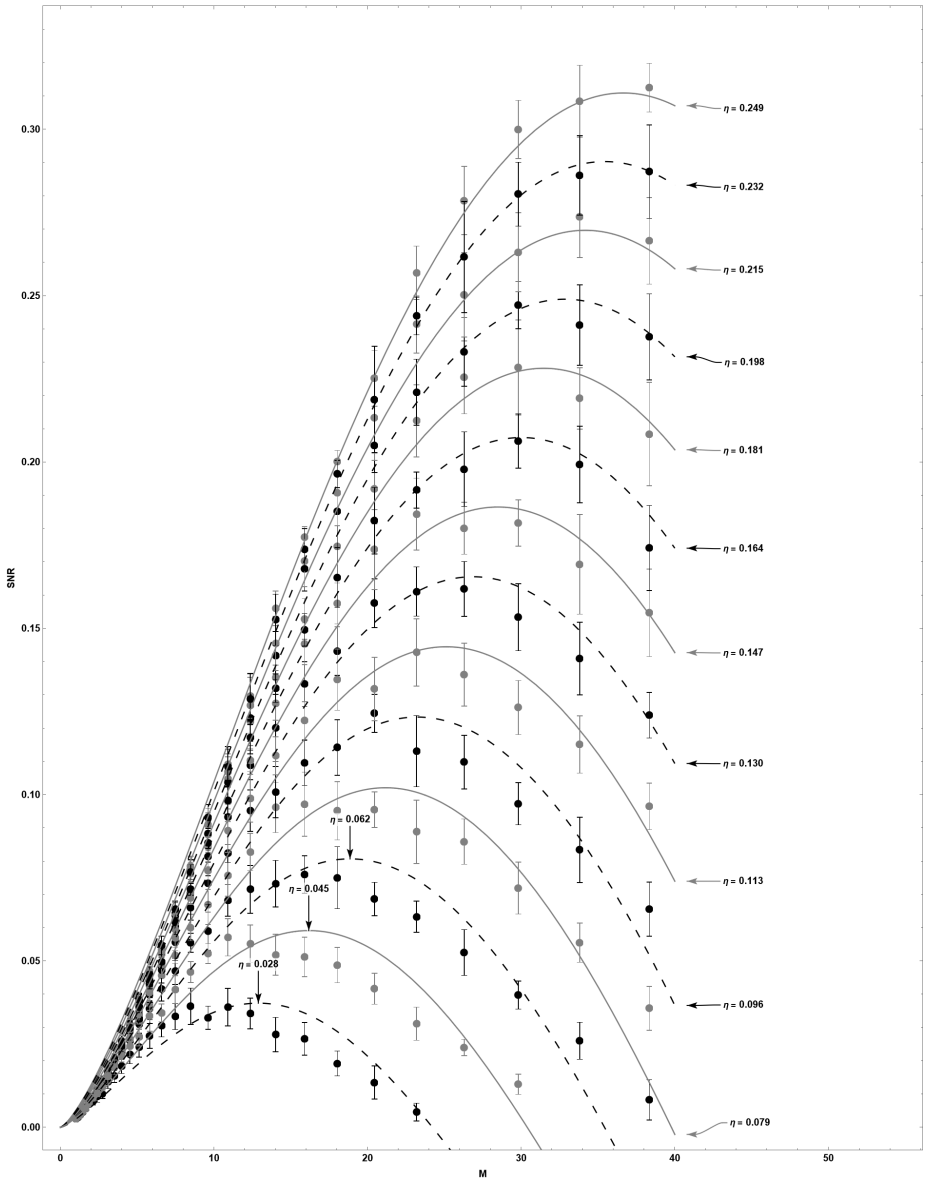


Figure B.22: Power SNR of NS2 with tensor + W modes.

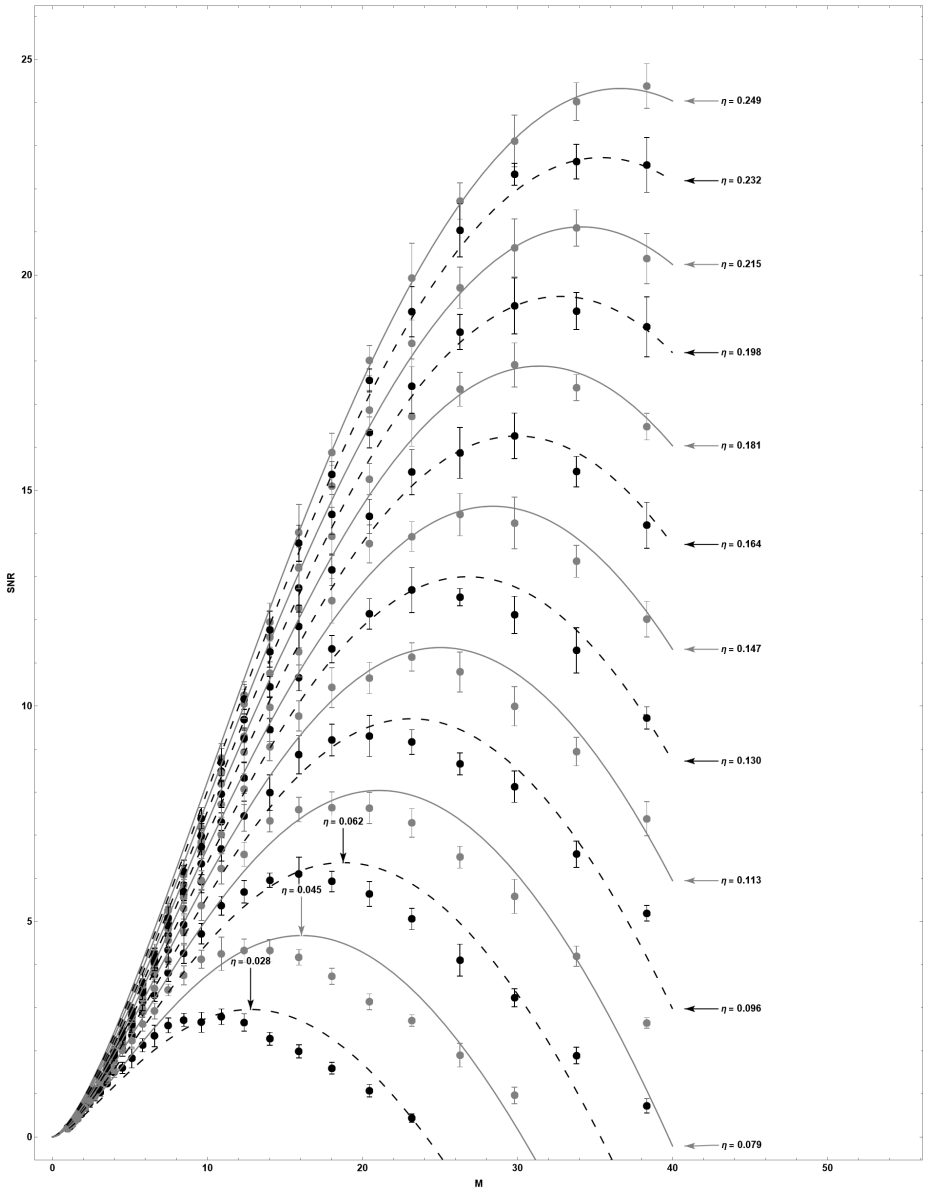


Figure B.23: Power SNR of NS3 with tensor + S modes.

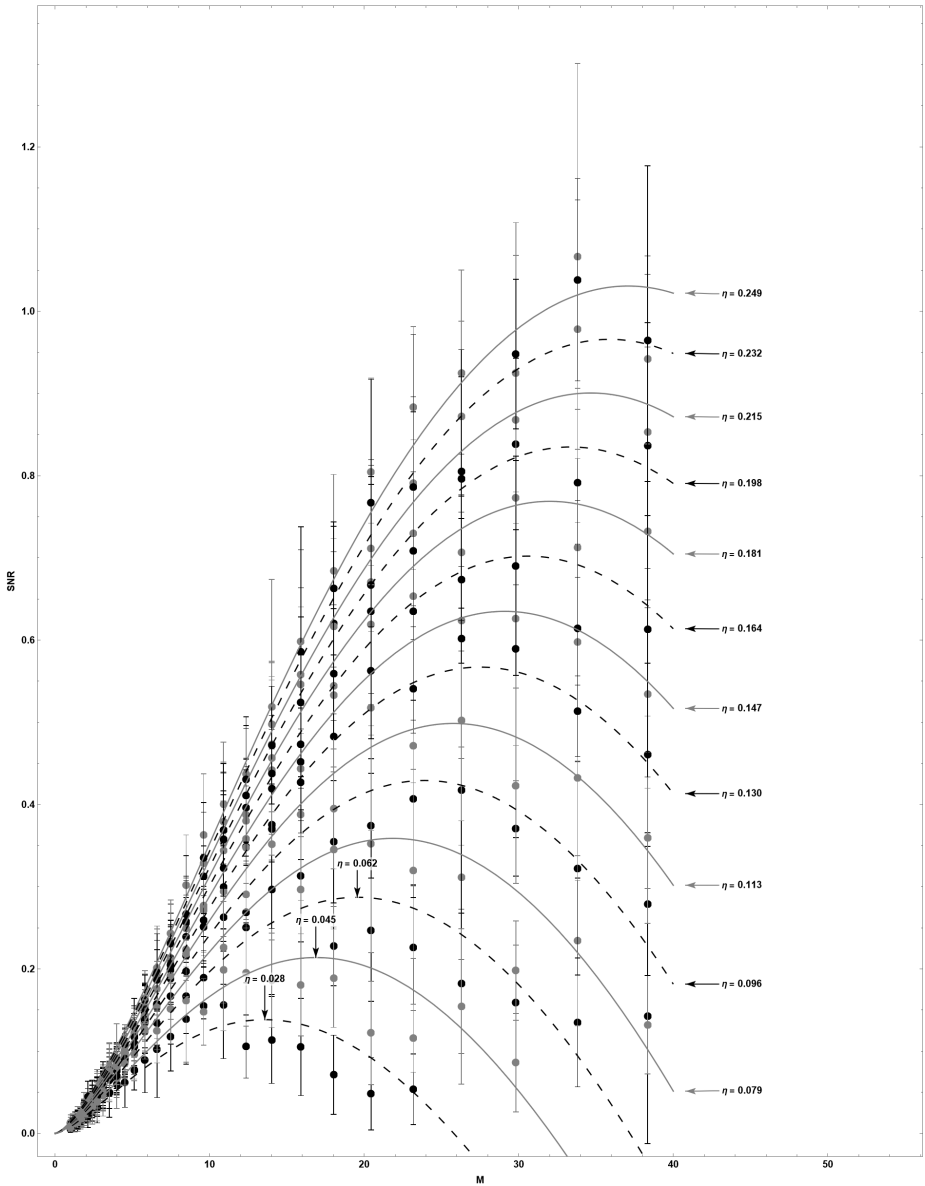


Figure B.24: Power SNR of NS3 with tensor + V modes.

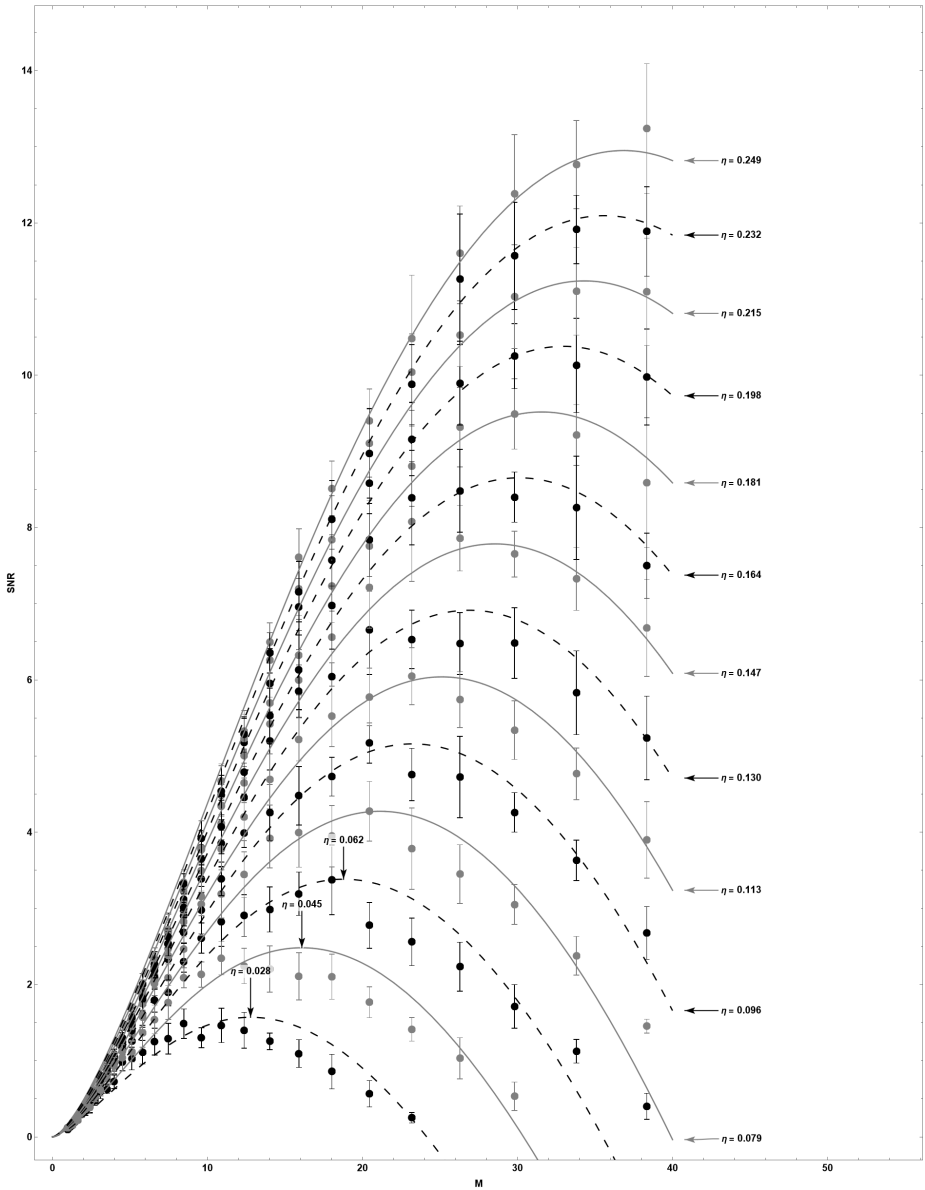


Figure B.25: Power SNR of NS3 with tensor + W modes.

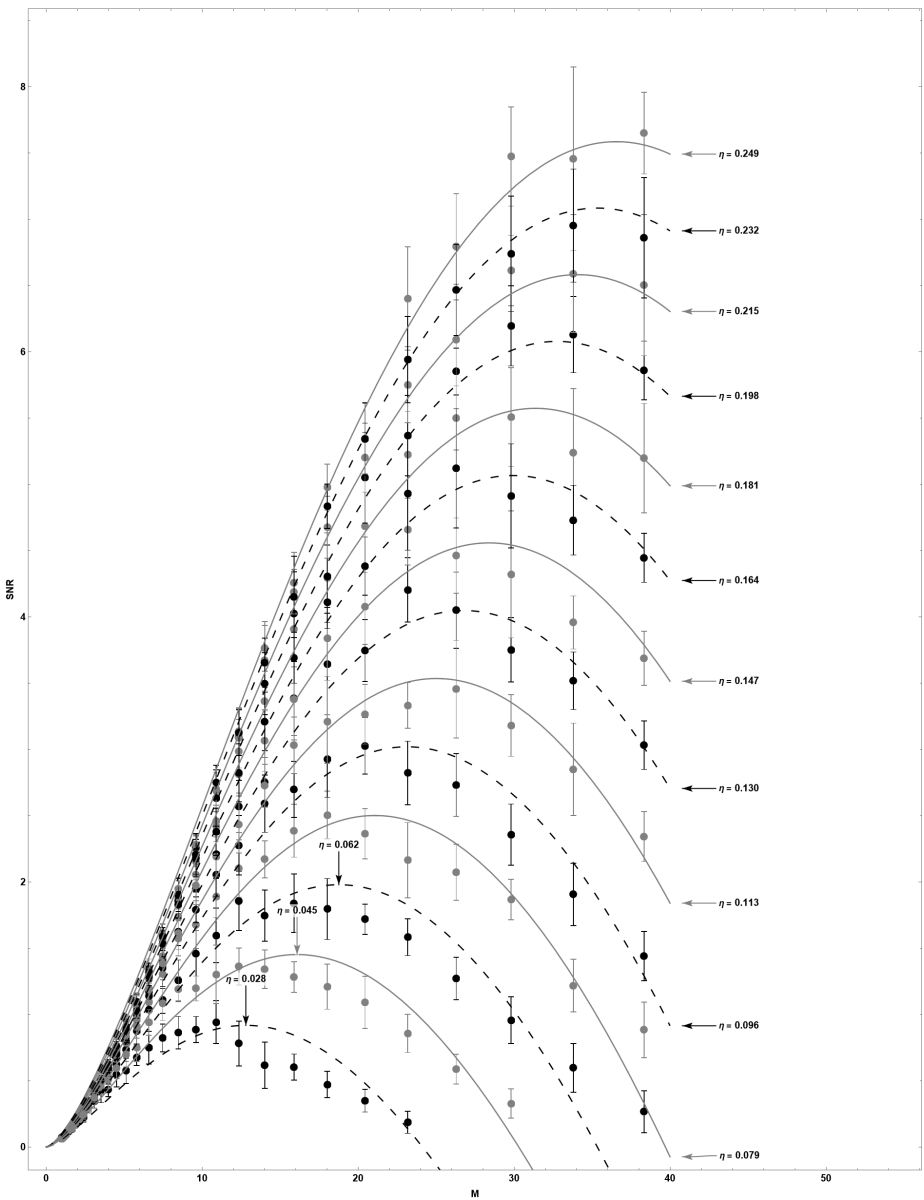


Figure B.26: Power SNR of NS4 with tensor + S modes.

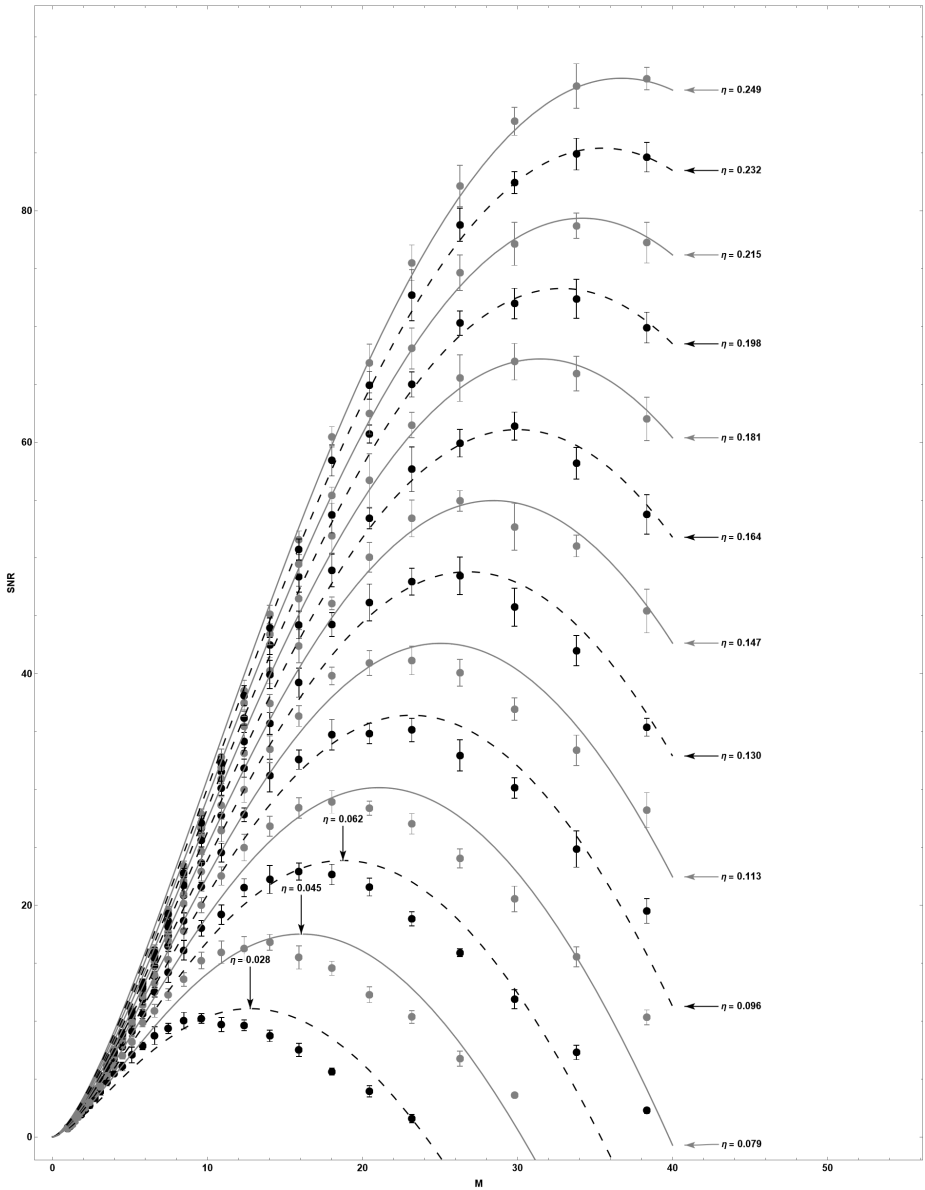


Figure B.27: Power SNR of NS4 with tensor + V modes.

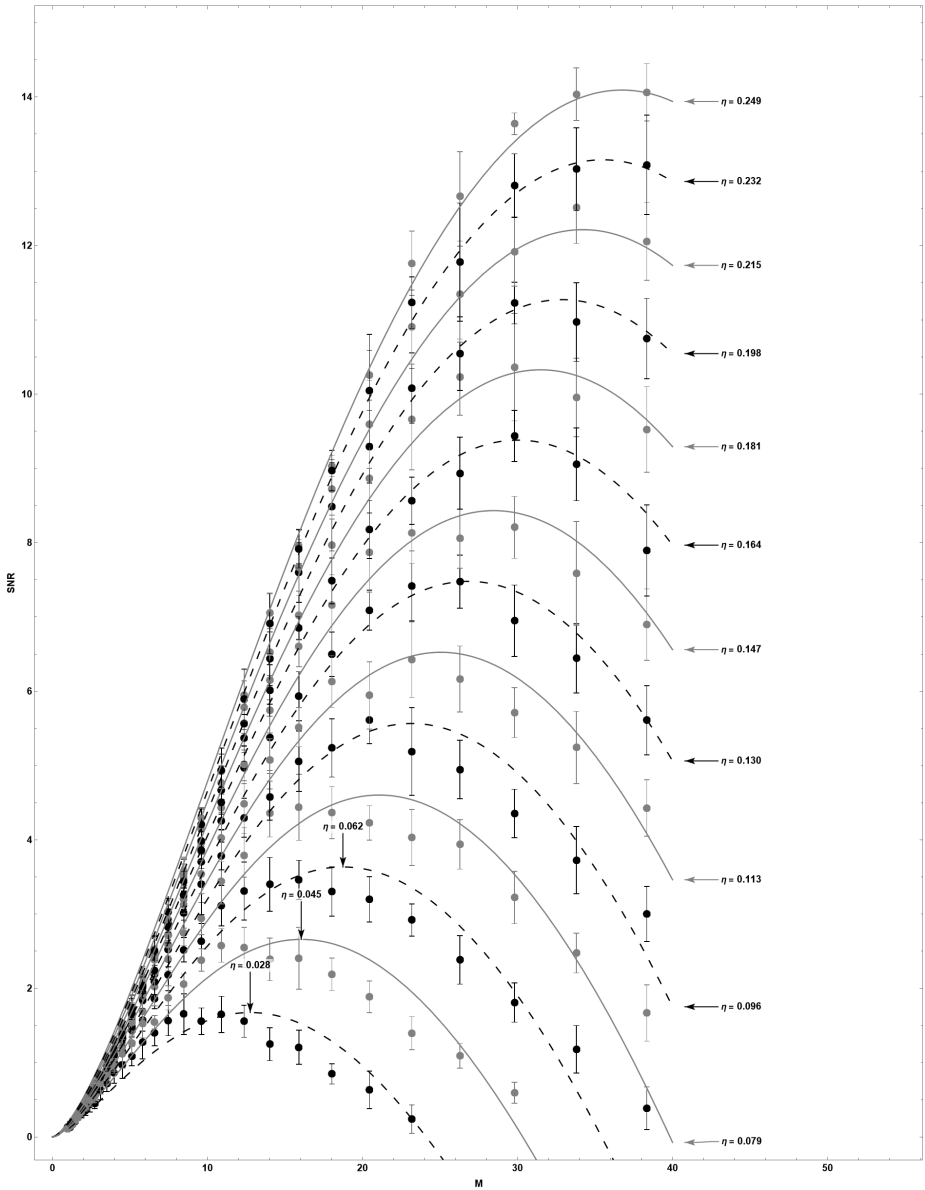


Figure B.28: Power SNR of NS4 with tensor + W modes.

HLVKI

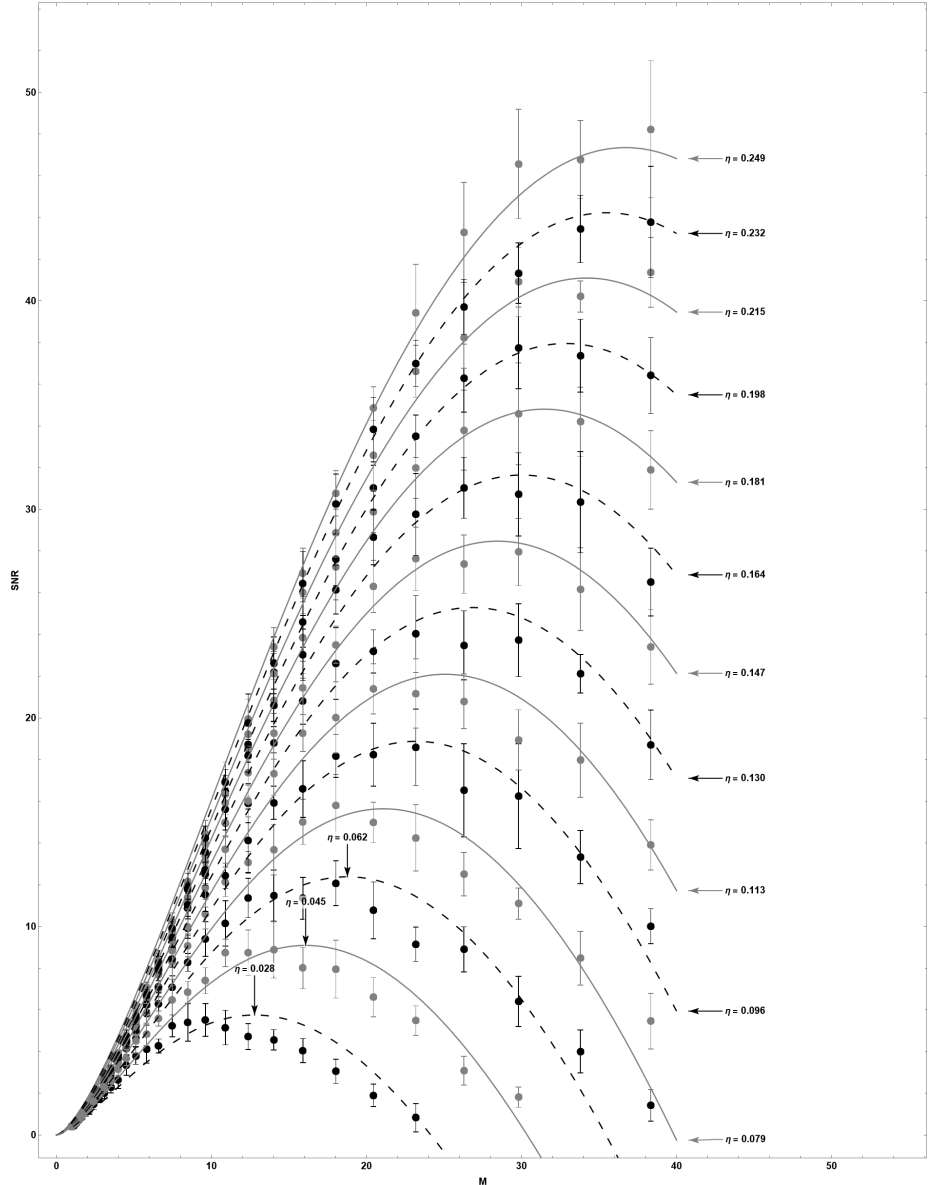


Figure B.29: Power SNR of NS1 with tensor + V modes.

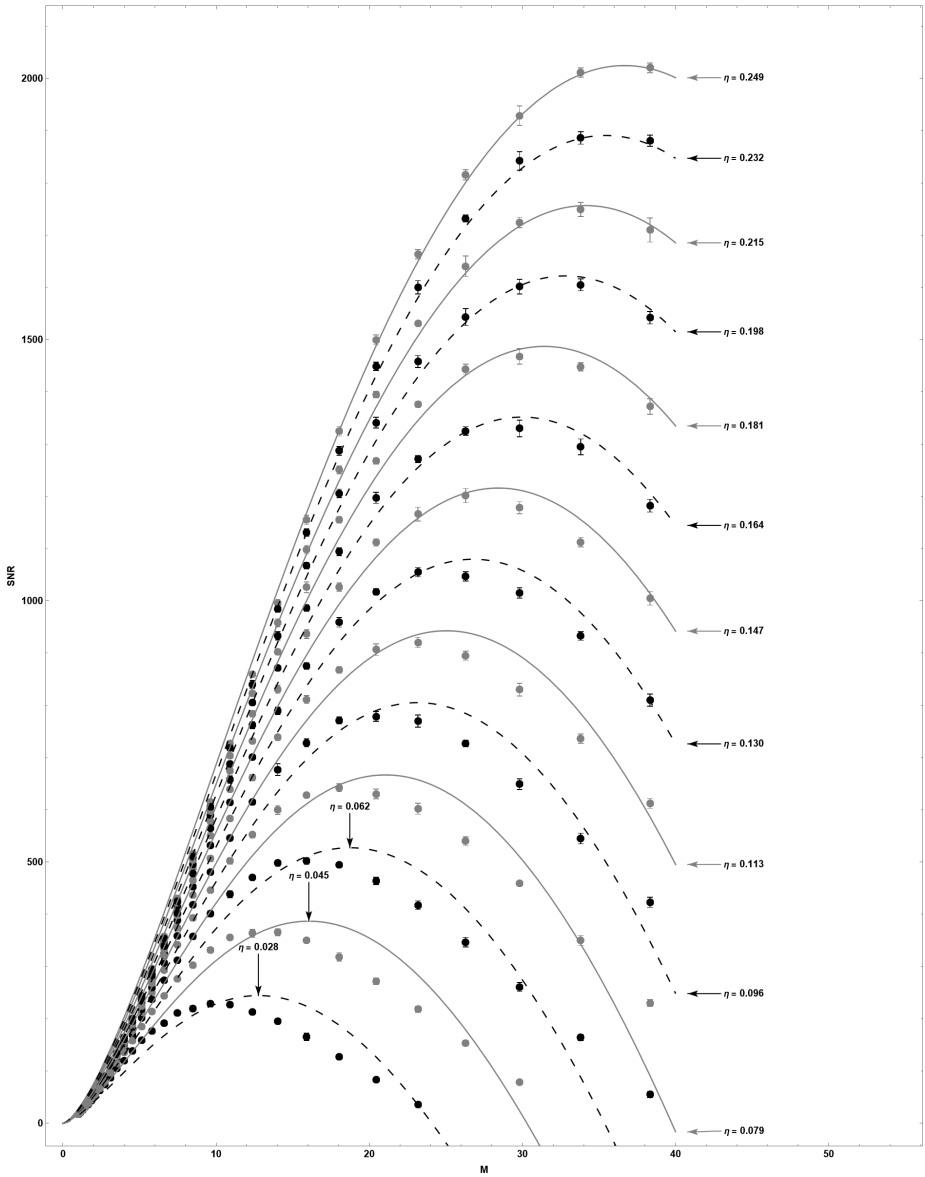


Figure B.30: Power SNR of NS1 with tensor + W modes.

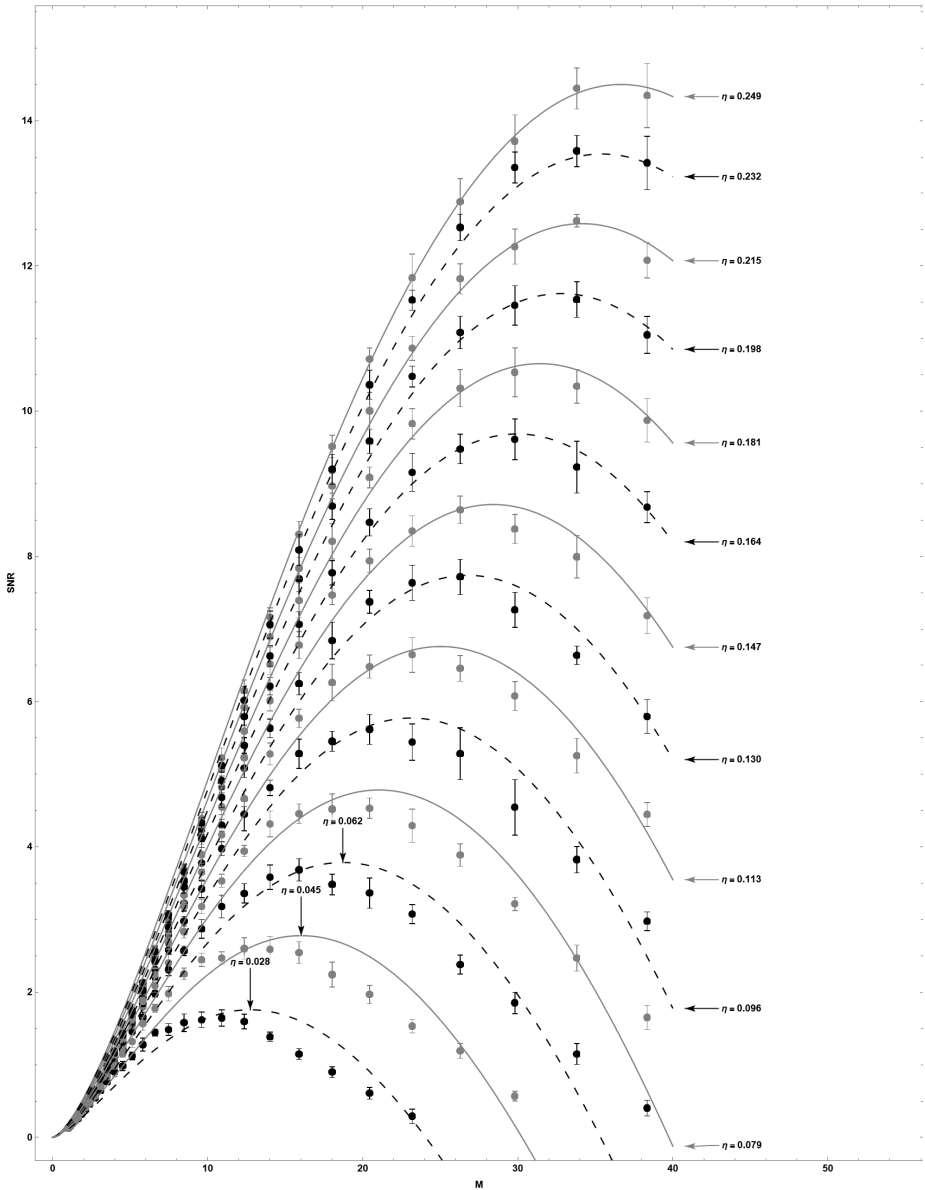


Figure B.31: Power SNR of NS2 with tensor + V modes.

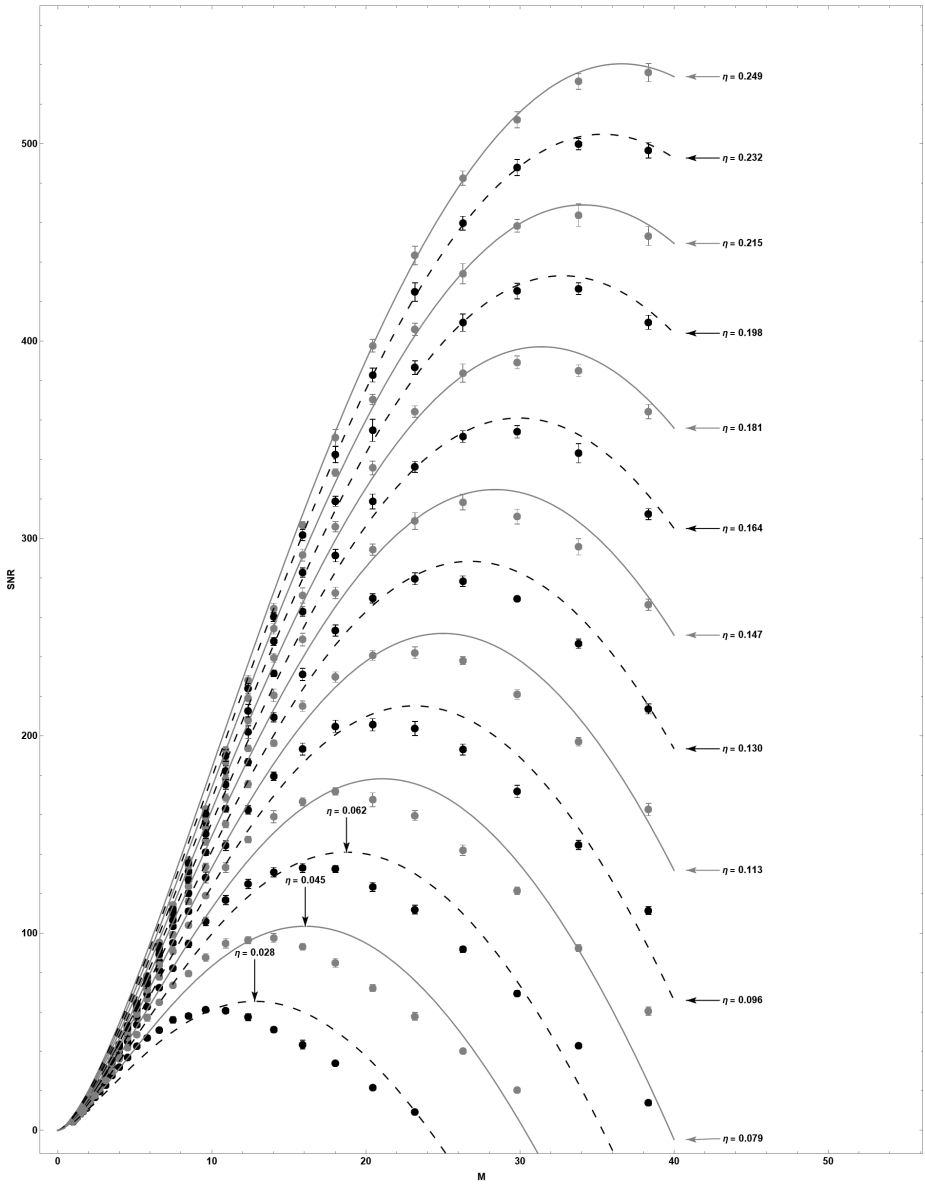


Figure B.32: Power SNR of NS2 with tensor + W modes.

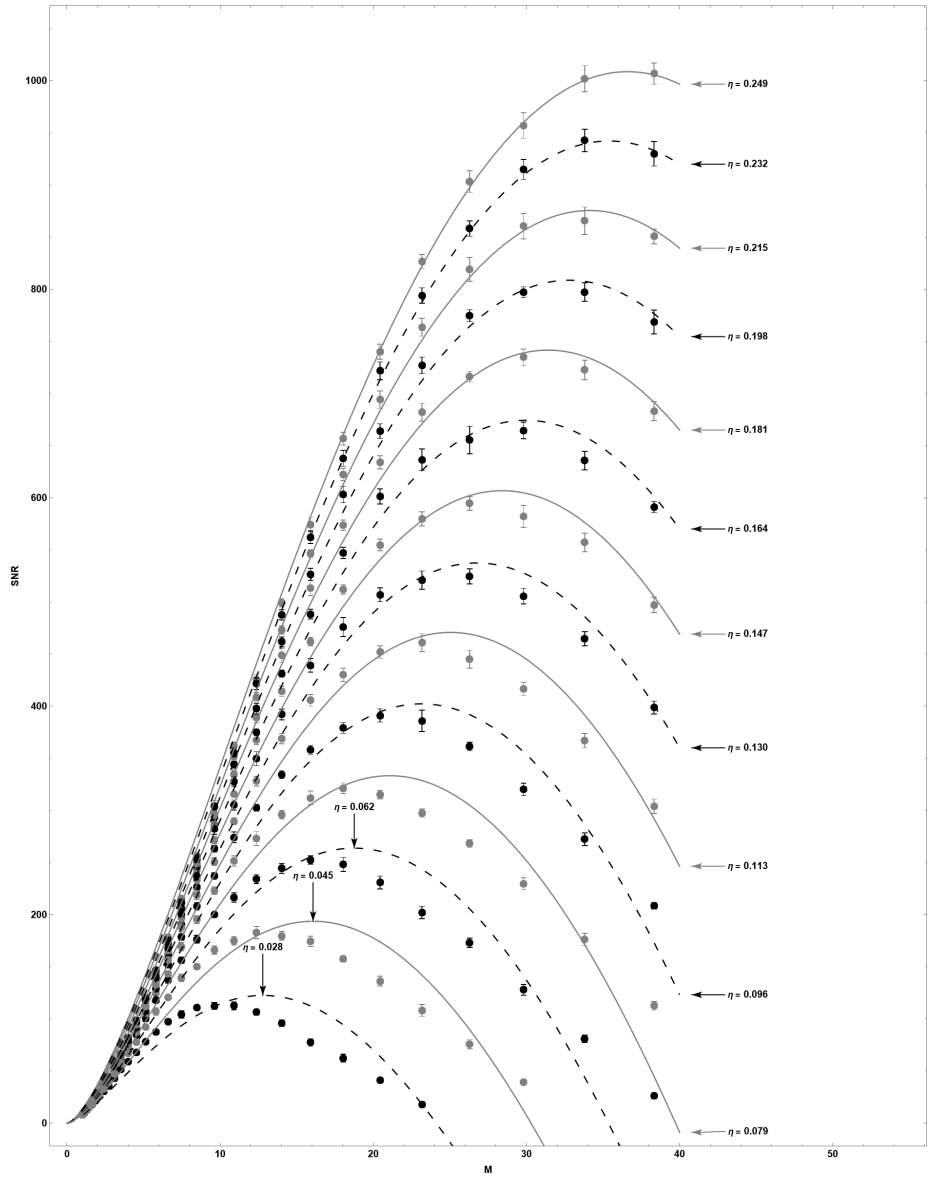


Figure B.33: Power SNR of NS3 with tensor + S modes.

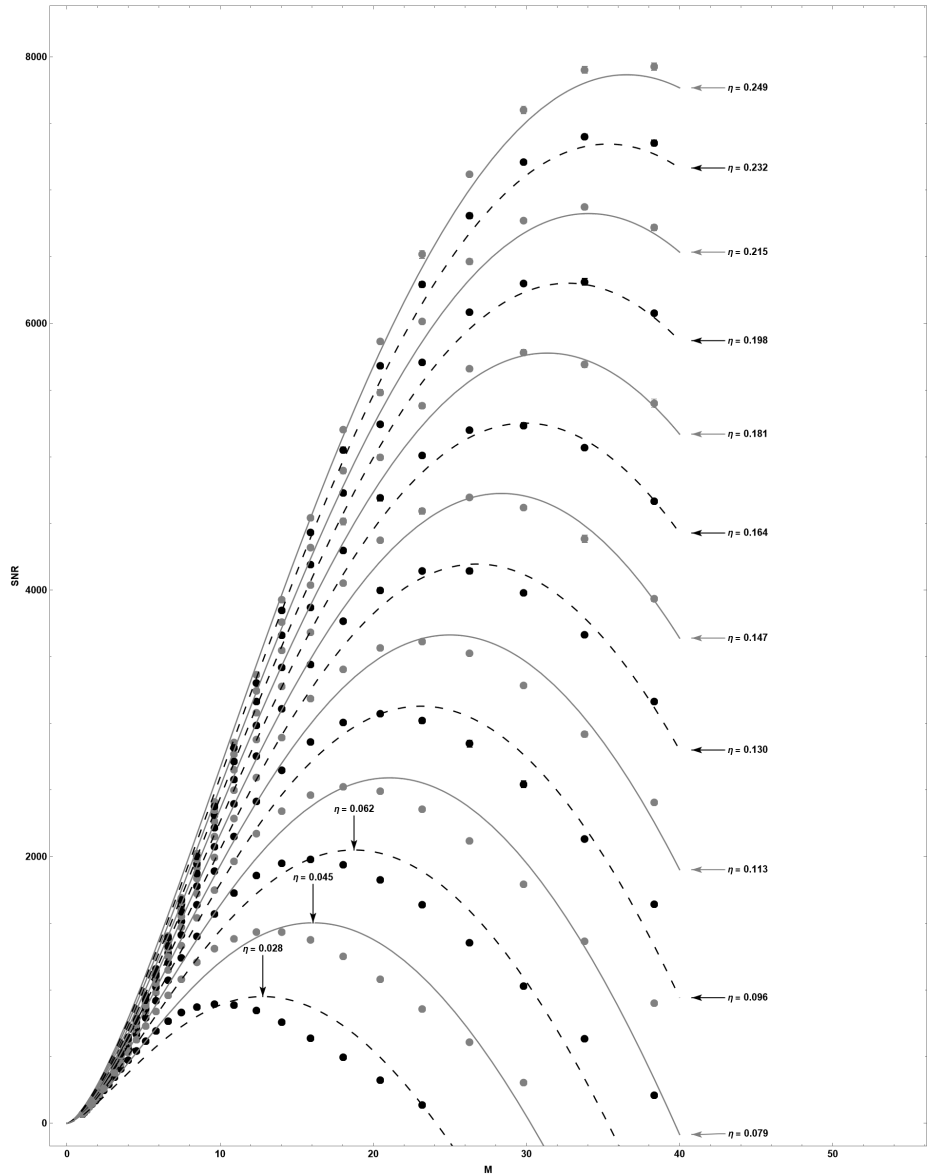


Figure B.34: Power SNR of NS3 with tensor + V modes.

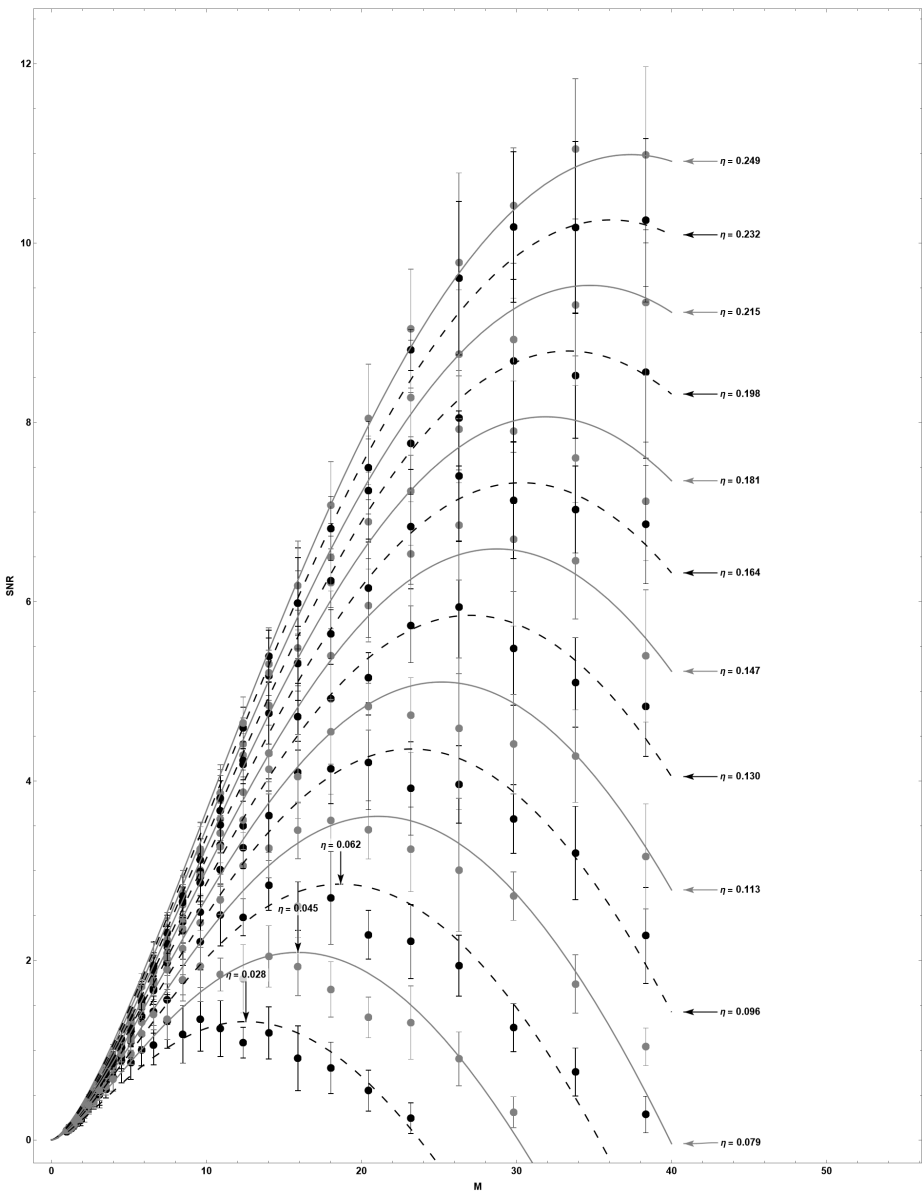


Figure B.35: Power SNR of NS4 with tensor + S modes.

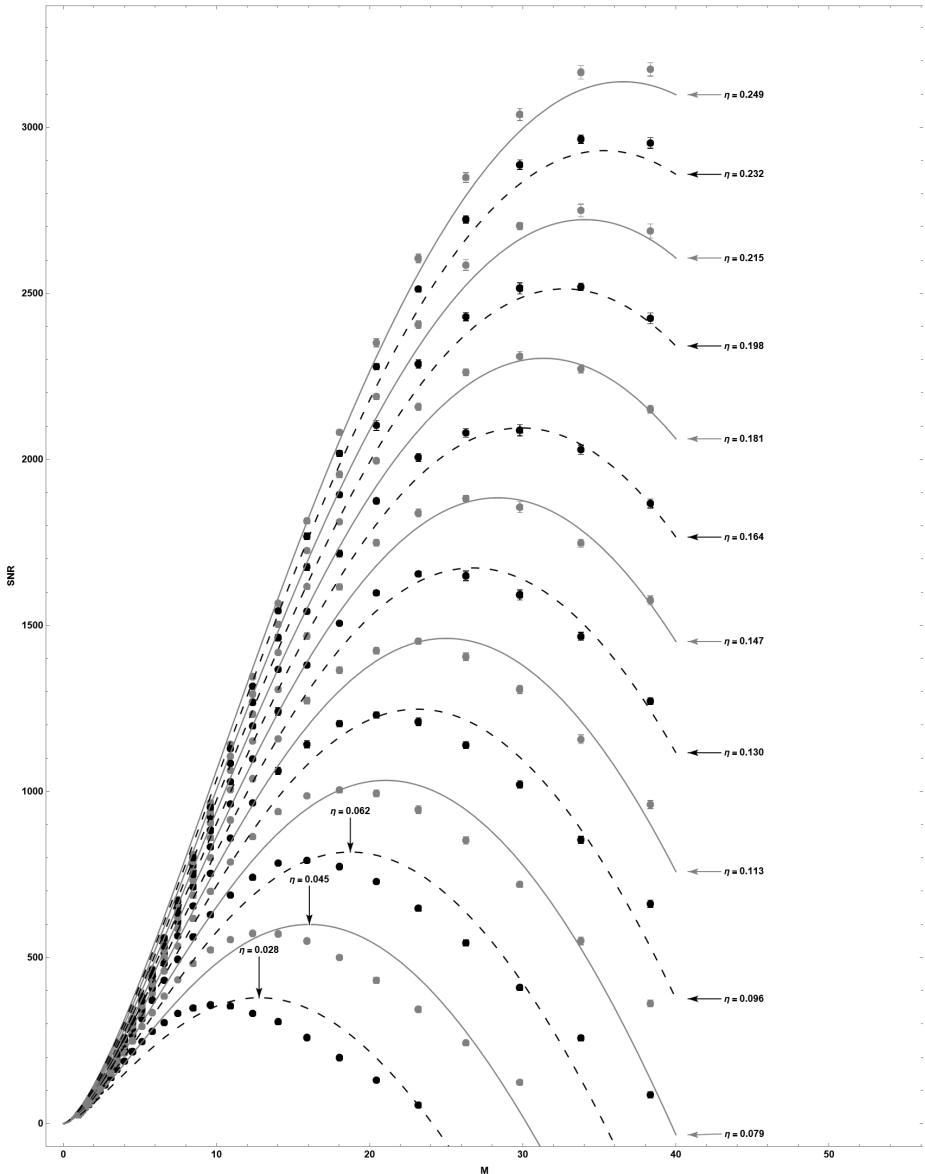


Figure B.36: Power SNR of NS4 with tensor + W modes.

ETCE

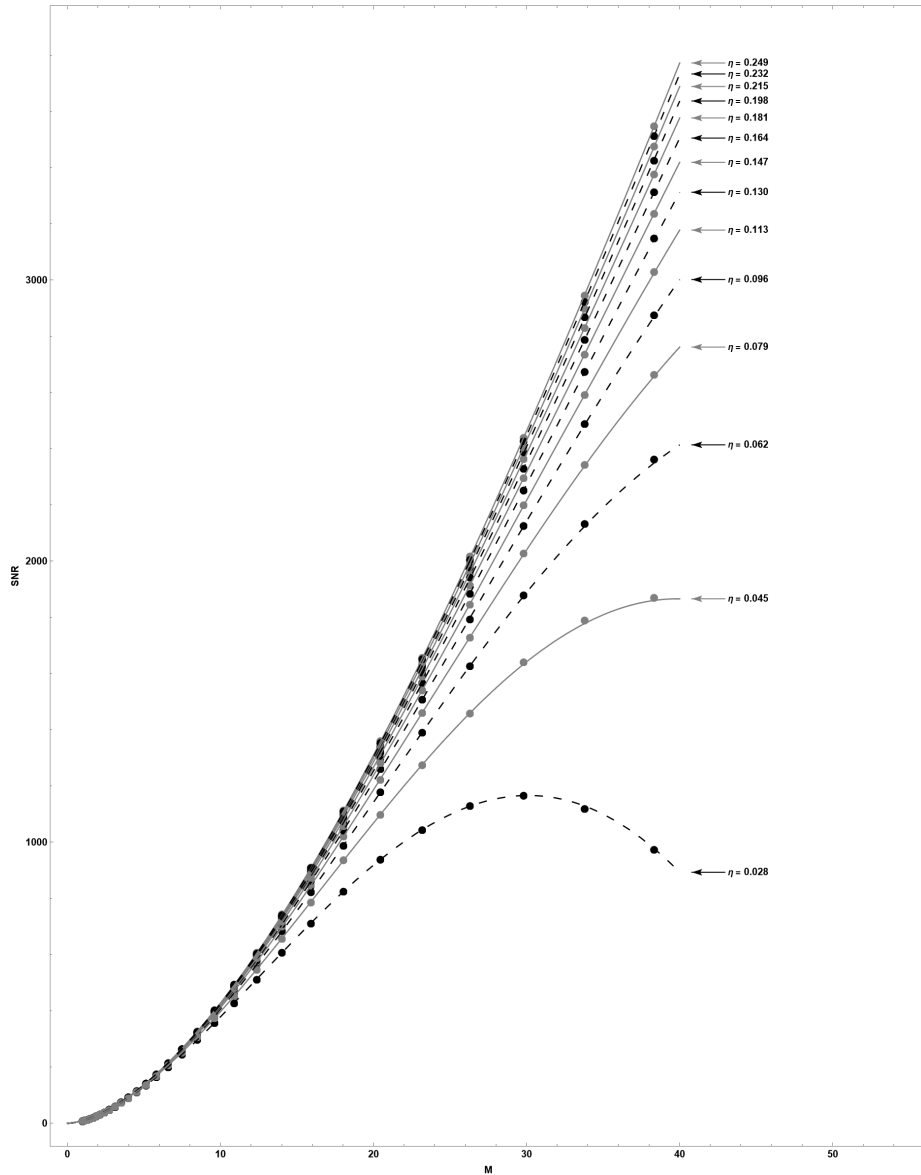


Figure B.37: Power SNR of NS1 with tensor + S modes.

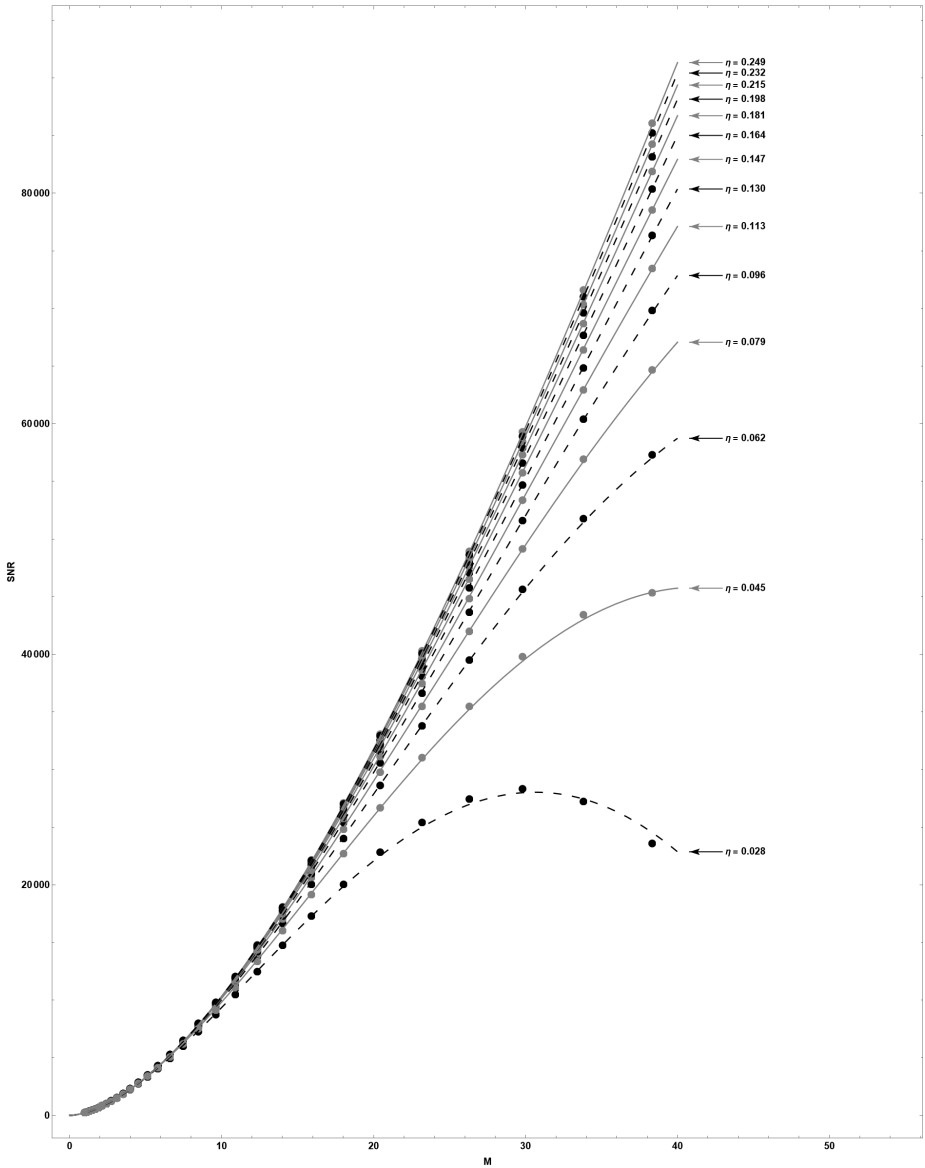


Figure B.38: Power SNR of NS1 with tensor + V modes.

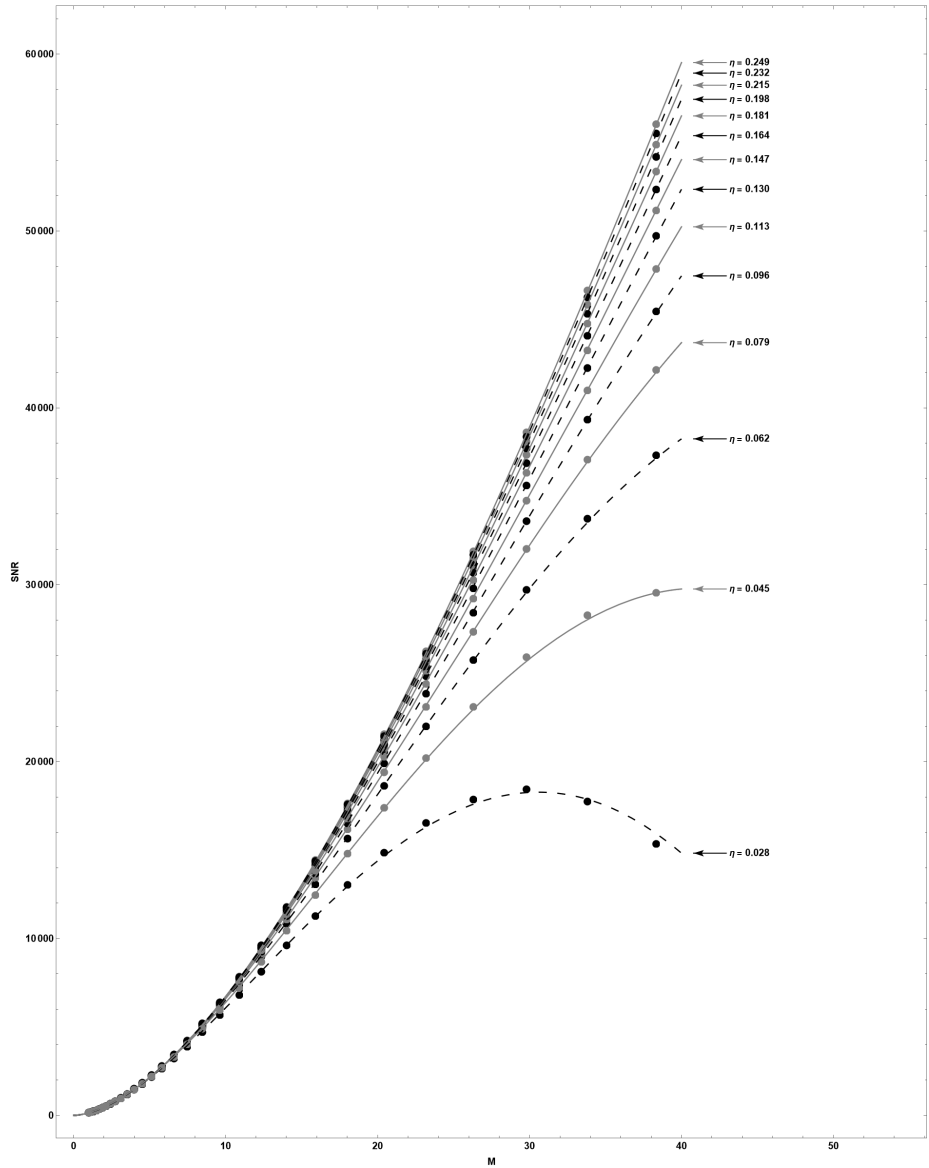


Figure B.39: Power SNR of NS1 with tensor + W modes.

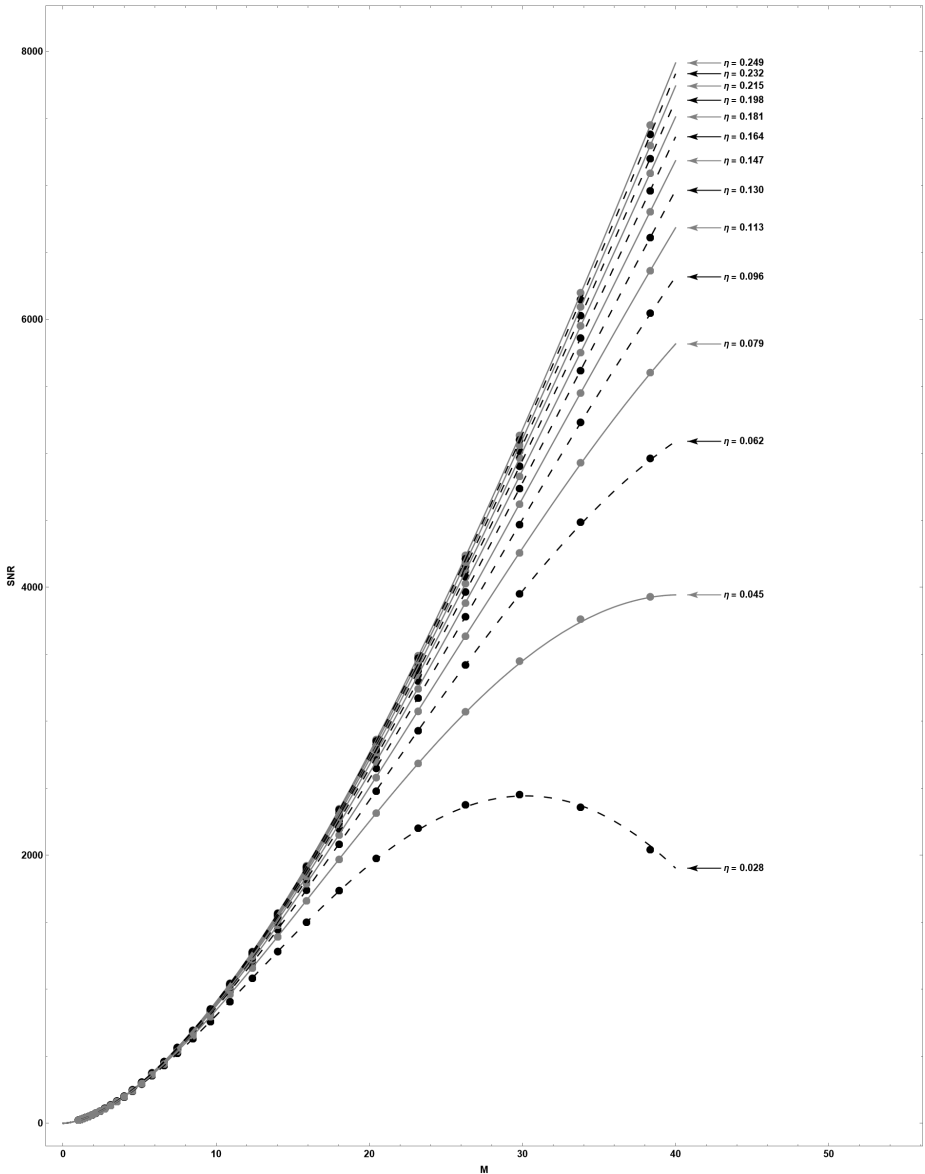


Figure B.40: Power SNR of NS2 with tensor + V modes.

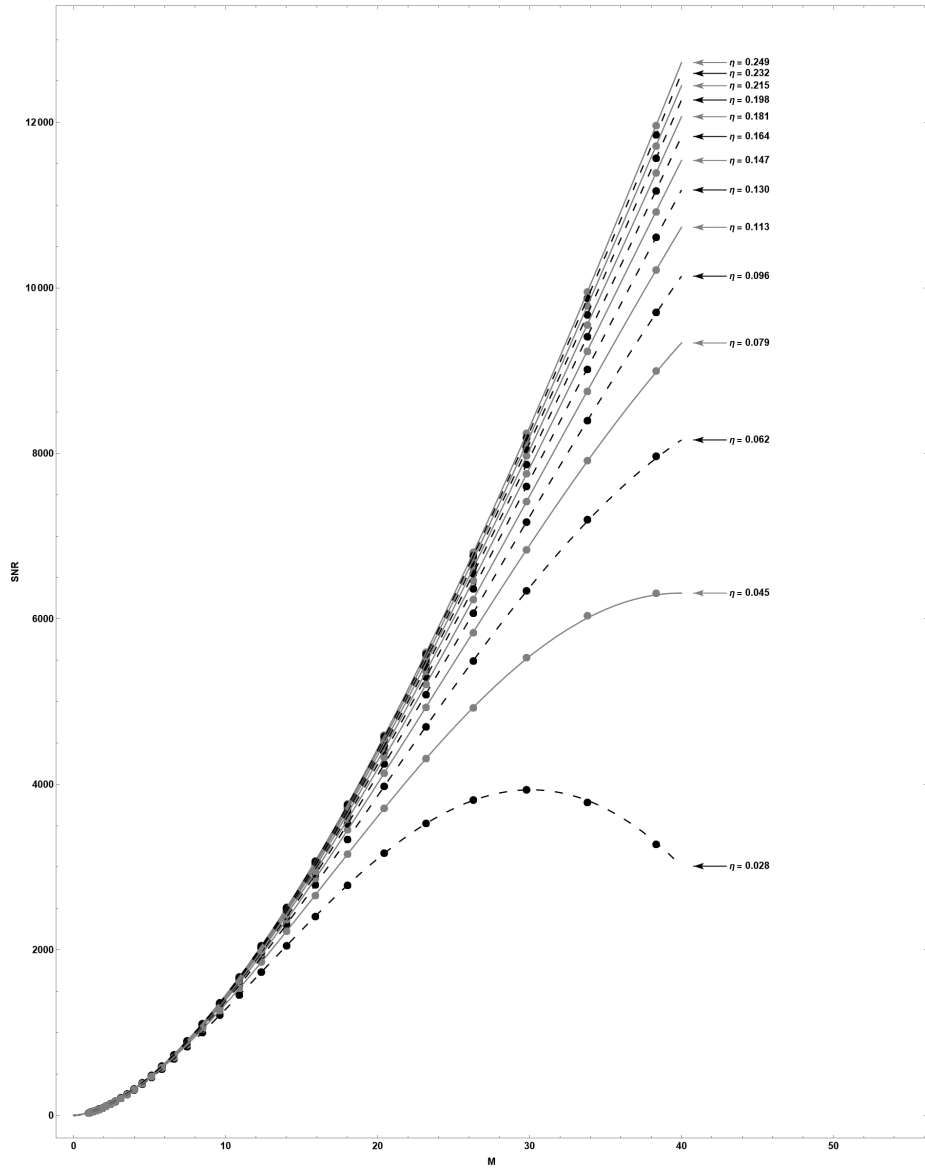


Figure B.41: Power SNR of NS2 with tensor + W modes.

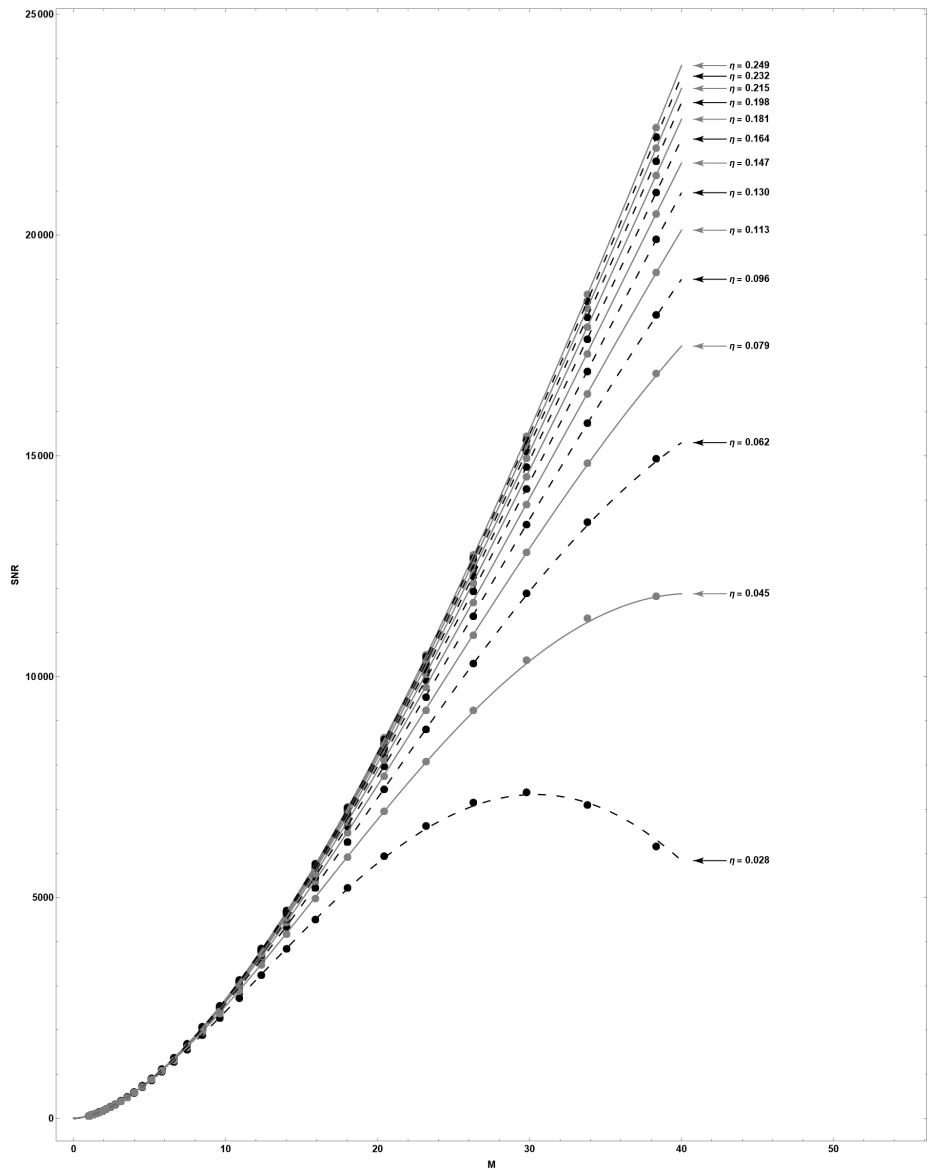


Figure B.42: Power SNR of NS3 with tensor + S modes.

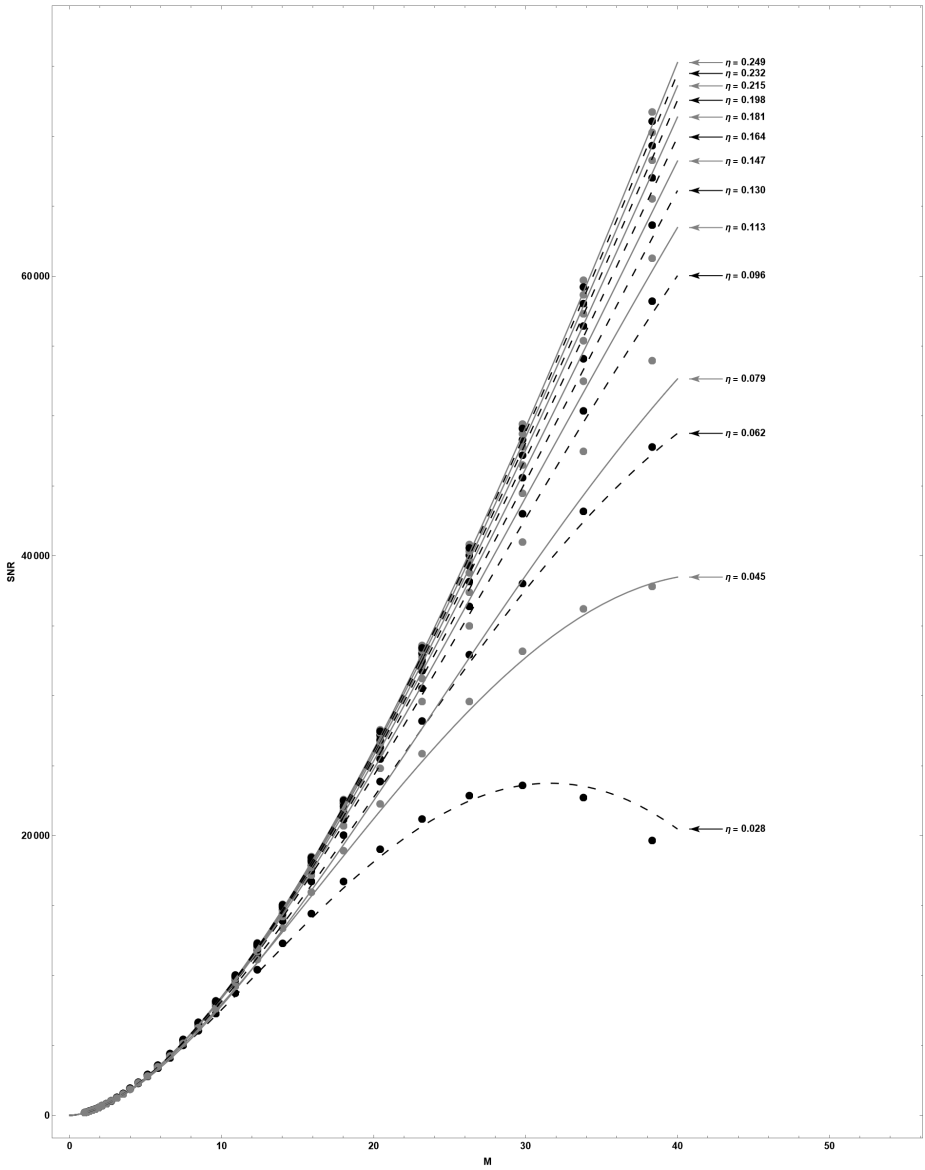


Figure B.43: Power SNR of NS3 with tensor + V modes.

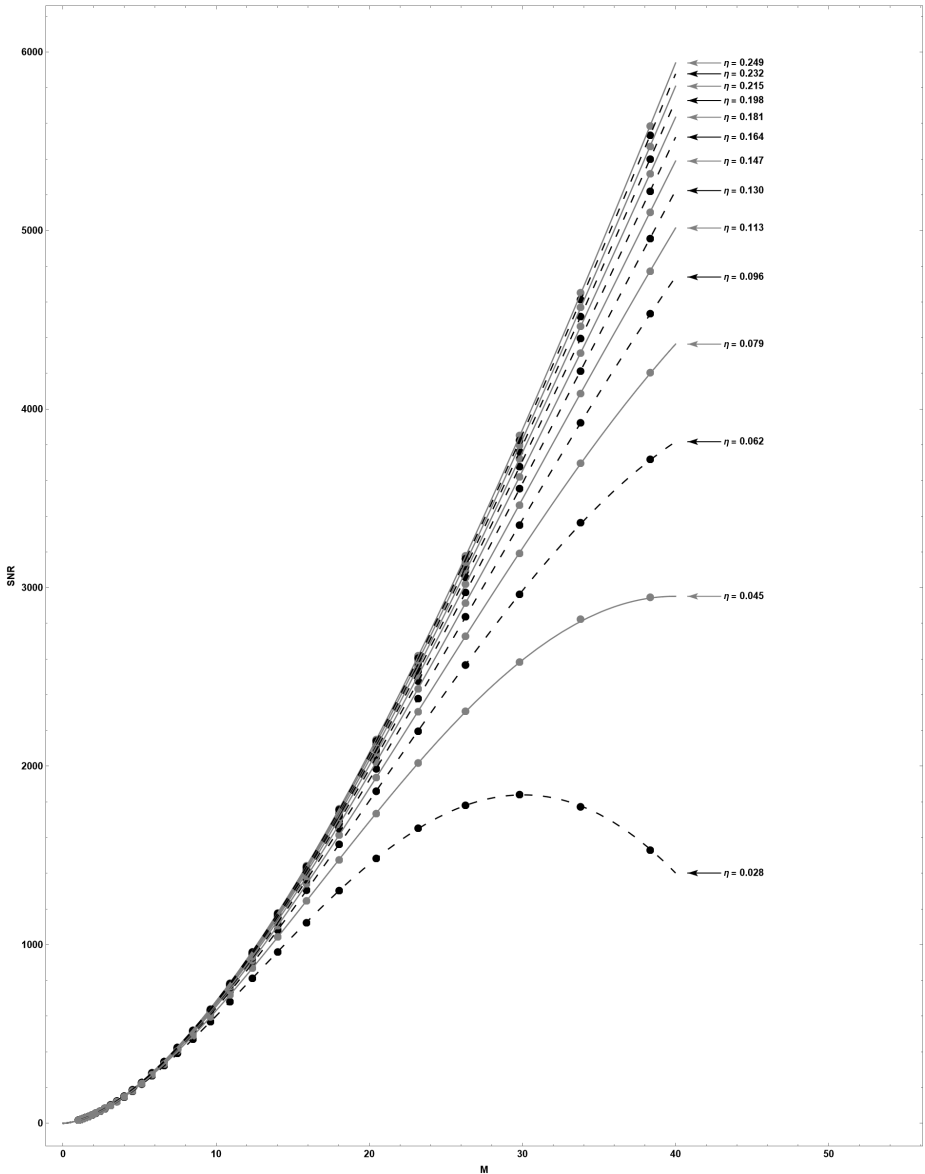


Figure B.44: Power SNR of NS4 with tensor + S modes.

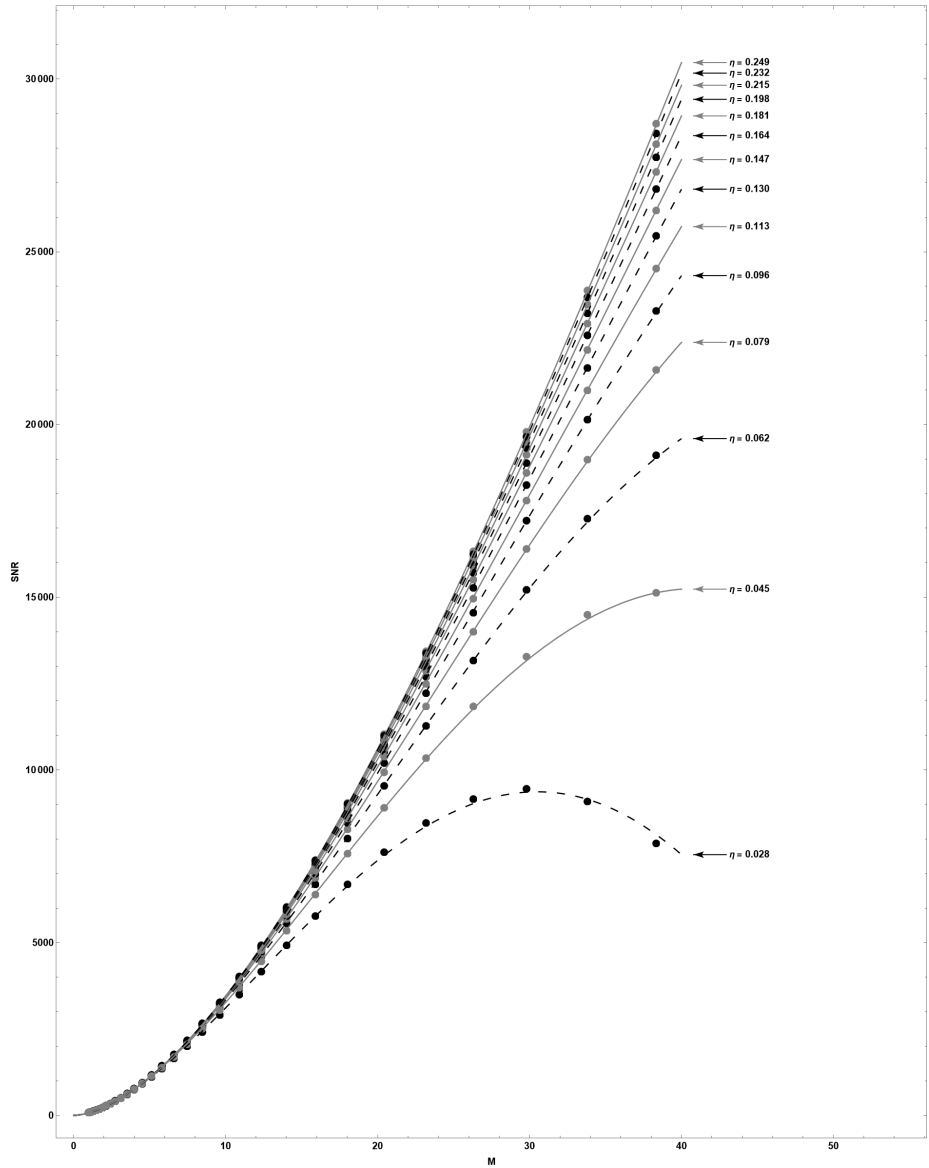


Figure B.45: Power SNR of NS4 with tensor + W modes.

B.3 Three Detector Maps

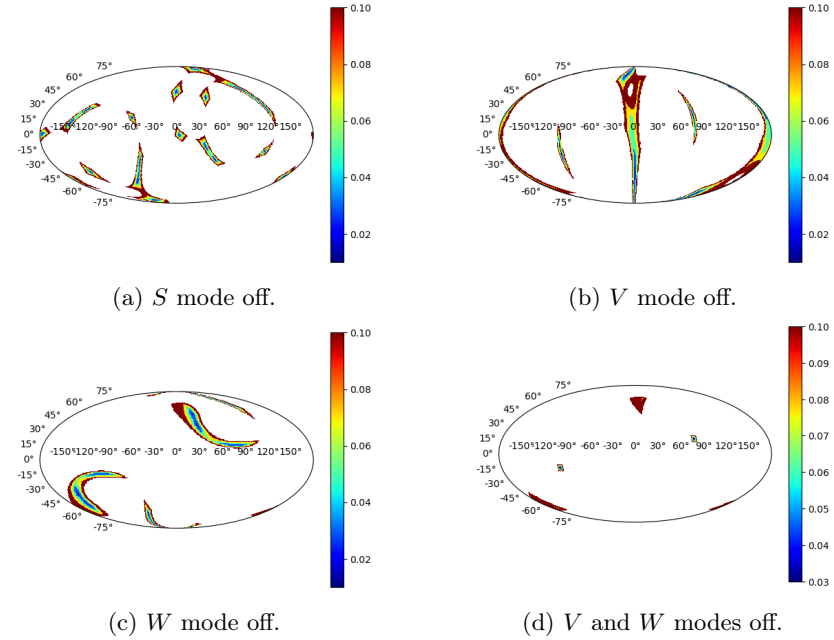


Figure B.46: LVKI

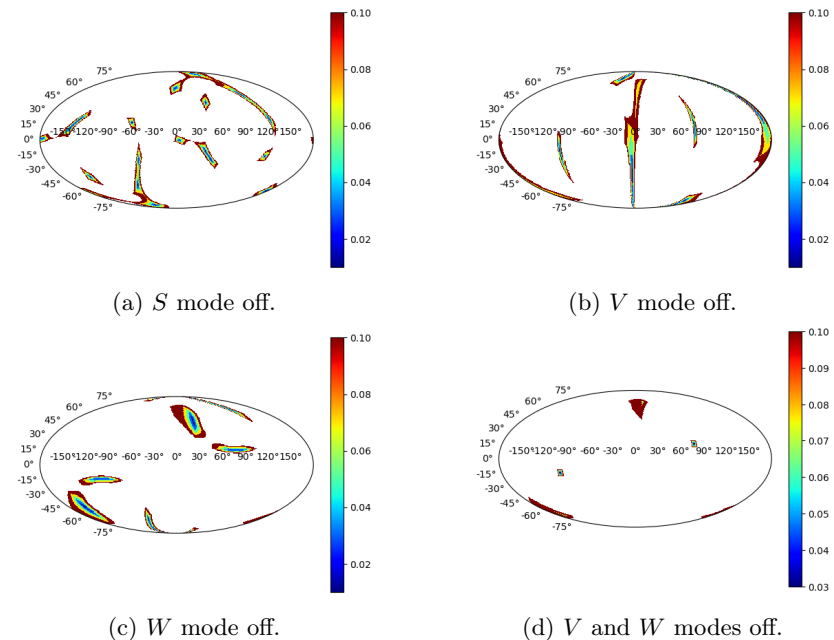


Figure B.47: HVKI

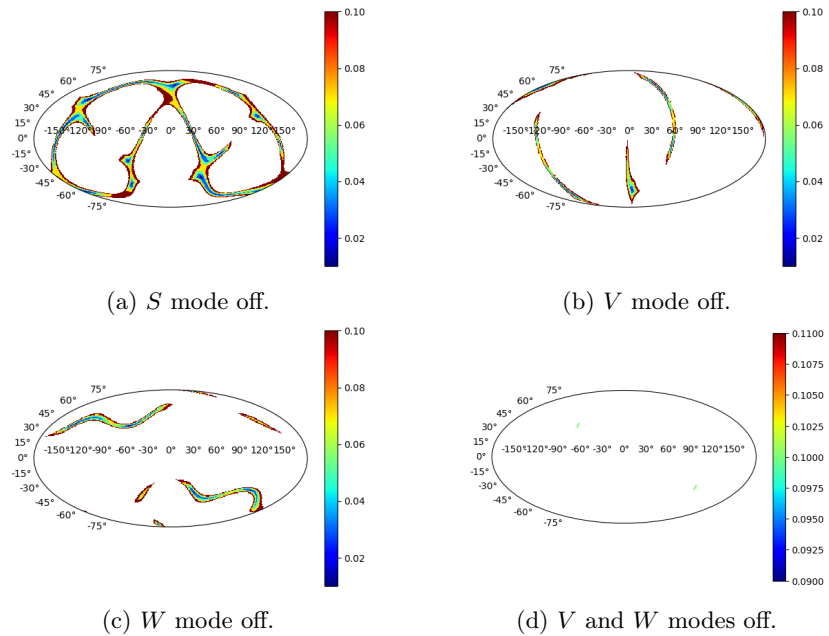


Figure B.48: HLKI

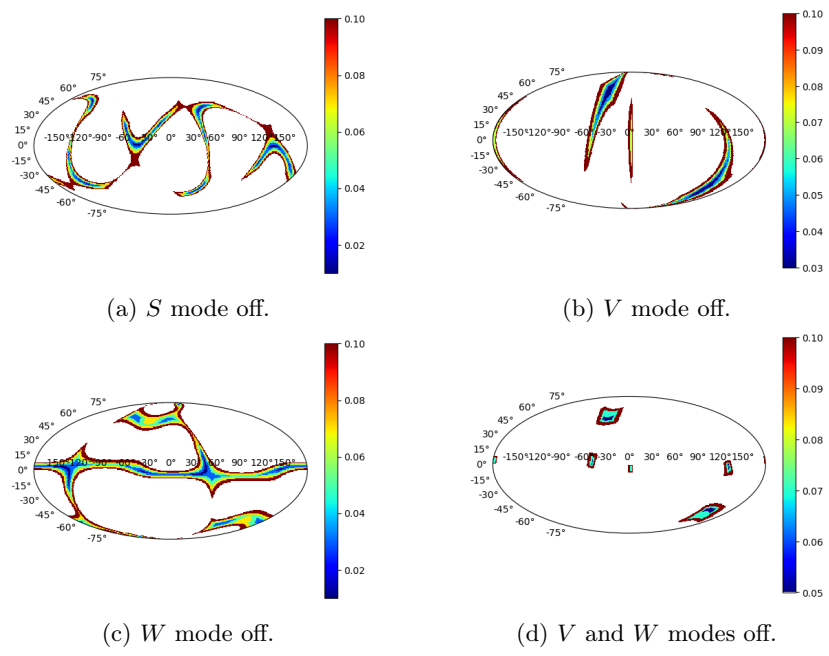


Figure B.49: HLV1

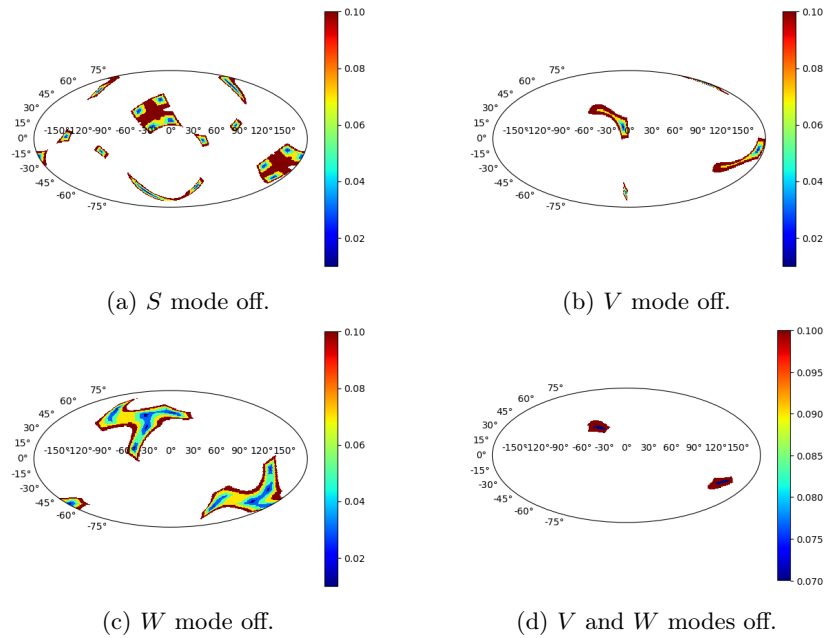


Figure B.50: 2 ET + 2 CE

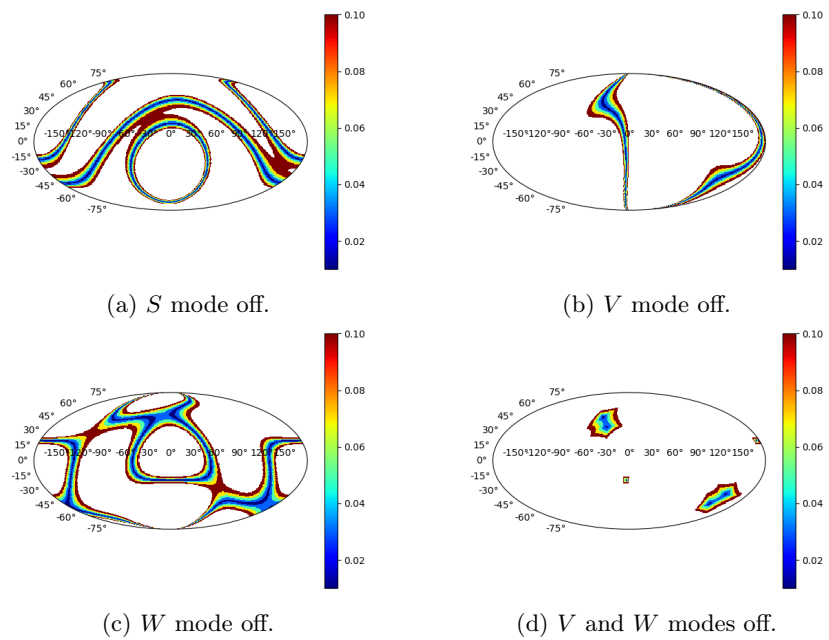


Figure B.51: 3 ET + CE South

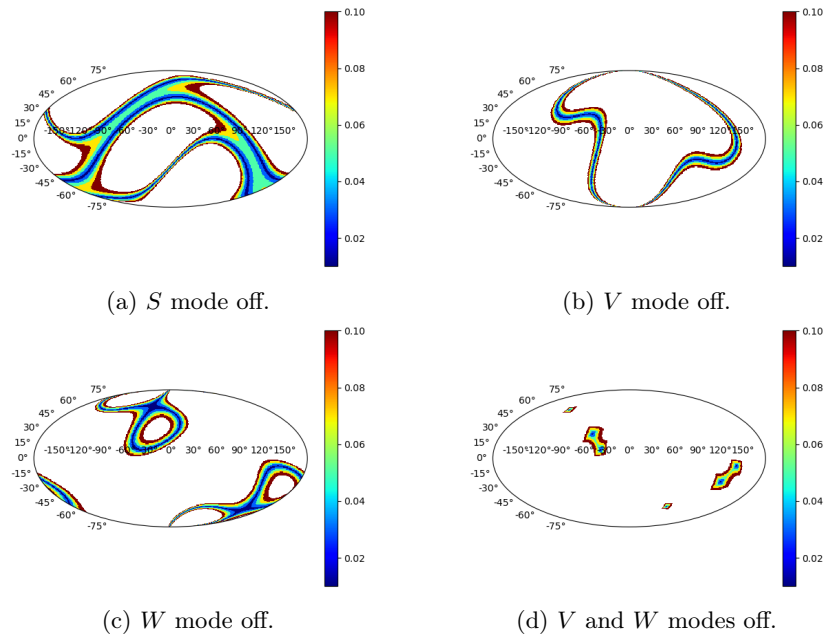


Figure B.52: 3 ET + CE North

Bibliography

- [1] Albert Einstein. Die feldgleichungen der gravitation. *Sitzungsberichte der Königlich Preußischen Akademie der Wissenschaften*, pages 844–847, 1915.
- [2] Albert Einstein. Näherungsweise integration der feldgleichungen der gravitation. *Sitzungsberichte der Königlich Preußischen Akademie der Wissenschaften*, pages 688–696, 1916.
- [3] Albert Einstein. Über gravitationswellen. *Sitzungsberichte der Königlich Preussischen Akademie der Wissenschaften*, pages 154–167, 1918.
- [4] Benjamin P. Abbott, Richard Abbott, T. De. Abbott, M.R. Abernathy, Fausto Acernese, Kendall Ackley, Carl Adams, Thomas Adams, Paolo Adesso, R.X. Adhikari, et al. Observation of gravitational waves from a binary black hole merger. *Physical review letters*, 116(6):061102, 2016.
- [5] Maximiliano Isi and Alan J. Weinstein. Probing gravitational wave polarizations with signals from compact binary coalescences. *arXiv preprint arXiv:1710.03794*, 2017.
- [6] Hiroki Takeda, Atsushi Nishizawa, Yuta Michimura, Koji Nagano, Kentaro Komori, Masaki Ando, and Kazuhiro Hayama. Polarization test of gravitational waves from compact binary coalescences. *Physical Review D*, 98(2):022008, 2018.
- [7] Ssohrab Borhanian. GWBENCH: a novel Fisher information package for gravitational-wave benchmarking. *Classical and Quantum Gravity*, 38(17):175014, 2021.
- [8] Abraham Pais. Subtle is the lord- " : the science and the life of albert einstein. 1982.
- [9] Dean Rickles and Cécile M DeWitt. The role of gravitation in physics: report from the 1957 Chapel Hill Conference. In *The Role of Gravitation in Physics: Report from the 1957 Chapel Hill Conference*, 2011.
- [10] Frederic A. Rasio and Stuart L. Shapiro. Coalescing binary neutron stars. *Classical and Quantum Gravity*, 16(6):R1, 1999.
- [11] Swetha Bhagwat. Finding nonlinearities in black hole ringdowns. *Physics*, 16:29, 2023.
- [12] Kip S. Thorne, John Archibald Wheeler, and Charles W. Misner. *Gravitation*. Freeman San Francisco, CA, 2000.

- [13] Michele Maggiore. *Gravitational waves: Volume 1: Theory and experiments*. OUP Oxford, 2007.
- [14] Joseph Weber. Detection and generation of gravitational waves. *Physical Review*, 117(1):306, 1960.
- [15] Sabrina D’Antonio, Archana Pai, and Pia Astone. Validating delta-filters for resonant bar detectors of improved bandwidth foreseeing the future coincidence with interferometers. In *Journal of Physics: Conference Series*, volume 32, page 192. IOP Publishing, 2006.
- [16] Fulvio Melia. The Friedmann–Lemaître–Robertson–Walker metric. *Modern Physics Letters A*, 37(03):2250016, 2022.
- [17] Dong Lai and Alan Wiseman. Innermost stable circular orbit of inspiraling neutron-star binaries: Tidal effects, post-newtonian effects and the neutron-star equation of state. *Physical Review D*, 54, 09 1996.
- [18] Pradeep Kumar Chaudhary, Vipin Gupta, and Ram Bilas Pachori. Fourier-bessel representation for signal processing: A review. *Digital Signal Processing*, page 103938, 2023.
- [19] Alan Weinstein. Advanced LIGO optical configuration and prototyping effort. *Classical and Quantum Gravity*, 19(7):1575, 2002.
- [20] Malvin C. Teich and Bahaa E.A. Saleh. Squeezed state of light. *Quantum Optics: Journal of the European Optical Society Part B*, 1(2):153, 1989.
- [21] Peter R. Saulson. Thermal noise in mechanical experiments. *Physical Review D*, 42(8):2437, 1990.
- [22] David Blair, Li Ju, ChunNong Zhao, LinQing Wen, HaiXing Miao, RongGen Cai, JiangRui Gao, XueChun Lin, Dong Liu, Ling-An Wu, et al. The next detectors for gravitational wave astronomy. *Science China Physics, Mechanics & Astronomy*, 58:1–34, 2015.
- [23] Edward K. Porter and Neil J. Cornish. Fisher versus Bayes: A comparison of parameter estimation techniques for massive black hole binaries to high redshifts with eLISA. *Physical Review D*, 91(10):104001, 2015.
- [24] Curt Cutler and Eanna E. Flanagan. Gravitational waves from merging compact binaries: How accurately can one extract the binary’s parameters from the inspiral waveform? *Physical Review D*, 49(6):2658, 1994.
- [25] KAGRA Collaboration, LIGO Scientific Collaboration, and Virgo Collaboration. Advanced ligo, advanced virgo and kagra observing run plans, 2019.
- [26] Carlo Bradaschia, R. Del Fabbro, A. Di Virgilio, A. Giazotto, H. Kautzky, V. Montelatici, D. Passuello, A. Brillet, O. Cregut, P. Hello, et al. The Virgo project: a wide band antenna for gravitational wave detection. *Nuclear Instruments and Methods in Physics Research Section A: Accelerators, Spectrometers, Detectors and Associated Equipment*, 289(3):518–525, 1990.

- [27] Stanislav Babak, Martin Hewitson, and Antoine Petiteau. LISA Sensitivity and SNR Calculations, 2021.
- [28] Matthew Evans, Rana X. Adhikari, Chaitanya Afle, Stefan W. Ballmer, Sylvia Biscoveanu, Ssohrab Borhanian, Duncan A. Brown, Yanbei Chen, Robert Eisenstein, Alexandra Gruson, et al. A horizon study for Cosmic Explorer: science, observatories, and community. *arXiv preprint arXiv:2109.09882*, 2021.
- [29] Massimo Granata, Christelle Buy, Robert Ward, and Matteo Barsuglia. Higher-order Laguerre-Gauss mode generation and interferometry for gravitational wave detectors. *Physical review letters*, 105(23):231102, 2010.
- [30] Matt Abernathy, F. Acernese, P. Ajith, B. Allen, P. Amaro Seoane, N. Andersson, S. Aoudia, P. Astone, B. Krishnan, L. Barack, et al. Einstein gravitational wave telescope conceptual design study. 2011.
- [31] Tarun Souradeep, Sendhil Raja, Ziauddin Khan, C.S. Unnikrishnan, and Bala Iyer. LIGO-India—a unique adventure in Indian science. *Current Science*, pages 672–677, 2017.
- [32] C.S. Unnikrishnan. IndIGO and LIGO-India: Scope and plans for gravitational wave research and precision metrology in India. *International Journal of Modern Physics D*, 22(01):1341010, 2013.
- [33] Yuki Haghara, Naoya Era, Daisuke Iikawa, Atsushi Nishizawa, and Hideki Asada. Constraining extra gravitational wave polarizations with advanced LIGO, advanced Virgo, and KAGRA and upper bounds from GW170817. *Physical Review D*, 100(6):064010, 2019.
- [34] Yuki Haghara, Naoya Era, Daisuke Iikawa, Naohiro Takeda, and Hideki Asada. Condition for directly testing scalar modes of gravitational waves by four detectors. *Physical Review D*, 101(4):041501, 2020.
- [35] Wolfram Research, Inc. Mathematica, Version 13.3. Champaign, IL, 2023.
- [36] Linqing Wen and Bernard F. Schutz. Coherent network detection of gravitational waves: the redundancy veto. *Classical and Quantum Gravity*, 22(18):S1321, 2005.
- [37] Piotr Jaranowski, Andrzej Krolak, and Bernard F. Schutz. Data analysis of gravitational-wave signals from spinning neutron stars: The signal and its detection. *Physical Review D*, 58(6):063001, 1998.
- [38] Alan P. Lightman and David L. Lee. New two-metric theory of gravity with prior geometry. *Physical Review D*, 8(10):3293, 1973.
- [39] G.A. Alekseev and V.I. Khlebnikov. Newman-Penrose formalism and its application in the general theory of relativity. *Sov. J. Particles Nucl. (Engl. Transl.);(United States)*, 9(5), 1978.
- [40] Marcio E.S. Alves, Oswaldo D. Miranda, and Jose C.N. de Araujo. Probing the f(R) formalism through gravitational wave polarizations. *Physics Letters B*, 679(4):401–406, 2009.

- [41] Douglas M. Eardley, David L. Lee, and Alan P. Lightman. Gravitational-wave observations as a tool for testing relativistic gravity. *Physical Review D*, 8(10):3308, 1973.
- [42] Hiroki Takeda, Atsushi Nishizawa, Koji Nagano, Yuta Michimura, Kentaro Komori, Masaki Ando, and Kazuhiro Hayama. Prospects for gravitational-wave polarization tests from compact binary mergers with future ground-based detectors. *Physical Review D*, 100(4):042001, 2019.
- [43] Yekta Gürsel and Massimo Tinto. Near optimal solution to the inverse problem for gravitational-wave bursts. *Physical Review D*, 40(12):3884, 1989.
- [44] Yuki Haghara, Naoya Era, Daisuke Iikawa, and Hideki Asada. Probing gravitational wave polarizations with advanced ligo, advanced virgo, and kagra. *Physical Review D*, 98(6):064035, 2018.
- [45] B. P. Abbott et al. GW170817: Observation of gravitational waves from a binary neutron star inspiral. *Physical Review Letters*, 119(16), oct 2017.
- [46] Kevin Hurley, I.G. Mitrofanov, D. Golovin, M.L. Litvak, A.B. Sanin, W. Boynton, C. Fellows, K. Harshman, R. Starr, S. Golenetskii, et al. The interplanetary network. *EAS Publications Series*, 61:459–464, 2013.
- [47] Kevin C. Hurley. Gamma-ray burst triangulation with a near-earth network. *The Astrophysical Journal*, 905(1):82, 2020.
- [48] O.J. Roberts, Péter Veres, M.G. Baring, M.S. Briggs, C. Kouveliotou, E. Bissaldi, G. Younes, S.I. Chastain, J.J. DeLaunay, D. Huppenkothen, et al. Rapid spectral variability of a giant flare from a magnetar in ngc 253. *Nature*, 589(7841):207–210, 2021.
- [49] Benjamin P. et al. Abbott. GW170814: a three-detector observation of gravitational waves from a binary black hole coalescence. *Physical review letters*, 119(14):141101, 2017.
- [50] Vaibhav Tiwari and Stephen Fairhurst. The emergence of structure in the binary black hole mass distribution. *The Astrophysical Journal Letters*, 913(2):L19, 2021.
- [51] J. Veitch et al. Parameter estimation for compact binaries with ground-based gravitational-wave observations using the LALInference software library. *Physical Review D*, 91(4), feb 2015.
- [52] N. Aghanim et al. Planck 2018 results. VI. Cosmological Parameters. *Astronomy & Astrophysics*, 641:A6, sep 2020.
- [53] Alessandra et al. Buonanno. Comparison of post-Newtonian templates for compact binary inspiral signals in gravitational-wave detectors. *Physical Review D*, 80(8):084043, 2009.
- [54] Kip S. Thorne, S. Hawking, and W. Israel. 300 years of gravitation, 1987.
- [55] Matteo Turisini, Giorgio Amati, and Mirko Cestari. LEONARDO: A Pan-European Pre-Exascale Supercomputer for HPC and AI Applications. *arXiv preprint arXiv:2307.16885*, 2023.